

**Climate change impacts on river water availability for irrigation, crop
irrigation water requirements and canal system capacity needs in an
irrigation scheme in Nepal**

Santosh Kaini

B. Eng. (Civil), M.Sc. (Water Science and Eng.), M.A. (Sociology)

Institute for Sustainable Industries & Liveable Cities

College of Engineering and Science

Victoria University

Submitted in fulfilment of the requirements for the degree of
Doctor of Philosophy

March 2021



Abstract

The impacts of climate change on water resources and agriculture, accompanied by a growing population, have contributed to increasing food and water scarcity. Due to the continuing growth in population and changes in food requirement habits, the demand for agricultural products is increasing continuously. It has been projected that the rise in food demand will increase by 50-100% between 2009 to 2050. The irrigation sector plays a crucial role in the agricultural food production system, utilizing about 70% of the world's total annual water consumption. About 16% of the world's cropland is irrigated, accounting for about 44% of the world's food production.

Climate variability influences water availability for agriculture, crop water demand, and crop grain yield, rendering global food security vulnerable to climate change. Research has shown that South Asia will face negative impacts on agriculture due to climate change, and food scarcity will increase if adaptation measures are not considered.

In this regard, there is a need to investigate existing irrigation schemes by assessing the impacts of climate change on both the supply and demand sides of irrigation water simultaneously to cope with changes in future water availability and food scarcity. This research aims to holistically investigate the climate change impacts on both the supply and demand sides of irrigation water. The methodology developed in this research investigated climate change impacts on the supply and demand sides of irrigation water in the Sunsari Morang Irrigation Scheme in the Koshi River basin of Nepal. The irrigation command area is 68,000 hectares.

With this background, the objective of this research is to assess the climate change impacts on the supply and demand sides of irrigation water. This research is divided into four major components.

1. Selection of global climate models and downscaling of global climate model outputs to assess climate change impacts on daily rainfall and temperature (minimum and maximum) in the river basin and irrigation command area.
2. Future impacts of climate change on river water availability at the main irrigation canal intake.

3. Crop water requirements due to climate change.
4. The irrigation canal system's hydraulic capacity requirements for irrigation water supply in the climate change context.

Climate change is the main driver in assessing river water availability for irrigation, crop irrigation requirements, and canal system capacity needs for the future. In this study, climate change scenarios Representative Concentration Pathways (RCPs) 4.5 and 8.5 for the short-term (2016–2045), mid-century (2036–2065), and end-of-century (2071–2100) periods were considered. Representative General Circulation Models (GCMs) were selected for the study area under each climate change scenario and study period. Daily precipitation and temperature data based on selected GCMs were downscaled to a higher resolution ($10 \times 10 \text{ km}^2$). The downscaled daily precipitation and temperature data were applied to assess the climate change impacts on water availability in the river, and irrigation water demand in the irrigation command area. The irrigation canal system capacity assessment was based on water availability in the river, and irrigation water demand.

The selection of global climate models for a specific geographical location, with high capacities to represent the past and to project the likely future climate, is a crucial step when assessing climate change impacts. An advanced envelope-based selection approach for the selection of a representative global climate model has been used in this research to select a representative climate model for the Koshi River basin. A total of 105 GCM simulations and 78 GCM simulations were taken for RCP4.5 and RCP8.5 scenarios respectively for the initial selection of GCMs. The GCMs selection process involved three steps: (a) initial model selection considering changes in climatic means (mean air temperature and annual precipitation), (b) refined model selection based on projected changes in climatic extremes, and (c) final model selection based on past performance. One GCM/ensemble was selected at each corner of four climate extremes (cold/dry, warm/dry, cold/wet, and warm/wet) for RCP4.5 and RCP8.5 in the short-term (2016-2045), mid-century (2036-2065), and end-of-century (2071-2100) periods. After the selection of representative GCMs/ensembles, quantile mapping was applied for bias correction at a finer resolution of $10 \text{ km} \times 10 \text{ km}$.

The Soil and Water Assessment Tool (SWAT) hydrological model was used for hydrological modelling, and was calibrated and validated using observed river flow data measured near the headworks (intake) of the Sunsari Morang Irrigation Scheme in the Koshi River. Impacts of climate change on the flow of the Koshi River were projected for the short-term, mid-century, and end-of-century periods considering climate change scenarios RCP4.5 and RCP8.5 using downscaled daily precipitation and temperature data.

The Agricultural Production Systems Simulator (APSIM) crop model was selected for crop modelling, and was calibrated and validated using measured field data which included phenological development, biomass yield, and grain yield for the winter wheat crop in the Sunsari Morang Irrigation Scheme command area over two years. Impacts of climate change on the irrigation water demand, biomass yield, and grain yield were predicted for the short-term, mid-century, and end-of-century periods considering climate change scenarios RCP4.5 and RCP8.5, using downscaled daily precipitation and temperature data. In addition, the irrigation demand (mm/cropping period) required to reach potential wheat grain yields under current climate conditions was compared with observed irrigation practices and crop grain yield.

The hydraulic capacity of the main canal networks in the Sunsari Morang Irrigation Scheme, in terms of water losses and flow carrying capacity, were assessed using the Personal Computer Stormwater Management Model (PCSWMM) hydraulic model, which was calibrated and validated using measured canal characteristics, discharge, flow velocity, and water depth data. Information on daily water availability at the headwork of Sunsari Morang Irrigation Scheme in the Koshi River, drawn from hydrological assessments, was used to estimate water intakes into the canal network system. Based on irrigation water availability at the headwork, and the amount of irrigation water required for winter wheat crops, (both present and future), the winter wheat crop area coverage and the water carrying capacity of the main canal were assessed.

The key innovation of this research is the development of a comprehensive methodology to assess the climate change impacts on the supply and demand sides of irrigation water. The research has demonstrated its effectiveness through its successful

application in the Sunsari Morang Irrigation Scheme in the Koshi River of Nepal. The methodology and outcome of the research could be adapted to similar physical-climatic conditions around the world to holistically assess the climate change impacts on both the supply and demand sides of irrigation water. The findings of this research are beneficial to water practitioners, the agricultural community, policymakers, planners, and researchers in Nepal and internationally.

The findings on representative General Circulation Models (GCMs) selection for the Koshi River basin could also be used by research and scientific communities. Findings on climate change impacts on precipitation and temperature, and projected Koshi River flows could be used by the National Planning Commission, Nepal and Water and Energy Commission Secretariat, Nepal, for sectoral and water resources project planning, and in formulating water resources policies and basin plans for the Koshi River basin respectively. Findings on climatic changes and their potential implications could be used by the relevant sectors for the development of adaptation strategies, including the National Planning Commission, Nepal. It could also be used by the Department of Water Resources and Irrigation, Nepal, for planning and management of irrigation projects and the expansion of the irrigation command areas. The findings on projected climate change impacts on water resources, irrigation water demand and hydraulic assessment of the irrigation canal network could be used by the Department of Water Resources and Irrigation, Nepal, to manage irrigation projects in the region and by local farmers to increase crop yield in study area. It is also hoped that the challenge of agricultural production for the growing population in the developing world could be addressed with some insights provided by this research, despite the negative impacts of climate change on the irrigation and water resources sector.

Declaration

I, Santosh Kaini, declare that the PhD thesis entitled ‘Climate change impacts on river water availability for irrigation, crop irrigation water requirements and canal system capacity needs in an irrigation scheme in Nepal’ is no more than 80,000 words in length, including quotes and exclusive of tables, figures, appendices, bibliography, references, and footnotes. This thesis contains no material that has been submitted previously, in whole or in part, for the award of any other academic degree or diploma. Except where otherwise indicated, this thesis is my own work.

I have conducted my research in alignment with the Australian Code for the Responsible Conduct of Research and Victoria University’s Higher Degree by Research Policy and Procedures.



Santosh Kaini

March 2021

This PhD thesis is dedicated to my mother, the late Thaga Kumari Kaini, who opted to live in heaven, after being infected with COVID-19, during the last month of my thesis submission.

Acknowledgements

Foremost, I would like to express my deepest sense of gratitude to my principal supervisor Assoc. Prof. Ashok Sharma for his continuous support, guidance, encouragement, and patience during my PhD research at Victoria University. His guidance has helped me in improving the quality of research as well as thesis writing. His endless guidance, patience, and knowledge sharing enabled me to complete my PhD. He has played a major role in developing my overall scholarly skills. I could not have imagined having a better PhD supervisor.

I am equally grateful to my co-supervisors Prof. Ted Gardner and Dr. Santosh Nepal for their valuable advice, comments, and support during this journey. I am also thankful to A/Prof. Matthew Harrison for his support in APSIM crop modelling component of my thesis. Their continuous support, guidance, and motivation have significantly contributed to improving the quality of research, and the successful completion of PhD thesis. Without their support, my PhD journey would not have been possible. Thanks to ICIMOD's Koshi Basin initiative by providing Dr Santosh Nepal's time to co-supervise my PhD, relevant data of Koshi basin and work space at ICIMOD during my field visit.

I acknowledge the Australia Awards Scholarship program for financial support to pursue my PhD. Thanks to Elizabeth Smith, Johnny Ko, Keith Ong, and Margaret Jones at Victoria University for their support. I thank Alison Vieritz and Saurav Pradhananga for sharing their knowledge, Dr. Angus McElnea for arranging soil tests in Queensland, CHI-Canada for providing PCSWMM license, and Ian Demack for thesis editing.

Special thanks to Dr. Dinesh Pandey, Dr. Saurav Dahal, Mr. Ravinder Singh and colleagues of the Sunsari Morang Irrigation Scheme for their support during my PhD.

I am grateful to my mother for her countless sacrifices made to support all dimensions of my life and for visiting me in Australia during my PhD journey. I thank my dear wife, Manju, and daughter, Shuddhatma, for providing unending care and inspiration during this PhD journey, especially during the last month of thesis submission when I was infected with COVID-19. I appreciate Badri Nath Jaishi/family and Damber Dev Kaini/family for their support on my education since childhood.

Last but not least, I thank almighty God for showering blessings to complete my PhD.

List of Publications

Papers published in peer-reviewed journals

1. Kaini S, Nepal S, Pradhananga S, Gardner T, Sharma AK. Representative general circulation models selection and downscaling of climate data for the transboundary Koshi river basin in China and Nepal. *International Journal of Climatology*. 2020; 40:4131–4149. <https://doi.org/10.1002/joc.6447> (**Q1 Journal**)
2. Kaini S, Nepal S, Pradhananga S, Gardner T, Sharma AK. Impacts of climate change on the flow of the transboundary Koshi River, with implications for local irrigation. *International Journal of Water Resources Development*. 2020; <https://doi.org/10.1080/07900627.2020.1826292> (**Q1 Journal**)
3. Kaini, S., Gardner, T., Sharma, A.K., Assessment of socio-economic factors impacting on the cropping intensity of an irrigation scheme in developing countries. *Irrigation and Drainage*. 2020; 69: 363–375; <https://doi.org/10.1002/ird.2427> (**Q2 Journal**)

Papers under development

1. Impacts of climate change on irrigation water demand, yield, and biomass of winter wheat in Sunsari Morang Irrigation scheme command area in Nepal. (based on crop yield and water demand modelling)
2. Irrigation canal systems hydraulic capacity requirements and constraints for irrigation water supply in the climate change context. (based on hydraulic modelling and crop irrigation water modelling)
3. A novel approach to assess climate change impacts on demand and supply sides of irrigation water. (based on overall research)

Table of Contents

Abstract.....	i
Declaration.....	v
Acknowledgements	vii
List of Publications.....	viii
List of Tables.....	xiv
List of Figures.....	xviii
Chapter 1: Introduction.....	1
1.1 Background	1
1.2 Research aims	3
1.3 Scope of the study.....	4
1.4 Research significance and innovations	5
1.5 Thesis layout	6
Chapter 2: Literature review.....	10
2.1 General circulation model selection and climate data downscaling	10
2.2 Climate change impacts on the hydrological regime of a river basin.....	14
2.3 Climate change impacts on irrigation water requirement and crop grain yield within an irrigation scheme	16
2.4 Canal water losses and canal hydraulic capacity assessment of an irrigation scheme	18
Chapter 3: Study area	22
3.1 The Koshi River basin	22
3.1.1 Catchment characteristics of the Koshi River basin.....	22
3.1.2 Average discharge in the Koshi River.....	23
3.2 The Sunsari Morang Irrigation Scheme.....	24
3.2.1 Development of Sunsari Morang Irrigation Scheme.....	24

3.2.2 Crop water requirement considerations in the Sunsari Morang Irrigation Scheme	26
3.2.3 Headworks and canal networks in the Sunsari Morang Irrigation Scheme...	27
Chapter 4: Methodology.....	34
4.1 Methodology for investigating climate change impacts on supply and demand sides of irrigation water under an irrigation command area.....	34
4.2 Data collection and processing	36
Chapter 5: General circulation models selection and climate data downscaling	38
5.1 Representative GCM selection for the Koshi River basin	38
5.1.1 General Circulation Models (GCMs)	38
5.1.2 Approach on GCMs selection	40
5.1.3 Methodology.....	40
5.1.4 Application of Methodology	43
5.1.5 Results and discussion	85
5.2 Climate data downscaling for the Koshi River basin	87
5.2.1 Downscaling methods	87
5.2.2 Quantile mapping approach for climate data downscaling	89
5.2.3 Application of quantile mapping downscaling	91
5.2.4 Results and discussion	91
5.3 Conclusion	103
Chapter 6: Hydrology of the river basin.....	106
6.1 Selection of Soil and Water Assessment Tool (SWAT) hydrological model	106
6.1.1 Selection of hydrological model.....	106
6.1.2 The SWAT model.....	107
6.2 Methodological framework for the SWAT modelling	112
6.2.1 SWAT input data processing and model development (Model initialisation).....	113

6.2.2	Sensitivity analysis and model calibration	114
6.2.3	Model validation.....	116
6.2.4	Scenario analysis	117
6.3	Application of methodology for SWAT hydrological modelling.....	117
6.3.1	SWAT input data processing and model development	117
6.3.2	Sensitivity analysis, calibration and validation of SWAT model.....	123
6.3.3	Model validation.....	127
6.3.4	Scenario analysis (future hydrological analysis).....	127
6.4	Results and discussion	129
6.5	Conclusion	142
Chapter 7: Crop water assessment for irrigation water requirement.....		145
7.1	Understanding local stakeholders' needs and crop area coverage under irrigation scheme	145
7.2	Crop types and cropping intensity in the Sunsari Morang Irrigation Scheme....	146
7.3	Selection of Agricultural Production Systems Simulator (APSIM) crop model for crop growth and irrigation water assessment.....	148
7.3.1	Selection of crop model.....	149
7.3.2	APSIM crop modelling.....	150
7.4	Approach for crop modelling using APSIM.....	152
7.4.1	APSIM input data processing and model development (Model initialisation).....	152
7.4.2	Model calibration.....	153
7.4.3	Model validation.....	153
7.4.4	Scenario analysis	153
7.5	Application of methodology for APSIM crop modelling.....	154
7.5.1	APSIM input data processing and model development (model initialisation).....	154

7.5.2	Model calibration.....	159
7.5.3	Model validation.....	162
7.5.4	Scenario analysis (future irrigation water demand analysis).....	162
7.6	Results and discussion	164
7.6.1	Changes in projected irrigation water demand, grain yield and biomass yield	164
7.6.2	Uncertainty (variability) in projected irrigation water demand, grain yield and biomass yield	167
7.6.3	Irrigation levels required to achieve potential grain yields under current climate	168
7.7	Conclusions	174
Chapter 8: Canal hydraulic capacity assessment.....		177
8.1	Canal discharge measurement and losses in the irrigation canal network	177
8.1.1	Canal discharge measurement	177
8.1.2	Losses in the irrigation canal network.....	179
8.2	Personal Computer Storm Water Management Model (PCSWMM) for canal hydraulic modelling.....	181
8.3	Methodological approach for PCSWMM hydraulic modelling	182
8.3.1	PCSWMM input data processing and model development (Model initialisation).....	183
8.3.2	Model calibration.....	183
8.3.3	Model validation.....	183
8.3.4	Scenario analysis (canal capacity assessment)	183
8.4	Application of methodology for PCSWMM hydraulic modelling.....	184
8.4.1	PCSWMM input data processing and model development.....	184
8.4.2	Model calibration.....	193
8.4.3	Model validation.....	196

8.4.4 Scenario analysis (canal capacity assessment)	198
8.5 Results and discussion	201
8.5.1 Average monthly water availability for irrigation at the irrigation canal intake for dry season during 1982-2010.....	201
8.5.2 Projected average monthly minimum flow availability for irrigation at canal intake	201
8.5.3 Projected area coverage for winter wheat crop	203
8.5.4 Canal flow capacity assessment	207
8.6 Conclusions	208
Chapter 9: Summary, conclusions and future research directions.....	212
9.1 Summary.....	212
9.2 Conclusions	214
9.2.1 General circulation models selection and climate data downscaling for the Koshi River basin	214
9.2.2 Hydrology of the Koshi River basin.....	214
9.2.3 Crop water assessment for irrigation water requirement.....	215
9.2.4 Canal hydraulic capacity assessment.....	216
9.3 Benefits, limitations and future research directions	217
Appendix	220
References	223

List of Tables

Table 5.1: Delta (ΔT and ΔP) values and percentile rank for short-term future period (2016-2045), mid-century future period (2036-2065) and end-of-century future period (2071-2100), of the first ten GCMs/ensembles for climate change scenario RCP4.5....	46
Table 5.2: Delta (ΔT and ΔP) values and percentile rank, for short-term future period (2016-2045), mid-century future period (2036-2065) and end-of-century future period (2071-2100), of the first ten GCMs/ensembles for climate change scenario RCP8.5....	47
Table 5.3: 10th and 90th percentile values of ΔT and ΔP for short-term (2016-2045), mid-century (2036-2065) and end-of-century (2071-2100) periods, from the pool of GCM/ensemble for climate change scenarios RCP4.5 and RCP8.5.	48
Table 5.4: ΔT and ΔP values, based on short-term (2016-2045), mid-century (2036-2065) and end-of-century (2071-2100) periods at four corners for climate change scenarios RCP4.5 and RCP8.5.	49
Table 5.5: Distance of the first ten GCMs/ensembles from the four corners, based on the short-term future period (2016-2045), for climate change scenario RCP4.5.	50
Table 5.6: Models selected for Step 2 based on changes in mean air temperature and annual precipitation considering short-term future period (2016-2045) and the reference period (1981-2010) for climate change scenarios RCP4.5 and RCP8.5.	58
Table 5.7: Models selected for Step 2 based on changes in mean air temperature and annual precipitation considering the mid-century future period (2036-2065) and reference period (1981-2010) for climate change scenarios RCP4.5 and RCP8.5.	59
Table 5.8: Models selected for Step 2 based on changes in mean air temperature and annual precipitation considering the end-of-century future period (2071-2100) and reference period (1981-2010) for climate change scenarios RCP4.5 and RCP8.5.	60
Table 5.9: Description of ETCCDI indices used for refined model selection.	61
Table 5.10: GCM runs analysed during the refined selection process for climate change scenario RCP4.5 considering the short-term future period (2016-2045).	67
Table 5.11: GCM runs analysed during the refined selection process for climate change scenario RCP8.5 considering the short-term future period (2016-2045).	68
Table 5.12: GCM runs analysed during the refined selection process for climate change scenario RCP4.5, considering the mid-century future period (2036-2065).	72

Table 5.13: GCM runs analysed during the refined selection process for climate change scenario RCP8.5, considering the mid-century future period (2036-2065).	73
Table 5.14: GCM runs analysed during the refined selection process for climate change scenario RCP4.5, considering the end-of-century future period (2071-2100).	76
Table 5.15: GCM runs analysed during the refined selection process for climate change scenario RCP8.5, considering the end-of-century future period (2071-2100).	77
Table 5.16: Biases between GCM runs and the reference climate dataset (1981-2010) for climate change scenarios RCP4.5 and RCP8.5, considering ensembles for the short-term period (2016-2045).	81
Table 5.17: Biases between GCM runs and the reference climate dataset (1981-2010) for climate change scenarios RCP4.5 and RCP8.5 considering ensembles for long term (2036-2065).	82
Table 5.18: Biases between GCM runs and the reference climate dataset (1981-2010) for climate change scenarios RCP4.5 and RCP8.5 considering ensembles for the end-of-century (2071-2100) period.	83
Table 5.19: Selected model/ensembles for the short-term future period (2016-2045) for climate change scenarios RCP4.5 and RCP8.5.	84
Table 5.20: Selected models/ensembles for the mid-century future period (2036-2065) for climate change scenarios RCP4.5 and RCP8.5.	84
Table 5.21: Selected models/ensembles for the end-of-century future period (2071-2100) for climate change scenarios RCP4.5 and RCP8.5	85
Table 5.22: Uncertainty in absolute and percentages changes in average precipitation in the Koshi River basin compared to base period.	93
Table 5.23: Ensemble mean (4 GCMs) of absolute and percentages changes in average precipitation in the Koshi River basin compared to base period.	96
Table 5.24: Uncertainty in absolute changes in average temperature in the Koshi River basin compared to base period.	100
Table 5.25: Ensemble mean (4 GCMs) of absolute changes in average temperature in the Koshi River basin compared to reference period.	102
Table 6.1: SWAT calibrated parameter values.	125
Table 6.2: SWAT model performance for calibration and validation.	127

Table 6.3: Absolute and relative changes in projected annual and seasonal flows of the Koshi River.....	136
Table 7.1: Main crops and their planted area in the Sunsari Morang Irrigation command area in the period 2008-2016.	147
Table 7.2: Soil physical properties - bulk density (BD), air-dry (AD), lower limit-LL15 (wilting point), drained upper limit-DUL (field capacity), saturated volumetric water contents (Sat), saturated hydraulic conductivity (Ks), plant available water capacity (PAWC) and soil texture.	156
Table 7.3: Soil chemical properties - electrical conductivity (EC), pH, chloride (CL), boron (B), cation exchange capacity (CEC), calcium (Ca), Magnesium (Mg), Sodium (Na), Potassium (K), exchangeable sodium percentage (ESP) and Manganese (Mn).	157
Table 7.4: Observed and simulated phenological days after sowing for the calibration (2018-2019) and validation (2019-2020) periods.....	160
Table 7.5: Change in irrigation water demand, grain yield and biomass yield for winter wheat, based on average values from 4 GCMs and calculated against the reference period (1981-2010).	166
Table 8.1: Canal discharge measurement at 5.2 km from the irrigation intake along the main canal.....	186
Table 8.2: Canal discharge measurement at 11.8 km from the irrigation intake along the main canal.....	187
Table 8.3: Canal discharge measurement at 13 km from the irrigation intake along the main canal.....	188
Table 8.4: Canal discharge measurement at 15 km from the irrigation intake along the main canal.....	189
Table 8.5: Canal discharge measurement at 22.5 km from the irrigation intake along the main canal.....	190
Table 8.6: Canal discharge measurement at 25.3 km from the irrigation intake along the main canal.....	191
Table 8.7: Losses and Manning’s roughness coefficient at different portions of the main canal.....	192
Table 8.8: Projected average monthly minimum flow (m ³ /s) availability for irrigation at the canal intake, with reference (base) period flow for comparison.	202

Table 8.9: Irrigation water requirement (mm) for winter wheat crops at field level, derived from crop modelling.	204
Table 8.10: Irrigation water requirements (liter/sec/ha) for winter wheat crop at the irrigation canal intake.	205
Table 8.11: Potential area coverage by the winter wheat crop (in hectares).	206

List of Figures

Figure 1.1: Framework for systems approach to assess climate change impacts on demand and supply sides of irrigation water.....	5
Figure 1.2: Structure of the thesis.....	9
Figure 3.1: The Koshi River basin down to Chatara in Nepal. All the rivers are coloured blue.	23
Figure 3.2: Measured mean monthly discharge (m^3/s) of the Koshi River at Chatara for the period 1982-2010.....	24
Figure 3.3 Location of Sunsari Morang Irrigation Scheme in Nepal (blue lines represent the Sunsari Morang irrigation canal network).....	25
Figure 3.4: Headwork of the Sunsari Morang Irrigation Scheme.	28
Figure 3.5: Canal network of the Sunsari Morang Irrigation Scheme.....	29
Figure 3.6: Main canal of the Sunsari Morang Irrigation Scheme.	30
Figure 3.7: Reduced flow section at the tail portion of the main canal.	31
Figure 3.8: Schematic diagram of the canal system in the developed area (38000 ha)..	32
Figure 3.9: Schematic diagram of the canal system in the undeveloped area (30,000 ha).	32
Figure 4.1: Flowchart of methodology for investigating climate change impacts on demand and supply sides of irrigation water.....	35
Figure 5.1: Representation of world in General Circulation Models (National Oceanic and Atmospheric Administration, 2018).	39
Figure 5.2: RCPs with (a) CO ₂ concentration and (b) corresponding radiative forcing.	41
Figure 5.3: Steps of GCM selection (based on Lutz et al., 2016).	43
Figure 5.4: Initial model selection based on changes in mean air temperature and annual precipitation, considering changes in the short-term future period (2016-2045) and the reference period (1981-2010), for climate change scenario RCP4.5.	51
Figure 5.5: Initial model selection based on changes in mean air temperature and annual precipitation, considering changes in the short-term future period (2016-2045) and the reference period (1981-2010), for climate change scenario RCP8.5.	52
Figure 5.6: Initial model selection based on changes in mean air temperature and annual precipitation, considering changes in the mid-century future period (2036-2065) and the reference period (1981-2010), for climate change scenario RCP4.5.	53

Figure 5.7: Initial model selection based on changes in mean air temperature and annual precipitation, considering changes in the mid-century future period (2036-2065) and the reference period (1981-2010), for climate change scenario RCP8.5.	54
Figure 5.8: Initial model selection based on changes in mean air temperature and annual precipitation, considering changes in the end-of-century future period (2071-2100) and the reference period (1981-2010), for climate change scenario RCP4.5.....	55
Figure 5.9: Initial model selection based on changes in mean air temperature and annual precipitation, considering changes in the end-of-century future period (2071-2100) and the reference period (1981-2010), for climate change scenario RCP8.5.....	56
Figure 5.10: Flowchart to calculate CDD.....	63
Figure 5.11: Flowchart to calculate R95pTOT.....	64
Figure 5.12: Flowchart to calculate CSDI.....	65
Figure 5.13: Flowchart to calculate WSDI.....	66
Figure 5.14: Conceptualisation of downscaling and aggregation between atmospheric and hydrologic models (adapted from Wilby and Wigley, 1997).	88
Figure 5.15: Daily precipitation data for the years 2010, 2045, 2065 and 2100 for the model CanESM2_r3i1p1_RCP8.5.	92
Figure 5.16: Daily average temperature of the years 2010, 2045, 2065 and 2100 for the model CanESM2_r3i1p1_RCP8.5.	92
Figure 5.17: Ensemble mean monthly precipitation for end-of-century period.....	97
Figure 5.18: Ensemble mean of absolute change in average precipitation and temperature during the end-of-century period compared to reference period.....	98
Figure 5.19: Present and future average annual precipitation and temperature along with their standard deviation for the Koshi River basin.	99
Figure 6.1: Relationship of runoff to rainfall in SCS curve number method (Neitsch et al., 2011).	109
Figure 6.2: Framework for the SWAT model development and scenarios analysis. ...	113
Figure 6.3: Digital elevation model and major river network in the Koshi River basin.	118
Figure 6.4: Land use practices in the Koshi River basin (Blue colour represents grass and white colour represents snow).	119
Figure 6.5: Soil map of the Koshi River basin.	120

Figure 6.6: Slope variation in the Koshi River basin.	121
Figure 6.7: Precipitation and temperature stations used in the SWAT modelling.	122
Figure 6.8: Sensitivity analysis of 22 SWAT parameters.	124
Figure 6.9: Observed and simulated daily flows (m ³ /s) for the Koshi River at Chatara (the blue colour represents observed daily flows and the red colour represents simulated daily flows).	126
Figure 6.10: Precipitation and temperature grid stations for the reference and downscaled data.	129
Figure 6.11: Average monthly projected discharge in the Koshi River for the short-term, mid-century and end-of-century periods. Also shown is the modelled flow during the base (reference) period (1981-2010).	131
Figure 6.12: Uncertainty in projected annual and seasonal river flows (percentage change in flow based on outputs from four GCMs for the short term, mid-century, and end-of-century periods for climate change scenarios RCP4.5 and RCP8.5. Percentage changes in flows are relative to reference period flow data).	133
Figure 6.13: Changes in projected annual and seasonal river flows in percentage.	137
Figure 6.14: Percentage change in average minimum and maximum monthly river flows of the Koshi River at Chatara. Future projections are relative to the reference data for 1981–2010.	139
Figure 6.15: Monthly average river flow with standard deviation at Chatara of the Koshi River.	141
Figure 7.1: Flowchart of overall methodology for this study, including crop modelling, climate change impacts and summarization of outputs.	152
Figure 7.2: Location of selected field plots used for APSIM Wheat module calibration and validation.	155
Figure 7.3: A triangular V-notch (90°) weir used to measure irrigation water supplied in the experimental field.	158
Figure 7.4: Triangular V-notch (90°) used in the field.	159
Figure 7.5: Observed and simulated biomass yield and grain yield for the calibration (parameterisation) (2018-2019) and validation (2019-2020) periods (SD = standard deviation).	161

Figure 7.6: Changes in projected irrigation water demand, grain yield and biomass yield for the winter wheat crop at the Sunsari Morang Irrigation Scheme command area, considering RCP 4.5 and 8.5 climate change scenarios.	165
Figure 7.7: Uncertainty (variability) in projected irrigation water demand, biomass yield and grain yield compared to reference period (1981-2010).	168
Figure 7.8: Irrigation required to reach potential grain yields, and actual irrigation supplied for the winter wheat crop in the Sunsari Morang Irrigation scheme command area in 2018-2019 and 2019-2020.	170
Figure 8.1: Current meter used for discharge measurement in the main irrigation canal.	178
Figure 8.2: Losses measurement in an irrigation canal (Inflow-outflow method).	180
Figure 8.3: Flowchart of methodology for hydraulic modelling using the PCSWMM model.	182
Figure 8.4: A conceptual diagram showing the channel section, distances and depths for measuring discharge.	185
Figure 8.5: Observed and simulated discharge, velocity and water depth for the (a) calibration and (b) validation periods.	195
Figure 8.6: Stage-discharge relationship for the Koshi River at the irrigation canal intake, based on data available from 1996 to 2012.	199
Figure 8.7: Average monthly water availability for irrigation at the irrigation canal intake for dry seasons during 1982-2010.	201
Figure 8.8: Projected average monthly minimum flow availability for irrigation at the canal intake, along with their standard deviation of the mean.	203

Chapter 1: Introduction

Chapter One describes the research aims and scope of the research. This chapter also mentions the research significance and innovation followed by the layout of the thesis.

1.1 Background

The impacts of climate change on water resources and agriculture, accompanied by growing population, urbanization and industrialization, have contributed to increasing food and water scarcity. Due to continuing growth in population and change in food requirement habits, the demand for agricultural products is increasing continuously (Godfray et al., 2010, Liu and Savenije, 2008, Molden et al., 2007, Tilman et al., 2011). It has been predicted that the rise in food demand will increase by 50-100% between 2009 and 2050 (Baulcombe et al., 2009).

The irrigation sector plays a crucial role in the agricultural food production system, utilizing about 70% of the world's total annual water consumption (Moreno-Pérez and Roldán-Cañas, 2013, Schultz et al., 2009, FAO, 2016b). However, the overall performance of most of the irrigation schemes around the world is unsatisfactory due to inefficient water management practices (Awulachew and Ayana, 2011, Checkol and Alamirew, 2008, Asres, 2016, Moreno-Pérez and Roldán-Cañas, 2013, Nam et al., 2016). In many countries that don't have broad-acre farming, the majority of food is grown in irrigation areas. Globally, about 16% of cropland is irrigated, accounting for about 44% of total food production (Alexandratos and Bruinsma, 2012). Hence, higher water use efficiency on irrigated farmland produces more food.

One of the major issues in irrigation is ensuring the right amount of water at the right time in a crop field (Asres, 2016). Irrigation water management practices are still at an inception stage, and improved guidelines for efficient irrigation water management are required in many developing countries (Humphreys et al., 2005, Pundarikanthan and Santhi, 1996).

Climate variability also influences changes in crop water demand and water availability for agriculture, which renders global food security vulnerable to climate change (Alcamo et al., 2007). According to Lobell et al. (2008), South Asia will face negative impacts on agriculture due to climate change, and food scarcity will increase if

adaptation measures are not considered. Studies have shown that climate change would reduce crop grain yields in the South Asia region (Gupta et al., 2017, Tesfaye et al., 2017). Döll (2002) reports that the changes in precipitation and evaporative demands due to climate change may increase the net irrigation requirements in South Asia by 15% in the 2070s compared to 1995. Zhang et al. (2013) assessed the impacts of climate change on wheat (local varieties) grain yields in North China between 1961-1990 and the 2080s, projecting decrease of 4-6 % (A2 climate change scenario) and 1-5 % (B2 climate change scenario). Goodarzi et al. (2019) evaluated climate change impacts on irrigation water requirements for different crops in Iran between 2017 and 2046, considering climate change scenarios RCP4.5 and RCP8.5. They projected an increase in irrigation water requirements for wheat crops by 12-16% when compared to 1976-2005 period. Hence, studies on climate change impacts on the demand side of irrigation water are important.

Climate-driven changes in precipitation and temperature patterns are expected to affect water availability in the Himalayan region (Hock et al., 2019) and the hydrological regime of associated upstream basins (Immerzeel et al., 2012, Lutz et al., 2014, Nepal, 2016). Climate change effects on the hydrological regime of these river basins will directly affect irrigation water availability and irrigation crop area coverage in the nearby regions (Elliott et al., 2014, Malek et al., 2018). Assessment of climate change impacts on the supply side of irrigation water is important for the planning and management of irrigation schemes.

For the assessment of climate change impacts on demand and supply sides of irrigation water, high-resolution climate data are required as they increase the accuracy of hydrological predictions and hence allow for better projection of the water availability within a catchment. General Circulation Models (GCMs) are the main tools used to estimate future climate patterns at a catchment level. They represent numerous atmospheric processes of the global climate system. However, their outputs are of limited use for hydrological prognostication because of their coarse spatial resolution (Willems and Vrac, 2011). GCM outputs typically have a spatial resolution of about 100-250 km and the temporal resolutions of daily or monthly. Hence GCM outputs do not capture local spatial scales (Trzaska and Schnarr, 2014). However, the GCM outputs

can be downscaled to a finer resolution to generate climate data that represent local and regional climatic and topographic conditions.

In this regard, there is a need to increase the performance of existing irrigation schemes to cope with changes in future water availability and food scarcity, with consideration given to irrigation water availability and application (Bumbudsanpharoke and Prajamwong, 2015, Schultz et al., 2009, Pereira, 2017, Molden et al., 2007, Malano et al., 2004), which is only possible by assessing supply and demand sides of irrigation water simultaneously using high-resolution climate data. To address these issues, an assessment of climate change impacts on both supply and demand sides of irrigation water using high-resolution climate input data is required. A methodology is developed in this research to holistically investigate climate change impacts on the supply and demand sides of irrigation water. It has been successfully applied to the Sunsari Morang Irrigation Scheme in the Koshi river basin of Nepal using high-resolution climate input data.

1.2 Research aims

This research is aimed at developing a comprehensive methodology for assessing climate change impacts on supply and demand sides of irrigation water using high-resolution climate data, and applying the framework to Sunsari Morang Irrigation Scheme in the Koshi river basin of Nepal as a case study. These scientific objectives were realised through the following methodological approach.

- (I) Selection of global climate models and downscaling of climate data at a high spatial resolution (10 km x 10 km) in the river basin and irrigation command area.
- (II) Projection of climate change impacts on the river flows at the irrigation canal intake using high-resolution downscaled climate data.
- (III) Projection of climate change impacts on the irrigation water requirement using high-resolution downscaled climate data.
- (IV) Assessment of irrigation canal systems' hydraulic capacity requirements for irrigation water supply in the context of climate change.

Through this methodological approach, the following specific research questions will be addressed:

- (I) What will be the likely change on future daily rainfall and temperature patterns in the Koshi river basin of Nepal?
- (II) What are the present hydrological regimes of the Koshi river basin of Nepal and how will it change under projected climate change?
- (III) What will be the expected change on irrigation water requirement for winter wheat crop in the Sunsari Morang Irrigation Scheme command area?
- (IV) What is the existing hydraulic capacity of the irrigation canal systems in the Sunsari Morang Irrigation Scheme? What will be the likely future hydraulic performance?

1.3 Scope of the study

The main theoretical framework underpinning this research is the system-based approach to assessing irrigation water in a climate change context. Few studies have been conducted to predict the impact of climate change on crop water requirements. Döll (2002) and Fischer et al. (2007) have predicted the impact of atmospheric changes on future irrigation water requirements at a global scale. Likewise, De Silva et al. (2007) and Shrestha et al. (2013) assessed the climate change impacts on crop water demands of rice and wheat, and predicted that irrigation water requirements will increase by 20% at around 2050 in Sri Lanka and Nepal. Similarly, Ojeda-Bustamante et al. (2017) and Rotich and Mulungu (2017) have assessed climate change impacts on crop water demand in Mexico and Tanzania, and reported that crop water requirements will increase by about 30% in coming decades. These studies show that crop irrigation water demand per hectare will most likely increase in the future. They mainly focused on crop water requirements. However, the supply side of irrigation water management has not been assessed simultaneously within a systems-based approach. Issues affecting the supply side of irrigation water management include water availability at the source as well as in the canal distribution system. Effective irrigation water management is almost impossible in the future without assessing the availability of water at a source in a climate change context.

For this reason, it is important to consider a systems approach to irrigation water management. A systems approach in irrigation water management mainly includes the irrigation supply side, availability of water at source, the irrigation canal network and its

efficiency, and the irrigation demand side at a farm scale. This systems approach is shown in Figure 1.1. This research will be a milestone to holistically investigate the demand and supply sides of irrigation water in conjunction with the impacts of climate change.

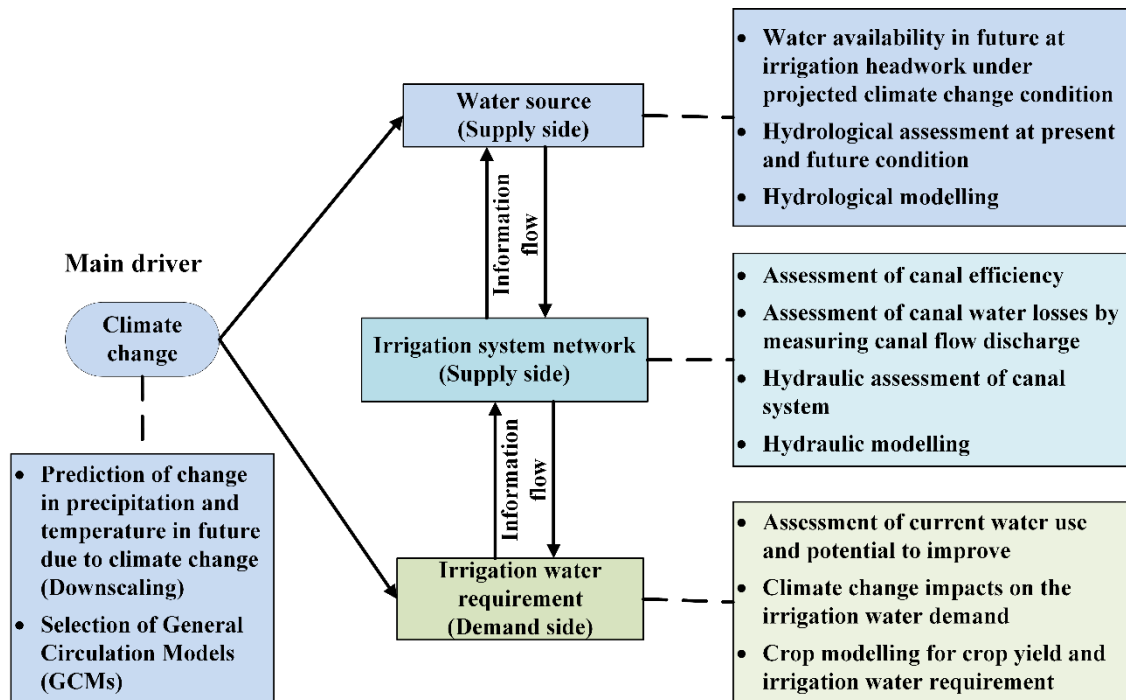


Figure 1.1: Framework for systems approach to assess climate change impacts on demand and supply sides of irrigation water.

1.4 Research significance and innovations

The novelty of this research is to explore irrigation water at a systems level to assess likely future changes in precipitation and temperature, water availability in the river, irrigation water requirements at farm level, and hydraulic capacity of the canal networks. The key innovation of this research is the development of a comprehensive methodology to assess the climate change impacts on the supply and demand sides of irrigation water. Moreover, this research has demonstrated its effectiveness through its successful application in Sunsari Morang Irrigation Scheme in the Koshi river basin of Nepal. The findings of this research are beneficial to water practitioners, the agricultural community, policymakers, planners, and researchers.

The findings on representative general circulation models (GCMs) selection for the Koshi River basin can be used by researchers and scientific communities. Findings on

climate change impacts on precipitation and temperature, and projected Koshi River flows can be used by the National Planning Commission, Nepal, and the Water and Energy Commission Secretariat, Nepal for future sectoral and water resources project planning and in formulating water resources policies and basin plans for the whole of the Koshi River basin respectively. Findings on climatic changes and their potential implications could be used by relevant sectors for the development of adaptation strategies including the National Planning Commission, Nepal. It could also be used by the Department of Water Resources and Irrigation, Nepal, for planning and management of irrigation projects and expansion of irrigation command areas.

The findings on projected climate change impacts on water resources, irrigation water demand and hydraulic assessment of the irrigation canal network could be used by the Department of Water Resources and Irrigation, Nepal, to manage irrigation projects in the region and by local farmers to increase crop yield in study area. The agricultural sector contributes around one-third of Nepal's gross domestic product. Since winter wheat crop grain yield per hectare could be doubled with adequate irrigation water supply, the national economy of Nepal would be increased. Local farmers could directly benefit from an increased grain yield resulting from proper irrigation application.

The methodology and outcome of the research could be adopted around the world to holistically assess climate change impacts on both (supply and demand) sides of irrigation water. It is also hoped that the challenge of agricultural production for the growing population in the developing world could be addressed using the insights from this research to counteract the expected negative impacts of climate change on the irrigation and water resources sector.

1.5 Thesis layout

This thesis has nine chapters. The **first chapter** introduces the research detailed in the thesis. Chapter One describes the challenges of climate change impacts on water resources and agriculture, which contributes to increasing food and water scarcity and associated future consequences. This chapter highlights the climate change impacts on the supply and demand sides of irrigation water. It mentions the aims of this research. This chapter further summarises the scope of the research. Finally, research significance and innovations are emphasized.

In **Chapter Two**, the literature review is presented. Existing research work related to climate change impacts on supply and demand sides of irrigation water is discussed. A literature review on general circulation model selection and climate data downscaling is presented. Climate change impacts on the hydrological regime of a river basin are discussed, along with irrigation water requirements and grain yields within an irrigation scheme. Furthermore, canal water losses and a canal hydraulic capacity assessment of an irrigation scheme are described.

The **third chapter** provides information on the study area of this research, the Koshi River basin and the Sunsari Morang Irrigation Scheme. It provides general information on catchment characteristics of the Koshi River basin, including size, elevations, location, land use and an average discharge of the basin. Likewise, it also mentions the salient features of the Sunsari Morang Irrigation Scheme such as the type of headwork, size of command area, and the canal network.

Chapter Four discusses a methodology developed to assess the climate change impacts on the supply and demand sides of irrigation water. It includes information on data collection and its processing. The framework for conducting research is also mentioned in this section.

The **fifth chapter** provides details on General Circulation Models (GCMs) and their downscaling. It is divided into two sections: representative GCM selection for the Koshi River basin, and climate data downscaling for the Koshi River basin. It starts with the introduction to GCMs and describes the GCMs selection approaches. This research uses the advanced envelope-based selection approach to select GCMs, which are then applied to the Koshi River basin. Representative GCMs are selected in this section, and then used for downscaling of climate data. The second part provides information on downscaling, quantile mapping, and its application to the selected GCMs for the Koshi River basin. It predicts climate (precipitation and temperature) in the future decades, short-term (2016-2045), mid-century (2036-2065), and end-of-century (2071-2100) time periods, considering the climate change scenarios Representative Concentration Pathways (RCPs) 4.5 and 8.5.

In **Chapter Six**, the use of future climate data (as identified in Chapter Five) in hydrological modelling is presented. It describes the hydrological process considered in

the Soil and Water Assessment Tool (SWAT), a hydrological model. Populating the SWAT model with future climate data predicts the likely future water availability in the short-term (2016-2045), mid-century (2036-2065), and end-of-century (2071-2100) time periods for climate change scenarios RCP4.5 and RCP8.5. This information on future water availability at the headwork of Sunsari Morang Irrigation Scheme in the Koshi River basin is then used to estimate discharge into the main irrigation canal.

In **Chapter Seven**, crop modelling is used to quantify the effects of climate change impacts on irrigation water requirements at a field level. A nexus of local stakeholders, irrigation practices, and cropping patterns in irrigation schemes is described. This information, along with crop types and cropping intensity, are essential in order to understand existing local water management practices. Calibration and validation of the Agricultural Production Systems Simulator (APSIM), a crop model, are described. Likely changes in irrigation water requirements and grain yields are predicted for the short-term (2016-2045), mid-century (2036-2065), and end-of-century (2071-2100) time periods considering climate change scenarios RCP4.5 and RCP8.5. Irrigation levels required to reach potential grain yields for the winter wheat crop in the Sunsari Morang Irrigation scheme command area under current climate conditions are also compared with observed irrigation application.

Chapter Eight addresses the canal hydraulics in the irrigation scheme. The results from Chapter Six, which addresses water availability at the headwork of Sunsari Morang Irrigation Scheme, are used to estimate water discharge entering the main canal. This section describes the water losses in the canal network, and the calibration, and validation of the hydraulic model, the Personal Computer Storm Water Management Model (PCSWMM). Hydraulic assessment in terms of canal discharge capacity of the irrigation network is carried out considering present and future water availability in the canal system. Based on water availability, potential area coverage by future winter wheat crops is also projected.

Finally, in **Chapter Nine**, the conclusions drawn from the overall study are presented together with some possible future works. The structure of the thesis is shown in Figure 1.2.

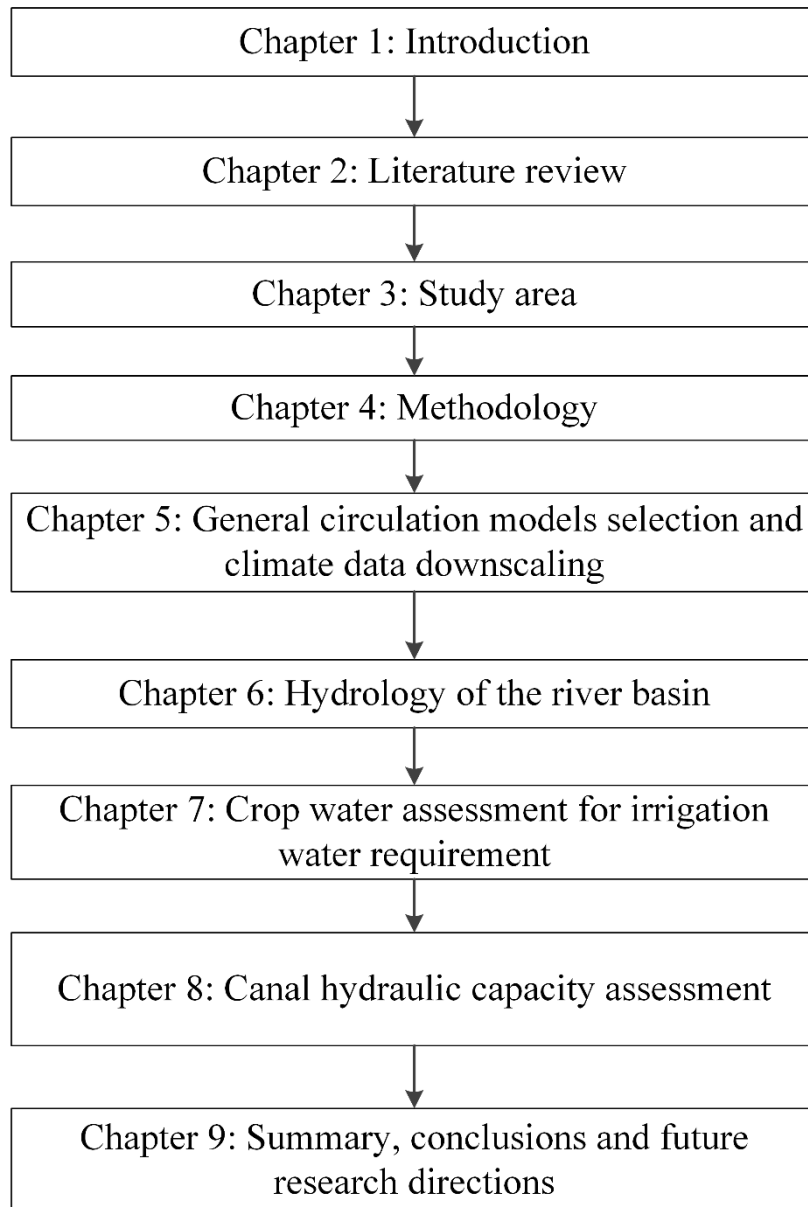


Figure 1.2: Structure of the thesis.

Chapter 2: Literature review

In this chapter, existing knowledge related to climate change impacts on supply and demand sides of irrigation water is reviewed. Firstly, a literature review on global climate model selection and downscaling is presented. Secondly, climate change impacts on the hydrological regime of a river basin are reviewed. Thirdly, climate change impacts on irrigation water requirements and crop grain yields within an irrigation scheme are described. Finally, canal water losses and a canal hydraulic capacity assessment of an irrigation scheme are reviewed.

2.1 General circulation model selection and climate data downscaling

General or Global Circulation Models (GCMs), representing numerous atmospheric processes of the global climate system, are the main tools used to estimate future climate patterns, and explore the implications of likely changes in precipitation and temperature patterns. The number of GCMs available to predict future climate changes is large and increasing. The number of GCM outputs applied in the Coupled Model Intercomparison Project Phase 3 (CMIP3) (Meehl et al., 2007) and the CMIP Phase 5 (CMIP5) (Taylor et al., 2012) are 25 and 61 respectively. The CMIP3 outcome archives were used in the *Fourth Assessment Report* (IPCC, 2007) whilst CMIP5 outcome archives were used in the *Fifth Assessment Report* (IPCC, 2013) of the Intergovernmental Panel on Climate Change (IPCC). Over this period of the time, there were significant improvements in the way these models represent the present climate system and future projections.

The capacity of climate models/ensembles to represent climatic characteristics varies spatially and temporally. Many models/ensembles cannot perfectly simulate climatic characteristics, nor can they represent local climates, which vary spatially and temporally (Lee et al., 2019). Gleckler et al. (2008) have reported that all climate models/ensembles are not equally able to represent accurately the annual cycle climatology and the variance of monthly anomalies. The complex topography of the Himalayan regions, combined with the coarse resolution of available GCMs, has resulted in a weak consensus amongst models for these regions (Wester et al., 2019). The selection of climate models can vary, depending on the objective of the model selection and future projections. In most cases, a single GCM is not sufficient to

represent the climatic characteristics of climatic extremes. These climatic extremes can be described as four corners of a quadrilateral representing *cold and dry*, *cold and wet*, *warm and dry*, and *warm and wet* conditions. For any chosen time and location, a specific climatic model/ensemble may demonstrate better abilities to represent climatic characteristics for a particular corner of a climatic extreme. Hence, selecting global climate models with the strongest ability to represent the past and likely future climate for a specific geographical location is a crucial first step in assessing climate change impacts. Selecting GCMs from the large set of available climate models for a given location of interest is a challenging task.

The common approaches for the selection of GCMs are:

- (a) include all the models/ensembles with available data and simply take an average of all the predicted outcomes (Seager et al., 2007), or
- (b) use a past performance approach focusing on the model's capacity to simulate past and present climate (Biemans et al., 2013, Pierce et al., 2009). In the past performance approach, hindcast data of model/ensemble are compared with observed data.

A major drawback of approach (a) is that equal weighting is given to the poor-performing and good-performing models (Pierce et al., 2009). However, the past performance approach (hindcasting) may lead to an oversight of the possible futures (Lutz et al., 2016), as hindcasting models which perform well may not be able to represent future climate equally well. Another approach for the selection of climate models is the envelop approach, whereby GCMs are selected from a pool of available global models covering all possible future climates. In the envelop approach, GCMs/ensembles are selected at each of the four climatic extremes (*cold and dry*, *cold and wet*, *warm and dry*, and *warm and wet*) based on annual means. Hence, four GCMs/ensembles are selected for a particular future study period to predict four possible future climatic scenarios. However, in approach (a), all the GCM runs are simply averaged, and projection from only one dataset is used. This contrasts with the four climatic corners utilized in the envelop approach. Hence, only one possible future is realized in approach (a). The main limitation of the envelope-based approach is that it only considers changes in annual means and does not consider the model's capacity to

simulate climate process, as all the (global) model runs are considered to have equal plausibility (Lutz et al., 2016).

Lutz et al. (2016) have recently developed a modified envelope-based approach for the selection of a representative global climate model, by combining the past-performance approach and the envelop approach. It focuses on simulating a workable number of climate model runs representing most likely future mean air temperature, annual precipitation and likely changes in climatic extremes. Such methods provide a range of possible future in terms of climate patterns.

In addition, future pathways which may be adopted to control Green House Gaseous (GHG) emissions remain uncertain. This uncertainty is mainly due to: i) understanding of atmospheric processes which could be improved in the future, ii) socio-economic pathways which may be adopted by the majority of the countries as a part of the UNFCCC Paris Agreement, and iii) future technologies that will be used to control GHG emission. To address this uncertain future, we have used a three-step methodology in this research.

The spatial resolution of GCMs is about 100-500 km in grid size with a temporal resolution of daily, monthly, or an even longer time-step. They are not able to represent local scales (eg 10 km x 10 km), and the results should only be adopted at continental or global spatial scales for \geq monthly time periods (Trzaska and Schnarr, 2014). GCMs are unable to represent sub-grid (small) scale features. For instance, local topography, land use and clouds cover as GCM outputs are rendered at a relatively coarse spatial resolution [i.e. approximately 250 km x 250 km] (Tisseuil et al., 2010). Hydrological assessment of climate change impacts needs climate data at finer spatial scales, which limits the direct use of GCM outputs at catchment level (Willems and Vrac, 2011). However, GCM outputs can be used to generate climate data at a finer scale to represent local climatic conditions. The process used to reduce the scale of any information finer than 100 km x 100 km scales (spatially) and shorter than monthly values is called downscaling, and it assumes that the local climate is a combination of local conditions and large-scale atmospheric features (Trzaska and Schnarr, 2014).

Shiru et al. (2020) used a multi-criteria decision-making approach in selecting the most suitable GCMs from 20 CMIP5 GCMs for Nigeria and reported that HadGEM2-ES,

CESM1-CAM5, CSIRO-Mk3.6.0, and MRI-CGCM3 were the best performing ensembles in replicating temperature characteristics in the region. Pickler and Mölg (2018) applied a two-tier approach to select the most robust GCM ensembles in Kilimanjaro area. Salman et al. (2018) applied a combination of the past performance and the envelope methods for selecting GCM ensembles from CMIP5 for the projection of changes in annual and seasonal temperatures in Iraq. Their study showed that HadGEM2-AO, HadGEM2-ES, MIROC5 and MIROC-ESM were most suitable GCM ensembles for projection of temperature in Iraq.

Previous studies conducted on climate projections for the Koshi River basin are based on a few selected GCMs and lack multiple criteria to select GCMs. Bharati et al. (2014) predicted the precipitation and temperature on the Koshi river basin for 2030s and 2050s considering *IPCC Special Report on Emission Scenarios (IPCC-SRES) A2 and B1* climate change scenarios. The study was done by simply averaging the outputs of 4 GCMs. Agarwal et al. (2014) conducted a study on Koshi River basin, considering 10 GCMs available in the Long Ashton Research Station Weather Generator (LARS-WG) and projected precipitation for 2011-2030, 2046-2065, and 2080-2099 considering the IPCC-SRES B1, A1B and A2 climate change scenarios. Likewise, Agarwal et al. (2016) predicted the temperature patterns in the Koshi River basin considering the same climate change scenarios, study periods and GCMs as adapted by Agarwal et al. (2014). Nepal (2016) studied the Koshi River basin considering IPCC-SRES A1B climate change scenario, and projected precipitation and temperature for 2040-2050 and 2086-2096. It used the Providing Regional Climates for Impact Studies (PRECIS) Regional Climate Model. Rajbhandari et al. (2017) also studied the Koshi River basin, and predicted precipitation and temperature parameters for 2011-2040, 2041-2070, and 2071-2098 considering IPCC-SRES A1B climate change scenario. They also considered the PRECIS Regional Climate Model. None of the above studies used CMIP5 GCM outputs and current RCPs. Furthermore, these studies did not apply any advanced envelop approach for GCM selection. Rather, they simply selected the GCM(s) from a pool of available GCMs.

Rajbhandari et al. (2016) considered Representative Concentration Pathways (RCPs) 4.5 and 8.5 for projecting precipitation and temperature patterns in the Koshi River basin for 2021-2050. They selected one GCM for each corner from a pool of 43 GCMs

for RCP4.5 and 41 GCMs for RCP8.5, basing their selection on the changes in the mean precipitation and temperature. Although Rajbhandari et al. (2016) has considered the current CMIP5 GCM outputs and RCP scenarios, the selection of the GCMs was made based on the projected changes in the mean precipitation and temperature from a limited sets of GCM outputs. It did not consider predicted changes in climatic extremes, or the past performance of GCMs to simulate the annual cycle. Also, they did not downscale their high resolution data, but rather relied on outcomes from GCM cells which were about 250 km x 250 km.

In this thesis, we explore the use of GCM outputs to estimate precipitation and temperature patterns against various global warming scenarios at short-term, mid-century and end-of-century time periods. Such analysis will be useful to understand the impact of climate change on the hydrological regime of river systems.

2.2 Climate change impacts on the hydrological regime of a river basin

Hydrological models have been extensively used to assess the impact of climate change in hydrology. Among the many hydrological models available, a few models like Agricultural Non-Point Source (AGNPS), Hydrological Simulation Program-Fortran (HSPF), Hydrological Engineering Centre – The Hydrologic Modelling System (HEC-HMS), MIKE SHE, and the Soil and Water Assessment Tool (SWAT), have been successfully verified in hydrological applications in many watersheds around the world (Gassman et al., 2007). Borah and Bera (2003) compared 11 different hydrological models and concluded that SWAT is a promising model to assess long term hydrological changes as well as overall river basin management. Khoi (2016) compared Hec-HMS and SWAT models to produce streamflow in a catchment and concluded that the SWAT model can be used to assess for hydrologic processes with a high accuracy. SWAT model has been successfully used to simulate climate changes impacts on hydrological regimes of rivers around the world including Australia (Saha et al., 2019, Shrestha et al., 2017), Europe (Kiesel et al., 2019, Piniewski et al., 2018), China (Liu et al., 2020a, Yan et al., 2019), and the USA (Chen and Chang, 2020).

Changes in climatic factors such as precipitation and temperature patterns significantly affect water availability in the mountainous region (Hock et al., 2019). The snowmelt is linked to the hydrological regime of the rivers originating from Himalayan regions.

Climate change impacts on precipitation and temperature are expected to affect the hydrological regime of the upstream basins in the Himalayan regions due to changes in snowfall and snowmelt patterns (Immerzeel et al., 2012, Lutz et al., 2014, Nepal, 2016). As climate change in the Himalayan regions is expected to have profound future implications on downstream water availability and dependent sectors (Eriksson et al., 2009, Hock et al., 2019, Nepal, 2016, Nie et al., 2021), it is of great concern to global scientific communities as well. Given these linkages, studies on climate change impacts on the hydrological regime of the Himalayan rivers are important.

Immerzeel et al. (2012) and Lutz et al. (2014) have reported that river flow in Himalayan river basins is projected to increase due to increased precipitation and temperature. Temperature increases have resulted in the rapid decline of the glacier area in Nepal (Shrestha and Aryal, 2011) and is likely to continue into the future, which in turn will contribute to increase in river flows. Similar studies have shown that river flows in most of the rivers in Nepal are likely to increase in future. For example Shrestha et al. (2016), Dahal et al. (2016), Bajracharya et al. (2018), Mishra et al. (2018), Pandey et al. (2019), and Dahal et al. (2020) assessed climate change impacts on hydrology of Indrawati, Bagmati, Kaligandaki, Bheri, Chamelia, and Karnali river basins in Nepal respectively and reported that annual river flows are projected to increase in future.

The hydrological assessment of climate change impacts needs climate input data at a finer spatial scale, which limits direct use of General Circulation Models (GCMs) outputs at a catchment level due to their coarse resolution (Willems and Vrac, 2011). Hence GCM outputs are less representative to local scales (Trzaska and Schnarr, 2014) and need conversion to a finer resolution to generate climate data that represent local and regional climatic and topographic conditions.

Previous studies conducted on climate change impacts on the hydrology of the Koshi River basin were based on low-resolution spatial data and lacked high-resolution precipitation and temperature data. Bharati et al. (2014) projected water availability in the Koshi River basin for 2030s and 2050s. Their study was conducted by using weather data at a spatial resolution of $0.5^\circ \times 0.5^\circ$ (~50 km x 50 km) and considering *the IPCC Special Report on Emission Scenarios* (IPCC-SRES) A2 and B1 climate change

scenarios. Agarwal et al. (2015) used downscaled data for 60 precipitation and 10 temperature stations in the Koshi river basin to estimate climate change impacts. Similarly, Nepal (2016) projected the hydrological regime of the Dudh Koshi River basin using the A1B climate change scenario from regional climate models, with precipitation and temperature data dynamically downscaled to a spatial resolution of 50 km x 50 km. However, impacts of climate change on the hydrological regime of the Koshi River basin have not been studied with high resolution daily precipitation and temperature data, such as 10 km x 10 km spatial resolution.

2.3 Climate change impacts on irrigation water requirement and crop grain yield within an irrigation scheme

Crop models have been extensively used to assess crop growth, development, water uptake, stresses due to various factors (water, nitrogen, and temperature) and crop grain yield. Among many crop models available, a few models like the Agricultural Production Systems Simulator (APSIM), the Decision Support System for Agrotechnology Transfer (DSSAT), CROPWAT, AquaCrop, ORYZA, CERES, Dynamic Computable General Equilibrium (DCGE), CropSyst, and Simple Simulation Models (SSM) have been successfully verified in crop modelling in many farmlands around the world (Kabir et al., 2018, Soltani and Sinclair, 2015).

Cropping system models including DSSAT, CROPWAT, AquaCrop, ORYZA, CERES, and DCGE, cannot identically represent actual farm practices and farm-specific contexts due to the complexity and dynamic nature of real farm systems. The resulting crop modelling is insensitive to adaptation options (Harrison et al., 2017, Harrison et al., 2011, Kabir et al., 2018). Soltani and Sinclair (2015) compared simpler crop models (CropSyst and SSM) with complex models (APSIM and DSSAT). They reported that (a) APSIM, CropSyst and DSSAT can simulate crop management effects like tillage and straw mulch while SSM cannot, and (b) access to the model codes is free for APSIM and SSM, while CropSyst and DSSAT provide limited access to the codes after permission.

There is a gap between crop irrigation water requirements and actual irrigation water application in many irrigation schemes around the world, especially in developing countries (Asres, 2016, Checkol and Alamirew, 2008, Moreno-Pérez and Roldán-Cañas,

2013, Nam et al., 2016). Knowing how to apply the correct amount of water at right time ensures that plant grain yield is not adversely affected by water stress. This is called irrigation scheduling, and is crucial for managing irrigation water. Fixing quantities and timings of irrigation water to meet the crop's water requirements also help water conserve. Although a small number of irrigation scheduling techniques and research findings are available, it is still at an inception stage in many developing countries (Pundarikanthan and Santhi, 1996). Improved guidelines for optimum irrigation scheduling are required in Asia for effective irrigation water management (Humphreys et al., 2005).

Farmers in most of the irrigation scheme command areas in the developing world generally do not have knowledge of the irrigation water required for crops. They apply either more or less than the required irrigation demand. Farmers often apply in excess of 2000 mm of water to paddy fields, although the seasonal water requirement is about 600 mm to 1400 mm in Punjab and Sindh Provinces of Pakistan respectively. This excess irrigation results in water loss (via deep drainage) and lower crop grain yield (Hossain et al., 2017).

Likewise, Chandran and Joseph (2015) based on their research in the Kerala state of India, found that more than 80% of farmers applied irrigation water that was either < 50% or > 100% of the required irrigation demand. Idnani and Kumar (2013) conducted a field experiment in New Delhi, which found that both wheat grain yield and water use efficiency could be increased by adopting optimal irrigation scheduling.

Estimation of optimal irrigation water requirements helps to increase grain yield whilst applying less water. However, it has not been widely utilized in developing countries due to inadequate knowledge about the practice. Paudel (2010) found that the main canal distribution system in Sunsari Morang Irrigation Scheme in Nepal followed no specific irrigation schedule protocol, but rather was being operated more or less randomly. Research on careful evaluation of soil moisture characteristics and optimal irrigation scheduling is still required as they are complex processes (Krupnik et al., 2015). In the climate change context, all irrigation schemes must practice optimal irrigation scheduling to cope with future water scarcity.

Farmers are not able to achieve their potential crop grain yield in agricultural farms. Khaliq et al. (2019) reported that farmers are harvesting about 50% of potential wheat grain yields at present. Li et al. (2014) assessed the grain yield of winter wheat in the North China Plain, and stated that regional average grain yield was around 55% of the potential grain yields in 1981-2010. Deihimfard et al. (2015) reported that average wheat grain yield was around 80-98% of the potential grain yields in the Khorasan province of Iran.

Mirgol et al. (2020) modelled climate change impacts on grain yields of winter wheat crops in the 2030s, 2050s and 2080s using a single GCM, The Canadian Earth System Model (CanESM2), and applying IPCC climate change scenarios RCPs 2.6, 4.5, and 8.5 in the Qazvin Plateau, Iran. Their study predicted that the grain yields of future winter wheat crops would decrease by 60-100% for all climate change scenarios. They also reported an increase in future irrigation water requirements by 40-80%, compared to the 1986-2015 period. Bouras et al. (2019) assessed climate change impacts on irrigation water requirements and grain yields of wheat crops in the Tensift region of Morocco for 2050s and 2090s using climate change scenarios RCP4.5 and RCP8.5. Their study reported that both future irrigation water demands and wheat grain yields would decrease by 13-42% and 7-30% respectively. Likewise, Goodarzi et al. (2019) evaluated climate change impacts on irrigation water requirements for different crops in Iran for the 2017-2046 period considering climate change scenarios RCPs 4.5 and 8.5. They used the CROPWAT model. They projected an increase in irrigation water requirements for wheat crops by 12-16%, compared to 1976-2005 period. Zhang et al. (2013) assessed climate change impacts on wheat grain yields in the 2080s compared to 1961-1990 in the North China, and predicted that wheat grain yields would decrease by 4-6 % and 1-5 %, considering climate change scenarios A2 and B2 respectively. They used the APSIM crop model in their study.

2.4 Canal water losses and canal hydraulic capacity assessment of an irrigation scheme

Seepage and operational losses in unlined irrigation canal networks are ongoing problems for water managers (Worstell, 1976). In most Indian irrigations systems, more than half of the water is lost in seepage and evaporation during delivery from the head

of the canal to the field (Sharma et al. cited in Swamee et al., 2002). Memon et al. (2013) reported water loss of 47% when water is conveyed from canal head to farm gate through the Dabu canal system in Pakistan.

Seepage losses from irrigation canals mainly depend upon the permeability of the subsoils, sediment quantity in irrigation water, the depth of the local water table relative to the canal bottom, distance of drainage, bed width and side slope of the canal, and the water depth and velocity in the canal. In India, the seepage losses from unlined canals range from 0.026-0.61 m³/m²/day (Indian Standards Institution, 1980). Working in an experimental field channel in arid Saudi Arabia, Moghazi and Ismail (1997) reported average seepage rates of 2.65, 2.16, 0.464 m³/m²/day in canals with uncompacted earthen beds, compacted channel beds and prefabricated bitumen jute mat respectively. According to Wilkinson (1985), a canal having a seepage loss >0.031 m³/m²/day is considered to be a good candidate for lining, whilst a canal with a seepage loss <0.031 m³/m²/day is considered to be “tight”. Seepage loss in unlined canals in permeable soils varies from 20 to 30% of the total irrigation water supply (FAO/UNESCO, 1973).

Kilic and Tuylu (2011) investigated water losses in the conveyance system of the Ahmetli irrigation scheme in Turkey using the inflow-out flow method. They reported that average water loss in the main canal was 0.067 l/s/m² with the loss varying from 0.012 – 0.142 l/s/m² at different sections of the main canal. Likewise, Eshetu and Alamirew (2018) evaluated water losses in irrigation canals in Ethiopia using the inflow-outflow method. They reported that the average water loss in main canal was 0.0126 l/s/m² with the loss varying from 0.0123 – 0.0129 l/s/m² at different sections of the main canal lined with geo-membrane. In the earthen portion of the irrigation main canal, the average water loss was 0.0180 l/s/m². Mohammadi et al. (2019) analysed water losses in irrigation channels in Iran and reported average water losses of 0.014 l/s/m² in the main canal. Water losses varied from 0.013 l/s/m² to 0.016 l/s/m². Akkuzu (2012) assessed water losses in an irrigation canal in Turkey using the inflow-outflow method and reported that the average water loss was 0.014 l/s/m² varying from 0.002 l/s/m² to 0.036 l/s/m² at different locations of the canal.

Factors affecting irrigation canal discharge capacity include flow obstructions, siltation, and reduction in canal bank height. Flow obstruction in irrigation canals is represented

by Manning's roughness coefficient in hydraulic modelling. Manning's roughness coefficient values for earthen canals is 0.02 for newly constructed very smooth canal sections without meandering, 0.1 for very high vegetation conditions, and 1.3 for severe meandering conditions (Department of Irrigation, 2014, United States Geological Survey, 1989). The branch irrigation channels in case study area are under severe meandering conditions in few places. Manning's roughness coefficient values for designing earthen irrigation canals in Nepal is generally taken as 0.025-0.03. Bakry et al. (1992) investigated the Manning's roughness coefficient in an irrigation canal in Egypt, and reported a maximum Manning's coefficient of 0.083 in earthen canal. Salah Abd Elmoaty and El-Samman (2020) conducted an investigation on Manning's roughness coefficient for different weed density scenarios in channels. They reported a maximum value of Manning's roughness coefficient for high weed, medium weed and low weed densities were 0.12, 0.08 and 0.07 respectively.

Storm Water Management Model (SWMM) model has been successfully used to simulate hydraulic characteristics of irrigation canals. Kim et al. (2016), Do et al. (2019) and Bang et al. (2019) assessed the hydraulic performance of irrigation canal in South Korea using Storm Water Management Model (SWMM) model. Schoenfelder et al. (2006) applied SWMM to evaluate hydraulic performance of irrigation canals in the USA. Banda and Kasitu (2018) used SWMM to assess the capacity of drainage system in South Africa.

The Sunsari Morang Irrigation Scheme in Nepal was designed by the British administration in the 1960s without considering crop water requirement criteria, since the main focus was to increase the cropped area, and protect crops from catastrophic drought failure (Paudel, 2010, Adhikari, 2016, Renault and Wahaj, 2006). The Sunsari Morang Irrigation Scheme was designed to supplement the monsoon rainfall, which allows only one crop of paddy rice per year over the entire area (FAO, 2016a, Adhikari, 2016, Renault and Wahaj, 2006).

Based on the analysis of data from 1970 to 1993, the Nepal Department of Irrigation (1995) reported that the design discharge of 60 cumec can irrigate about 57,000 hectares (nearly 84% of the command area) with an 80% reliability of supply in the monsoon season. A scheme performance assessment conducted by the World Bank showed that

the overall efficiency of Sunsari Morang Irrigation Scheme is below expectation, and is rated as very low due to poor water management. Although there was an increase in cropping intensity, the project had little impact on paddy rice grain yields.

A field survey by the Nepalese National Planning Commission (2012) reported that 52% of the households in the Sunsari Morang Irrigation Scheme do not receive sufficient water during the cropping period. This report also notes that only about 10% of the farmers get irrigation water when they require it; 33% receive water, but with delays; 30% have difficulty getting water; and about 19% are unable to get water at all. Entry of silt from the river into the canal network has been a problem since the Sunsari Morang Irrigation Scheme began operating. It is the largest irrigation scheme in Nepal. There are no scheduled operations and maintenance plans. Being a large scale irrigation scheme with a limited yearly operation and maintenance budget, the canal system in the Sunsari Morang Irrigation Scheme is not well maintained. Siltation and weed are very common in the canal system, reducing the canal discharge. However, studies have not been carried out to investigate the impacts of flow obstructions on canal flow capacity.

Overall, previous studies on irrigation water have been carried out in an isolation, mainly focusing on crop water requirement without considering the supply side of irrigation water. The supply and demand sides of irrigation water have not been assessed simultaneously using a systems approach. A comprehensive methodology to assess climate change impacts on irrigation water including both the supply and demand sides is still missing.

Chapter 3: Study area

Chapter Three provides information on study areas including general information on the catchment characteristics of the Koshi River basin, and the salient features of the Sunsari Morang Irrigation Scheme.

3.1 The Koshi River basin

3.1.1 Catchment characteristics of the Koshi River basin

The Koshi River, one of the largest tributaries of the Ganges, originates in China and flows through Nepal and India. The Koshi River basin is the largest river basin in Nepal. About 22% of Nepal's population (around 5.8 million people) lives within this basin (Dixit et al., 2009). The catchment area of the Koshi River basin near Chatara in Nepal (Figure 3.1) is about 54,0000 km² (28,080 km² in Tibet (China) and 25,920 km² in Nepal), delineated using ArcSWAT. The location of the catchment area of the Koshi River basin in China and Nepal is shown in Figure 3.1. The catchment areas in Nepal contain the High Himalaya (elevation >3000 m) and Lower Himalaya (elevation <3000 m) with area of are 8257 km² and 17669 km² respectively. The altitude in the Nepalese part of the catchment area varies from 97 m above mean sea level (AMSL) in the southern part, to > 8000 m AMSL in the northern part of the High Himalayas. The altitude in the Tibetan part of the catchment varies from 1018 m to 8792 m AMSL.

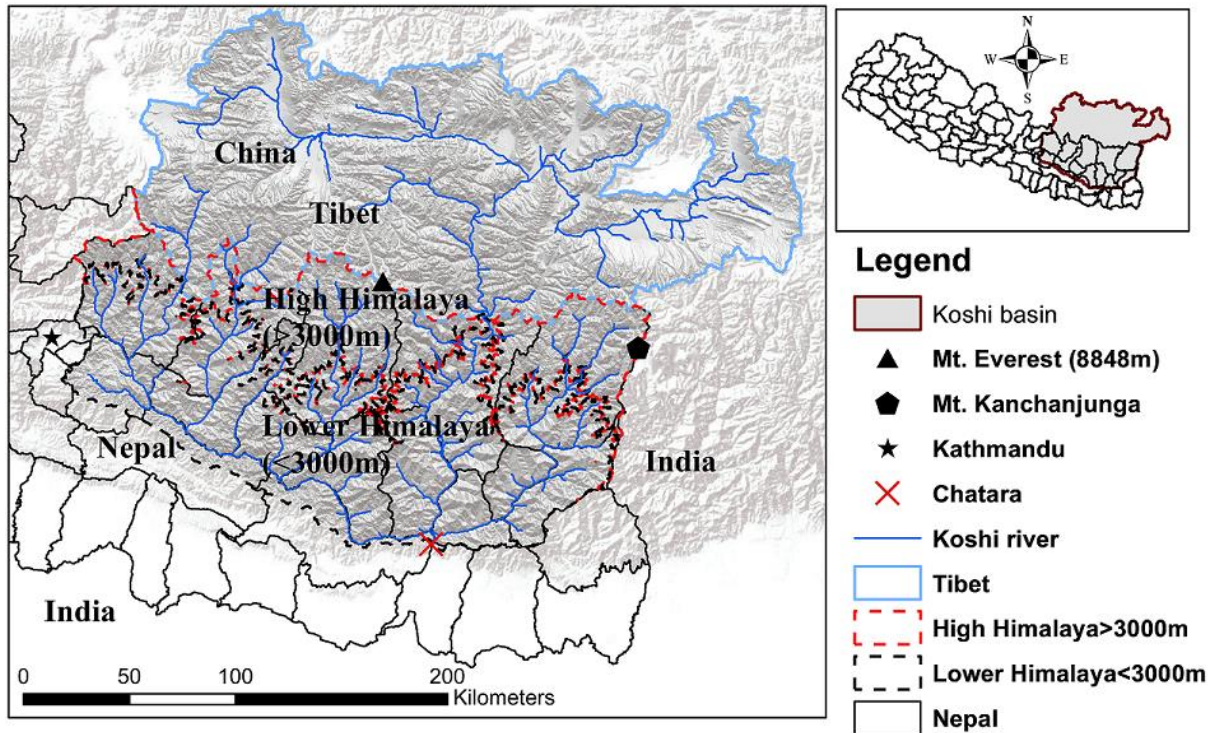


Figure 3.1: The Koshi River basin down to Chatara in Nepal. All the rivers are coloured blue.

3.1.2 Average discharge in the Koshi River

There is a large spatial and temporal variation in rainfall in the Koshi River basin, with approximately 80 % of the annual rainfall occurring in the monsoon season between June and September, (Dixit et al., 2009, Water and Energy Commission Secretariate, 2005). Increases in the severity and duration of droughts in the dry seasons, and floods in the monsoon season are the main climate trends in the Koshi River basin (NCVST, 2009). The large variation in rainfall results in significant variations in river discharge. Daily river discharge data at Chatara for the period 1982-2010 were obtained from the Department of Hydrology and Meteorology, Nepal. Mean monthly discharge, based on river discharge data from 1982-2010, is shown in Figure 3.2. The mean **monthly** flow varies from around 340 m³/s in February to 4,315 m³/s in August. The average yearly discharge is about 1,515 m³/s. The average monthly discharge in monsoon season (June-September) is about 3,300 m³/s, which is more than 200% of the average monthly discharge. In contrast, during the winter season (December, January, February) average discharge is about 410 m³/s which is around 25% of average annual river discharge.

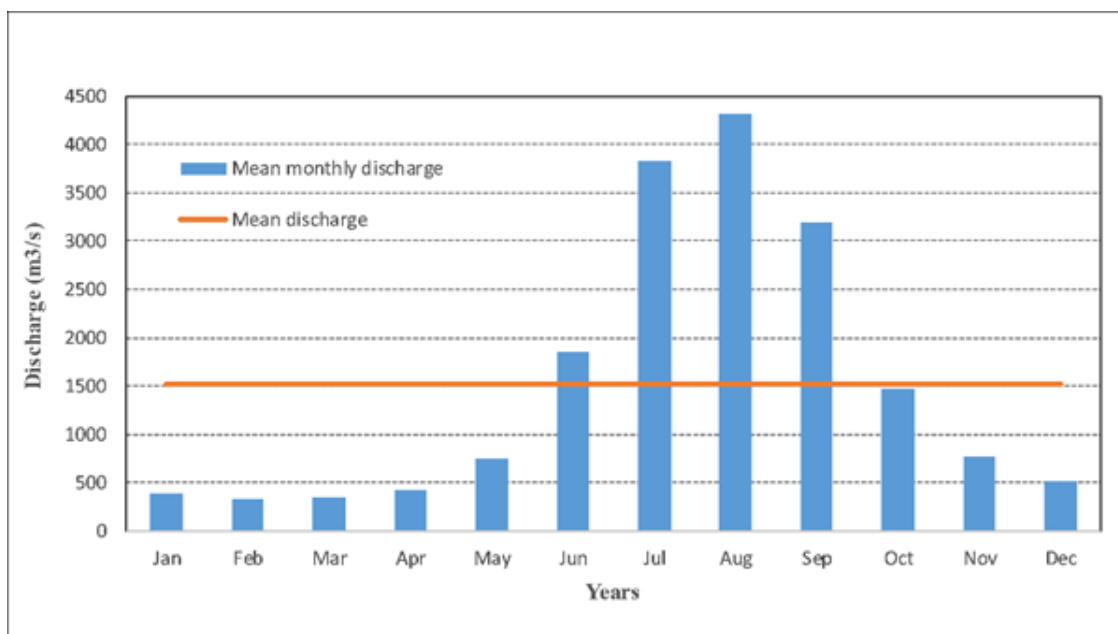


Figure 3.2: Measured mean monthly discharge (m^3/s) of the Koshi River at Chatara for the period 1982-2010.

3.2 The Sunsari Morang Irrigation Scheme

3.2.1 Development of Sunsari Morang Irrigation Scheme

The Sunsari Morang Irrigation Scheme lies in the south-eastern region of Nepal, and was constructed about 50 years ago. The southern part of Nepal is called the Terai region, a large plain, also known as the food basket of Nepal. The location of the Sunsari Morang Irrigation Scheme is shown in Figure 3.3. The blue lines in Figure 3.3 represent the Sunsari Morang irrigation canal network and the red dotted line is the boundary of the Koshi River basin. The irrigation canal intake is located at Chatara. In 1954, His Majesty's Government of Nepal (HMG/N) reached an agreement with the Government of India (GOI) under which GOI undertook to finance and construct the then Chatara Canal Project in Nepal. The objective of Chatara Canal Project was to command 68,000 ha of land encompassing the Sunsari and Morang districts, using water diverted from the left bank of Koshi River by a side intake regulator. Construction of the system started in 1964, and it was handed over Nepal in 1975 after a trial run of 5 years. The Chatara Canal Project was later renamed the Sunsari Morang Irrigation Project. When constructed in 1964, the main canal system was designed to divert $45.0 \text{ m}^3/\text{s}$ (Sunsari Morang Irrigation Project, 2015).

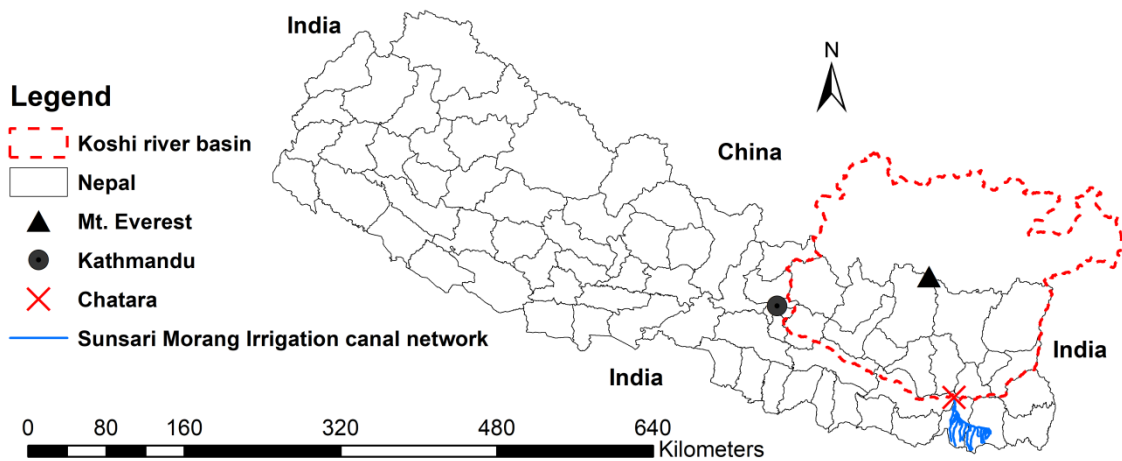


Figure 3.3 Location of Sunsari Morang Irrigation Scheme in Nepal (blue lines represent the Sunsari Morang irrigation canal network).

However, after only a few years of canal operation, the excessive entry of silt into the canals was observed. The silt reduced the discharging capacity of the system. Periodic removal of silt from main canal required the closure of the canal system, impairing its capacity to provide year-round irrigation. This reduced the usefulness of the canal system for food production (Sunsari Morang Irrigation Project, 2015). The problem was exacerbated by the continued westward advance (towards the side opposite to the canal intake) of the bed of the Koshi River, making it extremely difficult to divert water from the river into the system.

The Sunsari Morang Headworks project was started in 1993. It mainly included relocating the intake structure 1300 m upstream along the Koshi River in order to increase the capacity of intake to $60 \text{ m}^3/\text{s}$, and constructing a large capacity settling basin ($900 \text{ m} \times 60 \text{ m}$) (Sunsari Morang Irrigation Project, 2015). The headwork project aimed to increase water supply from $45.0 \text{ m}^3/\text{s}$ to $60.0 \text{ m}^3/\text{s}$, and was completed in 1996. The completion of the Sunsari Morang Headworks Project works and subsequent operation minimized the silt problem, assuring the availability of water in the system throughout the year. The completed components of the Sunsari Morang Headworks Project were put into full operation in June 1996. Different works have been continuously carried out at the intake, the canal network and the command area for the operation and maintenance of the canal system. However, the Koshi River is

continuously shifting westwards, which has proved challenging for the gravity flow of river water into the canal network.

3.2.2 Crop water requirement considerations in the Sunsari Morang Irrigation Scheme

Agriculture was the dominant source of revenues of colonial powers in Asia and irrigation systems were mainly designed to maximize crop productivity (ton/year) rather than land productivity (ton/ha/year) in the Colonial Era (1850 to 1950) (Barker and Molle, 2004). After the colonial period of the British in India, modernization of the irrigation system was carried out to prevent famine and to stabilize the revenues from irrigated land. Production and land tax from rain-fed agricultural land were low and heavily reliant on rainfall (Bolding et al., 1995). Jurriens et al. (1996) argue that protective design criteria which required spreading the available water thinly over a large command area (ML/ha/yr) rather than considering crop water requirements, have been followed in most of the irrigation schemes in India and nearby countries since 1880, and that is still the prevailing paradigm. Under a regime employing protective design criteria, water is not supplied to optimise the irrigation requirements. Instead, the water supply is merely enough to protect the crop from failure. The irrigation deficit means that crop productivity (ton/ha) is sub-optimal. However, large crop areas are covered in protective design criteria. In India, productive irrigation, where water is adequately supplied to fulfil the irrigation requirement, was practised in the first half of the nineteenth century, but protective irrigation commenced after 1860. Under productive irrigation, the crop productivity (ton/ha) is high while crop area coverage is low in comparison to land farmed under protective design criteria. Farmers showed less interest in protective irrigation due to the high cost in land preparation for irrigation and the limited increase in grain yield due to insufficient water allocation per hectare (Bolding et al., 1995). Barker and Molle (2004) identified changes in the system design of publicly managed irrigation schemes in South and Southeast Asia over the last 170 years. During the Colonial Era (1850 to 1950), supplemental principles prevailed. During the Cold War Era (1950 to 1990), irrigation schemes were supply-driven. In the New Era of Globalization (1990 onwards) there has been a switch to demand-driven design.

The crop water requirement estimation in the Sunsari Morang Irrigation Scheme was based on protective design criteria which provided only supplementary irrigation drawn from the monsoon rainfall, thereby guaranteeing one crop of monsoon rice per year over the entire command area (FAO, 2016a, Adhikari, 2016, Renault and Wahaj, 2006).

3.2.3 Headworks and canal networks in the Sunsari Morang Irrigation Scheme

The Sunsari Morang Irrigation Scheme has a command area of 68,000 hectares (about 3% of the total irrigable land of Nepal) and is designed to supply a peak discharge of 60 cubic meters per second. There is no permanent diversion structure (barrage or weir) in the headworks (Figure 3.4) and the water is diverted from the side intakes. The river water overflows into the main canal via the side intake utilizing gravity flow. The main irrigation development in the Colonial Era (1850 to 1950) was mainly river diversion and flood regulation. This shifted to storage dams and gravity irrigation during the Cold War Era (1950 to 1990), and is now focused on pumps and wells in the New Era of Globalization (1990 onwards) (Barker and Molle, 2004). Side intake headworks without permanent diversion structures or pumping mechanism are very common in developing countries, as diversion structures across the river (i.e. weirs) are costly, and normally beyond the financial capacity of these countries. Thus, water supply in to the canal system depends on the water level in the river.

(a) Side-intake in wet season



(b) Side-intake in dry season



(c) Side-intake orifice with gates (gravity flow)



Figure 3.4: Headwork of the Sunsari Morang Irrigation Scheme.

There are 12 intake orifice openings with a total width of 48 m, as shown in Figure 3.4. The reduced level of the orifice crest (the bottom of the orifice) is 107 m above mean sea level (AMSL). The opening size of each of the 12 orifice bays is 4 m wide by 5 m high. During monsoonal flood flows (June, July, August, and September), the water level in the river raises. It usually contains silts as well as other debris such as trees, and wooden planks. Consequently, a 1 m high stop log is kept at the bottom of the orifice, as

well as iron trash racks, to reduce the amount of silt and floating debris entering the canal. However, they are not installed during the low flow periods in the river (November to May).

The main canal length is 55 km. There are 25 branch (secondary) canals supplied from the main canal. These secondary canals then branch into distributary (sub-secondary) and tertiary canals. The total length of branch and distributary canals is about 425 km, whilst that of the tertiary canals is a further 410 km. In addition to the branch canals, a few direct outlets from the main canal also supply water to the command area. A schematic of the main canal and major branch canals network of the Sunsari Morang Irrigation Scheme is shown in Figure 3.5. The blue lines in Figure 3.5 represent the main and branch canals.

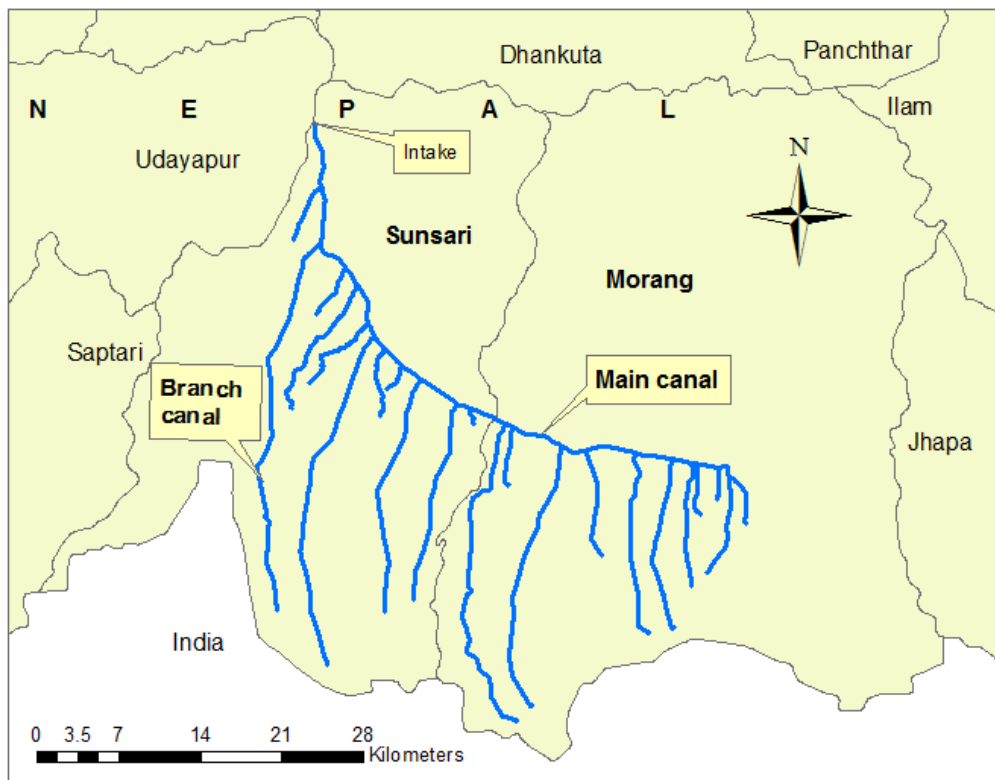


Figure 3.5: Canal network of the Sunsari Morang Irrigation Scheme.

Almost all the main and branch canals are unlined earthen canals. Parts of the canal sections adjacent to canal structures such as the head regulator, cross regulator, aqueduct, super passage, village road crossings, and escapes are lined with reinforced

cement concrete. Most of the structures are functioning inefficiently, as they were built about 50 years ago and the level of maintenance is low.

The main canal size varies from around 23.5 m wide by 2.5-3 m high at the head reaches to 20 m wide by 2 m high at the middle reaches and to 3 m wide by 1 m high at the tail reaches. Portions of the main canal are shown in Figure 3.6.

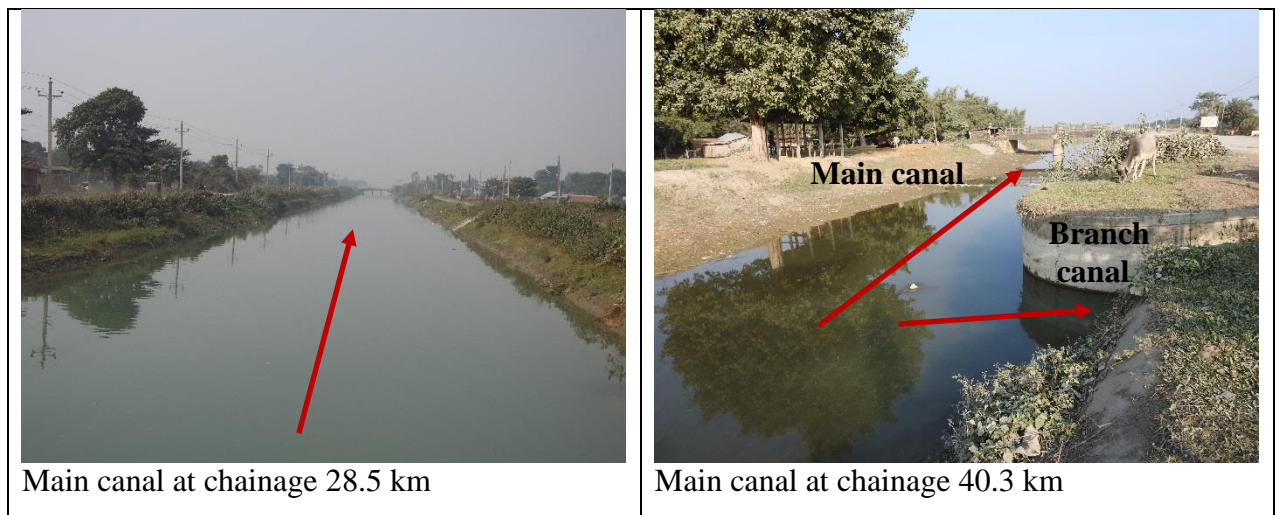


Figure 3.6: Main canal of the Sunsari Morang Irrigation Scheme.

Losses such as seepage loss and loss from structures like aqueducts (a bridge over the natural channels constructed to carry irrigation water) are common in earthen canals, and the Sunsari Morang Irrigation canal is no exception.

Operation and maintenance of the main canal is the responsibility of the Sunsari Morang Irrigation Project Office, under the Department of Water Resources and Irrigation. Due to a limited yearly operation and maintenance budget, the Project Office focuses on maintenance of structures to prevent failure, and the lining of the canal in places where the banks are prone to failure, rather than investing in silt and weed clearance. Farmers are not interested in removing the silt and weeds from the tail portion of the main canal as they do not receive water on a regular basis. These factors have substantially reduced the canal cross section as well as the flow capacity. Examples of poor maintenance and weed growth at the tail portions of the main canal are shown in Figure 3.7.

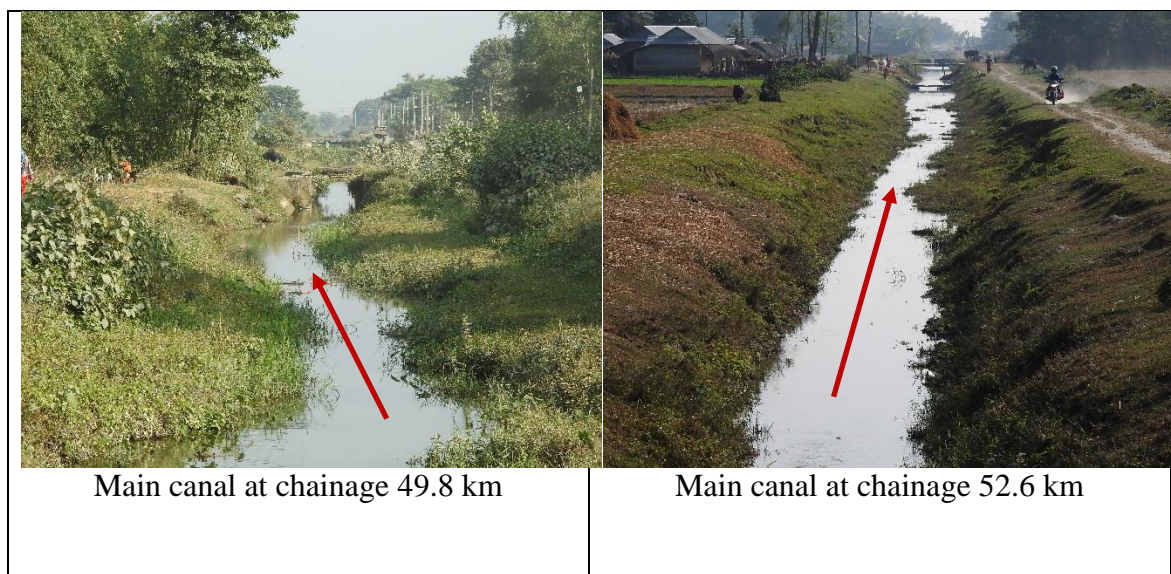


Figure 3.7: Reduced flow section at the tail portion of the main canal.

From the main canal to the field level, the canal network in the Sunsari Morang Irrigation Scheme follows six levels of canal covering 38,000 hectares of irrigation command area, also called the developed area (Figure 3.8). The remaining 30,000 hectares of command area remain undeveloped (Figure 3.9). The canals systems in the developed command area are the main canal, secondary canals, sub-secondary (distributary canals), tertiary canals, watercourses, and field channels. The Ministry of Water Resources (1997) has firstly defined the main, branch, and distributary canals as those which irrigate 30-500 ha, while minor canals irrigate 10-30 ha and watercourses irrigate 10 ha or less. It was mentioned in *Irrigation policy 1992* (first amendment 1996). The policy did not mention field channels, which suggests that field channels were not in common use at that time (1992).

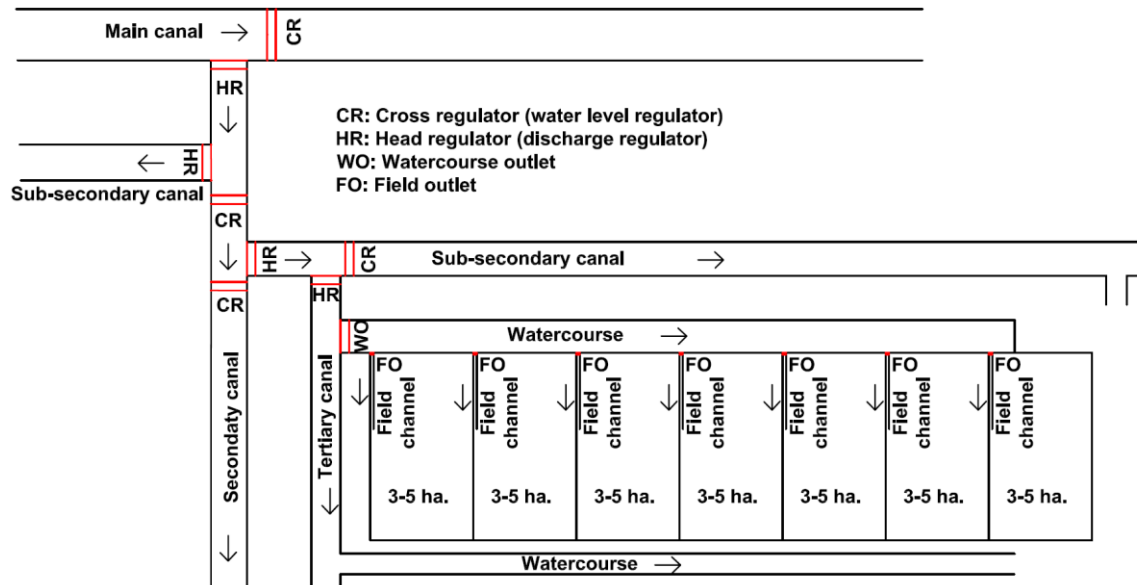


Figure 3.8: Schematic diagram of the canal system in the developed area (38000 ha).

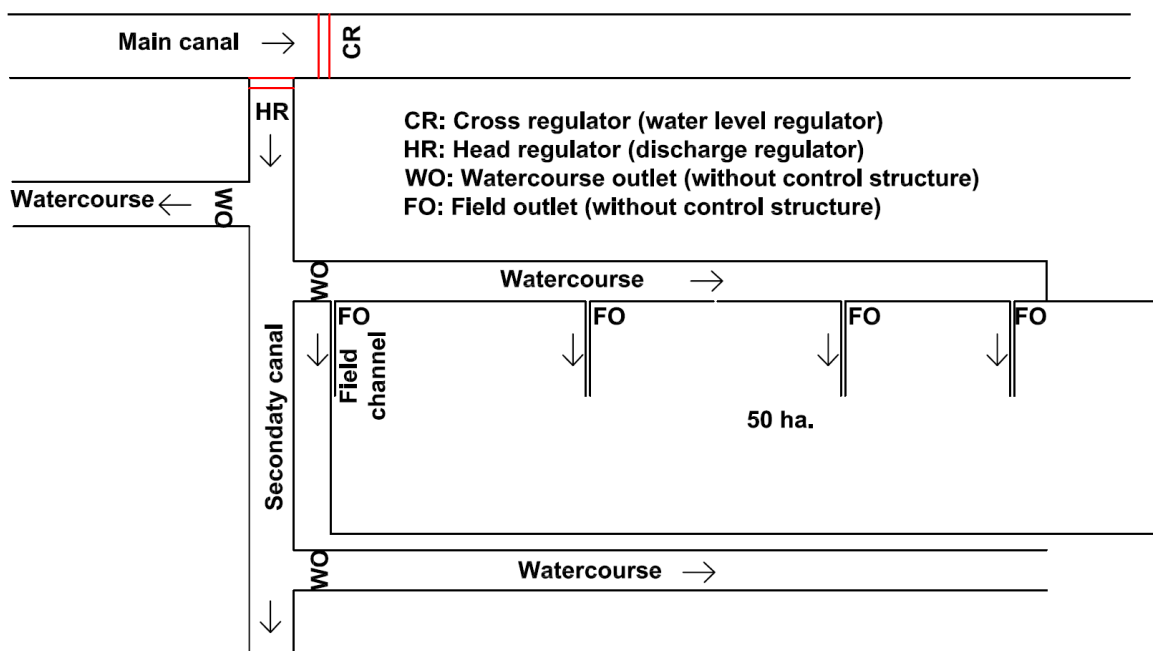


Figure 3.9: Schematic diagram of the canal system in the undeveloped area (30,000 ha).

The Ministry of Water Resources (2003), in *Irrigation policy (2003)*, defined the field channel. It defined distributary canals (which irrigate 100-500 ha), minor canals (which irrigate 30-100 ha), watercourses (which irrigate 10-30 ha) and field channels (which irrigate agricultural plots <10 ha inside the command area). Realizing the importance of field channels, Ministry of Irrigation (2013), in *Irrigation policy (2003)*, defined distributary (sub-secondary) canals as those which receive water from the main or a

branch canal, and irrigate 100-500 ha within the command area. Minor (tertiary) canals receive water from the main or a branch or a distributary canal, and irrigate 30-100 ha. Watercourse offtakes receive water from the main or a branch or a distributary or a minor canal, and irrigate 4-30 ha. Field channels irrigate agricultural plots <4 ha. The field channels receive water from the main or a branch or a distributary or a minor canal or a watercourse.

Agricultural areas receiving irrigation water supply following the canal network as shown in Figure 3.8 are considered as developed areas. Up to 2003, command area development works have been carried out on about 38000 ha of the total potentially commandable area of 68000 ha. The development works include construction of the sub-secondary canals, tertiary canals, watercourses, field outlets and field channels supplying up to 3-5 ha field plots. The supply system has gated or check structures installed from the main canal down to the field outlets. Each watercourse, having an average length of about 1.5 km, irrigates around 28 ha and consists of 7 field outlets. Each outlet supplies water to a 3-5 ha area. A field channel is needed to irrigate the 3-5 ha of land, and water must travel through a number of fields (usually <0.4 ha) to irrigate the tail end field.

In those portions of the command area without infrastructure development works, branch canals offtake water from the main canal, and outlets then provide water to the watercourses. There are no gated structures on the outlets and watercourses (unlike in canal systems in the developed areas). These portions of command area are locally known as undeveloped areas. There are no sub-secondary or tertiary canals in an undeveloped area. Each watercourse in the undeveloped area irrigates around 50 ha compared with 28 ha in the developed area. Each watercourse is 3 to 4 km long and contains 3 to 4 outlets. Field outlets and field channels do not have gated or check structures installed.

Chapter 4: Methodology

In this chapter, the comprehensive methodology to assess the climate change impacts on supply and demand sides of irrigation water is described. This chapter also explains the data collection and processing component of the research.

4.1 Methodology for investigating climate change impacts on supply and demand sides of irrigation water under an irrigation command area

The conceptual methodology to assess the climate change impacts on supply and demand sides of irrigation water is shown in Figure 4.1. The methodological framework is divided into four major components.

1. Understanding climate change impacts on daily rainfall and temperature (minimum and maximum) in river basins and irrigation command areas (GCMs selection and climate data downscaling)
2. Future impacts on river water availability due to climate change at irrigation canal intakes (hydrological assessment of river basin)
3. Crop water requirements due to climate change (irrigation water requirement assessment)
4. Irrigation canal systems' hydraulic capacity requirements for water supply in a climate change context (irrigation canal hydraulic capacity assessment).

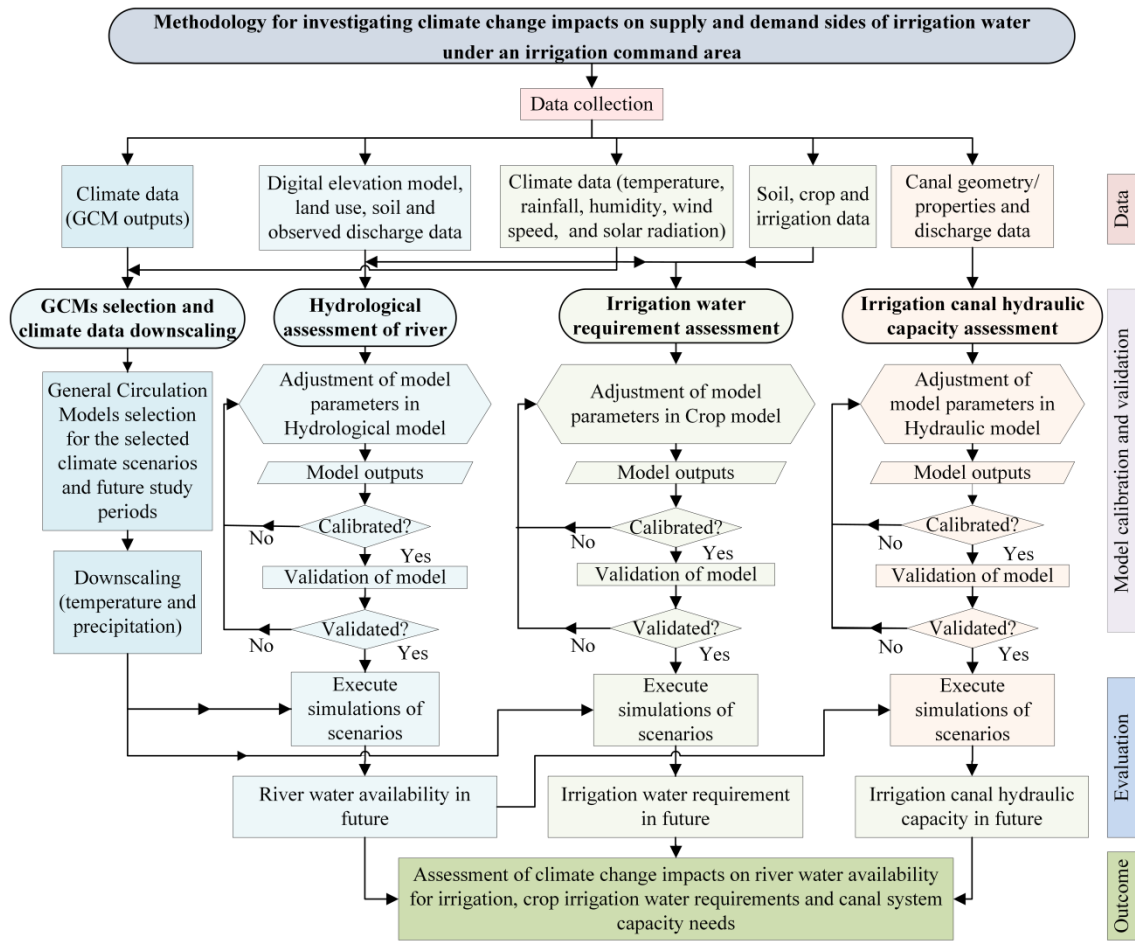


Figure 4.1: Flowchart of methodology for investigating climate change impacts on demand and supply sides of irrigation water.

The General Circulation Model selection and climate data downscaling are used to project climate data (precipitation and temperature) in future periods (2016-2045, 2036-2065, 2071-2100) considering different climate change scenarios (representative concentration pathways 4.5 and 8.5). These data are used in hydrological modelling to project future water availability at the headwork of the Sunsari Morang Irrigation Scheme in the Koshi River basin. These projections are used to estimate future discharge into the main irrigation canal. The predicted future climate data are also used in crop modelling to predict irrigation water requirements for crop in future time periods. Based on future water availability for irrigation in the river and irrigation water requirement for crop, the canal hydraulic capacity needs in the future are also assessed.

4.2 Data collection and processing

Global Circulation Models' outputs along with related data required for GCM selection and downscaling, were downloaded from the Royal Netherlands Meteorological Institute (KNMI) Climate Explorer (<https://climexp.knmi.nl/start.cgi>), climate4impact (<https://climate4impact.eu/impactportal/general/about.jsp>), the Max-Planck Institute for Meteorology (<https://code.mpimet.mpg.de/projects/cdo/files>), the International Centre for Integrated Mountain Development (<http://rds.icimod.org/clim>) and other publicly available resources.

Historic daily climate data including daily rainfall, temperature, solar radiation, wind speed and humidity were collected from the Department of Hydrology and Meteorology, Nepal. These data were used in the hydrological model. Historic runoff data of the Koshi River were also collected from the same source and used in the hydrological model.

Input data for crop modelling include soil, crop specific, management and time series climate data. The measured phenology, biomass yield and yield data for winter wheat crops were used for the calibration and validation of the crop model. The climate data for the Sunsari Morang Irrigation command area, obtained from APSIM Next Generation (Holzworth et al., 2018) for the years 2016-2020, were used in this research. The management data such as irrigation and fertilizer use were measured in the field. The soil data used were based on laboratory results.

Data on canal geometry (longitudinal section and cross section), canal discharge, flow velocity, and water depth data were measured in the field, and also obtained from the Sunsari Morang Irrigation Scheme office. Canal discharge, flow velocity, and water depth data were used for the calibration and validation of the crop model. The climate data were taken from APSIM Next Generation (Holzworth et al., 2018) for the years 2016-2020. Historical data on river water levels at the irrigation canal intake were obtained from the Sunsari Morang Irrigation Project Office, Nepal.

4.3 Model calibration and validation; evaluation and outcome

The details of each component of the methodology (as depicted in Figure 4.1) are demonstrated with a case study application in respective chapters (Chapters 5-8). General Circulation Models (GCMs) selection and downscaling is described in Chapter

Five. Hydrological assessment of river basin is described in Chapters Six. Irrigation water requirements assessment is mentioned in Chapter Seven and irrigation canal hydraulic capacity assessment is described in Chapter Eight.

Chapter 5: General circulation models selection and climate data downscaling

This section is divided into two parts. Firstly, it focuses on the selection of representative General Circulation Models (GCMs) for the Koshi River basin. Then, downscaling of the climatic parameters (precipitation and temperature) for the Koshi River basin is carried out based on the selected GCMs. It predicts the future climate for the short-term (2016-2045), mid- century (2036-2065) and end-of-century (2071-2100) time periods considering climate change scenarios RCP4.5 and RCP8.5. The predicted downscaled climate data will be used in the hydrological modelling to estimate water availability at the headwork of the Sunsari Morang Irrigation Scheme in the Koshi River basin of Nepal.

5.1 Representative GCM selection for the Koshi River basin

5.1.1 General Circulation Models (GCMs)

GCM computer models mathematically represent numerous atmospheric, oceanic and biotic processes of the world climate system, and are the main tools used to project climate changes under increased greenhouse gas concentrations (Trzaska and Schnarr, 2014). In climate models, researchers divide the world into a three-dimensional grid (Figure 5.1), apply the basic principles of physics, fluid motion and chemistry, and evaluate the results (National Oceanic and Atmospheric Administration, 2018). These models calculate radiation, heat transfer, relative humidity, wind and surface hydrology within each grid, and assess interactions with neighbouring grids. The atmospheric and oceanic processes were firstly combined in the late 1960s at the Geophysical Fluid Dynamics Laboratory (GFDL) of the National Oceanic and Atmospheric Administration (National Oceanic and Atmospheric Administration, 2018). Climate models provide quantitative estimates of future climate changes with a considerable confidence. The sources for confidence in model outcomes is that they are based on established physical laws, such as conservation of mass, energy and momentum, along with observations; as well as their ability to simulate various aspects of the current climate (IPCC, 2007).

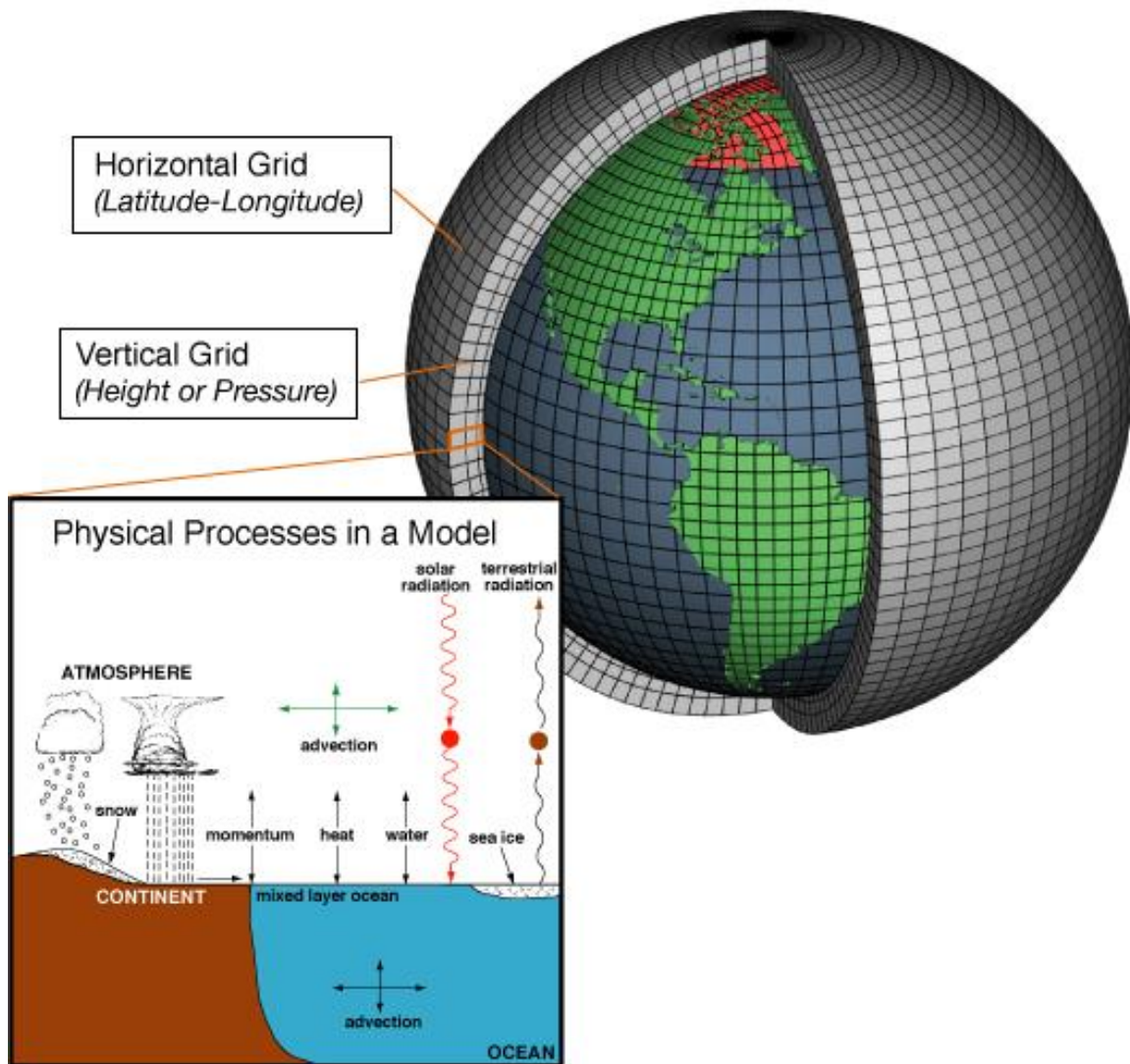


Figure 5.1: Representation of world in General Circulation Models (National Oceanic and Atmospheric Administration, 2018).

The number of GCMs available to predict future climate is increasing. The numbers of GCMs outputs applied in the Coupled Model Intercomparison Project Phase 3 (CMIP3) (Meehl et al., 2007) and the Coupled Model Intercomparison Project Phase 5 (CMIP5) (Taylor et al., 2012) were 25 and 61 respectively. The CMIP3 outcome archives were used for the Fourth Assessment Report (IPCC, 2007) and CMIP5 outcome archives were used for the Fifth Assessment Report (IPCC, 2013) of the Intergovernmental Panel on Climate Change (IPCC). Capacities of climate models/ensembles to represent climatic characteristics vary spatially and temporally.

5.1.2 Approach on GCMs selection

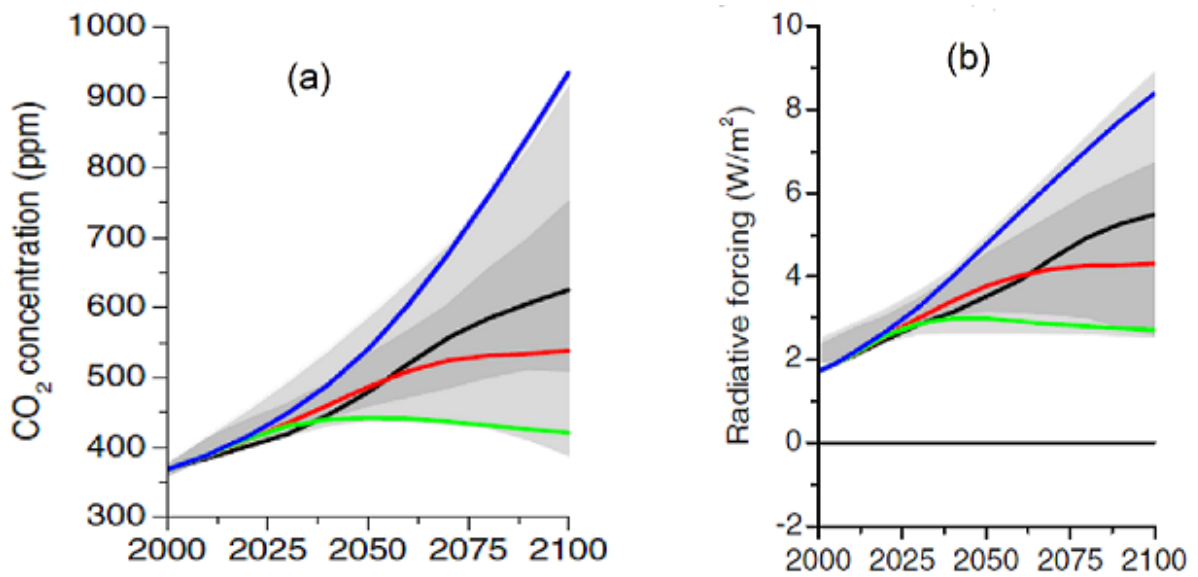
In most cases, a single GCM is not adopted to represent climatic characteristics at various corners of climatic extremes. For a chosen time and space, a specific climatic model/ensemble may demonstrate better abilities to represent climatic characteristics for a particular corner of a climatic extreme. The climatic extreme corners are cold and dry, cold and wet, warm and dry, and warm and wet. Hence, the selection of global climate models for a specific geographical location, with high capacities to represent the past and likely future climate, is a crucial step in assessing climate change impacts. A GCM selection from the large set of available climate models for the area of interest is a challenging task.

Lutz et al. (2016) have recently developed an advanced envelope-based selection approach for the selection of a representative global model, by combining the past-performance approach and envelop approach. It focuses on simulating a workable number of climate model runs representing the most likely futures with upcoming mean air temperature and annual precipitation, along with future changes in climatic extremes. This approach, which includes a three-step methodology, is used in this research to select a representative climate model for the Koshi River basin.

5.1.3 Methodology

Selection of Representative Concentration Pathways (RCPs)

IPCC (2014) has documented four RCPs to predict possible global future climate scenarios in the *Fifth Assessment Report*. The RCPs are based on the level of greenhouse gas concentration (CO₂, CH₄, N₂O etc), and represent the range of radiative forcing values by the year 2100. The RCPs and their corresponding radiative forcing, along with a CO₂-equivalent concentration in 2100 (IPCC, 2014), are represented in Figure 5.2 (adapted from Van Vuuren et al., 2011a), and summarised below:



Green RCP2.6, Red RCP4.5, Black RCP6.0, Blue RCP8.5 (adapted from Van Vuuren et al. 2011a)

Figure 5.2: RCPs with (a) CO₂ concentration and (b) corresponding radiative forcing.

- RCP2.6 (Green): Peak in radiative forcing at ~3 W/m² (430-480 ppm CO₂-eq) and then decline to 2.6 W/m² by 2100.
- RCP4.5 (Red): Stabilization without overshoot to 4.5 W/m² (580-720 ppm CO₂-eq) and then stabilized after 2100.
- RCP6.0 (Black): Stabilization without overshoot to 6.0 W/m² (720-1000 ppm CO₂-eq) and then stabilized after 2100.
- RCP8.5 (Blue): Rising radiative forcing to 8.5 W/m² (>1000 ppm CO₂-eq) by 2100.

The RCP2.6 represents the low end of the climate scenario in terms of emission and radiative forcing (Van Vuuren et al., 2011b). This pathway has been shown to be technically feasible, but requires the immediate and wide participation of all the countries in the world in deploying a large portfolio of mitigation options (Van Vuuren et al., 2010). As a major decline of greenhouse gas emission in the short run seems unrealistic (Lutz et al., 2016), it is unlikely that the RCP2.6 scenario can be accepted and is not considered further in this research. Among the remaining RCPs, one stabilization scenario, RCP4.5, and one high emission scenario, RCP8.5, are analyzed in

this research. Within these stabilization scenarios (RCP4.5 and RCP6.0), RCP4.5 is chosen as it represents the lower end of the stabilization scenarios. RCP4.5 and RCP8.5 should cover the entire range of stabilization and high emission scenarios, and hence were selected for this research.

Selection of study periods

A total of 197 parties (196 states and 1 regional economic integration organization) have agreed to the United Nations Framework Convention on Climate Change (UNFCCC, 2018). The Government of Nepal (GoN) is also one of the signatories to the United Nations Framework Convention on Climate Change. At the sixteenth session of the Conference of the Parties to the United Nations Framework Convention on Climate Change, held in 2010, the parties decided to formulate and implement a National Adaptation Plan (UNFCCC, 2011). In this regard, the Government of Nepal has initiated a National Adaptation Plan formulation process, with a launching workshop in 2015 (GoN-Climate Change Management Division, 2015). The National Adaptation Plan has envisioned the 2030s (2016-2045) and 2050s (2036-2065) for the adaptation measures (GoN-National Adaptation Plan Formulation Process, 2017). In addition, to the 2016-2045 (short-term) and the 2036-2065 (mid-century) scenarios considered in the National Adaptation Plan, GCMs were also selected to facilitate an assessment of climate changes impacts in the 2071-2100 (end-of-century) period.

GCMs selection approach

An advanced envelope-based selection approach developed by Lutz et al. (2016) was applied to select the representative climate models for climate change scenarios RCP4.5 and RCP8.5 for the short-term (2016-2045), mid-century (2036-2065), and end-of-century (2071-2100) periods. This approach included three main steps as shown in Figure 5.3.

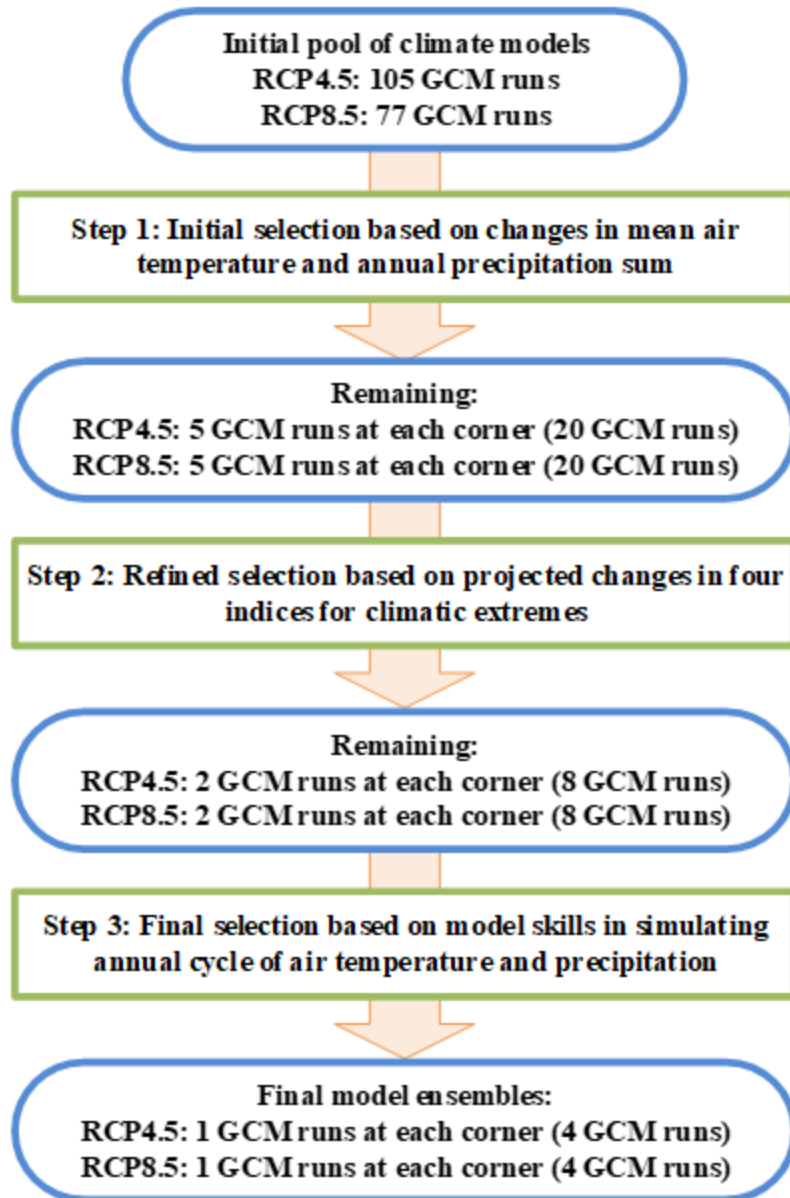


Figure 5.3: Steps of GCM selection (based on Lutz et al., 2016).

5.1.4 Application of Methodology

An advanced envelope-based selection approach developed by Lutz et al. (2016) is applied to select the representative climate models for the Koshi River basin, considering climate change scenarios RCP4.5 and RCP8.5 for the short-term (2016-2045), mid-century (2036-2065), and end-of-century (2071-2100) periods.

Step 1: Initial model selection based on changes in mean air temperature and annual precipitation

Firstly, area-averaged monthly mean air temperature and monthly total precipitation time series data for the climate change scenarios RCP4.5 and RCP8.5 model runs were downloaded from the Royal Netherlands Meteorological Institute (KNMI) Climate Explorer (<https://climexp.knmi.nl/start.cgi>) in July 2018. The KNMI datasets are available at a resolution of $2.5^{\circ} \times 2.5^{\circ}$. The Koshi River basin, down to Chatara in Nepal, lies within the extent of $26^{\circ}50'$ to $29^{\circ}8'$ N and $85^{\circ}23'$ to $88^{\circ}57'$ E (Agarwal et al., 2014, Bhattarai, 2013). So the boundary between 24° to 31° N and 84° to 91° E was selected in the KNMI dataset to cover the entire catchment of the study area. For climate change scenario RCP4.5, 105 GCMs and 108 GCMs were available for precipitation and temperature respectively. Likewise, 78 GCMs and 81 GCMs were available for climate change scenario RCP8.5, for precipitation and temperature respectively. The models/ensembles having both precipitation and temperature data were considered for the initial selection. Hence, 105 GCMs and 78 GCMs were taken for climate change scenarios RCP4.5 and RCP8.5 respectively. R programming (RStudio Team, 2016) was used to download and analyze the data.

Secondly, the mean air temperature and annual total precipitation for each year for the reference period (1981-2010) and future periods (short-term, mid-century and end-of-century) were calculated. The range of predicted changes in annual mean air temperature and annual total precipitation for the reference and future periods was calculated for the study area. The delta changes for temperature ($^{\circ}\text{C}$), ΔT , and precipitation (%), ΔP , in these three study periods were calculated. Based on the ΔT and ΔP values for all available GCMs/ensembles, the percentile rank of each GCM/ensemble for ΔT and ΔP was calculated separately.

To demonstrate the delta values and percentile values, the first ten GCMs/ensembles with their delta (ΔT and ΔP) values and corresponding percentile ranking for ΔT and ΔP for climate change scenario RCP4.5 are shown in Table 5.1. The ΔT values represent the difference in mean temperature ($^{\circ}\text{C}$) between the future periods (short-term, mid-century and end-of-century periods) and the reference period (1981-2010) for the respective future periods. The ΔP values represent the difference in annual precipitation

(%) between the future periods (short-term, mid-century and end-of-century periods) and the reference period (1981-2010) for the respective future periods. The first ten models are considered to demonstrate the calculation process. The same procedure was followed for all the ensemble members. Although only 10 GCMs/ensembles are shown in Table 5.1, this calculation was done for 105 GCMs and 78 GCMs for climate change scenarios RCP4.5 and RCP8.5 respectively. Table 5.1 shows the change in temperature and precipitation (ΔT and ΔP) between 2016-2045 and 1981-2010. For example, the model ACCESS1-0_r1i1p1 predicts that the temperature will increase by 1.1°C, 1.71°C and 2.65°C in short-term, mid-century and end-of-century periods respectively, as compared to the reference period (Table 5.1). Likewise, the model ACCESS1-0_r1i1p1 predicts that the precipitation will increase by 0.24%, 3.31% and 11.63% in short-term, mid-century and end-of-century periods respectively, as compared to the reference period (Table 5.1). The percentile rank values of ΔT and ΔP are used to calculate the proximity of the model run's percentile rank scores to each corner (Equation 1). The delta (ΔT and ΔP) values for the first ten GCMs/ensembles, the difference between the future (short-term, mid-century and end-of-century) periods and the reference period (1981-2010), and corresponding percentile ranking for ΔT and ΔP for RCP8.5 are shown in Table 5.2.

Table 5.1: Delta (ΔT and ΔP) values and percentile rank for short-term future period (2016-2045), mid-century future period (2036-2065) and end-of-century future period (2071-2100), of the first ten GCMs/ensembles for climate change scenario RCP4.5.

General circulation models (GCMs)	RCP4.5											
	Short-term future period (2016-2045)				Mid-century future period (2036-2065)				End-of-century future period (2071-2100)			
	ΔP (%)	ΔT (°C)	Percentile rank ΔP	Percentile rank ΔT	ΔP (%)	ΔT (°C)	Percentile rank ΔP	Percentile rank ΔT	ΔP (%)	ΔT (°C)	Percentile rank ΔP	Percentile rank ΔT
ACCESS1-0_r1i1p1	0.24	1.1	0.24	0.471	3.31	1.71	0.317	0.48	11.63	2.65	0.528	0.615
ACCESS1-3_r1i1p1	2.46	0.94	0.384	0.24	8.67	1.48	0.615	0.259	16.22	2.53	0.711	0.567
bcc-csm1-1_r1i1p1	5.17	1.04	0.673	0.384	12.74	1.47	0.74	0.221	9.81	2.05	0.48	0.403
bcc-csm1-1-m_r1i1p1	-3.35	1.22	0.067	0.673	2.06	1.73	0.24	0.5	0.19	2.04	0.125	0.384
BNU-ESM_r1i1p1	6.02	1.17	0.701	0.605	8.27	1.74	0.596	0.528	14.39	2.32	0.682	0.471
CanESM2_r1i1p1	8.12	1.23	0.788	0.682	12.33	2.18	0.711	0.846	28.49	2.63	0.971	0.605
CanESM2_r2i1p1	15.61	1.74	0.98	0.99	17.23	2.05	0.923	0.75	16.24	2.91	0.721	0.701
CanESM2_r3i1p1	4.48	1.55	0.634	0.961	14.59	2.36	0.865	0.961	30.41	3.09	0.99	0.836
CanESM2_r4i1p1	-0.05	1.52	0.23	0.942	2.24	2.03	0.25	0.711	15.8	2.79	0.701	0.663
CanESM2_r5i1p1	11.4	1.32	0.923	0.769	13.91	2.04	0.836	0.721	26.3	2.74	0.961	0.625

Table 5.2: Delta (ΔT and ΔP) values and percentile rank, for short-term future period (2016-2045), mid-century future period (2036-2065) and end-of-century future period (2071-2100), of the first ten GCMs/ensembles for climate change scenario RCP8.5.

General circulation models (GCMs)	RCP8.5											
	Short-term future period (2016-2045)				Mid-century future period (2036-2065)				End-of-century future period (2071-2100)			
	ΔP (%)	ΔT (°C)	Percentile rank ΔP	Percentile rank ΔT	ΔP (%)	ΔT (°C)	Percentile rank ΔP	Percentile rank ΔT	ΔP (%)	ΔT (°C)	Percentile rank ΔP	Percentile rank ΔT
ACCESS1-0_r1i1p1	2.69	1.1	0.421	0.302	4.9	2.31	0.368	0.46	12.75	4.3	0.368	0.407
ACCESS1-3_r1i1p1	2.17	1.02	0.381	0.157	3.74	2.02	0.315	0.315	21.63	3.98	0.697	0.328
bcc-csm1-1_r1i1p1	4.85	1.19	0.644	0.381	17.54	1.92	0.947	0.131	28.93	3.96	0.842	0.302
BNU-ESM_r1i1p1	3.26	1.4	0.486	0.697	7.09	2.33	0.552	0.486	10.07	4.43	0.171	0.421
CanESM2_r1i1p1	8.95	1.75	0.907	0.894	21.55	2.96	0.986	0.842	43.95	5.42	0.96	0.776
CanESM2_r2i1p1	6.16	1.62	0.802	0.828	17.16	2.91	0.934	0.815	53.32	5.52	0.973	0.815
CanESM2_r3i1p1	21.29	1.92	1	0.973	18.5	3.15	0.973	0.907	62.99	5.82	1	0.881
CanESM2_r4i1p1	7.25	2.06	0.855	0.986	8.57	3.22	0.657	0.934	40.39	5.57	0.934	0.828
CanESM2_r5i1p1	4.85	1.77	0.644	0.907	17.94	2.99	0.96	0.855	53.79	5.68	0.986	0.868
CCSM4_r1i1p1	5.14	1.25	0.684	0.486	5.4	2.38	0.421	0.513	15.54	4.06	0.5	0.368

Based on the ΔT values for all the models/ensembles, the 10th and 90th percentile values of ΔT were determined for climate change scenarios RCP4.5 and RCP8.5 as per standard practice (Lutz et al., 2016). The 10th and 90th percentile values of ΔT represent the cold and warm sides of the temperature extreme. Similarly, based on the ΔP values for all the models/ensembles, the 10th and 90th percentile values for ΔP were determined for RCP4.5 and RCP8.5. The 10th and 90th percentile values of ΔP represent the dry and wet sides of the precipitation extreme.

The 10th and 90th percentile values of ΔT and ΔP , considering short-term future period (2016-2045), mid-century future period (2036-2065) and end-of-century future period (2071-2100), from the pool of GCM/ensemble for the climate change scenarios RCP4.5 and RCP8.5 is shown in Table 5.3.

Table 5.3: 10th and 90th percentile values of ΔT and ΔP for short-term (2016-2045), mid-century (2036-2065) and end-of-century (2071-2100) periods, from the pool of GCM/ensemble for climate change scenarios RCP4.5 and RCP8.5.

Climate change scenario	Short-term future period (2016-2045)				Mid-century future period (2036-2065)				End-of-century future period (2071-2100)			
	ΔP (%)		ΔT (°C)		ΔP (%)		ΔT (°C)		ΔP (%)		ΔT (°C)	
	10 th percentile	90 th percentile	10 th percentile	90 th percentile	10 th percentile	90 th percentile	10 th percentile	90 th percentile	10 th percentile	90 th percentile	10 th percentile	90 th percentile
RCP4.5	-3.038	11.242	0.86	1.42	-3.45	16.214	1.34	2.262	-3.012	22.566	1.702	3.18
RCP8.5	-3.046	9.068	0.966	1.776	-1.412	16.798	1.878	3.152	-3.878	37.984	3.628	5.91

The four corners (in Figure 5.4), cold and dry, warm and dry, cold and wet, and warm and wet, represent the four extreme climates, which are 10th and/or 90th percentile values of ΔT and ΔP . For example, the cold and dry corner represents the 10th percentile of ΔT and 10th percentile of ΔP . Likewise; warm and dry represent the 90th percentile of ΔT and 10th percentile of ΔP . Similarly, cold and wet represent the 10th percentile of ΔT and 90th percentile of ΔP . The warm and wet corner represent the 90th percentile of ΔT and 90th percentile of ΔP . The ΔT and ΔP values, considering short-term future period (2016-2045), at four corners for climate change scenarios RCP4.5 and RCP8.5 are shown in Table 5.4.

Table 5.4: ΔT and ΔP values, based on short-term (2016-2045), mid-century (2036-2065) and end-of-century (2071-2100) periods at four corners for climate change scenarios RCP4.5 and RCP8.5.

Four corners (Four extreme climates)	Short-term future period (2016-2045)				Mid-century future period (2036-2065)				End-of-century future period (2071-2100)			
	RCP4.5		RCP8.5		RCP4.5		RCP8.5		RCP4.5		RCP8.5	
	ΔP (%)	ΔT (°C)	ΔP (%)	ΔT (°C)	ΔP (%)	ΔT (°C)	ΔP (%)	ΔT (°C)	ΔP (%)	ΔT (°C)	ΔP (%)	ΔT (°C)
Cold and dry corner	-3.04	0.86	-3.05	0.966	-3.45	1.34	-1.41	1.878	-3.01	1.702	-3.88	3.628
Warm and dry corner	-3.04	1.42	-3.05	1.776	-3.45	2.262	-1.41	3.152	-3.01	3.18	-3.88	5.91
Cold and wet corner	11.24	0.86	9.068	0.966	16.21	1.34	16.8	1.878	22.57	1.702	37.98	3.628
Warm and wet corner	11.24	1.42	9.068	1.776	16.21	2.262	16.8	3.152	22.57	3.18	37.98	5.91

The proximity of the model run's percentile rank scores to each corner with respect to their projections for ΔT and ΔP for the entire ensemble was calculated using Equation 5.1 as:

$$D_{p_j^P, p_j^T} = \sqrt{(P_i^P - P_j^P)^2 + (P_i^T - P_j^T)^2} \quad \text{Equation 5.1}$$

where $D_{p_j^P, p_j^T}$ is the distance of a model j's ΔP and ΔT (P_j^P and P_j^T respectively) to the corner under consideration, which are 10th and/or 90th percentile score of ΔP and ΔT for the entire ensemble (P_i^P and P_i^T respectively). P_i^P and P_i^T values are 10th and/or 90th percentile values of ΔP and ΔT for the entire ensemble for the particular corner. P_j^P and P_j^T are the percentile rank values of model j for ΔP and ΔT respectively.

The distance of the first ten GCMs/ensembles from the four corners, considering the short-term future period (2016-2045), is shown in Table 5.5. Following the same process, the proximity of first 10 models to each corner was calculated for climate change scenario RCP8.5 for the short term (2016-2035) and is shown in Appendix 1. Likewise, the distance of each of the GCMs/ensembles to the four corners, considering the mid-century period (2036-2065) for climate change scenarios RCP4.5 and RCP8.5, are presented in Appendix 2 and 3 respectively. The distance of each of the GCMs/ensembles to the four corners, considering the end-of-century period (2071-2100) for climate change scenarios RCP4.5 and RCP8.5, are presented in Appendix 4 and 5 respectively.

Table 5.5: Distance of the first ten GCMs/ensembles from the four corners, based on the short-term future period (2016-2045), for climate change scenario RCP4.5.

Model	Distance from Corner			
	Cold and Dry	Warm and Dry	Cold and Wet	Warm and Wet
ACCESS1-0_r1i1p1	0.3965	0.4513	0.7571	0.7872
ACCESS1-3_r1i1p1	0.3166	0.7185	0.5347	0.8378
bcc-csm1-1_r1i1p1	0.6395	0.7711	0.3636	0.5637
bcc-csm1-1-m_r1i1p1	0.5739	0.2294	1.011	0.8634
BNU-ESM_r1i1p1	0.785	0.6695	0.5428	0.3558
CanESM2_r1i1p1	0.9011	0.7217	0.5927	0.2451
CanESM2_r2i1p1	1.2516	0.8846	0.8936	0.1204
CanESM2_r3i1p1	1.0132	0.5375	0.9012	0.2729
CanESM2_r4i1p1	0.852	0.1366	1.076	0.6713
CanESM2_r5i1p1	1.0606	0.8334	0.6694	0.133

The location of the four corners and the proximity of the models/ensembles to each corner for climate change scenarios RCP4.5 and RCP8.5, considering changes in the short-term future period (2016-2045) and the reference period (1981-2010), are shown in Figure 5.4 and Figure 5.5 respectively.

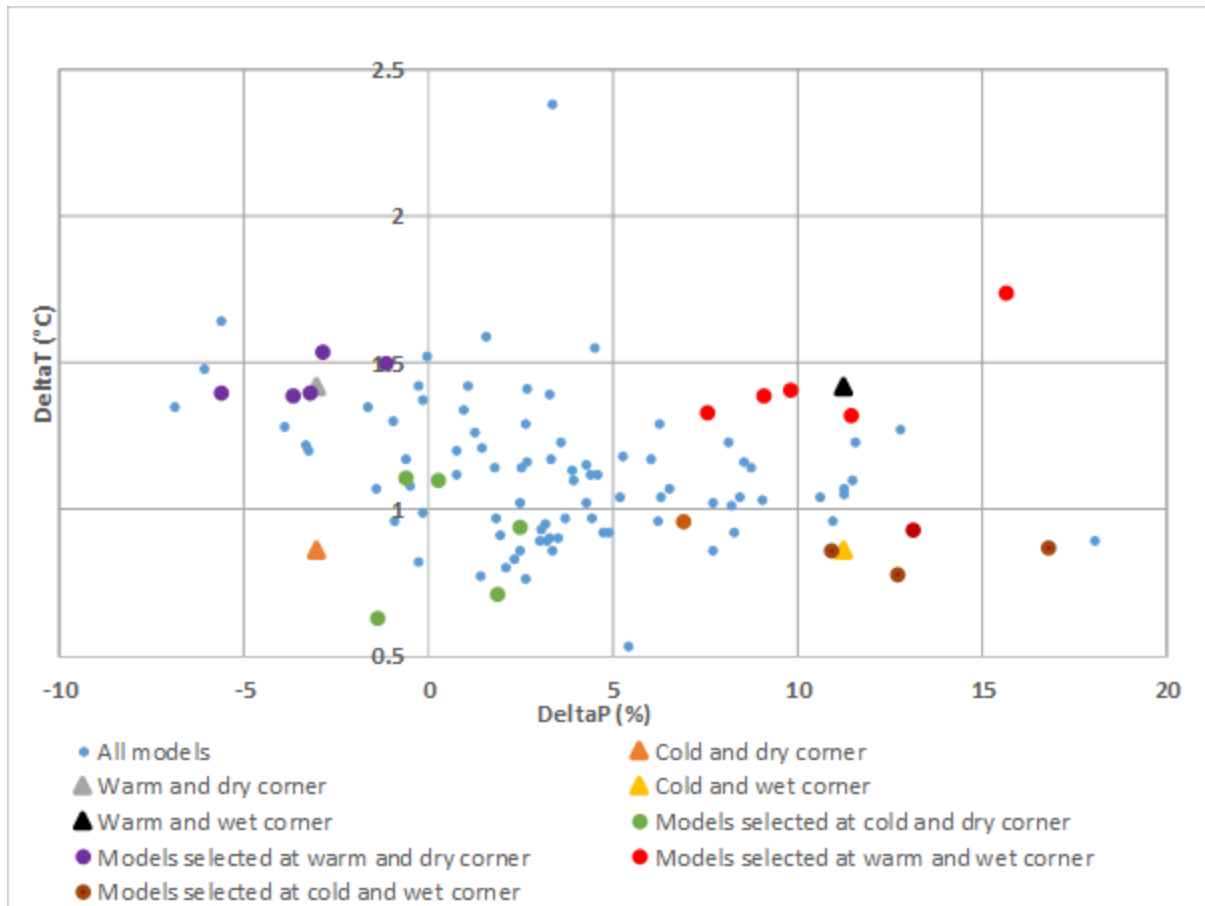


Figure 5.4: Initial model selection based on changes in mean air temperature and annual precipitation, considering changes in the short-term future period (2016-2045) and the reference period (1981-2010), for climate change scenario RCP4.5.

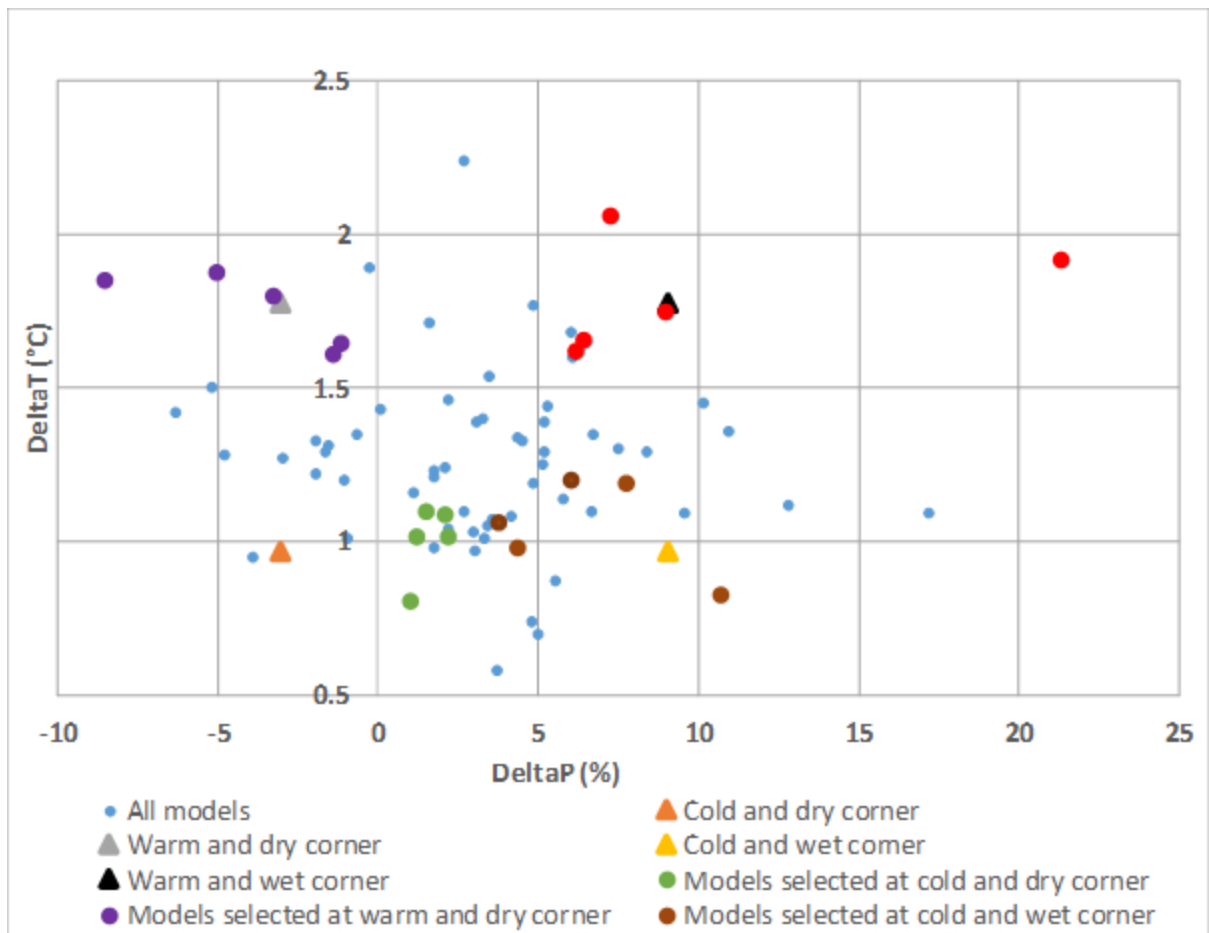


Figure 5.5: Initial model selection based on changes in mean air temperature and annual precipitation, considering changes in the short-term future period (2016-2045) and the reference period (1981-2010), for climate change scenario RCP8.5.

Applying a similar approach as discussed for short-term future period (2016-2045), the four corners and the proximity of models/ensembles to each corner for climate change scenarios RCP4.5 and RCP 8.5, considering changes in the mid-century future period (2036-2065) and the reference period (1981-2010), are shown in Figure 5.6 and Figure 5.7 respectively.

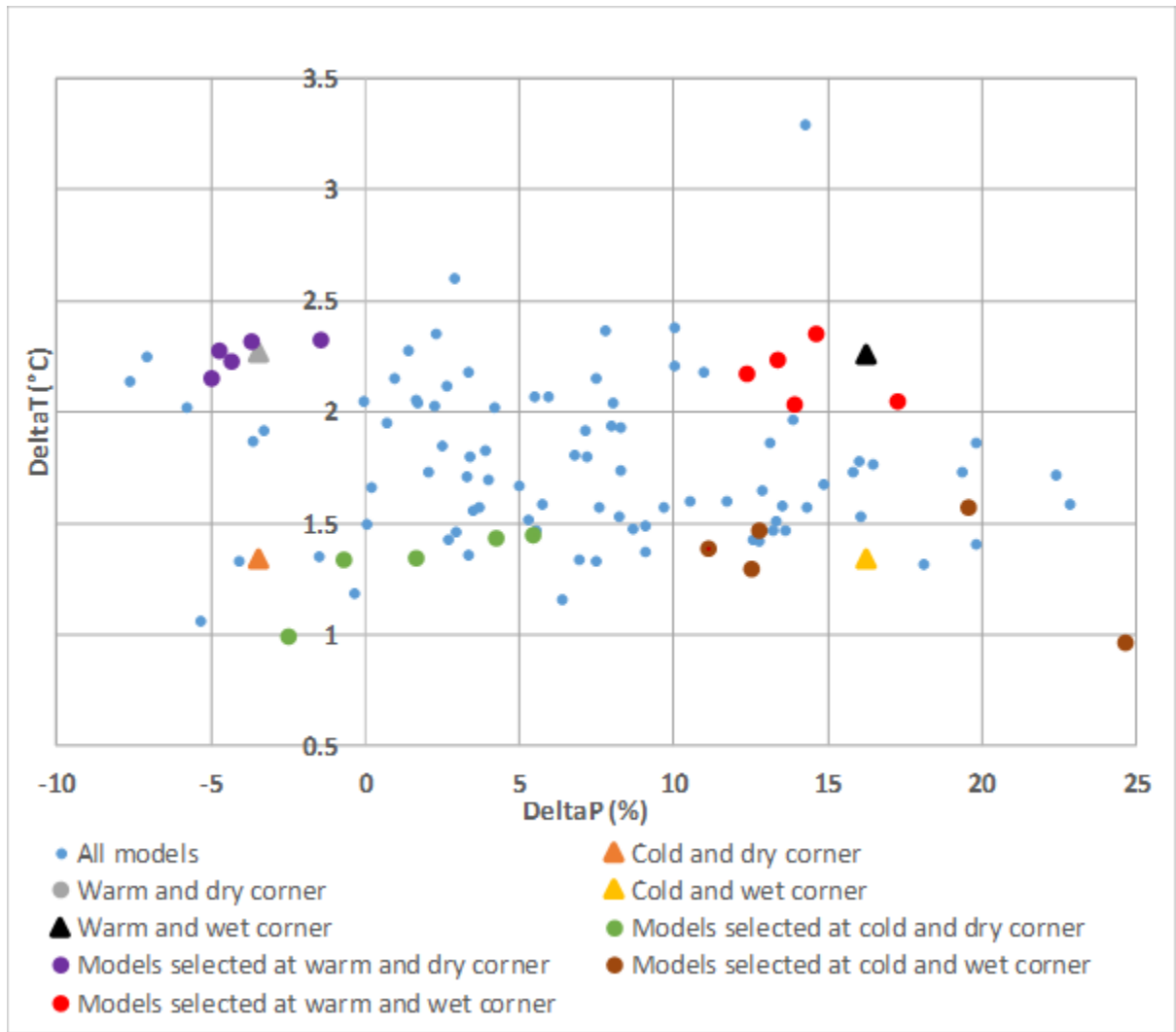


Figure 5.6: Initial model selection based on changes in mean air temperature and annual precipitation, considering changes in the mid-century future period (2036-2065) and the reference period (1981-2010), for climate change scenario RCP4.5.

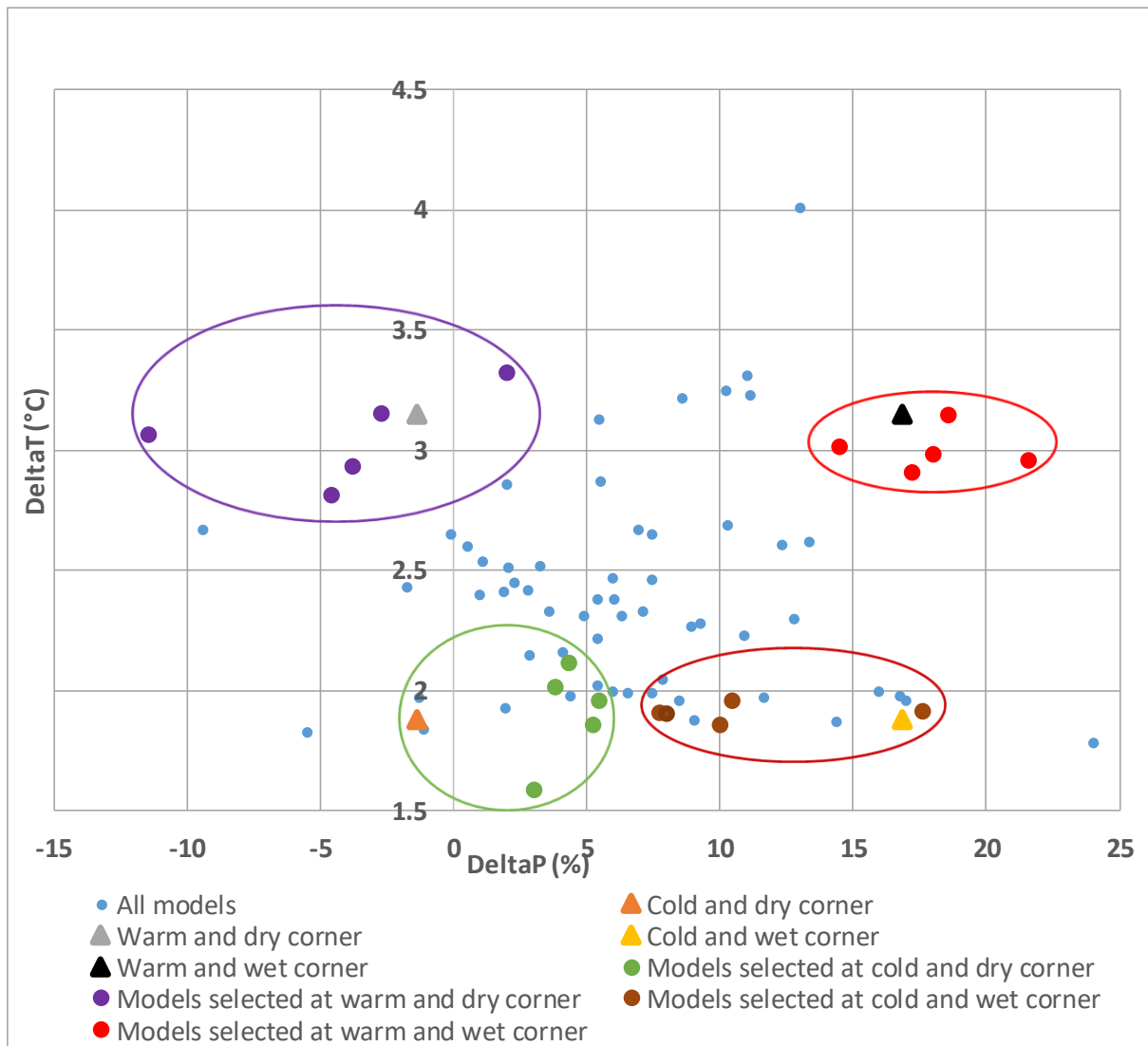


Figure 5.7: Initial model selection based on changes in mean air temperature and annual precipitation, considering changes in the mid-century future period (2036-2065) and the reference period (1981-2010), for climate change scenario RCP8.5.

Similarly, the four corners and the proximity of models/ensembles to each corner for climate change scenarios RCP4.5 and RCP 8.5, considering changes in the end-of-century future period (2071-2100) and the reference period (1981-2010), are shown in Figure 5.8 and Figure 5.9 respectively.

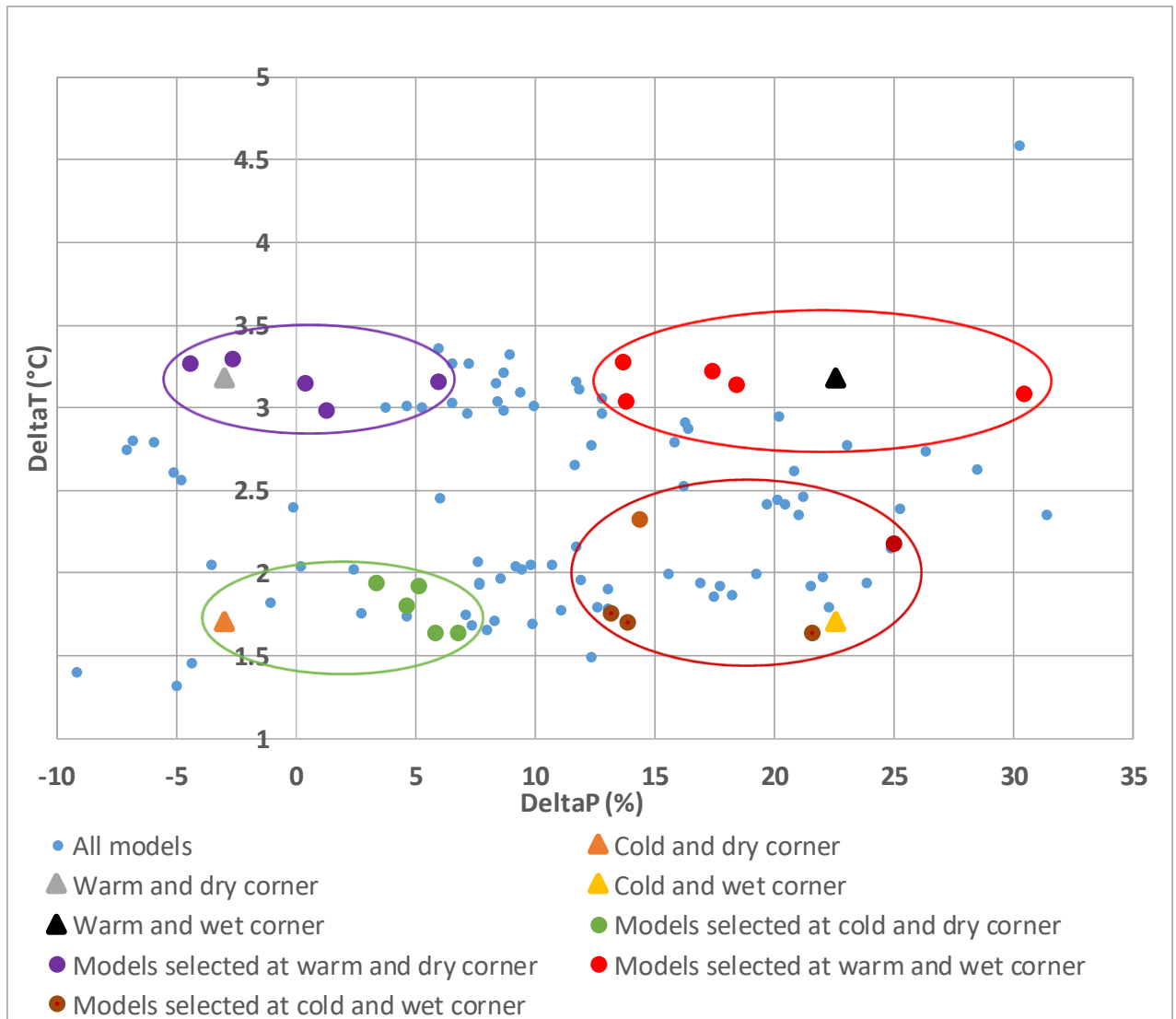


Figure 5.8: Initial model selection based on changes in mean air temperature and annual precipitation, considering changes in the end-of-century future period (2071-2100) and the reference period (1981-2010), for climate change scenario RCP4.5.

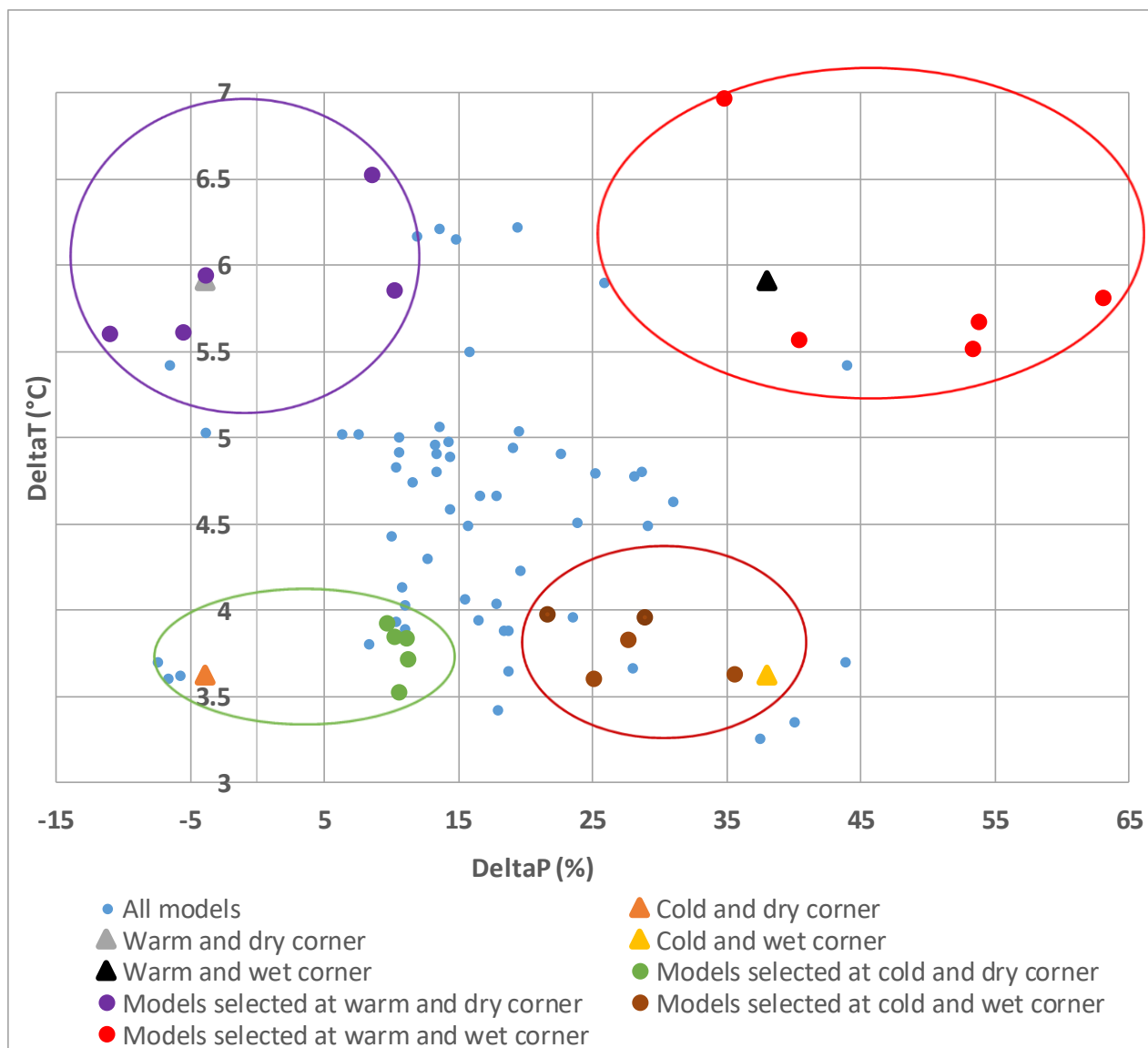


Figure 5.9: Initial model selection based on changes in mean air temperature and annual precipitation, considering changes in the end-of-century future period (2071-2100) and the reference period (1981-2010), for climate change scenario RCP8.5.

The GCMs/ensembles were then ranked based on their proximity to each corner. Data availability at a temporal resolution of daily time step for each model was then checked, as daily data is required for an empirical-statistical downscaling. In this study, daily data availability for parameters of interest (temperature and precipitation) for each model was checked from <https://climate4impact.eu/impactportal/general/about.jsp>. Based on the ranking of the models considering the proximity to the respective corner and daily data availability, five models at each corner were selected for the next step (Step 2). Models selected from Step 1 are highlighted in Figures 5.4 to 5.9.

Figures 5.4 to 5.9 show that although some models are closer to their respective corners, they were not selected due to the absence of daily data. Table 5.6 shows the list of models selected for the next step (Figure 5.3 – Step 2), considering the short term period (2016-2045) for climate change scenarios RCP4.5 and RCP8.5. The circle/oval at each corner encloses the models selected at their respective corners. The size of the circle/oval shows the daily data availability status of the GCMs/ensembles that are closer to the respective corner. If the daily data available for the GCMs/ensembles are closer to their respective corner, the size of the circle/oval is small (warm and dry corner in Figure 5.6). The size of circle/oval increases if the daily data are not available for the GCMs/ensembles that are closer to the corner (cold and wet corner in Figure 5.8). Likewise, Table 5.7 and Table 5.8 show the list of models selected for the next step (Figure 5.3 – Step 2), for climate change scenarios RCP4.5 and RCP8.5, considering the mid-century period (2036-2065) and the end-of-century period (2071-2100) respectively.

Table 5.6: Models selected for Step 2 based on changes in mean air temperature and annual precipitation considering short-term future period (2016-2045) and the reference period (1981-2010) for climate change scenarios RCP4.5 and RCP8.5.

Climate scenario	Rank	Cold and dry	Warm and Dry	Cold and Wet	Warm and Wet
RCP4.5	1	inmcm4_r1ilp1	CMCC-CMS_r1ilp1	NOAA_GFDL_GFDL-ESM2G_r1ilp1	IPSL-CM5A-MR_r1ilp1
	2	EC-EARTH_r8ilp1	MPI-ESM-LR_r3ilp1	MRI-CGCM3_r1ilp1	CESM1-CAM5_r1ilp1
	3	ACCESS1-3_r1ilp1	MIROC5_r2ilp1	GISS-E2-R_r6ilp3	CanESM2_r2ilp1
	4	ACCESS1-0_r1ilp1	MIROC-ESM_r1ilp1	CCSM4_r2ilp1	CanESM2_r5ilp1
	5	CMCC-CM_r1ilp1	MPI-ESM-MR_r3ilp1	EC-EARTH_r2ilp1	IPSL-CM5A-LR_r3ilp1
RCP8.5	1	inmcm4_r1ilp1	CMCC-CMS_r1ilp1	MRI-CGCM3_r1ilp1	CanESM2_r1ilp1
	2	CSIRO-Mk3-6-0_r8ilp1	MPI-ESM-LR_r3ilp1	NOAA_GFDL_GFDL-ESM2M_r1ilp1	IPSL-CM5A-LR_r4ilp1
	3	CSIRO-Mk3-6-0_r3ilp1	IPSL-CM5A-LR_r2ilp1	IPSL-CM5B-LR_r1ilp1	CanESM2_r4ilp1
	4	ACCESS1-3_r1ilp1	MPI-ESM-LR_r1ilp1	CMCC-CM_r1ilp1	CanESM2_r2ilp1
	5	NOAA_GFDL_GFDL-ESM2G_r1ilp1	MPI-ESM-LR_r2ilp1	EC-EARTH_r8ilp1	CanESM2_r3ilp1

Table 5.7: Models selected for Step 2 based on changes in mean air temperature and annual precipitation considering the mid-century future period (2036-2065) and reference period (1981-2010) for climate change scenarios RCP4.5 and RCP8.5.

Climate scenario	Rank	Cold and dry	Warm and Dry	Cold and Wet	Warm and Wet
RCP4.5	1	EC-EARTH_r8i1p1	CMCC-CMS_r1i1p1	IPSL-CM5B-LR_r1i1p1	CanESM2_r3i1p1
	2	inmcm4_r1i1p1	MIROC-ESM-CHEM_r1i1p1	MRI-CGCM3_r1i1p1	IPSL-CM5A-MR_r1i1p1
	3	NOAA_GFDL_GFDL-ESM2M_r1i1p1	MIROC5_r2i1p1	bcc-csm1-1_r1i1p1	CanESM2_r2i1p1
	4	EC-EARTH_r12i1p1	MPI-ESM-LR_r2i1p1	CCSM4_r2i1p1	CanESM2_r5i1p1
	5	EC-EARTH_r2i1p1	CSIRO-Mk3-6-0_r6i1p1	GISS-E2-R_r6i1p3	CanESM2_r1i1p1
RCP8.5	1	inmcm4_r1i1p1	CMCC-CMS_r1i1p1	bcc-csm1-1_r1i1p1	IPSL-CM5A-MR_r1i1p1
	2	EC-EARTH_r9i1p1	MPI-ESM-LR_r3i1p1	CESM1-BGC_r1i1p1	CanESM2_r3i1p1
	3	ACCESS1-3_r1i1p1	MPI-ESM-LR_r2i1p1	NOAA_GFDL_GFDL-ESM2M_r1i1p1	CanESM2_r5i1p1
	4	EC-EARTH_r2i1p1	MIROC-ESM-CHEM_r1i1p1	EC-EARTH_r8i1p1	CanESM2_r2i1p1
	5	CCSM4_r6i1p1	MPI-ESM-LR_r1i1p1	NOAA_GFDL_GFDL-ESM2G_r1i1p1	CanESM2_r1i1p1

Table 5.8: Models selected for Step 2 based on changes in mean air temperature and annual precipitation considering the end-of-century future period (2071-2100) and reference period (1981-2010) for climate change scenarios RCP4.5 and RCP8.5.

Climate scenario	Rank	Cold and dry	Warm and Dry	Cold and Wet	Warm and Wet
RCP4.5	1	GISS-E2-R_r6ilp1	CSIRO-Mk3-6-0_r1ilp1	IPSL-CM5B-LR_r1ilp1	CanESM2_r3ilp1
	2	inmcm4_r1ilp1	CSIRO-Mk3-6-0_r9ilp1	NOAA_GFDL_GFDL-ESM2M_r1ilp1	CNRM-CM5_r1ilp1
	3	EC-EARTH_r2ilp1	CMCC-CMS_r1ilp1	CCSM4_r2ilp1	IPSL-CM5A-MR_r1ilp1
	4	EC-EARTH_r12ilp1	CSIRO-Mk3-6-0_r6ilp1	GISS-E2-R_r6ilp3	IPSL-CM5A-LR_r1ilp1
	5	NOAA_GFDL_GFDL-ESM2G_r1ilp1	CSIRO-Mk3-6-0_r3ilp1	BNU-ESM_r1ilp1	HadGEM2-ES_r2ilp1
RCP8.5	1	EC-EARTH_r9ilp1	CMCC-CMS_r1ilp1	NOAA_GFDL_GFDL-ESM2G_r1ilp1	CanESM2_r4ilp1
	2	inmcm4_r1ilp1	MPI-ESM-LR_r3ilp1	IPSL-CM5B-LR_r1ilp1	CanESM2_r5ilp1
	3	EC-EARTH_r8ilp1	MIROC-ESM_r1ilp1	NOAA_GFDL_GFDL-ESM2M_r1ilp1	CanESM2_r3ilp1
	4	CCSM4_r6ilp1	MIROC-ESM-CHEM_r1ilp1	bcc-csml-1_r1ilp1	NOAA_GFDL_GFDL-CM3_r1ilp1
	5	EC-EARTH_r2ilp1	MPI-ESM-LR_r2ilp1	ACCESS1-3_r1ilp1	CanESM2_r2ilp1

Step 2: Refined model selection based on projected changes in four indices for climatic extremes

The five models at each corner for climate change scenarios RCP4.5 and RCP8.5 chosen from the initial selection were further refined in the selection process, based on projected changes in four indices for climatic extremes. Two climatic extremes from both air temperature and precipitation were assessed considering changes in indices based on the findings of the Expert Team on Climate Change Detection and Indices (ETCCDI) (Peterson, 2005). Warm Spell Duration Index (WSDI) and Cold Spell Duration Index (CSDI) were evaluated for climatic extremes in air temperature. Likewise, consecutive dry days and the precipitation due to very wet days (R95pTOT, as abbreviated in ETCCDI indices) were considered for climatic extremes in precipitation. Description of the four indices is given in Table 5.9.

Table 5.9: Description of ETCCDI indices used for refined model selection.

Meteorological variable	ETCCDI index	Index description
Air temperature	WSDI	Warm spell duration index: count of days in a span of at least 6 days when $TX_{ij} > TX_{in90}$ where TX_{ij} is the daily maximum temperature on day i in period j , and TX_{in90} is the 90th percentile of daily maximum temperature for the base period.
Air temperature	CSDI	Cold spell duration index: count of days in a span of at least 6 days when $TN_{ij} < TN_{in10}$ where TN_{ij} is the daily minimum temperature on day i in period j , and TN_{in10} is the 10th percentile of daily minimum temperature for the base period.
Precipitation	CDD	Consecutive dry days: maximum length of dry spell when $P_{ij} < 1$ mm where P_{ij} is daily precipitation amount on day i in period j .
Precipitation	R95pTOT	Precipitation due to very wet days: annual total precipitation when $P_{ij} > P_{in95}$ where P_{ij} is the daily precipitation amount on a wet day (precipitation ≥ 1 mm) i in period j , and P_{in95} is the 95th percentile of precipitation on wet days in the base period.

The results of the climate models/ensembles will be used to assess the impacts on hydrological aspects, especially water availability for irrigation purposes, and agricultural water management practices. In this regard, WSDI and CSDI are considered as they affect the snow and ice melt/ accumulation process, which is an important factor in the upstream part of the Himalayan river basin, where the Koshi River basin (the case study site) is situated. The study area is a part of the Himalayan region. These extreme temperature indices also affect the evapotranspiration and water requirements for the crops. The Consecutive Dry Days index (CDD) is vital for measuring both precipitation extremes and dry spells affecting crop growth. CDD and R95pTOT are important to assess hydrological aspects for irrigation and agricultural purposes in the study area. Precipitation due to very wet days, estimated using R95pTOT ($P_{ij} > P_{in95}$), is considered instead of precipitation due to extremely wet days, R99pTOT (annual total precipitation when $P_{ij} > P_{in99}$). Precipitation due to extremely wet days is important for flood-related studies. The results of climate models/ensembles in this research will be applied for irrigation and agricultural water management purposes and not for flood modeling activities. Therefore, R95pTOT is used in this research.

For the refined selection purpose, the changes in WSDI, CSDI, CDD and R95pTOT were calculated from the available database. These database were constructed by the Sillmann et al. (2013a) and Sillmann et al. (2013b), and available in Royal Netherlands Meteorological Institute (KNMI) Climate Explorer webpage (<https://climexp.knmi.nl/start.cgi>) in July 2018. This database does not include all the models/ensembles. For those models/ensembles which were chosen from the initial selection and not included in the database, the ETCCDI indices were calculated using the Climate Data Operator (CDO-version 1.6.4), developed by the Max-Planck Institute for Meteorology (<https://code.mpimet.mpg.de/projects/cdo/files>). The Climate Data Operator (CDO) is a collection of more than 600 command line operators for standard processing of climate data (Max-Planck Institute for Meteorology, 2018). The relevant CDO command line operators were used in R programming (RStudio Team, 2016) applying the same procedures as Sillmann et al. (2013a) and Sillmann et al. (2013b).

Initially, the indices were calculated from the daily model output for each individual year in the future periods and the reference period (1981-2010) for individual grid cell covering the study area. The indices were then averaged within the study area for each year. These indices were finally averaged over a period of 30 years for both future and reference periods. The percentage change was calculated with respect to the reference period (1981-2010). The

procedures to calculate precipitation indices, CDD and R95pTOT, are shown is shown in Figure 5.10 and Figure 5.11 respectively.

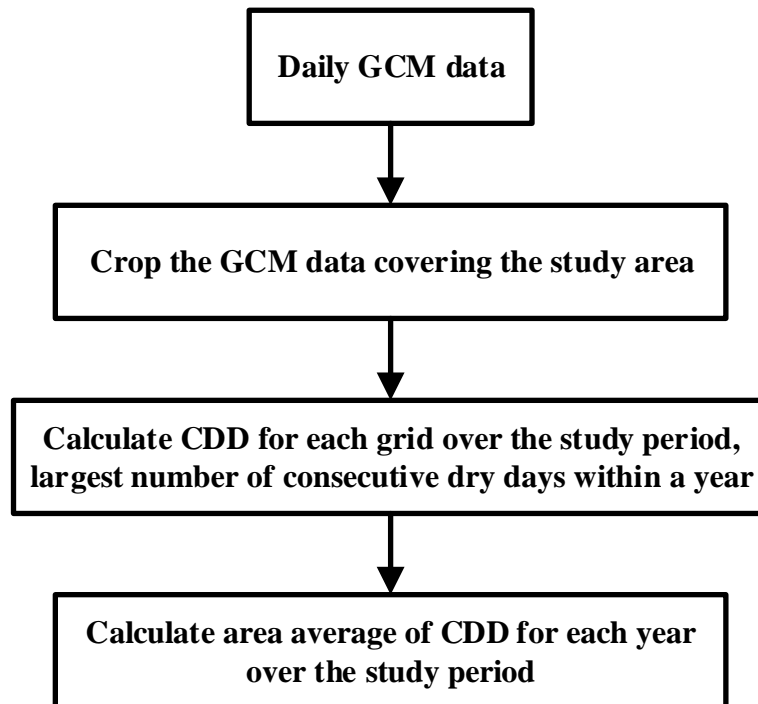


Figure 5.10: Flowchart to calculate CDD.

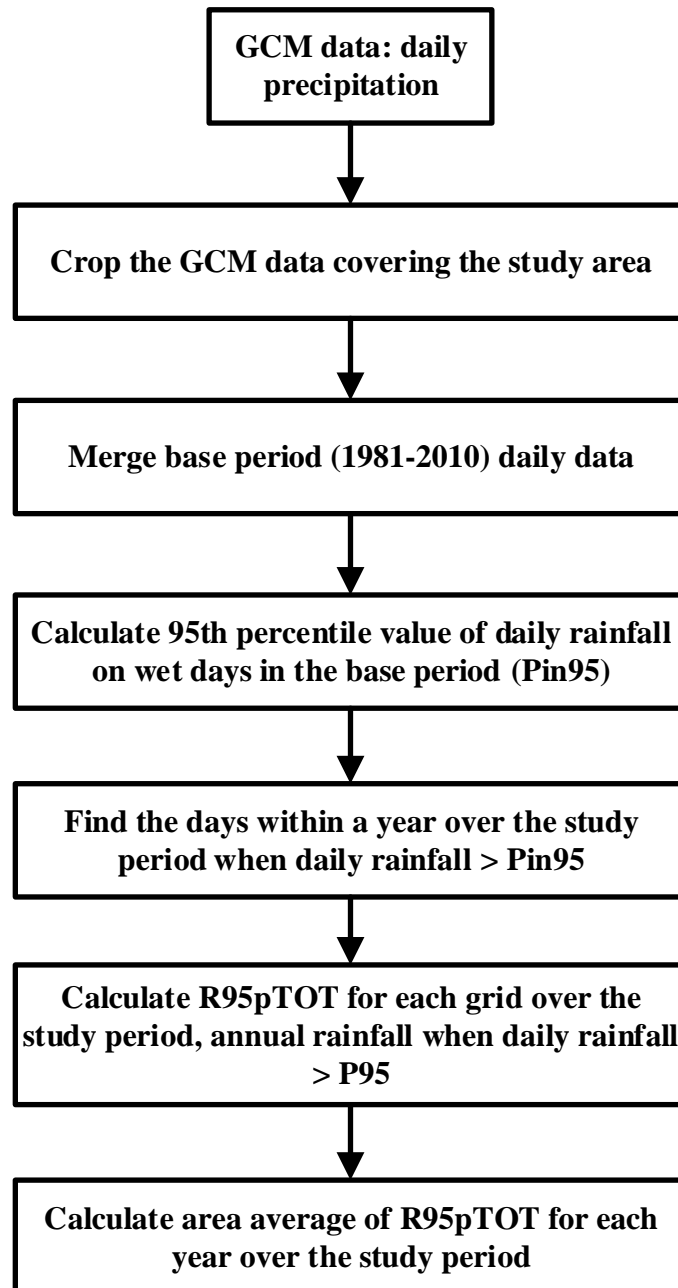


Figure 5.11: Flowchart to calculate R95pTOT.

The temperature indices, CSDI and WSDI, were calculated following the flowcharts shown in Figure 5.12 and Figure 5.13 respectively.

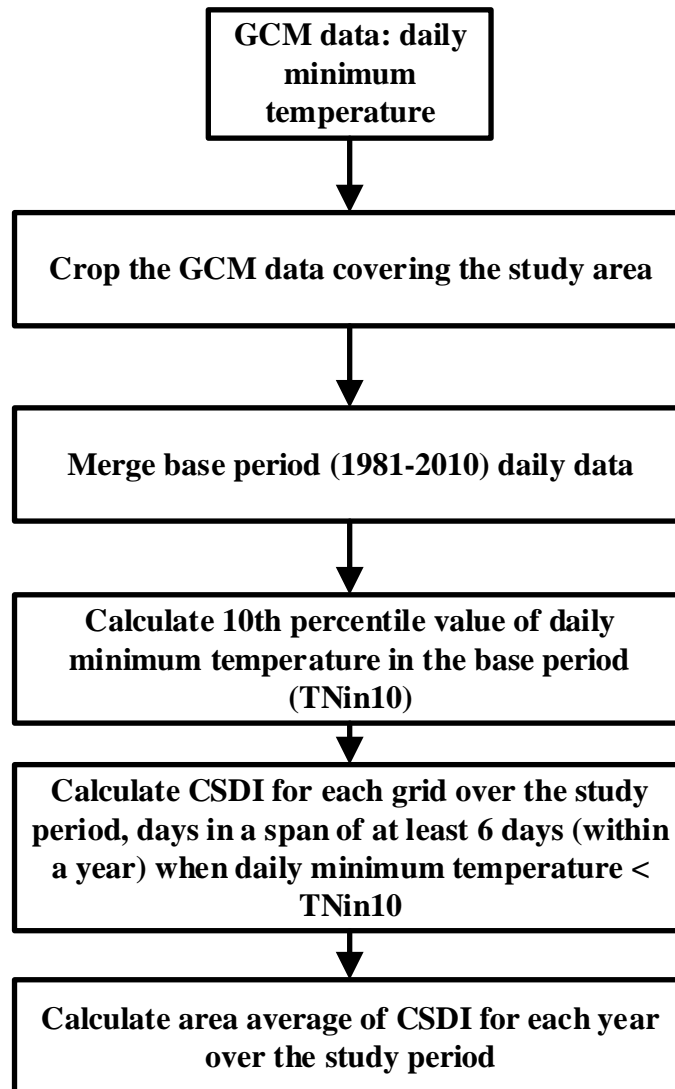


Figure 5.12: Flowchart to calculate CSDI.

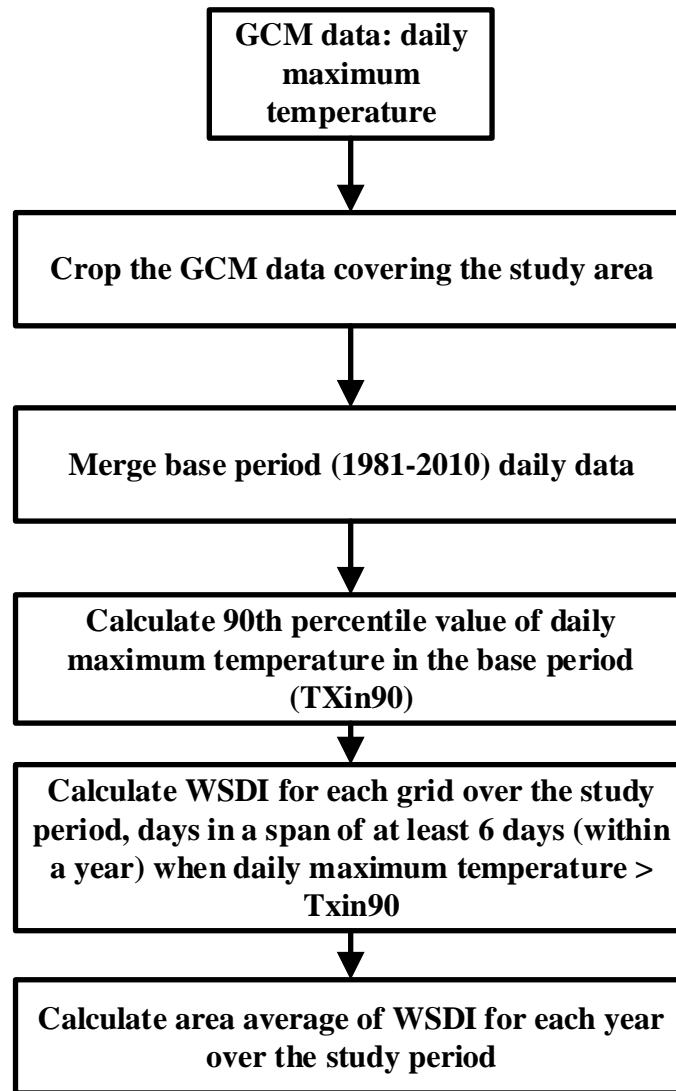


Figure 5.13: Flowchart to calculate WSDI.

After calculating all the indices' values for the initially selected models/ensembles (mentioned in Table 5.6 to Table 5.8) for each climate change scenarios RCP4.5 and RCP8.5 for the short-term, mid-century and end-of-century future periods, relevant indices were selected for each corner. For example, CSDI and CDD represent the cold and dry corner. Likewise, WSDI and CDD represent the warm and dry corner and CSDI and R95pTOT the cold and wet corner. Similarly, WSDI and R95pTOT represent the warm and wet corner. Following Lutz et al. (2016), the models/ensembles were scored, based on the percentage increase of the relevant indices. The largest increase scored five points, whereas the smallest increase scored one.

The ETCCDI indices, T index score, P index score and the combined score for climate change scenarios RCP4.5 and RCP8.5 for the short-term future period (2016-2045), are shown in Tables 5.10 and 5.11 respectively.

Table 5.10: GCM runs analysed during the refined selection process for climate change scenario RCP4.5 considering the short-term future period (2016-2045).

RCP	Projection (Climate extreme indices)	Model	Δ_T (°C)	Δ_P (%)	Δ_{CSDI} (%)	Δ_{CDD} (%)	Δ_{WSDI} (%)	$\Delta_{R95pTOT}$ (%)	T_index rank	P_index rank	Combined score
RCP 4.5	Cold and dry: CSDI, CDD	inmcm4_r1i1p1	0.63	-1.4	-33.08	7.46	84.2	-2.46	5	3	4
		EC-EARTH_r8i1p1	0.71	1.85	-33.82	-6.01	110.38	3	4	1	2.5
		ACCESS1-3_r1i1p1	0.94	2.46	-58.4	19.12	100.31	22.17	3	5	4
		ACCESS1-0_r1i1p1	1.1	0.24	-62.76	17.42	168.01	10.63	2	4	3
		CMCC-CM_r1i1p1	1.11	-0.61	-67.55	0.57	296.11	12.31	1	2	1.5
	Warm and dry: WSDI, CDD	CMCC-CMS_r1i1p1	1.4	-3.23	-67.76	7.28	150.58	-7.05	1	3	2
		MPI-ESM-LR_r3i1p1	1.5	-1.16	-73.99	7.65	221.24	-4.72	4	4	4
		MIROC5_r2i1p1	1.54	-2.91	-75.04	4.57	301.15	3.33	5	2	3.5
		MIROC-ESM_r1i1p1	1.39	-3.71	-83.75	-4.34	205.49	2.07	3	1	2
		MPI-ESM-MR_r3i1p1	1.4	-5.64	-75.96	8.77	163.46	-15.47	2	5	3.5
	Cold and wet: CSDI, $\Delta_{R95pTOT}$	NOAA_GFDL_GFDL-ESM2G_r1i1p1	0.86	10.89	-36.96	-4.43	162.34	36.1	5	3	4
		MRI-CGCM3_r1i1p1	0.78	12.67	-68.7	-7.31	82	36.54	1	5	3
		GISS-E2-R_r6i1p3	0.87	16.76	-63.87	-4.04	136.08	26.36	2	2	2
		CCSM4_r2i1p1	0.93	13.11	-51.77	-2.56	80.7	36.47	3	4	3.5
		EC-EARTH_r2i1p1	0.96	6.91	-50.54	5.56	104.9	9.81	4	1	2.5
	Warm and wet: WSDI, $\Delta_{R95pTOT}$	IPSL-CM5A-MR_r1i1p1	1.41	9.76	-49.06	5.83	110.06	21.25	3	2	2.5
		CESM1-CAM5_r1i1p1	1.39	9.06	-59.18	8.3	41.28	10.06	1	1	1
		CanESM2_r2i1p1	1.74	15.61	-72.28	3.11	194.4	42.9	5	5	5
		CanESM2_r5i1p1	1.32	11.4	-79.17	1.23	104.75	34.77	2	4	3
		IPSL-CM5A-LR_r3i1p1	1.33	7.51	-76.12	1.8	187.27	22.14	4	3	3.5

Table 5.11: GCM runs analysed during the refined selection process for climate change scenario RCP8.5 considering the short-term future period (2016-2045).

RCP	Projection (Climate extreme indices)	Model	Δ_T (°C)	Δ_P (%)	Δ_{CSDI} (%)	Δ_{CDD} (%)	Δ_{WSDI} (%)	$\Delta_{R95pTOT}$ (%)	T_index rank	P_index rank	Combined score
RCP 8.5	Cold and dry: CSDI, CDD	inmcm4_r1i1p1	0.81	0.99	-35.02	12.51	158.5	18.86	5	4	4.5
		CSIRO-Mk3-6-0_r8i1p1	1.02	1.16	-48.79	-6.87	183.36	-5.66	3	2	2.5
		CSIRO-Mk3-6-0_r3i1p1	1.1	1.49	-62.83	-0.55	303.5	-8.72	2	3	2.5
		ACCESS1-3_r1i1p1	1.02	2.17	-45.4	18.69	128.58	17.92	4	5	4.5
		NOAA_GFDL_GFDL-ESM2G_r1i1p1	1.09	2.07	-65.72	-8.23	174.59	5.45	1	1	1
	Warm and dry: WSDI, CDD	CMCC-CMS_r1i1p1	1.8	-3.31	-78.41	8.84	231.19	2.33	2	4	3
		MPI-ESM-LR_r3i1p1	1.88	-5.06	-93.37	5.87	290.66	-7.87	5	1	3
		IPSL-CM5A-LR_r2i1p1	1.65	-1.18	-79.42	14.47	233.11	12.52	3	5	4
		MPI-ESM-LR_r1i1p1	1.61	-1.4	-87.23	8.67	266.08	18.97	4	3	3.5
		MPI-ESM-LR_r2i1p1	1.85	-8.53	-84.37	7.73	229.76	-12.64	1	2	1.5
	Cold and wet: CSDI, $\Delta_{R95pTOT}$	MRI-CGCM3_r1i1p1	0.83	10.68	-69.85	-7.11	86.85	26.47	1	3	2
		NOAA_GFDL_GFDL-ESM2M_r1i1p1	1.19	7.73	-62.89	8.73	183.98	29.46	4	4	4
		IPSL-CM5B-LR_r1i1p1	0.98	4.35	-68.92	5.7	146.99	-0.83	2	1	1.5
		CMCC-CM_r1i1p1	1.2	6	-65.89	6.08	235.16	31.16	3	5	4
		EC-EARTH_r8i1p1	1.06	3.74	-50.1	-1.66	131.41	5.63	5	2	3.5
	Warm and wet: WSDI, $\Delta_{R95pTOT}$	CanESM2_r1i1p1	1.75	8.95	-60.51	0.05	168.16	36.4	1	3	2
		IPSL-CM5A-LR_r4i1p1	1.66	6.37	-82.91	12.27	216.32	38.56	4	4	4
		CanESM2_r4i1p1	2.06	7.25	-70.13	12.31	291.11	24.35	5	2	3.5
		CanESM2_r2i1p1	1.62	6.16	-72.23	-4.74	206.92	18.77	3	1	2
		CanESM2_r3i1p1	1.92	21.29	-82.57	-3.65	181.93	57.91	2	5	3.5

The CSDI values, at the cold and dry corner in Table 5.10 for models inmcm4_r1i1p1, EC-EARTH_r8i1p1, ACCESS1-3_r1i1p1, ACCESS1-0_r1i1p1 and CMCC-CM_r1i1p1 are -33.1, -33.8, -58.4, -62.8 and -67.6 respectively. The model inmcm4_r1i1p1 shows the highest value (the least decrease). Hence, is scored 5 in T index. In contrast, the model CMCC-CM_r1i1p1 shows the lowest value (the highest decrease). Therefore, is scored 1 in T index. Similarly, CDD values at cold and dry corner in Table 5-10 for inmcm4_r1i1p1, EC-EARTH_r8i1p1, ACCESS1-3_r1i1p1, ACCESS1-0_r1i1p1 and CMCC-CM_r1i1p1 are 7.5, -6.0, 19.1, 17.4 and 0.6 respectively. The model ACCESS1-0_r1i1p1 has the highest value and the model EC-EARTH_r8i1p1 has the lowest value. Thus, they were scored as 5 and 1 respectively in the P index.

For all the corners, the P index and T index were calculated in the same manner. The T index and P index were then averaged to calculate the combined score. For instance, at cold and dry corner in Table 5.10, the T index and P index for the model inmcm4_r1i1p1 are 5 and 3 respectively. Hence, the combined score is 4, which is the average of 5 and 3.

The negative values of the Cold Spell Duration Index, or CSDI, in Tables 5.10 and 5.11 show that the daily minimum temperature is expected to increase in future. A negative 33.1 % value of CSDI, in Table 5.10, for the model inmcm4_r1i1p1 at the cold and dry corner for climate change scenario RCP4.5 indicates that the Cold Spell Duration Index is likely to decrease by 33 % in the future period (2016-2045) compared to the reference period (1981-2010), which indicates that warmer nights are expected in future. The positive values of the Warm Spell Duration Index, or WSDI, in Tables 5.10 and 5.11 indicate that the daily maximum temperature is likely to increase in coming decades. For instance, at the warm and dry corner in Table 5.10, the WSDI is expected to increase by 150-301% in the future period (2016-2045) compared to the reference period (1981-2010). This increase in WSDI shows the likelihood of warmer days in the short-term future period compared to the reference period. Most of the models/ensembles predicted an increase in Consecutive Dry Days (CDD). It means dry spells with daily precipitation < 1 mm are likely to increase in future, indicating an increase in droughts. Although the dry spells are expected to increase, precipitation due to very wet days, R95pTOT, is also likely to increase. Precipitation due to very wet days at the warm and wet corner for climate change scenario RCP4.5 (Table 5.10) is predicted to increase by 10-42% in the short-term future period (2016-2045) compared to the reference period (1981-2010). Hence, more intense rainfall during the monsoon season is expected when compared to the reference period.

The two models/ensembles with highest combined score were selected for the third step (Figure 5.3- Step 3). In some corners, more than two models/ensembles were selected as they have same second-highest combined scores. Selected models for climate change scenarios RCP4.5 and RCP8.5 from Step 2, are highlighted in blue colour on Tables 5.10 and 5.11 respectively. Table 5.10 shows that for climate change scenario RCP4.5 models `inmcm4_r1i1p1` and `ACCESS1-3_r1i1p1` are selected at the cold and dry corner. Likewise, models `MPI-ESM-LR_r3i1p1`, `MIROC5_r2i1p1` and `MPI-ESM-MR_r3i1p1` are selected at the warm and dry corner. Similarly, models `NOAA_GFDL_GFDL-ESM2G_r1i1p1` and `CCSM4_r2i1p1` at the cold and wet corner; and models `CanESM2_r2i1p1` and `IPSL-CM5A-LR_r3i1p1` at the warm and wet corner are selected for climate change scenario RCP4.5.

Table 5.11 shows that for climate change scenario RCP8.5 models `inmcm4_r1i1p1` and `ACCESS1-3_r1i1p1` are selected at the cold and dry corner. Similarly, models `IPSL-CM5A-LR_r2i1p1` and `MPI-ESM-LR_r1i1p1`; `NOAA_GFDL_GFDL-ESM2M_r1i1p1` and `CMCC-CM_r1i1p1`; and `IPSL-CM5A-LR_r4i1p1`, `CanESM2_r4i1p1` and `CanESM2_r3i1p1` are selected at warm and dry, cold and wet, and warm and wet corners respectively.

Likewise, the ETCCDI indices, T index score, P index score and the combined score for climate change scenarios RCP4.5 and RCP8.5 for the mid-century future period (2036-2065) are shown in Tables 5.12 and 5.13 respectively.

The CSDI values at cold and dry corner on Table 5.12 for models `EC-EARTH_r8i1p1`, `inmcm4_r1i1p1`, `NOAA_GFDL_GFDL-ESM2M_r1i1p1`, `EC-EARTH_r12i1p1` and `EC-EARTH_r2i1p1`, are -55.8, -35.8, -49.8, -63.2, and -67.0 respectively. The model `inmcm4_r1i1p1` shows the highest value (the least decrease). Hence, it is scored 5 in the T index. In contrast, the model `EC-EARTH_r2i1p1` shows the lowest value (the highest decrease). Therefore, it is scored 1 in the T index. Similarly, CDD values at the cold and dry corner in Table 5.12 for models `EC-EARTH_r8i1p1`, `inmcm4_r1i1p1`, `NOAA_GFDL_GFDL-ESM2M_r1i1p1`, `EC-EARTH_r12i1p1` and `EC-EARTH_r2i1p1` are 0.6, 9.2, 5.7, 5.9 and 2.8 respectively. The model `inmcm4_r1i1p1` has the highest value, while the model `EC-EARTH_r8i1p1` has the lowest value. Thus, they are scored as 5 and 1 respectively in the P index.

For all the corners, the P index and T index were calculated in the same manner. The T index and P index were then averaged to calculate the combined score. For instance, at the cold and

dry corner in Table 5.12, the T index and P index values for the model EC-EARTH_r8i1p1 are 3 and 1 respectively. Hence, the combined score is 2, which is the average of 3 and 1.

Table 5.12: GCM runs analysed during the refined selection process for climate change scenario RCP4.5, considering the mid-century future period (2036-2065).

RCP	Projection (Climate extreme indices)	Model	Δ_T (°C)	Δ_P (%)	Δ_{CSDI} (%)	Δ_{CDD} (%)	Δ_{WSDI} (%)	$\Delta R95pTOT$ (%)	T_index rank	P_index rank	Combined score
RCP 4.5	Cold and dry: CSDI, CDD	EC-EARTH_r8i1p1	1.34	-0.72	-55.77	0.63	213.04	0.14	3	1	2
		inmcm4_r1i1p1	1	-2.51	-35.78	9.15	178.1	-2.29	5	5	5
		NOAA_GFDL_GFDL-ESM2M_r1i1p1	1.35	1.6	-49.81	5.67	274.83	17.56	4	3	3.5
		EC-EARTH_r12i1p1	1.44	4.22	-63.19	5.87	164.9	6.5	4	4	4
		EC-EARTH_r2i1p1	1.45	5.39	-67.01	2.84	177.91	7.92	1	2	1.5
	Warm and dry: WSDI, CDD	CMCC-CMS_r1i1p1	2.32	-3.72	-89.79	17.63	286.81	-1.06	1	4	2.5
		MIROC-ESM-CHEM_r1i1p1	2.33	-1.49	-96.42	-7.71	739.31	-2.19	5	1	3
		MIROC5_r2i1p1	2.23	-4.38	-96.69	0.64	585.54	-6.65	4	3	3.5
		MPI-ESM-LR_r2i1p1	2.28	-4.75	-89.29	21.52	326.06	11.03	2	5	3.5
		CSIRO-Mk3-6-0_r6i1p1	2.16	-5.03	-93.66	-3.42	468.08	-10.14	3	2	2.5
	Cold and wet: CSDI, $\Delta R95pTOT$	IPSL-CM5B-LR_r1i1p1	0.97	24.6	-72.92	-15.16	112.87	28.32	4	1	2.5
		MRI-CGCM3_r1i1p1	1.3	12.49	-86.94	-10.39	192.77	39.58	2	5	3.5
		bcc-csm1-1_r1i1p1	1.47	12.74	-74.33	-8.08	259.32	38.89	3	4	3.5
		CCSM4_r2i1p1	1.39	11.13	-65.94	-0.99	180.19	36.62	5	3	4
		GISS-E2-R_r6i1p3	1.58	19.55	-87.35	-2.92	314.97	29.67	1	2	1.5
	Warm and wet: WSDI, $\Delta R95pTOT$	CanESM2_r3i1p1	2.36	14.59	-96.32	7.19	219.78	58.72	4	5	4.5
		IPSL-CM5A-MR_r1i1p1	2.24	13.34	-68.51	1.71	145.51	26.51	1	1	1
		CanESM2_r2i1p1	2.05	17.23	-85.23	3.83	227.79	45.12	5	4	4.5
		CanESM2_r5i1p1	2.04	13.91	-87.19	-0.74	177.92	42.75	3	3	3
		CanESM2_r1i1p1	2.18	12.33	-86.85	6.57	163.27	41.25	2	2	2

Table 5.13: GCM runs analysed during the refined selection process for climate change scenario RCP8.5, considering the mid-century future period (2036-2065).

RCP	Projection (Climate extreme indices)	Model	Δ_T (°C)	Δ_P (%)	Δ_{CSDI} (%)	Δ_{CDD} (%)	Δ_{WSDI} (%)	$\Delta R95pTOT$ (%)	T_{index} rank	P_{index} rank	Combined score
RCP 8.5	Cold and dry: CSDI, CDD	inmcm4_r1i1p1	1.59	2.97	-61.34	4.98	326.23	27.84	5	4	4.5
		EC-EARTH_r9i1p1	1.86	5.2	-80.21	0.08	240.36	7.62	1	1	1
		ACCESS1-3_r1i1p1	2.02	3.74	-79.87	34.14	292.68	34.71	2	5	3.5
		EC-EARTH_r2i1p1	1.96	5.42	-73.04	1.05	251.24	8.54	3	2	2.5
		CCSM4_r6i1p1	2.12	4.3	-67.84	4.06	98.3	7.36	4	3	3.5
	Warm and dry: WSDI, CDD	CMCC-CMS_r1i1p1	3.16	-2.74	-97.98	9.62	475.53	6.26	2	2	2
		MPI-ESM-LR_r3i1p1	2.94	-3.85	-98.8	8.21	528.39	-3.6	3	1	2
		MPI-ESM-LR_r2i1p1	3.07	-11.51	-97.6	12.94	467.7	-7.59	1	4	2.5
		MIROC-ESM-CHEM_r1i1p1	3.33	1.93	-99.08	11.87	1240.63	19.06	5	3	4
		MPI-ESM-LR_r1i1p1	2.82	-4.64	-95.3	16.3	550.58	16.01	4	5	4.5
	Cold and wet: CSDI, $\Delta R95pTOT$	bcc-csm1-1_r1i1p1	1.92	17.54	-90.52	6.27	326.92	50	1	5	3
		CESM1-BGC_r1i1p1	1.96	10.38	-58.22	0.28	100.34	13.43	5	2	3.5
		NOAA_GFDL_GFDL-ESM2M_r1i1p1	1.86	9.96	-79.25	3.89	378	41.71	2	4	3
		EC-EARTH_r8i1p1	1.9	7.97	-68.81	-0.05	268.59	9.5	4	1	2.5
		NOAA_GFDL_GFDL-ESM2G_r1i1p1	1.91	7.68	-71.01	6.75	370.29	36.97	3	3	3
	Warm and wet: WSDI, $\Delta R95pTOT$	IPSL-CM5A-MR_r1i1p1	3.02	14.42	-96.84	8	620.66	46.28	5	1	3
		CanESM2_r3i1p1	3.15	18.5	-96.48	6.43	383.83	56.76	3	4	3.5
		CanESM2_r5i1p1	2.99	17.94	-93.6	10.3	320.72	52.09	1	3	2
		CanESM2_r2i1p1	2.91	17.16	-90.89	6.72	442.34	49.97	4	2	3
		CanESM2_r1i1p1	2.96	21.55	-88.55	8.65	321.26	78.79	2	5	3.5

The negative values of the Cold Spell Duration Index, or CSDI, in Tables 5.12 and 5.13 show that the daily minimum temperature is expected to increase in future. A negative 55.8 % value of CSDI for the model EC-EARTH_r8i1p1 at the cold and dry corner for RCP4.5, in Table 5.12, indicates that the Cold Spell Duration Index is likely to decrease by 55.8% in the mid-century future period (2036-2065) compared to the reference period (1981-2010), which indicates that warmer nights are expected in future. The positive values of the Warm Spell Duration Index, or WSDI, in Tables 5.12 and 5.13 indicate that the daily maximum temperature is likely to increase in coming decades. For instance, at the warm and dry corner in Table 5.12, the WSDI is expected to increase by 287-739% in the short-term future period (2036-2065) compared to the reference period (1981-2010). Most of the model ensembles predicted an increase in Consecutive Dry Days (CDD). It means dry spells with daily precipitation < 1 mm are likely to increase in future, indicating an increase in droughts. Although dry spells are expected to increase, precipitation due to very wet days, R95pTOT, is likely to increase. Precipitation due to very wet days at the warm and wet corner for RCP4.5 (Table 5.12) is predicted to increase by 26-59% in the mid-century future period (2036-2065) compared to the reference period (1981-2010). Hence, more intense rainfall during the monsoon season is expected compared to the reference period.

The two models/ensembles with the highest combined score were selected for next step (Figure 5.3 – Step 3). In some corners, more than two models/ensembles were selected as they have same second-highest combined scores. Selected models for climate change scenarios RCP4.5 and RCP8.5 from Step 2 are highlighted in blue colour on Tables 5.12 and 5.13 respectively. Table 5.12 shows that for climate change scenario RCP4.5, models inmcm4_r1i1p1 and EC-EARTH_r12i1p1 are selected at the cold and dry corner. Likewise, models MIROC5_r2i1p1 and MPI-ESM-LR_r2i1p1 are selected at the warm and dry corner. Similarly, models CCSM4_r2i1p1, MRI-CGCM3_r1i1p1 and bcc-csm1-1_r1i1p1 at the cold and wet corner; and CanESM2_r3i1p1 and CanESM2_r2i1p1 at the warm and wet corner are selected for climate change scenario RCP4.5.

Table 5.13 shows that for climate change scenario RCP8.5, models inmcm4_r1i1p1, ACCESS1-3_r1i1p1, and CCSM4_r6i1p1 are selected at the cold and dry corner. Models MPI-ESM-LR-r1i1p1 and MIROC-ESM-CHEM_r1i1p1; CESM1-BGC_r1i1p1, bcc-csm1-1_r1i1p1 and NOAA_GFDL_GFDL-ESM2G_r1i1p1; and CanESM2_r3i1p1 and CanESM2_r1i1p1 are selected at the warm and dry, cold and wet, and warm and wet corner respectively.

Similarly, the ETCCDI indices, T index score, P index score and the combined score for climate change scenarios RCP4.5 and RCP8.5 for the end-of-century future period (2071-2100) are shown in Tables 5.14 and 5.15 respectively.

The CSDI values at the cold and dry corner in Table 5.14 for models GISS-E2-R_r6i1p1, inmcm4_r1i1p1, EC-EARTH_r2i1p1, EC-EARTH_r12i1p1 and NOAA_GFDL_GFDL-ESM2G_r1i1p1 are -76.9, -68.5, -68.6, -70.6 and -46.56 respectively. The model NOAA_GFDL_GFDL-ESM2G_r1i1p1 shows the highest value (the least decrease). Hence, it is scored 5 in the T index. In contrast, the model GISS-E2-R_r6i1p1 shows the lowest value (the highest decrease). Therefore, it is scored 1 in the T index. Similarly CDD values at the cold and dry corner in Table 5.14 for models GISS-E2-R_r6i1p1, inmcm4_r1i1p1, EC-EARTH_r2i1p1, EC-EARTH_r12i1p1 and NOAA_GFDL_GFDL-ESM2G_r1i1p1 are -3.4, 0.3, 0.3, -4.7 and 1.2 respectively. The model NOAA_GFDL_GFDL-ESM2G_r1i1p1 has the highest value while the model EARTH_r12i1p1 has the lowest value. Thus, they are scored as 5 and 1 respectively in the P index.

For all the corners, the P index and T index were calculated in the same manner. The T index and P index were then averaged to calculate the combined score. For instance, at cold and dry corner in Table 5.14, the T index and P index values for the model GISS-E2-R_r6i1p1 are 1 and 2 respectively. Hence, the combined score is 1.5, which is the average of 1 and 2.

Table 5.14: GCM runs analysed during the refined selection process for climate change scenario RCP4.5, considering the end-of-century future period (2071-2100).

RCP	Projection (Climate extreme indices)	Model	Δ_T (°C)	Δ_P (%)	Δ_{CSDI} (%)	Δ_{CDD} (%)	Δ_{WSDI} (%)	$\Delta R95pTOT$ (%)	T_{index} rank	P_{index} rank	Combined score
RCP 4.5	Cold and dry: CSDI, CDD	GISS-E2-R_r6i1p1	1.81	4.57	-76.85	-3.42	445.29	-2.71	1	2	1.5
		inmcm4_r1i1p1	1.64	5.8	-68.51	0.27	307.64	20.07	4	3	3.5
		EC-EARTH_r2i1p1	1.92	5.12	-68.56	0.32	248.37	8.25	3	4	3.5
		EC-EARTH_r12i1p1	1.94	3.32	-70.62	-4.71	255.44	5.46	2	1	1.5
		NOAA_GFDL_GFDL-ESM2G_r1i1p1	1.64	6.8	-46.56	1.22	395.91	33.28	5	5	5
	Warm and dry: WSDI, CDD	CSIRO-Mk3-6-0_r1i1p1	3.15	0.36	-93.83	3.69	851.16	16.48	3	3	3
		CSIRO-Mk3-6-0_r9i1p1	3.27	-4.44	-93.29	4.36	1192.68	6.04	5	4	4.5
		CMCC-CMS_r1i1p1	3.3	-2.68	-96.85	10.31	475.36	6.96	1	5	3
		CSIRO-Mk3-6-0_r6i1p1	3.16	5.93	-93.14	2.85	798.97	41.7	2	2	2
		CSIRO-Mk3-6-0_r3i1p1	2.99	1.24	-92.17	1.16	1152.21	6.87	4	1	2.5
	Cold and wet: CSDI, $\Delta R95pTOT$	IPSL-CM5B-LR_r1i1p1	1.64	21.53	-84.49	-13.99	237.36	18.64	2	1	1.5
		NOAA_GFDL_GFDL-ESM2M_r1i1p1	1.71	13.86	-73.79	7.71	359.22	47.09	4	3	3.5
		CCSM4_r2i1p1	1.76	13.16	-73.06	-0.15	341.99	50.53	5	4	4.5
		GISS-E2-R_r6i1p3	2.18	24.97	-81.79	-2.46	507.26	56.68	3	5	4
		BNU-ESM_r1i1p1	2.32	14.39	-91.39	-2.28	59.58	45.2	1	2	1.5
	Warm and wet: WSDI, $\Delta R95pTOT$	CanESM2_r3i1p1	3.09	30.41	-96.52	-4.64	313.76	105.92	2	5	3.5
		CNRM-CM5_r1i1p1	3.14	18.37	-95.27	-1.57	708.17	26.86	4	1	2.5
		IPSL-CM5A-MR_r1i1p1	3.23	17.35	-94.77	3.24	249.63	33.7	1	2	1.5
		IPSL-CM5A-LR_r1i1p1	3.28	13.63	-99.09	10.36	703.74	49.87	3	3	3
		HadGEM2-ES_r2i1p1	3.04	13.79	-92.73	24.55	1080.29	69.54	5	4	4.5

Table 5.15: GCM runs analysed during the refined selection process for climate change scenario RCP8.5, considering the end-of-century future period (2071-2100).

RCP	Projection (Climate extreme indices)	Model	Δ_T (°C)	Δ_P (%)	Δ_{CSDI} (%)	Δ_{CDD} (%)	Δ_{WSDI} (%)	$\Delta R95pTOT$ (%)	T_index rank	P_index rank	Combined score
RCP 8.5	Cold and dry: CSDI, CDD	EC-EARTH_r9i1p1	3.85	10.23	-92.24	6.04	470.92	13.88	3	4	3.5
		inmcm4_r1i1p1	3.53	10.57	-91.66	16.2	794.68	71.7	4	5	4.5
		EC-EARTH_r8i1p1	3.93	9.65	-92.62	-2.32	504.24	11.28	2	2	2
		CCSM4_r6i1p1	3.72	11.21	-90.18	-4.06	234.4	15.52	5	1	3
		EC-EARTH_r2i1p1	3.84	11.04	-95.22	0.54	453.09	14.4	1	3	2
	Warm and dry: WSDI, CDD	CMCC-CMS_r1i1p1	5.95	-3.95	-99.35	23.78	989.58	32.78	2	3	2.5
		MPI-ESM-LR_r3i1p1	5.62	-5.53	-99.83	25.67	1198.85	8.79	4	4	4
		MIROC-ESM_r1i1p1	5.86	10.15	-100	5.66	1149.58	48.83	3	1	2
		MIROC-ESM-CHEM_r1i1p1	6.53	8.52	-100	12.36	2601.41	41.45	5	2	3.5
		MPI-ESM-LR_r2i1p1	5.61	-11.02	-100	26.32	954.88	7.92	1	5	3
	Cold and wet: CSDI, $\Delta R95pTOT$	NOAA_GFDL_GFDL-ESM2G_r1i1p1	3.63	35.59	-96.36	-9.55	858.2	138.59	5	5	5
		IPSL-CM5B-LR_r1i1p1	3.83	27.63	-99.14	0.63	750.06	36.1	2	1	1.5
		NOAA_GFDL_GFDL-ESM2M_r1i1p1	3.61	25	-96.84	2.09	910.22	99.84	4	4	4
		bcc-csm1-1_r1i1p1	3.96	28.93	-100	-4.55	812.87	94.41	1	3	2
		ACCESS1-3_r1i1p1	3.98	21.63	-98.38	38.47	521.66	92.39	3	2	2.5
	Warm and wet: WSDI, $\Delta R95pTOT$	CanESM2_r4i1p1	5.57	40.39	-100	-3.07	977.93	115.67	4	1	2.5
		CanESM2_r5i1p1	5.68	53.79	-100	1.2	701.29	153.11	1	3	2
		CanESM2_r3i1p1	5.82	62.99	-100	-5.58	822.12	204.27	2	5	3.5
		NOAA_GFDL_GFDL-CM3_r1i1p1	6.97	34.8	-100	24.49	1398.51	157.66	5	4	4.5
		CanESM2_r2i1p1	5.52	53.32	-98.5	-9.68	917.65	145.57	3	2	2.5

The negative values of the Cold Spell Duration Index, or CSDI, in Tables 5.14 and 5.15 show that the daily minimum temperature is expected to increase in future. A negative 76.8 % value of CSDI for the model GISS-E2-R_r6i1p1, at the cold and dry corner for climate change scenario RCP4.5 in Table 5.14, indicates that the Cold Spell Duration Index is likely to decrease by 76.8% in the end-of-century future period (2071-2100) compared to the reference period (1981-2010), which indicates that warmer nights are expected in future. The positive values of the Warm Spell Duration Index, or WSDI, in Tables 5.14 and 5.15 indicate that the daily maximum temperature is likely to increase in coming decades. For instance, at the warm and dry corner in Table 5.14, WSDI is expected to increase by 475-1193% in the end-of-century future period (2071-2100) compared to the reference period (1981-2010). Most of the models/ensembles predicted an increase in Consecutive Dry Ddays (CDD). It means dry spells with daily precipitation < 1 mm are likely to increase in future, indicating an increase in droughts. Although the dry spells are expected to increase, precipitation due to very wet days, R95pTOT, is likely to increase. Precipitation due to very wet days at the warm and wet corner for climate change scenario RCP4.5 (Table 5.14) is predicted to increase by 27-102% in the end-of-century future period (2071-2100) compared to the reference period (1981-2010). Hence, more intense rainfall during the monsoon season is expected compared to the reference period.

The two model ensembles with the highest combined score were selected for the next step (Figure 5.3 – Step 3). In some corners, more than two models/ensembles were selected as they have the same second-highest combined scores. Selected models for climate change scenarios RCP4.5 and RCP8.5 from Step 2 are highlighted in blue colour on Tables 5.14 and 5.15 respectively. Table 5.14 shows that for climate change scenario RCP4.5 models NOAA_GFDL_GFDL-ESM2G_r1i1p1, inmcm4_r1i1p1 and EC-EARTH_r2i1p1 are selected at the cold and dry corner. Likewise, models CSIRO-Mk3-6-0_r9i1p1, CSIRO-Mk3-6-0_r1i1p1 and CMCC-CMS_r1i1p1 are selected at the warm and dry corner. Similarly, models CCSM4_r2i1p1 and GISS-E2-R_r6i1p3 at the cold and wet corner; and CanESM2_r3i1p1 and HadGEM2-ES_r2i1p1 at the warm and wet corner are selected for climate change scenario RCP4.5.

Table 5.15 shows that for climate change scenario RCP8.5 models inmcm4_r1i1p1 and EC-EARTH_r9i1p1 are selected at the cold and dry corner. Models MPI-ESM-LR_r3i1p1 and MIROC-ESM-CHEM_r1i1p1; NOAA_GFDL_GFDL-ESM2G_r1i1p1 and NOAA_GFDL_GFDL-ESM2M_r1i1p1; and NOAA_GFDL_GFDL-CM3_r1i1p1 and

CanESM2_r3i1p1 are selected at the warm and dry, cold and wet, and warm and wet corners respectively.

Step 3: Final model selection based on model capability in simulating the annual cycle of air temperature and precipitation (past performance)

The models/ensembles selected from the refined selection were then assessed for their capability to simulate the annual cycle of air temperature and precipitation for the reference period (1981-2010). The Hi-AWARE reference climate dataset developed by Lutz and Immerzeel (2015) was downloaded from <http://rds.icimod.org/clim>. For air temperature, total bias, monsoon bias, and winter bias were considered. The biases represent the difference between the reference value and the GCMs/ensembles' runs for the same period. Precipitation in the study area is highly influenced by the monsoon season. Winter (dry) season precipitation is also crucial for irrigation purposes. So winter bias, monsoon bias and total bias (annual) were used to calculate biases for precipitation between the reference data and the GCM/ensemble data. The biases for precipitation and temperature were calculated in percentages and °C respectively. The precipitation bias (P bias) and temperature bias (T bias) values were used to evaluate the GCM/ensemble's ability to simulate the annual cycle of air temperature and precipitation.

The bias values (P bias and T bias) were then normalized (each absolute bias value is expressed as a fraction of the largest absolute bias value) within the models/ensembles for both climate change scenarios, RCP4.5 and RCP8.5. The P bias score and T bias score were calculated by averaging the precipitation biases and temperature biases respectively. Then, the sum of the P bias score and the T bias score was calculated to find the combined score.

The biases and the combined scores for climate change scenarios RCP4.5 and RCP8.5, considering the models/ensembles for the short term period (2016-2045), are shown in Table 5.16. For a demonstration of the calculation process, the first ensemble member from Table 5.16 (inmcm4_r1i1p1) is considered as an example. For climate change scenario RCP4.5 (Table 5.16), the P bias winter normalized, P bias monsoon normalized and P bias total normalized values of the model inmcm4_r1i1p1 are 0.56, 0.16 and 0.24 respectively. The model inmcm4_r1i1p1 is considered for a demonstration of the calculation process as it is the first member in the Table 5.16. The same procedure was followed for all the ensemble members. The P bias score, 0.32, was calculated by averaging 0.56, 0.16 and 0.24. Similarly, the T bias winter normalized, T bias monsoon normalized and T bias total normalized values

of the model, cold and dry corner in Table 5.16 are 1.0, 1.0 and 1.0. The T bias score, 1.0, is the average of these three values. The combined score, 1.32, is the sum of the P bias score and the T bias score. The models/ensemble with the least combined score, representing the least variation in reference values and GCM runs for the reference period (1981-2010), was selected at each corner.

Table 5.16: Biases between GCM runs and the reference climate dataset (1981-2010) for climate change scenarios RCP4.5 and RCP8.5, considering ensembles for the short-term period (2016-2045).

RCP	Projection	Model	P bias winter (%)	P bias monsoon (%)	P bias total (%)	T bias winter (°C)	T bias monsoon (°C)	T bias total (°C)	P bias winter normalized	P bias monsoon normalized	P bias total normalized	T bias winter normalized	T bias monsoon normalized	T bias total normalized	P bias score	T bias score	Combined score
RCP 4.5	Cold and dry	inmcm4_r1i1p1	134.07	13.54	20.08	-7.76	-2.02	-4.91	0.56	0.16	0.24	1.00	1.00	1.00	0.32	1.00	1.32
		ACCESS1-3_r1i1p1	241.42	19.81	32.94	-1.64	0.41	-0.95	1.00	0.24	0.39	0.21	0.20	0.19	0.54	0.20	0.74
	Warm and dry	MPI-ESM-LR_r3i1p1	75.66	66.40	56.26	-3.33	-0.67	-1.36	0.31	0.80	0.67	0.43	0.33	0.28	0.59	0.35	0.94
		MIROC5_r2i1p1	91.89	83.27	83.89	-1.36	0.68	-0.10	0.38	1.00	1.00	1.00	0.18	0.34	0.02	0.79	0.18
	Cold and wet	MPI-ESM-MR_r3i1p1	69.09	61.41	53.17	-3.52	-0.18	-1.25	0.29	0.74	0.63	0.45	0.09	0.26	0.55	0.27	0.82
		NOAA_GFDL_GFDL-ESM2G_r1i1p1	52.32	40.52	33.28	-1.47	-0.43	-0.87	0.22	0.49	0.40	0.19	0.22	0.18	0.37	0.19	0.56
	Warm and wet	CCSM4_r2i1p1	174.86	32.31	32.72	-3.95	0.53	-1.18	0.72	0.39	0.39	0.51	0.26	0.24	0.50	0.34	0.84
		CanESM2_r2i1p1	24.66	-14.87	-16.42	-4.42	-0.62	-2.54	0.10	0.18	0.20	0.57	0.31	0.52	0.16	0.46	0.62
	IPSL-CM5A-LR_r3i1p1	134.31	-36.61	-29.80	-2.45	0.16	-1.63	0.56	0.44	0.36	0.32	0.08	0.33	0.45	0.24	0.69	
RCP 8.5	Cold and dry	inmcm4_r1i1p1	116.78	12.89	18.83	-7.43	-2.01	-4.87	0.51	0.21	0.33	1.00	1.00	1.00	0.35	1.00	1.35
		ACCESS1-3_r1i1p1	228.71	22.54	34.67	-1.59	0.37	-0.96	1.00	0.37	0.60	0.21	0.19	0.20	0.66	0.20	0.86
	Warm and dry	IPSL-CM5A-LR_r2i1p1	118.75	-36.01	-28.40	-2.14	0.32	-1.57	0.52	0.59	0.49	0.29	0.16	0.32	0.53	0.26	0.79
		MPI-ESM-LR_r1i1p1	95.36	61.04	57.66	-3.13	-0.57	-1.24	0.42	1.00	1.00	0.42	0.28	0.25	0.81	0.32	1.13
	Cold and wet	NOAA_GFDL_GFDL-ESM2M_r1i1p1	80.54	44.31	40.49	-1.65	-0.26	-0.90	0.35	0.73	0.70	0.22	0.13	0.18	0.59	0.18	0.77
		CMCC-CM_r1i1p1	184.69	29.53	25.58	-3.37	1.30	-0.50	0.81	0.48	0.44	0.45	0.65	0.10	0.58	0.40	0.98
	Warm and wet	IPSL-CM5A-LR_r4i1p1	100.89	-37.17	-31.22	-2.22	0.23	-1.63	0.44	0.61	0.54	0.30	0.12	0.33	0.53	0.25	0.78
		CanESM2_r4i1p1	14.61	-7.86	-12.64	-4.02	-0.75	-2.52	0.06	0.13	0.22	0.54	0.37	0.52	0.14	0.48	0.62
	CanESM2_r3i1p1	18.76	-15.76	-17.57	-4.42	-0.80	-2.72	0.08	0.26	0.30	0.60	0.40	0.56	0.21	0.52	0.73	

The biases and the combined scores for climate change scenarios RCP4.5 and RCP8.5, considering the models/ensembles for the mid-century (2036-2065), are shown in Table 5.17. For RCP4.5 (Table 5.17), the P bias winter normalized, P bias monsoon normalized and P bias total normalized values of the model inmcm4_r1i1p1 are 0.31, 0.16 and 0.24 respectively. The model inmcm4_r1i1p1 is considered for a demonstration of the calculation process as it is the first member in the Table 5.17. The same procedure was followed for all the ensemble members. The P bias score, 0.24, was calculated by averaging 0.31, 0.16 and 0.24. Similarly, the T bias winter normalized, T bias monsoon normalized, and T bias total normalized values of inmcm4_r1i1p1, in the cold and dry corner in Table 5.17, are 1.0, 0.72 and 1.0 respectively. The T bias score, 0.91, is the average of these three values. The combined score, 1.15, is the sum of the P bias score and the T bias score. The

models/ensemble with the least combined score, representing the least variation in reference values and GCM runs for the reference period (1981-2010), was selected at each corner.

Table 5.17: Biases between GCM runs and the reference climate dataset (1981-2010) for climate change scenarios RCP4.5 and RCP8.5 considering ensembles for long term (2036-2065).

RCP	Projection	Model	P bias winter (%)	P bias monsoon (%)	P bias total (%)	T bias winter (°C)	T bias monsoon (°C)	T bias total (°C)	P bias winter normalized	P bias monsoon normalized	P bias total normalized	T bias winter normalized	T bias monsoon normalized	T bias total normalized	P bias score	T bias score	Combined score	
RCP 4.5	Cold and dry	inmcm4_r1i1p1	134.07	13.54	20.08	-7.76	-2.02	-4.91	0.31	0.16	0.24	1.00	0.72	1.00	0.24	0.91	1.15	
		EC-EARTH_r12i1p1	21.09	-10.34	-5.36	-2.57	-2.74	-2.61	0.05	0.12	0.06	0.33	0.98	0.53	0.08	0.61	0.69	
	Warm and dry	MIROC5_r2i1p1	91.89	83.27	83.89	-1.36	0.68	-0.10	0.21	1.00	1.00	0.18	0.24	0.02	0.74	0.15	0.89	
		MPI-ESM-LR_r2i1p1	96.44	66.37	59.34	-3.26	-0.73	-1.39	0.22	0.80	0.71	0.42	0.26	0.28	0.58	0.32	0.90	
	Cold and wet	CCSM4_r2i1p1	174.86	32.31	32.72	-3.95	0.53	-1.18	0.40	0.39	0.39	0.51	0.19	0.24	0.39	0.31	0.70	
		MRI-CGCM3_r1i1p1	85.23	-33.17	-33.09	-4.38	1.34	-1.34	0.20	0.40	0.39	0.56	0.48	0.27	0.33	0.44	0.77	
	Warm and wet	bcc-csm1-1_r1i1p1	433.47	-17.46	-2.96	-2.24	2.81	1.17	1.00	0.21	0.04	0.29	1.00	0.24	0.41	0.51	0.92	
		CanESM2_r3i1p1	19.29	-16.31	-18.63	-4.19	-0.80	-2.59	0.04	0.20	0.22	0.54	0.28	0.53	0.15	0.45	0.60	
			CanESM2_r2i1p1	24.66	-14.87	-16.42	-4.42	-0.62	-2.54	0.06	0.18	0.20	0.57	0.22	0.52	0.14	0.44	0.58
	RCP 8.5	Cold and dry	inmcm4_r1i1p1	116.78	12.89	18.83	-7.43	-2.01	-4.87	0.28	0.21	0.33	1.00	0.73	1.00	0.27	0.91	1.18
ACCESS1-3_r1i1p1			228.71	22.54	34.67	-1.59	0.37	-0.96	0.56	0.37	0.60	0.21	0.14	0.20	0.51	0.18	0.69	
CCSM4_r6i1p1			145.95	41.66	39.78	-3.98	0.44	-1.27	0.36	0.68	0.69	0.54	0.16	0.26	0.58	0.32	0.90	
Warm and dry		MPI-ESM-LR_r1i1p1	95.36	61.04	57.66	-3.13	-0.57	-1.24	0.23	1.00	1.00	0.42	0.21	0.25	0.74	0.29	1.03	
		MIROC-ESM-CHEM_r1i1p1	170.16	-6.20	16.13	-4.57	-0.48	-1.88	0.41	0.10	0.28	0.62	0.17	0.39	0.27	0.39	0.66	
Cold and wet		CESM1-BGC_r1i1p1	157.73	39.00	36.08	-3.99	0.50	-1.23	0.38	0.64	0.63	0.54	0.18	0.25	0.55	0.32	0.87	
		bcc-csm1-1_r1i1p1	410.65	-16.10	-2.48	-2.13	2.74	1.21	1.00	0.26	0.04	0.29	1.00	0.25	0.44	0.51	0.95	
		NOAA_GFDL_GFDL-ESM2M_r1i1p1	80.54	44.31	40.49	-1.65	-0.26	-0.90	0.20	0.73	0.70	0.22	0.10	0.18	0.54	0.17	0.71	
		NOAA_GFDL_GFDL-ESM2G_r1i1p1	37.35	40.91	34.19	-1.37	-0.47	-0.86	0.09	0.67	0.59	0.18	0.17	0.18	0.45	0.18	0.63	
Warm and wet		CanESM2_r3i1p1	18.76	-15.76	-17.57	-4.42	-0.80	-2.72	0.05	0.26	0.30	0.60	0.29	0.56	0.20	0.48	0.68	
	CanESM2_r1i1p1	44.17	-14.02	-16.91	-4.29	-0.61	-2.44	0.11	0.23	0.29	0.58	0.22	0.50	0.21	0.43	0.64		

Similarly, the biases and the combined scores for climate change scenarios RCP4.5 and RCP8.5, considering the models/ensembles for the end-of-century period (2071-2100), are shown in Table 5.18. For climate change scenario RCP4.5 (Table 5.18), the P bias winter normalized, P bias monsoon normalized and P bias total normalized values of the model NOAA_GFDL_GFDL-ESM2G_r1i1p1 are 0.30, 0.87 and 0.73 respectively. The model NOAA_GFDL_GFDL-ESM2G_r1i1p1 is considered for a demonstration of the calculation process as it is the first

member in the Table 5.18. The same procedure was followed for all the ensemble members. The P bias score, 0.64, was calculated by averaging 0.30, 0.87 and 0.73. Similarly, the T bias winter normalized, T bias monsoon normalized, and T bias total normalized values of NOAA_GFDL_GFDL-ESM2G_r1i1p1, in the cold and dry corner in Table 5.18, are 0.19, 0.14 and 0.18 respectively. The T bias score, 0.17, is the average of these three values. The combined score, 0.81, is the sum of the P bias score and the T bias score. The models/ensemble with the least combined score, representing the least variation in reference values and GCM runs for the base period (1981-2010), was selected at each corner.

Table 5.18: Biases between GCM runs and the reference climate dataset (1981-2010) for climate change scenarios RCP4.5 and RCP8.5 considering ensembles for the end-of-century (2071-2100) period.

RCP	Projection	Model	P bias winter (%)	P bias monsoon (%)	P bias total (%)	T bias winter (°C)	T bias monsoon (°C)	T bias total (°C)	P bias winter normalized	P bias monsoon normalized	P bias total normalized	T bias winter normalized	T bias monsoon normalized	T bias total normalized	P bias score	T bias score	Combined score
RCP 4.5	Cold and dry	NOAA_GFDL_GFDL-ESM2G_r1i1p1	52.32	40.52	33.28	-1.47	-0.43	-0.87	0.30	0.87	0.73	0.19	0.14	0.18	0.64	0.17	0.81
		inmcm4_r1i1p1	134.07	13.54	20.08	-7.76	-2.02	-4.91	0.77	0.29	0.44	1.00	0.67	1.00	0.50	0.89	1.39
		EC-EARTH_r2i1p1	2.10	-12.19	-6.47	-2.29	-2.74	-2.56	0.01	0.26	0.14	0.29	0.91	0.52	0.14	0.58	0.72
	Warm and dry	CSIRO-Mk3-6-0_r9i1p1	37.06	-24.64	-24.74	-3.88	0.07	-1.40	0.21	0.53	0.54	0.50	0.02	0.29	0.43	0.27	0.70
		CSIRO-Mk3-6-0_r1i1p1	24.05	-23.29	-26.38	-3.60	0.00	-1.26	0.14	0.50	0.58	0.46	0.00	0.26	0.41	0.24	0.65
		CMCC-CMS_r1i1p1	161.83	35.02	37.44	-3.73	0.43	-0.93	0.93	0.76	0.82	0.48	0.14	0.19	0.83	0.27	1.10
	Cold and wet	CCSM4_r2i1p1	174.86	32.31	32.72	-3.95	0.53	-1.18	1.00	0.70	0.72	0.51	0.18	0.24	0.81	0.31	1.12
		GISS-E2-R_r6i1p3	-39.23	-46.37	-45.45	3.77	3.01	3.12	0.22	1.00	1.00	0.49	1.00	0.64	0.74	0.71	1.45
	Warm and wet	HadGEM2-ES_r2i1p1	160.15	11.19	19.48	-3.23	0.32	-1.71	0.92	0.24	0.43	0.42	0.11	0.35	0.53	0.29	0.82
		CanESM2_r3i1p1	19.29	-16.31	-18.63	-4.19	-0.80	-2.59	0.11	0.35	0.41	0.54	0.27	0.53	0.29	0.44	0.73
RCP 8.5	Cold and dry	inmcm4_r1i1p1	116.78	12.89	18.83	-7.43	-2.01	-4.87	0.59	0.20	0.35	1.00	0.74	1.00	0.38	0.91	1.29
		EC-EARTH_r9i1p1	-2.59	-11.16	-6.22	-2.49	-2.71	-2.57	0.01	0.18	0.11	0.34	1.00	0.53	0.10	0.62	0.72
	Warm and dry	MPI-ESM-LR_r3i1p1	65.30	63.75	54.19	-3.33	-0.63	-1.37	0.33	1.00	1.00	0.45	0.23	0.28	0.78	0.32	1.10
		MIROC-ESM-CHEM_r1i1p1	170.16	-6.20	16.13	-4.57	-0.48	-1.88	0.87	0.10	0.30	0.62	0.18	0.39	0.42	0.39	0.81
	Cold and wet	NOAA_GFDL_GFDL-ESM2G_r1i1p1	37.35	40.91	34.19	-1.37	-0.47	-0.86	0.19	0.64	0.63	0.18	0.17	0.18	0.49	0.18	0.67
		NOAA_GFDL_GFDL-ESM2M_r1i1p1	80.54	44.31	40.49	-1.65	-0.26	-0.90	0.41	0.70	0.75	0.22	0.10	0.18	0.62	0.17	0.79
	Warm and wet	NOAA_GFDL_GFDL-CM3_r1i1p1	196.33	-11.85	0.66	-6.34	-1.51	-3.59	1.00	0.19	0.01	0.85	0.56	0.74	0.40	0.72	1.12
		CanESM2_r3i1p1	18.76	-15.76	-17.57	-4.42	-0.80	-2.72	0.10	0.25	0.32	0.60	0.30	0.56	0.22	0.48	0.70

Models/ensembles selected for the short-term future period (2016-2045) for climate change scenarios RCP4.5 and RCP8.5 are shown in Table 5.19. Table 5.19 shows that, for climate change scenario RCP4.5, climate models ACCESS1-3_r1i1p1, MPI-ESM-MR_r3i1p1, NOAA_GFDL_GFDL-ESM2G_r1i1p1 and CanESM2_r2i1p1 were selected at the cold and dry, warm and dry, cold and wet, and warm and wet corners respectively. Likewise, for climate change scenario RCP8.5, the models ACCESS1-3_r1i1p1, IPSL-CM5A-LR_r2i1p1, NOAA_GFDL_GFDL-ESM2M_r1i1p1 and CanESM2_r4i1p1 were selected at the cold and dry, warm and dry, cold and wet, and warm and wet corner respectively.

Table 5.19: Selected model/ensembles for the short-term future period (2016-2045) for climate change scenarios RCP4.5 and RCP8.5.

Projection	RCP4.5	RCP8.5
Cold and dry	ACCESS1-3_r1i1p1	ACCESS1-3_r1i1p1
Warm and dry	MPI-ESM-MR_r3i1p1	IPSL-CM5A-LR_r2i1p1
Cold and wet	NOAA_GFDL_GFDL-ESM2G_r1i1p1	NOAA_GFDL_GFDL-ESM2M_r1i1p1
Warm and wet	CanESM2_r2i1p1	CanESM2_r4i1p1

Similarly, models/ensembles selected for the mid-century future period (2036-2065) for climate change scenarios RCP4.5 and RCP8.5 are shown in Table 5.20.

Table 5.20: Selected models/ensembles for the mid-century future period (2036-2065) for climate change scenarios RCP4.5 and RCP8.5.

Projection	RCP4.5	RCP8.5
Cold and dry	EC-EARTH_r12i1p1	ACCESS1-3_r1i1p1
Warm and dry	MIROC5_r2i1p1	MIROC-ESM-CHEM_r1i1p1
Cold and wet	CCSM4_r2i1p1	NOAA_GFDL_GFDL-ESM2G_r1i1p1
Warm and wet	CanESM2_r2i1p1	CanESM2_r1i1p1

Table 5.20 shows that, for climate change scenario RCP4.5, the models EC-EARTH_r12i1p1, MIROC5_r2i1p1, CCSM4_r2i1p1 and CanESM2_r2i1p1 were selected at the cold and dry, warm and dry, cold and wet, and warm and wet corners respectively. Likewise, for climate change scenario RCP8.5, the ACCESS1-3_r1i1p1, MIROC-ESM-CHEM_r1i1p1, NOAA_GFDL_GFDL-ESM2G_r1i1p1 and CanESM2_r1i1p1 global climate models were

selected at the cold and dry, warm and dry, cold and wet, and warm and wet corners respectively.

The models/ensembles selected for the end-of-century future period (2071-2100) for climate change scenarios RCP4.5 and RCP8.5 are shown in Table 5.21.

Table 5.21: Selected models/ensembles for the end-of-century future period (2071-2100) for climate change scenarios RCP4.5 and RCP8.5

Projection	RCP4.5	RCP8.5
Cold and dry	EC-EARTH_r2i1p1	EC-EARTH_r9i1p1
Warm and dry	CSIRO-Mk3-6-0_r1i1p1	MIROC-ESM-CHEM_r1i1p1
Cold and wet	CCSM4_r2i1p1	NOAA_GFDL_GFDL-ESM2G_r1i1p1
Warm and wet	CanESM2_r3i1p1	CanESM2_r3i1p1

Table 5.21 shows that, for climate change scenario RCP4.5, the models EC-EARTH_r2i1p1, CSIRO-Mk3-6-0_r1i1p1, CCSM4_r2i1p1 and CanESM2_r3i1p1 were selected at the cold and dry, warm and dry, cold and wet, and warm and wet corners respectively. Likewise, for RCP8.5, the EC-EARTH_r2i1p1, MIROC-ESM-CHEM_r1i1p1, NOAA_GFDL_GFDL-ESM2G_r1i1p1 and CanESM2_r3i1p1 global climate models were selected at the cold and dry, warm and dry, cold and wet, and warm and wet corners respectively.

5.1.5 Results and discussion

Step 1: Initial model selection based on changes in mean air temperature and annual precipitation

The initial selection was made based on the projected changes in mean air temperature and total annual precipitation between the short-term (2016-2045), mid-century (2036-2065) and end-of-century (2071-2100) future periods; and the reference period (1981-2010).

The ΔT and ΔP ranges from 0.5°C to 2.4°C and -6.9% to +18.1% respectively, considering the short-term period (2016-2045) for climate change scenario RCP4.5, whereas for climate change scenario RCP8.5, these ranges are 0.6°C to 2.2°C and -8.5% to +21.3% (Figures 5.4 and 5.5). The ΔT and ΔP ranges from 0.97°C to 3.29°C and -7.63% to +3.29% respectively, considering the mid-century period (2036-2065) for climate change scenario RCP4.5, whereas for climate change scenario RCP8.5, these ranges are 1.59°C to 4.01°C and -11.51% to +23.98% (Figures 5.6 and 5.7). Likewise, the ΔT and ΔP ranges from 1.3°C to 4.6°C and -

9.1% to +31.4% respectively, considering the end-of-century period (2071-2100) for climate change scenario RCP4.5, whereas for climate change scenario RCP8.5, these ranges are 3.3°C to 7.0°C and -11.0% to +63.0% (Figures 5.8 and 5.9).

The proximity of the selected models/ensembles (marked with colour in Figures 5.4 to 5.9) to their respective corners differs substantially, as most of the model outputs are not available at daily time-steps. The models/ensembles which are close to their respective corners and have outputs at daily time-steps were selected (Tables 5.6 to 5.8).

Step 2: Refined model selection based on projected changes in four indices for climatic extremes

For the models chosen from the initial selection (Figure 5.3- Step 1), the projected changes in four ETCCDI indices between the short-term (2016-2045), mid-century (2036-2065) and end-of-century (2071-2100) future periods and the reference period (1981-2010) were calculated. In general, models projecting large changes in means (ΔT and ΔP) also project large changes in extreme indices. The model CanESM2_r2i1p1 (Table 5.10) projected the largest changes in ΔT (1.7°C) and ΔP (15.6%) in the warm and wet corner for the short-term (2016-2045) period, and also projected the largest increase in WSDI (194.4%) and R95pTOT (42.9%). The models were selected based on the highest combined scores (Tables 5.10 to 5.15).

Step 3: Final model selection based on model capability in simulating the annual cycle of air temperature and precipitation (past performance)

The final selection of models/ensembles was carried out based on the validation of model performance to the Hi-AWARE reference climate dataset. The models were selected based on the lowest combined bias score (sum of precipitation bias score and temperature bias score) as shown in Tables 5.16 to 5.18. This method of calculating a combined bias score can lead to models with the least P bias score not being selected due to a high T bias score. For example, in the cold and dry corner, climate change scenario RCP4.5, in Table 5.16, the model inmcm4_r1i1p1 is not selected although it has the least P bias score (0.32), as it has a high T bias score (1.0), resulting in a combined bias score of 1.32. In contrast, its counterpart model, ACCESS1-3_r1i1p1, has a combined bias score of 0.75, with a P bias score and a T bias score of 0.54 and 0.2 respectively. The model ACCESS1-3_r1i1p1 was selected as it has the least combined score in the cold and dry corner.

The representative global climate models selected for the Koshi River basin for climate change scenarios RCP4.5 and RCP8.5 considering the short-term (2016-2045), mid-century (2036-2065) and end-of-century (2071-2100) future periods are shown in Tables 5.19, 5.20 and 5.21 respectively.

For the short-term (2016-2045) future period, the model/ensemble ACCESS1-3_r1i1p1 is selected in the cold and dry corner (Table 5.19). Likewise, the same model/ensemble CanESM2_r1i1p1 is selected for both climate change scenarios RCP4.5 and RCP8.5 for the mid-century (2036-2065) study period. Similarly, the model/ensemble CanESM2_r3i1p1 is selected for both climate change scenarios RCP4.5 and RCP8.5 for the end-of-century (2071-2100) future period. For the remaining corners and RCPs, different models/ensembles were selected. Although the GCM selection was carried out for the same Koshi River basin, different GCMs are selected for the short-term (2016-2045), long term (2035-2065) and end-of-century (2071-2100) periods for future climate change scenarios RCP4.5 and RCP8.5. This indicates that GCM selection for a catchment varies with different future climate change scenarios (RCP4.5 and RCP8.5), as well as different future analysis periods. Therefore, representative GCM selection should be given a high priority when conducting climate change impact studies.

5.2 Climate data downscaling for the Koshi River basin

5.2.1 Downscaling methods

As the GCM outputs are at a coarser resolution, they are used to generate climate data at a finer scale to represent local climatic conditions. Conceptualisation of downscaling and aggregation between atmospheric and hydrologic models is shown in Figure 5.14. The process used to reduce the scale of any information finer than 100 km x 100 km scales (spatially) and finer than monthly values (temporally) is called downscaling. It assumes that the local climate is a combination of local conditions (land surface, topography and water bodies) and large-scale atmospheric features (regional, continental, hemispheric and global) (Trzaska and Schnarr, 2014). Downscaling methods have been developed to generate climate variables at a finer resolution using the GCM outputs at a coarse resolution (Chen et al., 2010c).

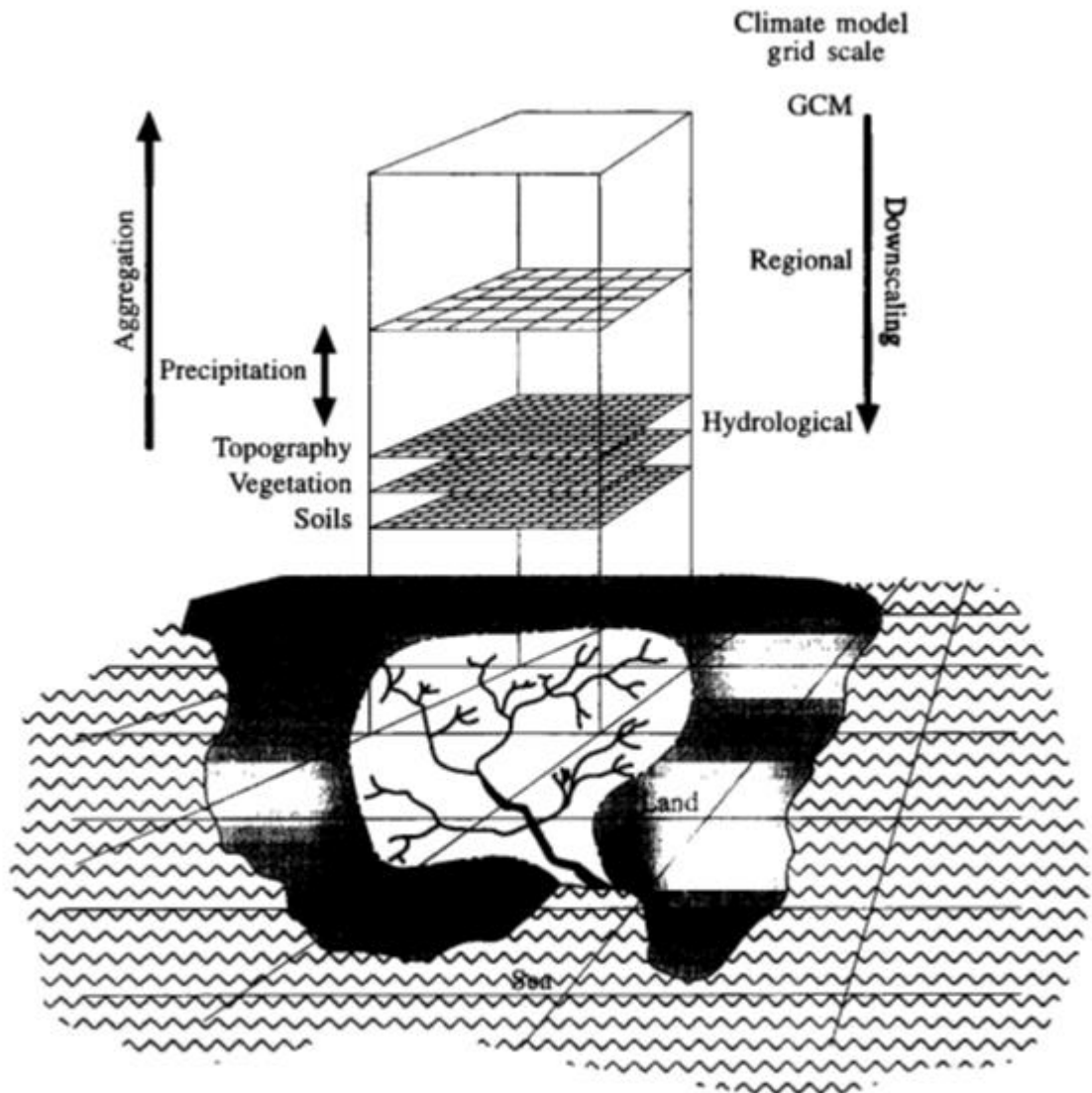


Figure 5.14: Conceptualisation of downscaling and aggregation between atmospheric and hydrologic models (adapted from Wilby and Wigley, 1997).

Basically, downscaling techniques are classified into two types: statistical and dynamic downscaling. Statistical downscaling techniques develop a statistical relationship between local climate variables and large-scale GCM outputs, and dynamic downscaling techniques use high-resolution Regional Climate Models (RCMs) nested in a GCM to generate local weather variables (Chen et al., 2010c). The RCMs use GCM outputs as lateral boundaries and represent physical processes at a spatial resolution of about 20 - 50 square km to generate regional climate variables (Trzaska and Schnarr, 2014). Dynamic downscaling is computationally expensive and is not always a feasible option for downscaling to the local scales with the required spatial resolution (Ahmed et al., 2013). Dynamic downscaling requires huge data sets, making it computationally intensive and time consuming. Dynamic

downscaling is recommended for projects having research periods of more than two years (Trzaska and Schnarr, 2014). Furthermore, RCM outputs are generally not free from biases, so bias correction of RCM outputs is normally required in climate change impact studies (Chen et al., 2013, Chen et al., 1999, Themeßl et al., 2011, Wood et al., 2004). In contrast, statistical downscaling methods are easy not only to apply but also to interpret, and the spatial resolution is also finer than that of an RCM (Trzaska and Schnarr, 2014). Statistical downscaling has been commonly used in climate change impact studies because it is computationally efficient, and can be appropriately used for spatial downscaling and the bias correction of GCM outputs (Ahmed et al., 2013). Thus, a statistical downscaling approach has been adopted for this research.

5.2.2 Quantile mapping approach for climate data downscaling

The common approaches for bias correction in statistical downscaling are delta change, multiple linear regression, analogue, local intensity scaling and quantile mapping. Delta change is the simplest and most common method used to address the biases between the observed historical and GCM output data, which adds the difference of the climatological means (e.g. monthly, seasonal, or seasonal) between the future study and the observed baseline of the climate variable (Boé et al., 2007, Themeßl et al., 2012). However, because the delta change method only considers differences in the mean, it fails to consider temporal variability (Themeßl et al., 2012). Themeßl et al. (2011) compared the performance of seven empirical-statistical downscaling and error-correction methods (multiple linear regression, multiple linear regression with cube root transformation, multiple linear regression with randomization, analogue, nearest neighbour analogue, local intensity scaling and quantile mapping) and concluded that quantile mapping outperforms all other methods.

Quantile mapping is classified as distribution-based (calibrated on climatological distributions) and parameter-free, as it uses empirical cumulative density functions (ecdfs). The empirical cumulative distribution function of a parameter is a non-parametric estimator of the underlying cumulative distribution function. Basically, an ecdf sorts all the data (n , number of data) in ascending order and assigns a probability of $1/n$ to each datum. Quantile mapping originated from the empirical transformation of Panofsky and Brier (1968), and has been successfully applied in hydrological applications (Boé et al., 2007, Themeßl et al., 2011). Quantile mapping compares the distributions (empirical cumulative distribution function) of a climate variable in historical observations and GCMs outputs, and defines the correction function depending upon the quantile, which is used to correct the variable data

sets of GCM outputs based on the respective quantile (Boé et al., 2007, Themeßl et al., 2012, Themeßl et al., 2011). As mentioned in Themeßl et al. (2012), it is applied on a daily basis (t) and for each grid cell (i) separately resulting in a corrected time series $Y_{t,i}^{cor}$ (Eq. 5.2) using the correction function $CF_{t,i}$ (Eq. 5.3).

$$Y_{t,i}^{cor} = X_{t,i}^{GCM} + CF_{t,i} \quad 5.2$$

$$CF_{t,i} = ecdf_{month,i}^{obs,ref^{-1}}(P_{t,i}) - ecdf_{month,i}^{GCM,ref^{-1}}(P_{t,i}) \quad 5.3$$

$$P_{t,i} = ecdf_{month,i}^{GCM,ref}(X_{t,i}^{GCM}) \quad 5.4$$

where, $Y_{t,i}^{cor}$ is a corrected time series on a daily basis (t) within the study period and for each grid cell (i) over the study area, $X_{t,i}^{GCM}$ is the GCM time series on a daily basis (t) within the study period and for each grid cell (i) over the study area, $CF_{t,i}$ is a correction function on a daily basis (t) within the study period and for each grid cell (i) over the study area. Likewise, $ecdf_{month,i}^{obs,ref^{-1}}(P_{t,i})$ is the observed inverse ecdf ($ecdf^{-1}$) for the particular day of the year in the reference period at probability P ($P_{t,i}$), $ecdf_{month,i}^{GCM,ref^{-1}}(P_{t,i})$ is the GCM inverse ecdf ($ecdf^{-1}$) for the particular day of the year in the reference period at probability P ($P_{t,i}$) and $ecdf_{month,i}^{GCM,ref}(X_{t,i}^{GCM})$ is the GCM ecdf for the particular day of the year in the reference period for each grid cell (i) over the study area.

The correction function represents the difference between observed (obs) and the GCM inverse ecdf ($ecdf^{-1}$) for the particular day of the year in the reference period at probability P ($P_{t,i}$). P is obtained by relating the GCM data (X^{GCM}) to the corresponding ecdf in the reference period. This results in a corrected time series Y^{cor} to create the bias corrected dataset.

This basic quantile mapping procedure may result in a methodological problem when the dry-day frequency in the GCM data ($ecdf^{GCM,ref}$) is greater than in the observations ($ecdf^{obs,ref}$) (Themeßl et al., 2012). This results in a systematic wet precipitation bias as any dry day in X^{GCM} is mapped to a precipitation day in the observed dataset. So, frequency adaptation (FA) is applied to extend the basic QM procedure, in order to account for this methodological problem (Themeßl et al., 2012). With FA, only the fraction (ΔP_o) (Eq. 5-5) of such dry-day cases with probability P_o are corrected randomly by linearly interpolating between zero

precipitation and the precipitation amount of $ecdf_{month,i}^{obs,ref-1}(ecdf_{month,i}^{GCM,ref}(0))$ (the first precipitation class in QM without FA). It will reduce the wet bias in the GCM dataset.

$$\Delta P_0 = \frac{ecdf_{month,i}^{GCM,ref}(0) - ecdf_{month,i}^{obs,ref}(0)}{ecdf_{month,i}^{GCM,ref}(0)} \quad 5.5$$

In climate change impact studies, precipitation and temperature values in future may exceed the greatest value found in the reference period. For values of extremes that are outside the range of the reference period, corrections are made by including constant linear extrapolation of the correction value (i.e. the difference between $ecdf^{obs,ref}$ and $ecdf^{GCM,ref}$ at the highest and lowest quantiles) (Boé et al., 2007, Themeßl et al., 2012). In such cases, the future corrected values would be calculated applying Eq. 5.6.

$$P_{fut,cor} = \max(P_{obs}) * \frac{P_{fut,GCM}}{\max(P_{fut,GCM})} \quad 5.6$$

5.2.3 Application of quantile mapping downscaling

A quantile mapping downscaling approach is applied for the selected GCM outputs as mentioned in Tables 5.19, 5.20 and 5.21.

Quantile mapping with frequency adaptation and extreme value extrapolation, as mentioned in Section 5.2.2, was applied for the selected GCM outputs. Daily precipitation, average temperature, maximum temperature and minimum temperature GCM data are downscaled for each grid (grid size= 10 km x 10 km) for the entire Koshi River basin down to Chatara in Nepal.

5.2.4 Results and discussion

GCM data were downscaled for each of the selected GCMs at different time periods and climatic extreme corners. For exemplar purposes, the daily precipitation and temperature data for the years 2010, 2045, 2065 and 2100 (the ending years of the reference period, short-term, mid-century and end-of-century periods) for the selected model CanESM2_r3i1p1, which represents the warm and wet corner for climate change scenario RCP8.5 and the end-of-century period, are shown in Figures 5.15 and 5.16.

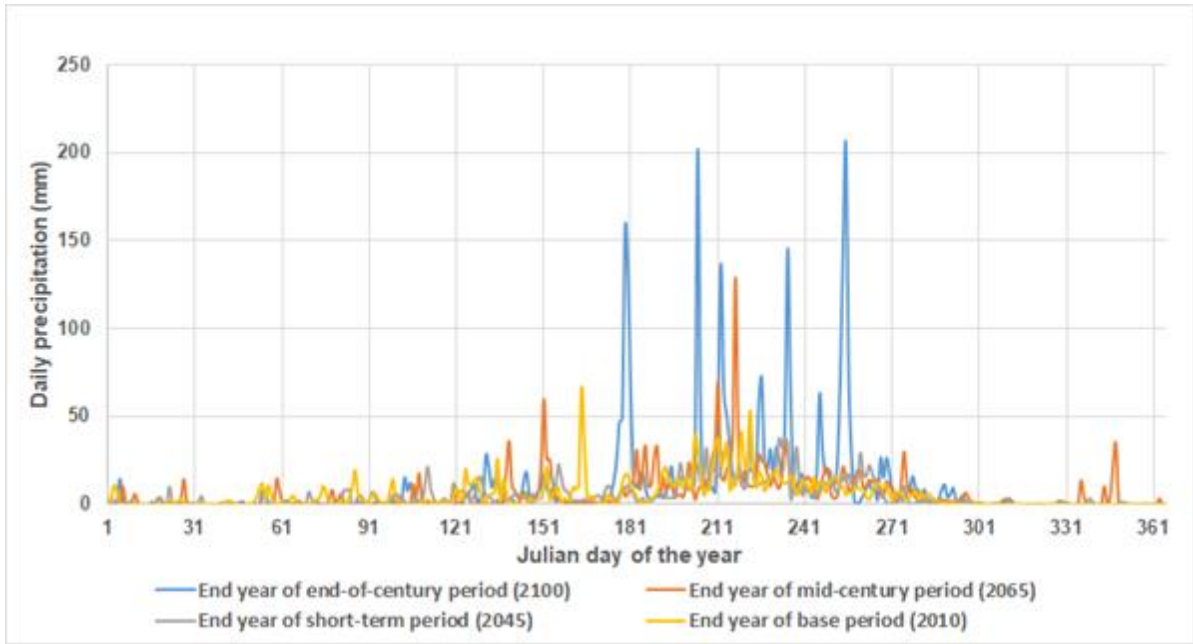


Figure 5.15: Daily precipitation data for the years 2010, 2045, 2065 and 2100 for the model CanESM2_r3i1p1_RCP8.5.

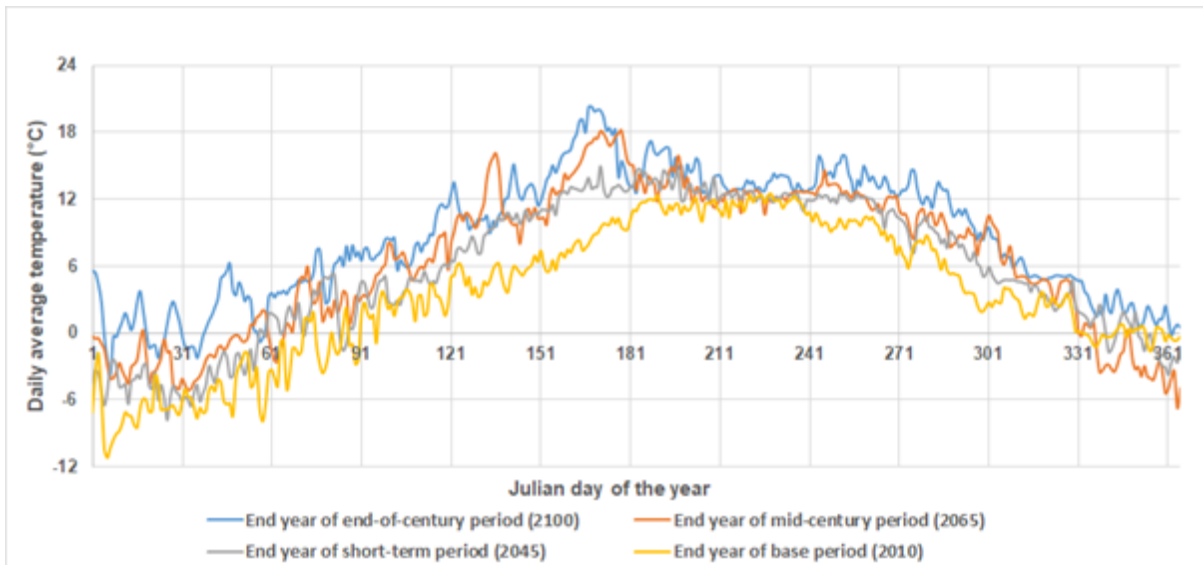


Figure 5.16: Daily average temperature of the years 2010, 2045, 2065 and 2100 for the model CanESM2_r3i1p1_RCP8.5.

Precipitation

The absolute and percentage changes in average annual, winter, pre-monsoon, monsoon and post-monsoon precipitation in the short-term, mid-century and end-of-century periods compared to the reference precipitation datasets are shown in Table 5.22. The winter, pre-monsoon, monsoon, and post-monsoon seasons refer to December-February, March-May, June-September, and October-November respectively.

Table 5.22: Uncertainty in absolute and percentages changes in average precipitation in the Koshi River basin compared to base period.

Annual / seasonal precipitation	Short-term				Mid-century				End-of-century			
	RCP4.5		RCP8.5		RCP4.5		RCP8.5		RCP4.5		RCP8.5	
	Absolute (mm)	Relative (%)	Absolute (mm)	Relative (%)	Absolute (mm)	Relative (%)						
Annual	4 to 288	0 to 16	103 to 365	6 to 20	70 to 417	4 to 23	107 to 663	6 to 36	79 to 441	4 to 24	242 to 890	13 to 49
Winter	-30 to 12	-53 to 21	-24 to -6	-42 to -10	-18 to 8	-32 to 13	-32 to 4	-55 to 6	-14 to -1	-24 to -2	5 to 10	9 to 18
Pre-monsoon	-71 to -4	-26 to -1	-89 to -23	-32 to -8	-109 to 42	-39 to 15	-116 to 10	-42 to 4	-156 to -8	-56 to -3	-149 to 36	-54 to 12
Monsoon	-70 to 257	-5 to 18	83 to 331	6 to 24	-8 to 381	-1 to 27	159 to 574	12 to 41	34 to 448	3 to 32	282 to 788	21 to 56
Post-monsoon	42 to 132	48 to 152	28 to 147	32 to 169	28 to 163	33 to 187	36 to 237	41 to 272	27 to 151	31 to 173	77 to 217	88 to 249
Regional annual precipitation												
Tibet	-9 to 180	-0.5 to 10	71 to 168	4 to 9	86 to 367	5 to 21	122 to 366	7 to 21	167 to 431	7 to 24	253 to 766	14 to 43
High Himalaya	-31 to 312	-1 to 12	107 to 450	4 to 18	37 to 534	1 to 21	110 to 852	4 to 33	57 to 485	2 to 19	290 to 1189	11 to 46
Lower Himalaya	-15 to 504	-0.7 to 25	71 to 625	4 to 31	42 to 476	2 to 24	54 to 1077	3 to 54	-35 to 447	-2 to 22	198 to 992	10 to 50

Average annual precipitation is expected to increase in the future. Modelling based on the climate change scenario RCP4.5 suggests increases of 0 to 16% in the short-term, 4 to 23% by mid-century and 4-24% at the end-of-century periods. Higher precipitation is expected under climate change scenario RCP8.5 with average annual precipitation projected to increase by 6 to 20% in the short-term, 6 to 36% by mid-century and 13 to 49% at the end-of-century periods. Winter precipitation is expected to decrease for all the scenarios and study periods, except for the end-of-century period under climate change scenario RCP8.5. While pre-monsoon precipitation is expected to decrease in coming decades, monsoonal precipitation is expected to increase in all scenarios and study periods. Similarly, post-monsoon precipitation is also expected to increase in future. Decreased winter and pre-monsoon precipitation, combined with increased monsoon, post-monsoon precipitation and annual precipitation indicate that more dry winters and wetter monsoon seasons are expected in the future.

Table 5.22 shows large uncertainty in terms of future precipitation. For the short-term period, three of the four GCMs have predicted a decrease in precipitation during winter (-53 to -9%). However, one GCM has predicted an increase in precipitation by 21% for climate change scenario RCP4.5 scenario. In contrast, only one GCM out of four has predicted a decrease in monsoon precipitation (-5%), while the three GCMs remaining have predicted an increase in precipitation (13 to 18%).

For the mid-century period, three of the four GCMs have predicted decrease in precipitation during winter (-32 to -9%) and pre-monsoon (-39 to -9%). However, one GCM has predicted increases of 13% and 15% for winter and the pre-monsoon season respectively under climate change scenario RCP4.5. In contrast, only one GCM out of four has predicted a decrease in precipitation during the monsoon season (-1%), while the remaining GCMs have predicted increases of between 13 and 27%. For the RCP8.5 climate change scenario, three out of four GCMs have predicted decreases in precipitation during winter (-55 to -1%) and pre-monsoon (-42 to -2%). However, one GCM has predicted increases of 6% and 4% during winter and the pre-monsoon respectively.

For the end-of-century period, all the selected GCMs have predicted decreases in precipitation in winter and the pre-monsoon season under the RCP4.5 climate change scenario. For climate change scenario RCP8.5, three out of four GCMs have predicted decreases (-54 to -8%) in precipitation during pre-monsoon; however, one GCM has predicted an increase of 12%. The uncertainty in the post-monsoon period is large in all three

study periods under both climate change scenarios RCP4.5 and RCP8.5. Although the percentage increase in precipitation in post-monsoon is high compared with the monsoon season, the absolute increase in post-monsoon season is less compared to the monsoon season. The rainfall quantity in post-monsoon season is less in the reference period and a small increase in the precipitation amount in the post-monsoon season results in higher percentage increase compared to monsoon season.

Precipitation patterns in the Tibet region, including the High Himalaya in Nepal with elevation >3000 m, and the Lower Himalaya in Nepal with elevation <3000 m (see Figure 2.1) were also analysed, and are summarised in Table 5.22.

Table 5.22 also shows that higher uncertainty in precipitation, with figures -0.7 to 25% considering RCP4.5 and 4 to 31% considering climate change scenario RCP8.5 being expected in the Lower Himalaya region during the short-term period. Likewise, higher uncertainty in precipitation is expected in the Lower Himalaya region during the mid-century period, 2 to 24% and 3 to 54% under climate change scenarios RCP4.5 and RCP8.5 respectively. Similarly, higher uncertainty in precipitation is predicted in the Lower Himalaya regions during the end-of-century period, being -2 to 22% and 10 to 50% under climate change scenarios RCP4.5 and RCP8.5 respectively. The ensemble mean (average of 4 GCMs) of absolute and percentage changes in average precipitation compared to the reference period in the Koshi River basin is shown in Table 5.23. Table 5.23 shows that higher increase in precipitation are expected in the High Himalaya region compared to Tibet and the Lower Himalaya regions.

Table 5.23: Ensemble mean (4 GCMs) of absolute and percentages changes in average precipitation in the Koshi River basin compared to base period.

Annual / seasonal precipitation	Short-term				Mid-century				End-of-century			
	RCP4.5		RCP8.5		RCP4.5		RCP8.5		RCP4.5		RCP8.5	
	Absolute (mm)	Relative (%)	Absolute (mm)	Relative (%)	Absolute (mm)	Relative (%)						
Annual	178	10	196	11	237	13	335	18	297	16	701	39
Winter	-8	-14	-14	-25	-7	-12	-8	-14	-5	-9	7	13
Pre-monsoon	-44	-16	-45	-16	-34	-12	-55	-20	-54	-19	-64	-23
Monsoon	142	10	187	13	206	15	294	21	276	20	619	44
Post-monsoon	88	101	69	79	71	82	105	120	80	92	139	160
Regional annual precipitation												
Tibet	114	6	124	7	206	12	249	14	223	13	631	36
High Himalaya	199	8	229	9	291	11	419	16	391	16	922	36
Lower Himalaya	231	12	270	14	252	13	431	22	226	11	770	39

The ensemble mean of monthly precipitation for the end-of-century period is shown in Figure 5.17. The ensemble mean for the reference period for both climate change scenarios RCP4.5 and RCP8.5 is close to reference data, which shows that the accuracy of downscaling for the reference period is satisfactory. The spatial pattern of absolute change in ensemble mean precipitation compared to reference data during the end-of-century period is shown in Figure 5.18. Figures 5.18 (a) and 5.18 (b) show the ensemble mean of absolute change in precipitation during the end-of-century period considering climate change scenarios RCP4.5 and RCP8.5 scenarios respectively. Higher increase in precipitation is expected in the High Himalaya region compared to Tibet and the Lower Himalaya region at the end-of-century period.

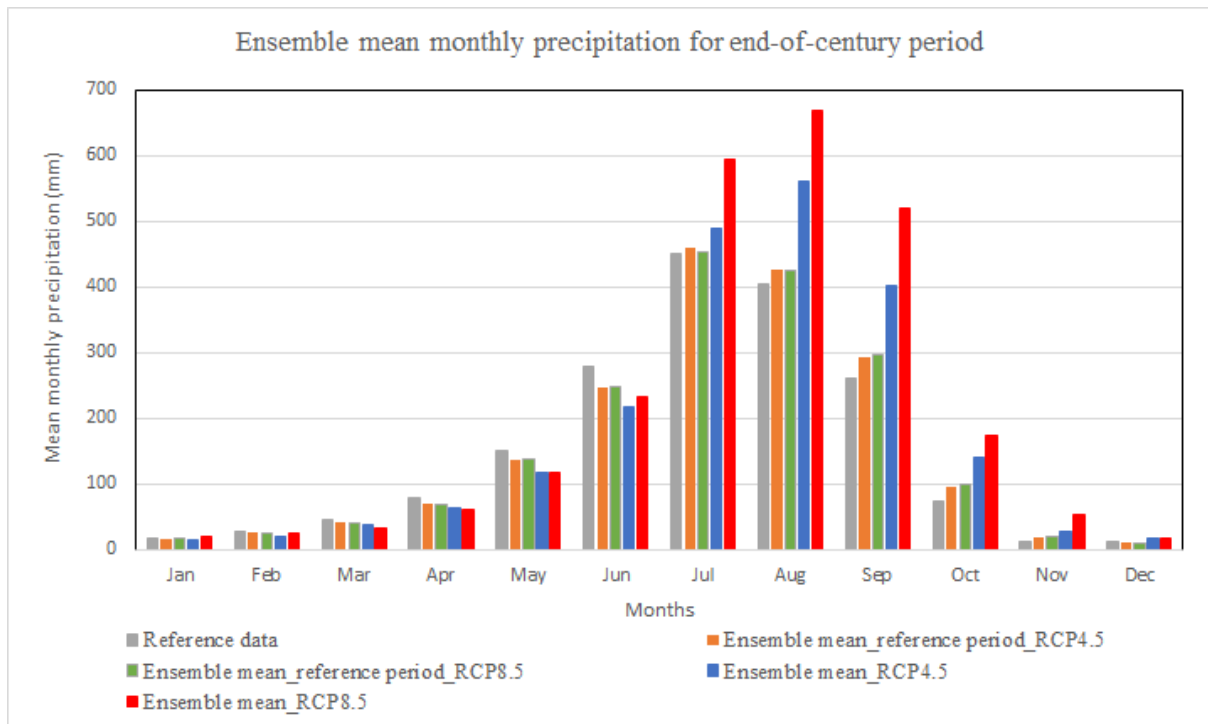


Figure 5.17: Ensemble mean monthly precipitation for end-of-century period.

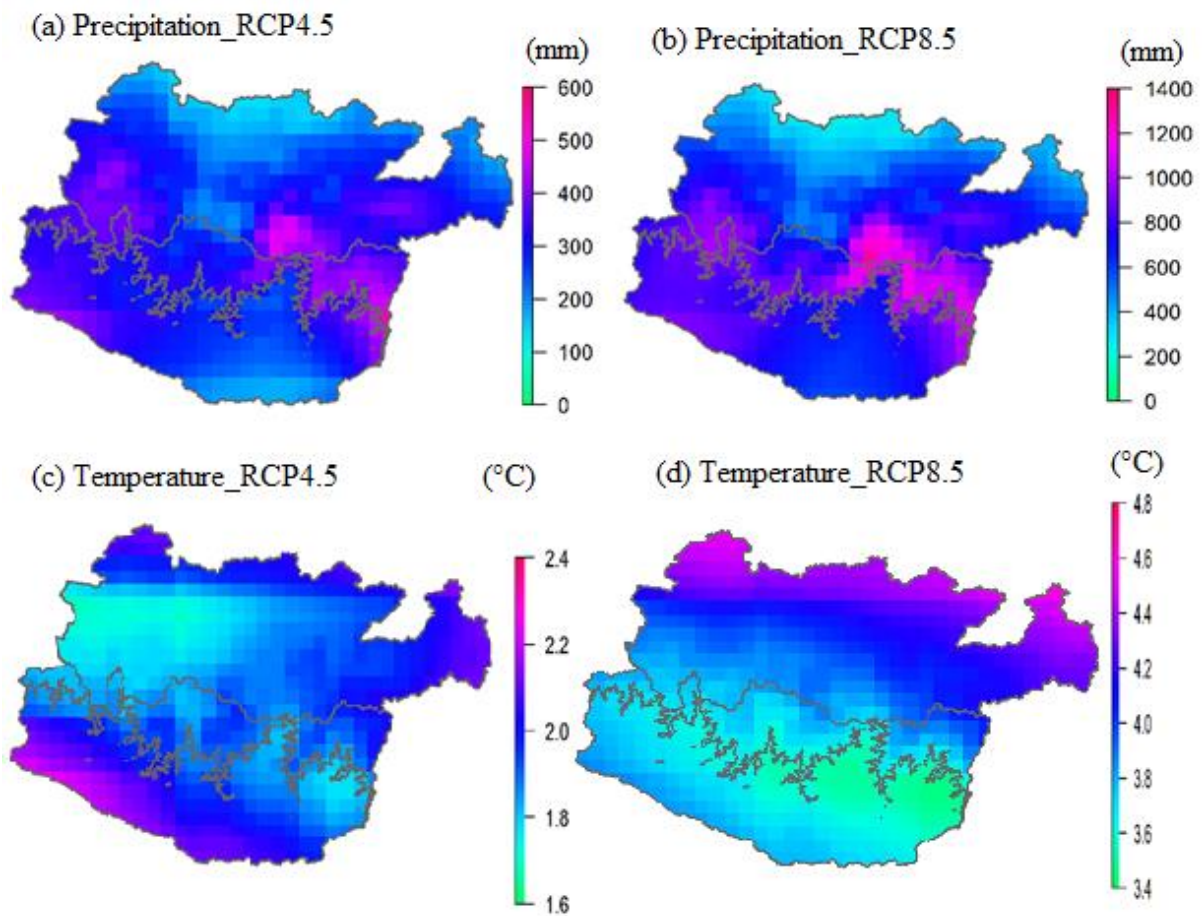


Figure 5.18: Ensemble mean of absolute change in average precipitation and temperature during the end-of-century period compared to reference period.

Present and future average annual precipitation values along with their standard deviation for four GCMs selected for climate change scenarios RCP4.5 and RCP8.5 considering the end-of-century period, are shown in Figure 5.19(a). Temperature values are shown at Figure 5.19(b). In both parts of Figure 5.19, the blue and red lines represent the corresponding average values of four GCMs selected for climate change scenarios RCP4.5 and RCP8.5 respectively. The black line represents the average values of the reference data. The sky blue and pink areas represent the standard deviation for the four GCMs selected for climate change scenarios RCP4.5 and RCP8.5 respectively. The average annual precipitation in the reference period is 1817mm. The average annual precipitation values in the short-term, mid-century and end-of-century periods are 2011mm, 2060mm and 2114 mm respectively for the climate change scenario RCP4.5 and 2018mm, 2098mm and 2518mm respectively for the climate change scenario RCP8.5.

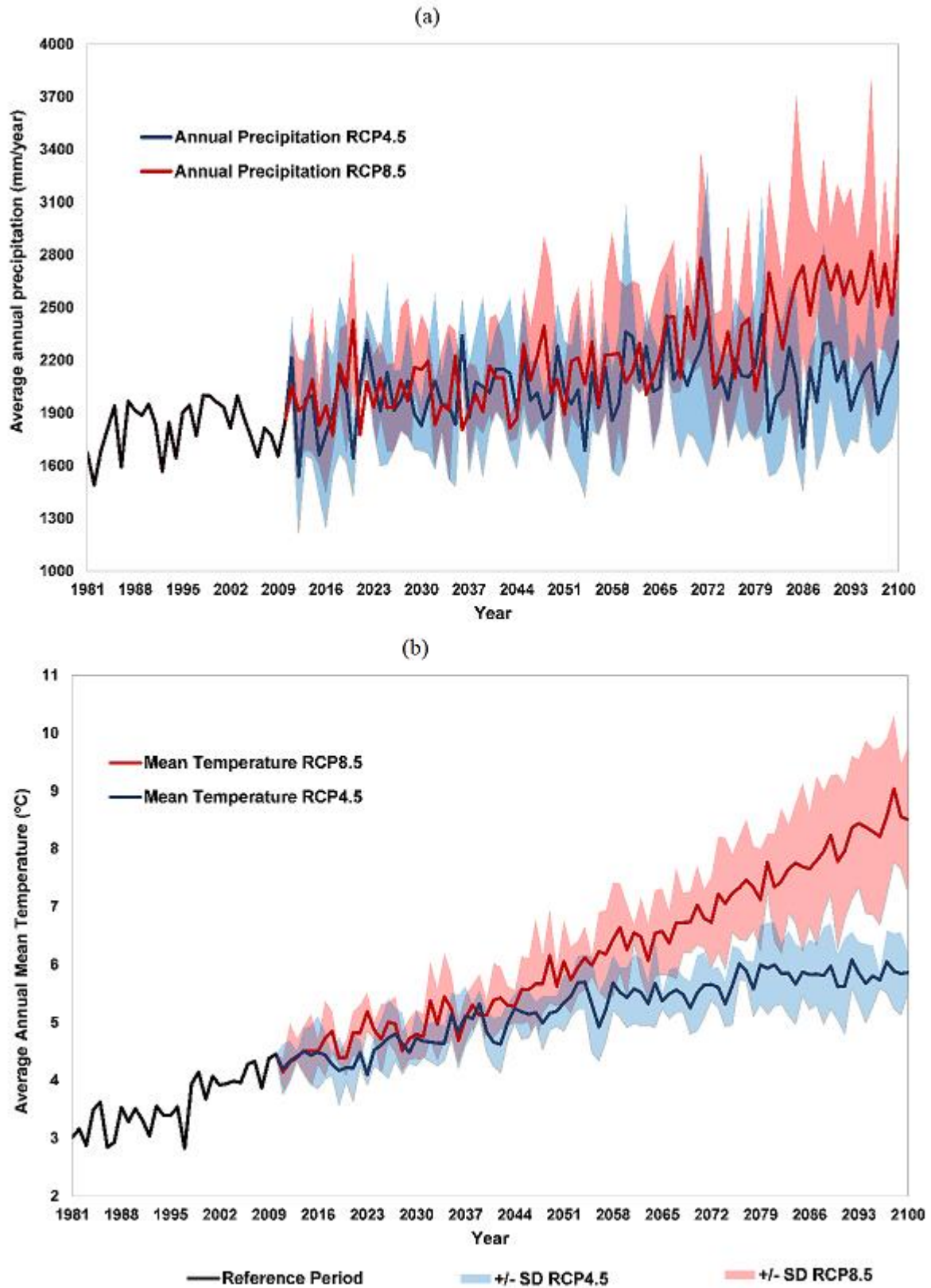


Figure 5.19: Present and future average annual precipitation and temperature along with their standard deviation for the Koshi River basin.

Temperature

The uncertainty in average increases in annual, winter and monsoon temperature in the short-term, mid-century and end-of-century periods as compared to the reference average temperature datasets, is shown in Table 5-24.

Table 5.24: Uncertainty in absolute changes in average temperature in the Koshi River basin compared to base period.

Annual / seasonal mean temperature	Short-term (°C increase)		Mid-century (°C increase)		End-of-century (°C increase)	
	RCP4.5	RCP8.5	RCP4.5	RCP8.5	RCP4.5	RCP8.5
Annual	1.0 to 1.4	1.0 to 1.6	1.3 to 1.9	1.8 to 2.9	1.6 to 2.8	3.1 to 5.6
Winter	0.9 to 1.7	1.1 to 1.6	1.3 to 2.1	1.8 to 3.9	1.7 to 2.9	2.9 to 7.8
Monsoon	0.7 to 1.3	0.8 to 1.4	1.3 to 1.9	1.8 to 2.9	1.4 to 2.8	3.0 to 4.4
Regional mean annual temperature						
Tibet	0.7 to 1.4	0.8 to 1.8	0.9 to 1.9	1.7 to 2.8	1.2 to 2.5	3.2 to 5.6
High Himalaya	0.7 to 1.1	0.8 to 1.3	1 to 1.5	1.4 to 2.5	1.3 to 2.5	2.7 to 5.1
Lower Himalaya	0.6 to 1.0	0.8 to 1.4	1.2 to 1.4	1.4 to 2.4	1.5 to 2.6	2.5 to 5.0

The results show that there is a strong seasonal variability for temperature changes in the Koshi River basin. Average annual temperature is expected to increase in the future (1 to 1.4°C in the short-term, 1.3 to 1.9°C by mid-century and 1.6 to 2.8°C in the end-of-century periods, considering the RCP4.5 climate change scenario). Higher increases in temperature are expected under climate change scenario RCP8.5 as compared to the RCP4.5 scenario. Under climate change scenario RCP8.5, the average annual temperature is expected to increase in future by 1 to 1.6°C in the short-term, 1.8 to 2.9°C by mid-century and 3.1 to 5.6°C in the end-of-century period. The incremental increases in winter temperature vary from 0.9 to 1.7°C, 1.3 to 2.1°C and 1.7 to 2.9°C for the short-term, mid-century and end-of-century periods considering the RCP4.5 climate change scenario. However, such incremental increases in monsoon temperature vary

from 0.7 to 1.3°C, 1.3 to 1.9°C and 1.4 to 2.8°C for the short-term, mid-century and end-of-century periods considering the climate change scenario RCP4.5. Table 5.24 shows large uncertainty in terms of future mean temperature. Uncertainty in annual mean temperature is higher under the climate change scenario RCP8.5 compared to RCP4.5 scenario in all study periods. The results show that the uncertainty increases approaching the end-of-century period. For example, the predicted increase in annual mean temperature in the short-term, mid-century and end-of-century periods varies between 1.0 to 1.4°C, 1.3 to 1.9°C, and 1.6 to 2.8°C for climate change scenario RCP4.5, and 1.0 to 1.6°C, 1.8 to 2.9°C, and 3.1 to 5.6°C for climate change scenario RCP8.5 respectively. All the GCMs have predicted increases in annual mean temperatures in future. Uncertainty about winter mean temperatures is large compared to monsoon temperatures.

The ensemble mean (average of 4 GCMs) of absolute and percentage changes in average temperature compared to the reference period in the Koshi River basin is shown in Table 5-25. Table 5-25 shows that higher increases in temperature are expected in the Tibet region compared to the High Himalaya and Lower Himalaya regions. Winter temperatures are expected to increase more than temperatures in the monsoon season for all study periods. The temperature patterns in the Tibet region, the High Himalaya in Nepal, and the Lower Himalaya in Nepal (see Figure 2-1) were also analysed and are summarised in Table 5-25. There is a high temperature variation between these regions. The average annual temperatures in the Tibet, High Himalaya and Lower Himalaya regions during the reference period were -3.7°C, -0.5°C and 14.4°C respectively.

Table 5.25: Ensemble mean (4 GCMs) of absolute changes in average temperature in the Koshi River basin compared to reference period.

Annual / seasonal mean temperature	Short-term (°C increase)		Mid-century (°C increase)		End-of-century (°C increase)	
	RCP4.5	RCP8.5	RCP4.5	RCP8.5	RCP4.5	RCP8.5
Annual	1.1	1.4	1.6	2.2	2.0	4.1
Winter	1.4	1.4	1.6	2.6	2.3	4.7
Monsoon	1	1.1	1.6	2.2	2.1	3.6
Regional mean annual temperature						
Tibet	1.2	1.6	1.7	2.3	1.9	4.3
High Himalaya	0.8	1.1	1.3	1.9	1.9	3.9
Lower Himalaya	0.8	1.1	1.3	1.8	2	3.6

Table 5.24 indicates that increases in temperature for each climate scenario are almost the same throughout the regions during the short-term, with increases in temperature from 0.6°C to 1.4°C and 0.8°C to 1.8°C considering the climate change scenarios RCP4.5 and RCP8.5 respectively. Average temperature is expected to increase up to 1.9°C considering RCP4.5 and up to 2.8°C considering climate change scenario RCP8.5 in Tibet in the mid-century period. However, in end-of-century period higher increases in temperature are expected in the Lower Himalaya region (1.5 to 2.6°C) considering the climate change scenario RCP4.5, and in the Tibet region (3.2 to 5.6°C) considering the RCP8.5 scenario. The ensemble mean (4 GCMs) of absolute changes in average temperatures compared to the reference period in the Koshi River basin is shown in Table 5-25. Higher increase in temperature is projected in the Tibet region compared to High Himalaya and Lower Himalaya regions.

The spatial pattern of absolute change in ensemble mean temperature compared to reference data during end-of-century period is shown in Figure 5.18. Figures 5.18 (a) and 5.18 (b) show the ensemble mean of absolute changes in temperatures during the end-of-century period considering climate change scenarios RCP4.5 and RCP8.5

respectively. Higher increases in temperature are expected in the Tibet region compared to the High Himalaya and Lower Himalaya regions at the end-of-century period.

Present and future average annual temperature values along with their standard deviation for four GCMs selected for the climate change scenarios RCP4.5 and RCP8.5 considering the end-of-century period is shown in Figure 5.19(b). The average annual temperature in reference period is 3.6°C. The average annual temperature values in the short-term, mid-century and end-of-century periods are 4.7°C, 5.2°C and 5.6°C respectively for climate change scenario RCP4.5 and 5.0°C, 5.8°C and 7.8°C respectively for climate change scenario RCP8.5.

5.3 Conclusion

The GCMs selection is a critical step for climate change impact studies in different sectors. The advanced envelope-based selection approach, which combines the past-performance approach and the envelope approach, is applied in this research to the selection of a representative global climate model for the transboundary Koshi River basin, down to Chatara in Nepal. Previous studies conducted on climate projections for the Koshi River basin are based on few GCMs and lack multiple criteria to select GCMs. This study addresses the limitations of the previous studies and provides new climatological insights for the region. A systematic approach for the selection of representative GCM runs from a large pool of climate models and downscaling of climate data for the river basin has been used. The precipitation and temperature data have been downscaled for the short-term (2016-2045), mid-century (2036-2065) and end-of-century (2071-2100) periods. The findings for short-term periods could be immediately used by the National Planning Commission, Nepal for the forthcoming Five-Year Periodic plan. The ensembles of 105 GCM outputs for RCP4.5 and 77 GCM outputs for RCP8.5 show that the uncertainty of future climate changes in the Koshi River basin is large. Based on these ensembles outputs, the change in future temperature and precipitation ranges have been estimated.

The main outcomes of this research are as follows:

- The GCM selection for a catchment varies with the future scenario chosen (climate change scenarios RCP4.5 or RCP8.5) as well as the future analysis periods (short-term, mid-century and end-of-century periods).

- The changes in temperature and precipitation range from 0.97 to 3.29°C and -7.63% to +3.29% respectively for the mid-century period under climate change scenario RCP4.5, whereas under climate change scenario RCP8.5, these ranges are 1.59 to 4.01°C and -11.51% to +23.98%.
- Similarly, the change in temperature and precipitation ranges from 1.3 to 4.6°C and -9.1% to +31.4% respectively for the end-of-century under climate change scenario RCP4.5, whereas, these ranges are 3.3 to 7.0°C and -11.0% to +63.0% under climate change scenario RCP8.5.

Downscaled data (10 km x 10 km grid) for the entire Koshi River basin were developed for each grid point. The downscaled data from the selected GCMs predict the following likely future climatic conditions:

- Uncertainty in the average increase in annual precipitation is large in the future: 0 to 16% in the short-term, 4 to 23% in mid-century and 4 to 24% in end-of-century period, considering the climate change scenario RCP4.5. Higher uncertainty in precipitation is expected in the climate change scenario RCP8.5 as compared to the RCP4.5 scenario. The uncertainty in average increases in annual precipitation is 6 to 20% in the short-term, 6 to 36% in mid-century and 13 to 49% in the end-of-century periods, considering the climate change scenario RCP8.5.
- However, winter precipitation is projected to decrease in future. The pre-monsoon precipitation is also expected to decrease in coming decades. Monsoon precipitation is expected to increase in all scenarios and study periods. Similarly, post-monsoon precipitation is also expected to increase in future.
- Based on the ensemble mean of average precipitation, higher absolute increases in precipitation are expected in the Lower Himalaya region in the short-term period (231 mm for climate change scenario RCP4.5 and 270 mm for climate change scenario RCP8.5) and in the High Himalaya region at mid-century (291 mm for climate change scenario RCP4.5 and 419 mm for climate change scenario RCP8.5) and end-of-century periods (391 mm for climate change scenario RCP4.5 and 922 mm for climate change scenario RCP8.5). Based on the ensemble mean of average temperatures, Tibet is more sensitive to climate change, with changes in temperature indicated for all scenarios and study

periods. Higher absolute increases in temperature are expected in Tibet region in the short-term (1.2°C for climate change scenario RCP4.5 and 1.6°C for climate change scenario RCP8.5), mid-century (1.7°C for climate change scenario RCP4.5 and 2.3°C for climate change scenario RCP8.5) and end-of-century periods (1.9°C for climate change scenario RCP4.5 and 4.3°C for climate change scenario RCP8.5) compared to the High Himalaya and Lower Himalaya regions.

- Uncertainty in average increases in annual temperature is large in the future (1 to 1.6°C in the short-term, 1.3 to 2.9°C in the mid-century and 1.6 to 5.6°C in the end-of-century periods).
- Increase in temperature during winter is expected to be higher than increases in the monsoon period.

Chapter 6: Hydrology of the river basin

This chapter describes the hydrological process simulated by the Soil and Water Assessment Tool (SWAT) hydrological model. This chapter then explains how future climate data has been used in conjunction with the SWAT model to project likely future water availability in the Koshi River basin in the short-term (2016-2045), mid-century (2036-2065) and end-of-century (2071-2100) time periods, under different climate change scenarios (RCP4.5 and RCP8.5). These projections of future water availability at the headwork of the Sunsari Morang Irrigation Scheme in the Koshi River basin were then used to estimate future flows into the irrigation canal.

6.1 Selection of Soil and Water Assessment Tool (SWAT) hydrological model

6.1.1 Selection of hydrological model

Hydrological models have been extensively used to assess the impact of climate change in hydrology. Of the many hydrological models available, only a few models such as the Agricultural Non-Point Source (AGNPS), the Hydrological Simulation Program-Fortran (HSPF), the Hydrological Engineering Centre – The Hydrologic Modelling System (HEC-HMS), MIKE SHE, and the Soil and Water Assessment Tool (SWAT) have been successfully verified in hydrological applications in many watersheds around the world (Khoi, 2016). Physically-based distributed hydrological models with input parameters which incorporate physical interpretation and explicit representation of spatial variability are being used to understand the effects of climate change on water resources, and on water resource planning and management (Cao et al., 2006). Physically-based hydrological models are derived deductively from established physical principles, as defined by appropriate assumptions and laws, and imply consistency with observations (Beven, 2002). Distributed hydrological models attempt to address the spatial distribution of topography, soil characteristics, land use, rainfall and evapotranspiration within the watershed. Physically based models are mathematically idealized representations of the real phenomenon (Devi et al., 2015).

SWAT (Arnold et al., 1998), a physically-based distributed model developed by the United States Department of Agriculture, is used in this research as it is freely available. It has been shown to be a robust watershed modelling tool, used to assess climate

change impacts on hydrology in many parts of the world (Gassman et al., 2007). Borah and Bera (2003) compared 11 different hydrological models and concluded that SWAT is a promising model for assessing long-term hydrological changes, as well as basin management. Khoi (2016) compared the HEC-HMS and SWAT models' abilities to produce streamflow in a catchment, and concluded that the SWAT model simulates hydrologic processes with a high degree of accuracy. In addition, the SWAT model has been successfully applied in the Asian Himalayan catchments (Bharati et al., 2016, Devkota and Gyawali, 2015, Agarwal et al., 2015, Gurung and Bharati, 2012, Manjan and Aggarwal, 2014, Thakuri and Salerno, 2016). Furthermore, SWAT provides good hydrologic projection, provided effort is spent on its calibration (Devi et al., 2015). An overview of major applications of the SWAT worldwide is reported by Gassman et al. (2007).

6.1.2 The SWAT model

The SWAT model is computationally efficient and capable of continuous long time period simulations which compute the effects of climate change impacts on the hydrological behaviours of a watershed. The SWAT model is also able to handle spatially and temporally distributed input data for estimating streamflow by considering various hydrological process (Arnold et al., 1998).

Water balance: The hydrologic cycle simulated by SWAT is based on the water balance Equation 6.1.

$$SW_t = SW_0 + \sum_{i=1}^t (R_{day} - Q_{surf} - E_a - w_{seep} - Q_{gw}) \quad \text{Equation 6.1}$$

where SW_t is the final soil water content (mm H₂O), SW_0 is the initial soil water content on day i (mm H₂O), t is the time (days), R_{day} is the amount of precipitation on day i (mm H₂O), Q_{surf} is the amount of surface runoff on day i (mm H₂O), E_a is the amount of evapotranspiration on day i (mm H₂O), w_{seep} is the amount of water entering the vadose zone from the soil profile (ie deep drainage) on day i (mm H₂O), and Q_{gw} is the amount of return flow on day i (mm H₂O).

The subdivision of the watershed into sub-basins enables the SWAT model to reflect differences in evapotranspiration for various soil and crop types. The sub-basins are

further divided into hydrologic response units (HRUs). The HRUs are used to describe spatial heterogeneity in terms of land cover, soil type and slope class within a watershed (Setegn et al., 2008). Runoff is estimated separately for each HRU, and routed to obtain the total runoff for the catchment. This increases accuracy and gives a much better physical description of the water balance (Neitsch et al., 2011).

Surface runoff: Surface runoff occurs when water flows over the soil surface due to impervious areas, locally saturated areas or from areas where the rainfall rate exceeds the infiltration capacity of soil (Brooks et al., 2013). Basically, surface runoff takes place when the rate of water application to the soil surface is higher than the rate of infiltration. The amount of surface runoff largely depends upon topographic factors such as slope, land use, soil, soil moisture, etc. The soil percolation component of SWAT uses a storage routing technique to estimate flow through each soil layer in the root zone. SWAT simulates the surface runoff at the HRU level and uses the Muskingum routing technique to project total runoff from the catchment (Neitsch et al., 2011).

The surface runoff from daily rainfall is projected by means of the modified curve number (CN) method of the United States Department of Agriculture – Soil Conservation Service (SCS), which estimates the amount of runoff based on local land use, soil type and the antecedent soil moisture conditions (Neitsch et al., 2011). The surface runoff is estimated using Equation 6.2.

$$Q_{surf} = \frac{(R_{day} - I_a)^2}{(R_{day} - I_a + S)} \quad 6.2$$

where Q_{surf} is the accumulated runoff or rainfall excess (mm H₂O), R_{day} is the rainfall depth for the day (mm H₂O), I_a is the initial abstraction which includes surface storage, interception and infiltration prior to runoff (mm H₂O), and S is the retention parameter (mm H₂O). The retention parameter varies spatially due to changes in soils, land use, management and slope, and varies temporally due to changes in soil water content. The retention parameter is defined in Equation 6.3:

$$S = 25.4 \left(\frac{1000}{CN} - 10 \right) \quad 6.3$$

where CN is the curve number for the day. The curve number is a function of the soil's permeability, land use and antecedent soil water conditions. The initial abstraction, I_a , is usually approximated as $0.2S$ and Equation 6-2 then becomes as Equation 6.4

$$Q_{surf} = \frac{(R_{day} - 0.2S)^2}{(R_{day} + 0.8S)} \quad 6.4$$

Runoff will occur when $R_{day} > I_a$. The details of the soil and curve number relationships can be found in *SWAT theoretical documentation, Version 2009* (Neitsch et al., 2011). The relationship between rainfall, runoff and curve number is shown in Figure 6.1.

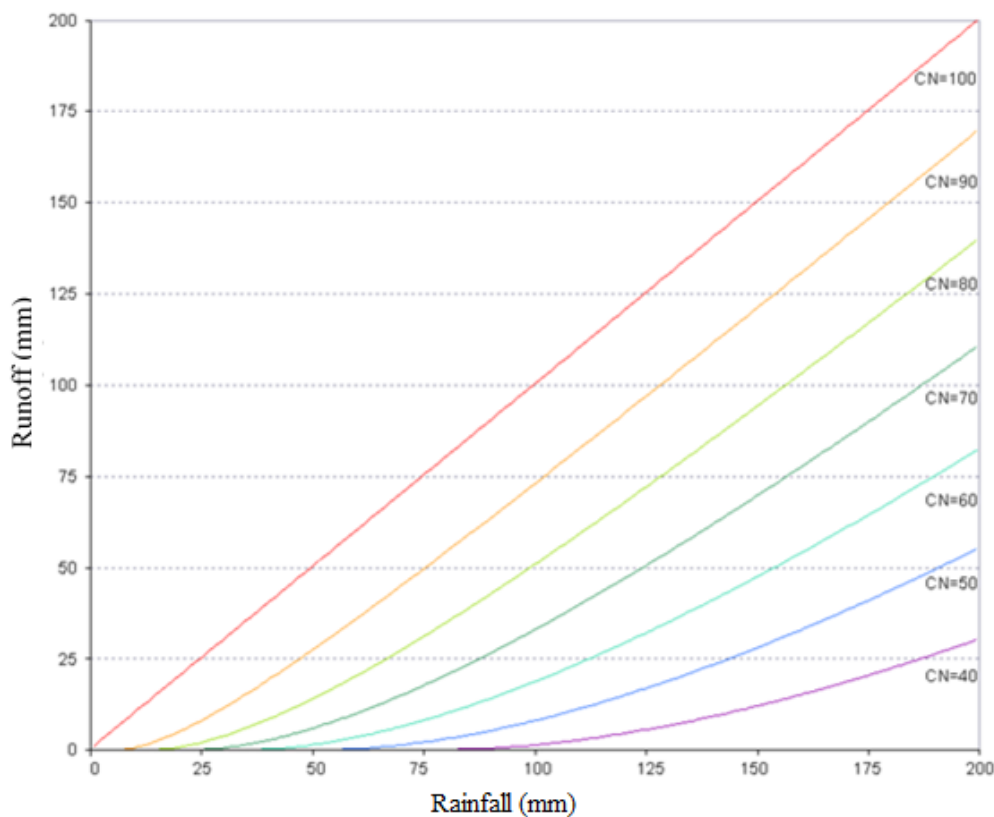


Figure 6.1: Relationship of runoff to rainfall in SCS curve number method (Neitsch et al., 2011).

Snowfall-Snowmelt process: The snowfall-snowmelt process largely affects the hydrologic response in the mountainous part of a river basin. SWAT classifies precipitation as rain or freezing rain (snow), using a threshold air temperature. Precipitation is treated as snow when the daily mean temperature is less than a defined threshold, and water equivalent to snow precipitation is added to the snowpack in the HRU (Neitsch et al., 2011). Surface runoff from snow cover is also included in the

SWAT. Snow melts on days when the maximum temperature exceeds 0°C using a linear function of the difference between the average maximum air temperature of snow pack and the base or threshold temperature for snow melt. Equation 6.5 represents snowmelt process.

$$SNO_{mIt} = b_{mIt} \cdot sno_{cov} \cdot \left[\frac{T_{snow} + T_{mx}}{2} - T_{mIt} \right] \quad 6.5$$

where, SNO_{mIt} is amount of snow melt on a given day (mm H₂O), b_{mIt} is the melt factor for the day (mm H₂O/day-°C), sno_{cov} is the fraction of the HRU area covered by snow, T_{snow} is the snow pack temperature on a given day (°C), T_{mx} is maximum air temperature on a given day (°C), and T_{mIt} is threshold temperature above which snow melt is allowed (°C) (Neitsch et al., 2011).

The melt factor varies during the season (1.4-8.0 mm H₂O/day-°C), and is estimated based on maximum and minimum melt rate as mentioned in Equation 6.6.

$$b_{mIt} = \frac{(b_{mIt6} + b_{mIt12})}{2} + \frac{(b_{mIt6} - b_{mIt12})}{2} \cdot \sin\left(\frac{2\pi}{365} \cdot (d_n - 81)\right) \quad 6.6$$

Where, b_{mIt} is the melt factor for the day (mm H₂O/day-°C), b_{mIt6} and b_{mIt12} are the melt factors for June 21 and December 21 respectively (mm H₂O/day-°C) and d_n is the day number of the year (Neitsch et al., 2011).

The amount of melted snow is considered as precipitation for estimating percolation (i.e. deep drainage) and runoff. The snowfall that accumulates on the ground is termed as snowpack. Snowpack decreases with snowmelt or sublimation, and increases with additional snowfall. Snowpacks are not uniformly distributed over the subbasin due to variability in topography, shading and drifting. SWAT uses an aerial depletion curve to define the fraction of snow cover area, which shows the functional relationship between the areal snow coverage and amount of snow present in the sub-basin at a given time (Neitsch et al., 2011).

The SWAT model has provision to split the sub-basins into a maximum of ten elevation bands. The snow cover and snowmelt are simulated separately for each elevation band. Thus, the SWAT model is able to address snowfall-snowmelt process caused by orographic variation in precipitation and temperature.

Evapotranspiration: Evapotranspiration (ET) includes all the processes by which water from the Earth's surface is converted into evaporation, and transpiration, which is water vapour emitted by plants. Evapotranspiration is the combination of evaporation from the soil and plant canopy transpiration. The water available for human use and management is the difference between precipitation and evapotranspiration (Neitsch et al., 2011). Potential evapotranspiration (PET) is the maximum evapotranspiration that occurs in existing climatic conditions when the surface is well-supplied with water (Milly and Dunne, 2016). In the SWAT model, three potential evapotranspiration metrics are available: Hargreaves, Priestley-Taylor and Penman-Monteith (Neitsch et al., 2011). The Hargreaves method requires air temperature data only, while the Priestley-Taylor method requires air temperature, solar radiation and relative humidity data. In contrast, the Penman-Monteith method requires data on air temperature, solar radiation, relative humidity, wind speed and an estimation of the canopy resistance. The Penman-Monteith method (Equation 6.7) was used in this study.

$$\lambda E = \frac{\Delta \cdot (H_{net} - G) + \rho_{air} \cdot C_p \cdot [e_z^0 - e_z] / r_a}{\Delta + \gamma \cdot (1 + r_c / r_a)} \quad 6.7$$

where, λE is latent heat flux density (MJ/m²/d), E is depth rate evaporation (mm/day), Δ is the slope of the saturation vapour pressure-temperature curve (kPa/°C), H_{net} is the net radiation (MJ/m²/d), G is the heat flux density to the ground (MJ/m²/d), ρ_{air} is the air density (kg/m³), C_p is the specific heat at constant pressure (MJ/kg/°C), e_z^0 is the saturation vapour pressure of air at height z (kPa), e_z is the water vapour pressure of air at height z (kPa), γ is the psychrometric constant (kPa/°C), r_c is the plant canopy resistance (s/m); and r_a is the diffusion resistance of the air layer (aerodynamic resistance) (s/m). The details of the each component can be found in *SWAT theoretical documentation, Version 2009* (Neitsch et al., 2011).

In SWAT, actual evaporation is derived from potential evapotranspiration in two steps. Firstly, rainfall intercepted by the plant canopy is evaporated. Then, SWAT calculates soil evaporation/sublimation and plant transpiration (Neitsch et al., 2011). Sublimation will occur only when snow is present, otherwise evaporation will take place from the

soil. The details on actual evapotranspiration can be found in *SWAT theoretical documentation, Version 2009* (Neitsch et al., 2011).

Soil water: Water entering into soil is partitioned into three components: soil evaporation and plant uptake (transpiration); percolation (deep drainage) below the root zone to the bottom aquifer; and lateral flow from the aquifer to the stream (base flow). In the SWAT model, the vertical soil profile is classified as root zone, vadose (unsaturated) zone, shallow aquifer and deep aquifer. The SWAT model uses a storage routing technique to project the flow through each soil layer (up to 10 layers) in the root zone. Downward flow (percolation) from any layer occurs only when its water content exceeds the field capacity. The downward flow rate is governed by a function related to the saturated hydraulic conductivity. The SWAT partitions groundwater into two aquifer systems; shallow and deep aquifers. The shallow aquifer is an unconfined aquifer, and contributes return flow (base flow) to streams within the watershed. The deep aquifer is confined, and contributes return flow to streams outside the watershed. Water flow in a soil layer will not occur if that soil layer is frozen (Neitsch et al., 2011).

6.2 Methodological framework for the SWAT modelling

The overall methodology for the SWAT modelling is schematised in Figure 6.2. The main steps in the SWAT modelling include input data processing and model development/set up, sensitivity analysis and calibration, validation, and scenario analysis. These steps are described in the following sections:

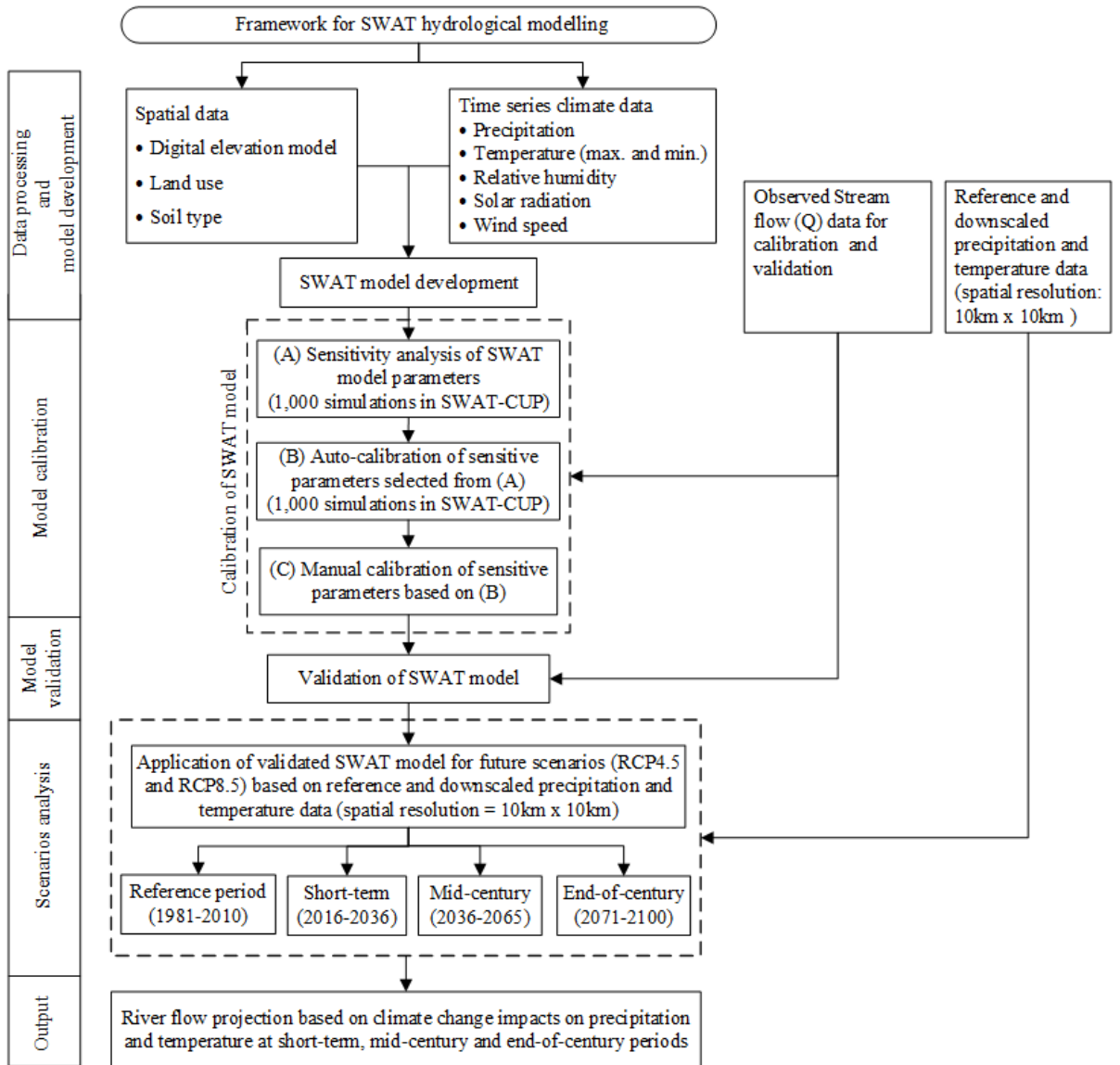


Figure 6.2: Framework for the SWAT model development and scenarios analysis.

6.2.1 SWAT input data processing and model development (Model initialisation)

SWAT model input data includes spatial data and time series data. The spatial data are digital elevation model, land use, and soil type. The time series data are daily precipitation, temperature (minimum and maximum), relative humidity, solar radiation and wind speed. The observed discharge data after separation into two independent data sets is used for the calibration and validation of the SWAT model. The SWAT model was run with spatial and time series data for the reference period (1981-2010). The latest available version of SWAT, version 2012.10.21, which is included in the ArcSWAT extension with in ArcGIS, was used in this research.

6.2.2 Sensitivity analysis and model calibration

Physically-based distributed hydrological models lack sufficient data to fully represent spatial variability, and include scale problems of field measurements integration and model parameter elements. This results in the requirement for model calibration and subsequent validation (Cao et al., 2006). The SWAT Calibration and Uncertainty Program (SWAT-CUP) with Sequential Uncertainty Fitting – Version 2 (SUFI2) Optimization Algorithm was used for calibration sensitivity analysis purposes. The SWAT-CUP program is mainly developed for sensitivity analysis and calibration of SWAT models, and thus was applied. As SWAT-CUP is recommended by the SWAT model developer and is a freely available tool, the latest version of SWAT-CUP at the time of this research period, Swat-CUP version 5.2.1.1, was downloaded from <https://www.2w2e.com/home/SwatCup> and used in this research. In SWAT-CUP, a t-test is used to assess the relative significance of each parameter. A multiple regression analysis is applied to obtain the statistics of parameter sensitivity. The t-stat and p-value are used to identify the significance of parameter sensitivity. The t-stat is a measure of the precision with which the regression coefficient is measured, and is estimated by the coefficient of a parameter divided by its standard error. A parameter is sensitive when its coefficient is large compared to its standard error. The p-value tests the null hypothesis that the coefficient is equal to zero (i.e. has no effect on prediction). A low p-value (<0.05) means the null hypothesis can be rejected. Rejection of the null hypothesis indicates that the coefficient is not equal to zero, and there is a meaningful contribution of the parameter in the model. A predictor that has a low p-value is likely to be a sensitive parameter in the model, because changes in the predictor's value are related to changes in the corresponding variable. In contrast, a large p-value indicates that changes in the predictor are not associated with changes in the response, and the parameter is not very sensitive. A p-value of < 0.05 is the generally accepted value at which the null hypothesis can be rejected (Abbaspour, 2015).

After the SWAT model development (as mentioned in 6.2.1), sensitivity analysis is carried out to identify sensitive SWAT parameters which are then used to calibrate the model using measured discharge data. Observed discharge data at Chatara in the Koshi River basin (Figures 3.1 and 3.3) for the period 1996-2000 were used for the calibration of the SWAT model.

Model performance evaluation

The Nash-Sutcliffe efficiency (NSE), Percent bias (PBIAS) and the coefficient of determination (R^2) are model performance metrics commonly used to evaluate the precision of hydrological models (Bharati et al., 2019, Bouraoui et al., 2005, Cao et al., 2006, Neupane et al., 2014, Yan et al., 2013). Kling–Gupta efficiency (KGE) has also been used to evaluate hydrological model performance in recent studies.

Nash-Sutcliffe efficiency (Equation 6.8) represents how well the plot of observed versus simulated value fits the 1:1 line (Santhi et al., 2001). A perfect match between observed and predicted values occurs when $NSE=1$ (Golmohammadi et al., 2014). The optimal value of NSE is 1, and it should be >0 for acceptable model performance (Golmohammadi et al., 2014, Gupta et al., 1999). A value less than zero indicates unacceptable model performance (Golmohammadi et al., 2014, Gupta et al., 1999). A model with $NSE>0.75$ is considered to have good prediction precision, and a model between 0.36 to 0.75 is considered satisfactory (Motovilov et al., 1999).

$$NSE = 1 - \frac{\sum_{i=1}^n (Q_{obs(i)} - Q_{sim(i)})^2}{\sum_{i=1}^n (Q_{obs(i)} - \overline{Q_{obs}})^2} \quad 6.8$$

where, NSE is Nash-Sutcliffe efficiency, $Q_{obs(i)}$ is the observed daily discharge on day i , $Q_{sim(i)}$ is the simulated daily discharge on day i and $\overline{Q_{obs}}$ is the mean observed daily discharge during the simulation period.

Percent bias (Equation 6.9) shows the percentage difference between the volume of observed and simulated flows. It measures the average tendency of the simulated flows to be smaller or larger than the observed flow (Gupta et al., 1999). The optimal value of the P bias is zero, and a positive value indicates a model bias towards underestimation, while a negative value indicates a model bias towards overestimation (Gupta et al., 1999). A low magnitude value indicates a better model simulation. A model calibration with $PBIAS < 25\%$ is considered acceptable (Van Liew et al., 2007).

$$PBIAS = \frac{\sum_{i=1}^n (Q_{obs(i)} - Q_{sim(i)})}{\sum_{i=1}^n Q_{obs(i)}} * 100 \quad 6.9$$

where, $PBIAS$ is Percent bias, $Q_{obs(i)}$ is the observed daily discharge on day i and $Q_{sim(i)}$ is the simulated daily discharge on day i during the simulation period.

The coefficient of determination (Equation 6.10) describes the strength of the relationship between the observed and simulated values (Santhi et al., 2001). It indicates the proportion of the variance in the measured data, and a higher value indicates less error variance (Golmohammadi et al., 2014). A model with $R^2 > 0.6$ is acceptable for hydrological applications (Santhi et al., 2001).

$$R^2 = \frac{[\sum_{i=1}^n (Q_{obs(i)} - \overline{Q_{obs}})(Q_{sim(i)} - \overline{Q_{sim}})]^2}{\sum_{i=1}^n (Q_{obs(i)} - \overline{Q_{obs}})^2 \sum_{i=1}^n (Q_{sim(i)} - \overline{Q_{sim}})^2} \quad 6.10$$

where, R^2 is coefficient of determination, $Q_{obs(i)}$ is the observed daily discharge on day i , $Q_{sim(i)}$ is the simulated daily discharge on day i and $\overline{Q_{obs}}$ is the mean observed daily discharge, and $\overline{Q_{sim}}$ is the mean simulated daily discharge during the simulation period.

The Kling–Gupta efficiency (KGE) (Equation 6.11) is based on the decomposition of NSE and provides information on the relative importance of the correlation, variability bias and mean bias components of NSE (Gupta et al., 2009). The modified KGE ensures that bias and variability ratios are not cross-correlated, which may occur when the precipitation inputs are biased (Kling et al., 2012). KGE is expressed as:

$$KGE = 1 - \sqrt{(\gamma - 1)^2 + (\beta - 1)^2 + (r - 1)^2} \quad 6.11$$

where r is the correlation coefficient between simulated and observed runoff (dimensionless), $\beta = \mu_s/\mu_o$ is the bias ratio (dimensionless), $\gamma = (\sigma_s/\mu_s)/(\sigma_o/\mu_o)$ is the variability ratio (dimensionless), σ_s and σ_o are the standard deviation of simulated and observed runoff in m^3/s , μ_s and μ_o are the mean simulated and observed runoff in m^3/s . The Kling–Gupta efficiency addresses the limitations of NSE and is increasingly used for model performance evaluation (Knoben et al., 2019). The ideal value of KGE is unity (Gupta et al., 2009).

6.2.3 Model validation

The calibrated model (as mentioned in Section 6.2.2) is used for the validation. Observed discharge flow data at Chatara in the Koshi River basin for the period 2001–2005 were used for the validation of the SWAT model.

6.2.4 Scenario analysis

The validated SWAT model (as mentioned in Section 6.2.2) is applied to project hydrological changes based on precipitation and temperature data for different time periods and climate scenarios. The short-term (2016-2045), mid-century (2036-2065) and end-of-century (2071-2100) periods with the downscaled precipitation and temperature data for RCP4.5 and RCP8.5 were considered for the future scenarios.

6.3 Application of methodology for SWAT hydrological modelling

The application of the methodological framework described in Figure 6.2 is demonstrated in the following sections.

6.3.1 SWAT input data processing and model development

The SWAT model was developed based using the Digital Elevation Model (DEM), land-use, soil type, slope, precipitation, temperature, relative humidity, solar radiation, and wind speed data as mentioned in Section 6.2.1. The developed SWAT model was used for model calibration.

Digital elevation model (DEM)

The Shuttle Radar Topography Mission (SRTM) 90 m x 90 m resolution (<http://srtm.csi.cgiar.org>) DEM for the transboundary Koshi River basin was used as an input to represent the topography of the basin. The maximum and minimum elevations within the catchment are 8806 m and 97 m respectively (Figure 6.3). The DEM was then used to generate a representation of the stream network and delineate the watershed using ArcSWAT 2012. The minimum and maximum area for stream definition given by ArcSWAT were about 27,000 ha and 5,000,000 ha respectively, noting that the SWAT recommended area was about 108,050 ha. The stream definition area plays a vital role in generating streams at the sub-basin level. The SWAT recommended area was not able to generate streams at the sub-basin level where measured discharge data are available from the Department of Hydrology and Meteorology in the Nepal part. Hence, the stream definition area was assigned as 54,000 ha. It covered all the streams where measured discharge data is available for the Nepalese part. The Koshi River basin was divided into 294 sub-basins for this study. The meteorological data for the Tibet part were derived from data globally available in the public domain. As the hydro-

meteorological data in the Nepalese part are available at sub-basin scales, the size of sub-basins in the Nepalese part are smaller compared to Chinese part.

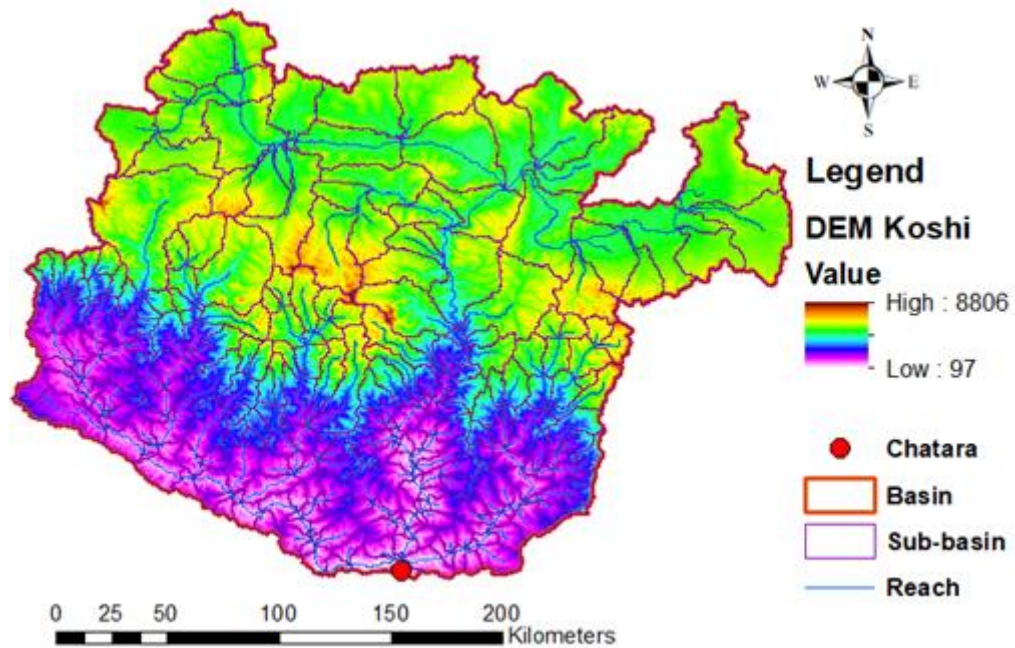


Figure 6.3: Digital elevation model and major river network in the Koshi River basin.

Land use

The land use and land cover (LULC) map for the Koshi River basin was obtained from the International Centre for Integrated Mountain Development (ICIMOD) (<http://geoportals.icimod.org/>) to represent the different land use practices in the Koshi River basin. Land use practices carried out in the Koshi River basin down to Chatara in Nepal are shown in Figure 6.4. The spatial resolution of the processed land use map is 90 m x 90 m.

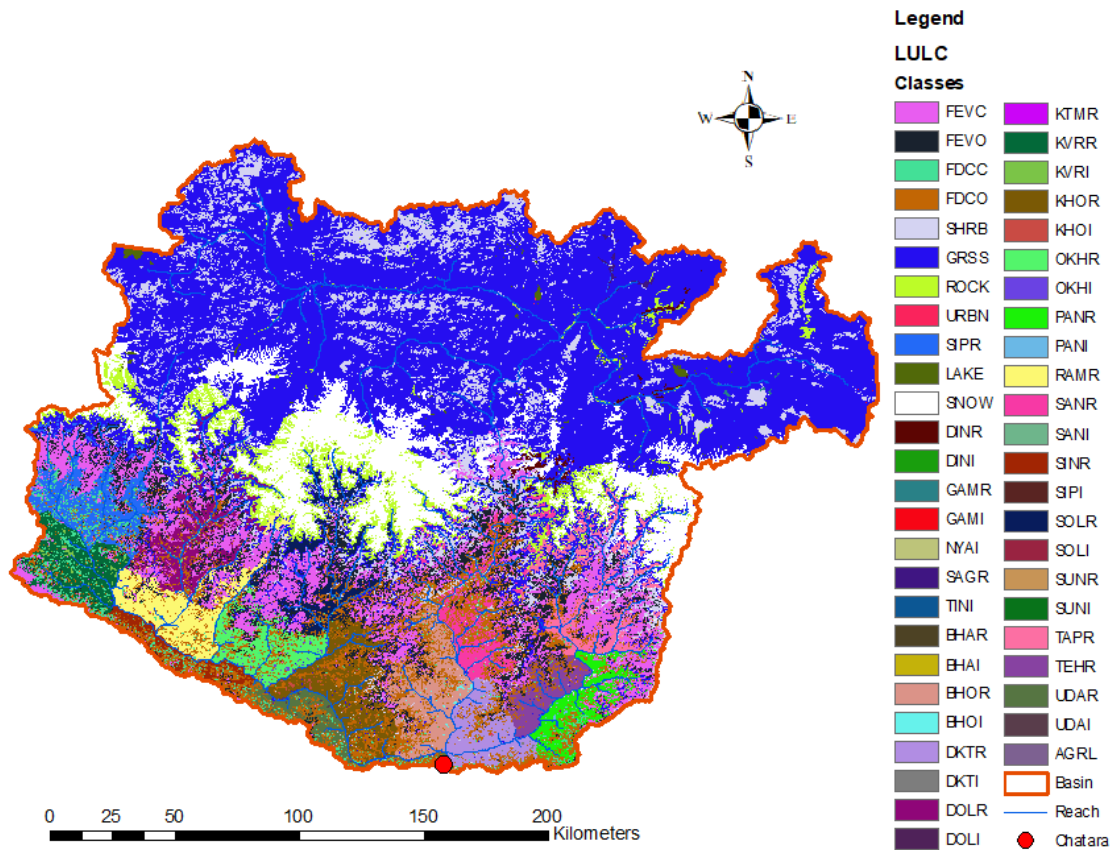


Figure 6.4: Land use practices in the Koshi River basin (Blue colour represents grass and white colour represents snow).

For hydrologic response unit analysis, land-use areas of less than 100 km² are merged into nearby dominant land-use practices as small portions of land-use practices have negligible impact on total surface runoff in the catchment. Hence, 49 land-use practices, as shown in Figure 6.4, have been reduced to 23 land-use practices. Grass land is the dominant land practice in the Koshi River basin covering around 25630 km² or 47% of the total catchment area. The blue colour in Figure 6.4 represents grass (denoted by GRSS in Legend). Around 12% of the total catchment area is covered by snow. The white colour in Figure 6.4 represents snow (denoted by SNOW in Legend). Other land-use practices include open forest, closed forest, rock outcrop, and agricultural crop land.

Soils

The soil map for the Koshi River basin was downloaded from the soil and terrain (SOTER) database program (<https://www.isric.org>). The soil map represents the different soil types available in the Koshi River basin. Different soil types (as per the

FAO soil classification system 2015) in the Koshi River basin down to Chatara in Nepal are shown in Figure 6.5. The spatial resolution of the processed soil map is 90 m x 90 m.

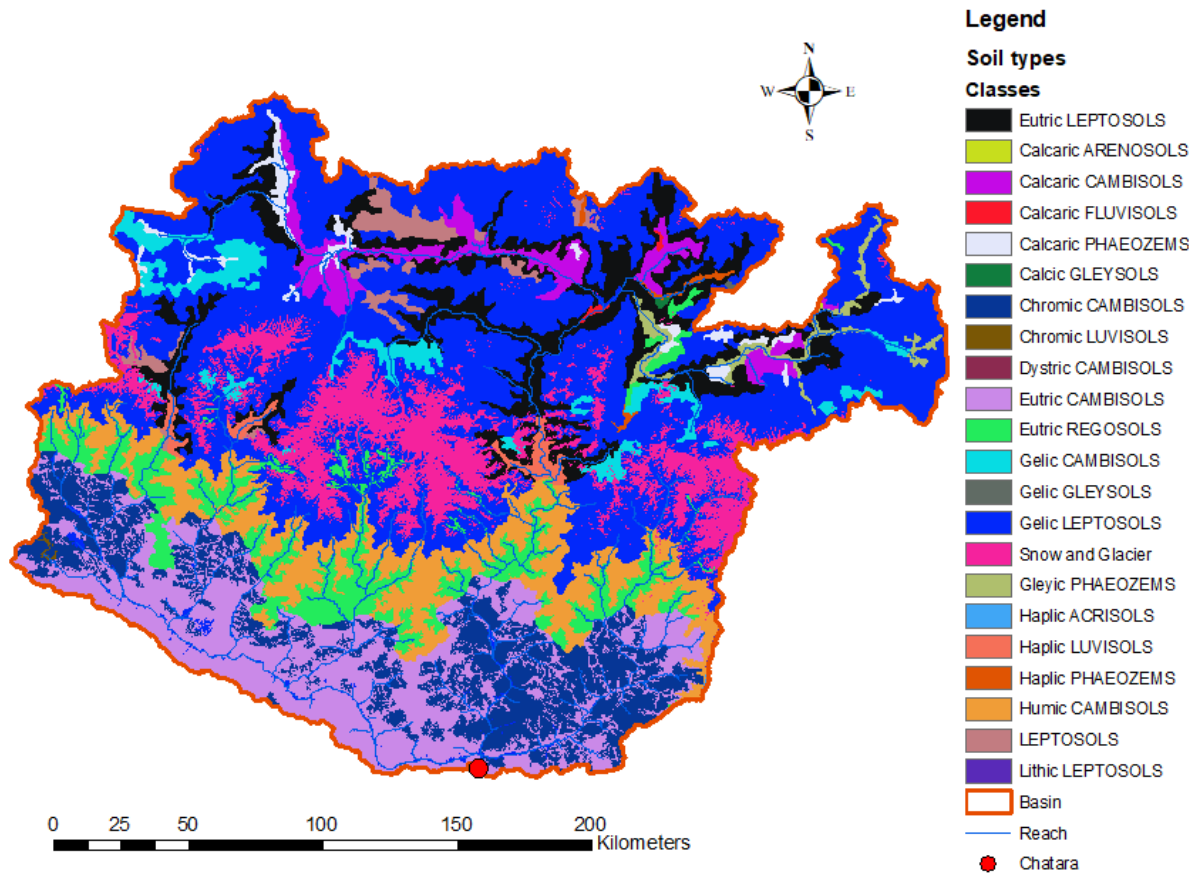


Figure 6.5: Soil map of the Koshi River basin.

For hydrologic response unit analysis, soil type of less than 100 km² are merged into nearby dominant soil types as small portions of soil types have negligible impact on the total surface runoff in the catchment. Hence, the 22 soil types as shown in Figure 6.5 have been reduced to 12 major soil types. Gelic leptosols are the dominant soil type in the Koshi River basin, covering around 21715 km² which is around 40% of the total catchment area. The blue colour in Figure 6.5 represents Gelic leptosols (denoted by Gelic LEPTOSOLS in Legend). Eutric cambisols cover around 13% of the total catchment area. The purple colour in Figure 6.5 represents Eutric cambisols (denoted by Eutric CAMBISOLS in Legend). Snow and glaciers cover around 12% of the total catchment area. Other dominant soil types include chromic cambisols, eutric leptosols, humic cambisols, and eutric regosols.

Slope classification

A maximum five slope categories can be defined in the SWAT model. The slope types are classified as 0-17%, 17-32%, 32-46%, 46-64% and 64-9999%. These slope types are chosen so that the areas under each slope type are almost equal. As the five slope classes are defined, each slope class covers around 20% of the total catchment area (i.e. 10,800 km²). As each slope category has equal area coverage, the chosen slope classification system ensures equal representation of all slope categories in the catchment. Spatial distribution of different slope types in the Koshi River basin down to Chatara in Nepal is shown in Figure 6.6. The spatial resolution of the processed slope map is 90 m x 90 m.

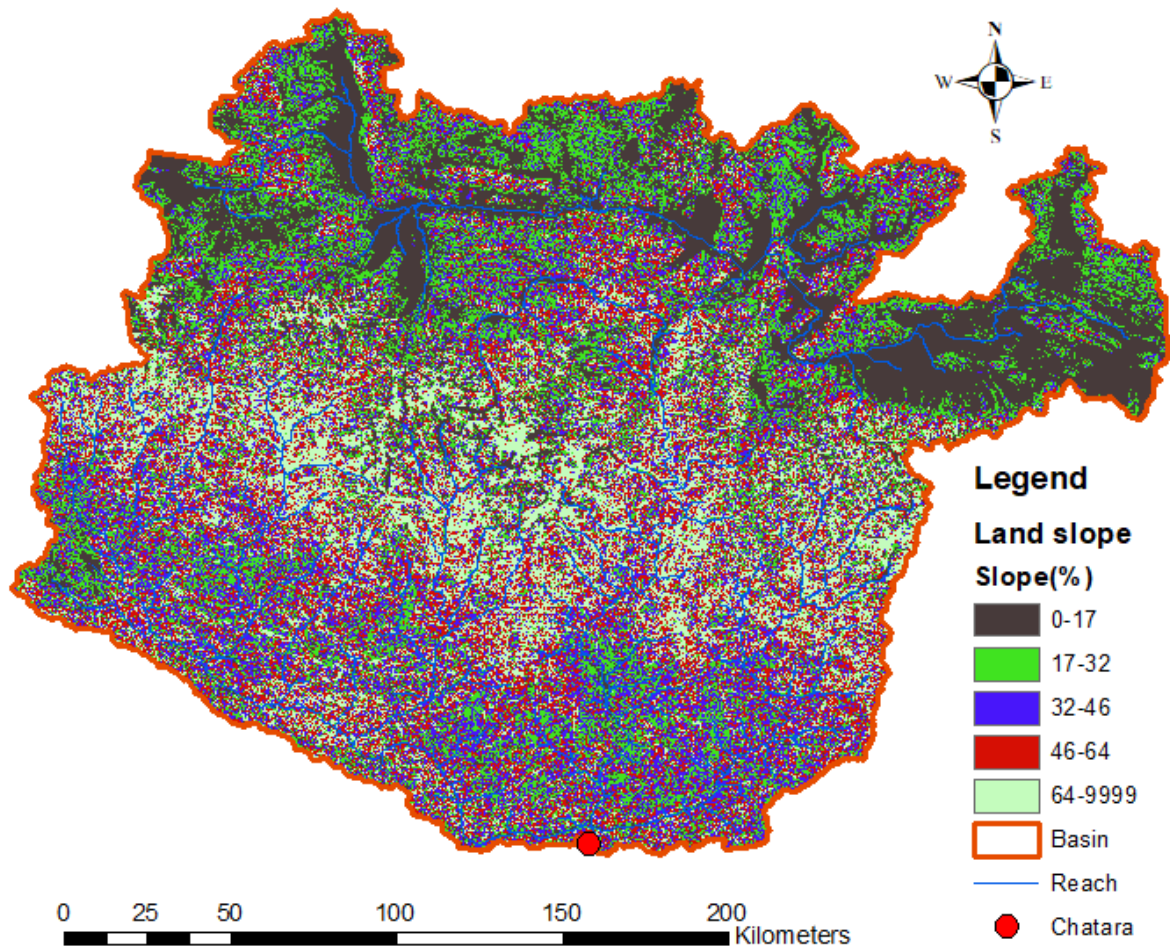


Figure 6.6: Slope variation in the Koshi River basin.

The hydrologic response units are defined based on HRU thresholds of 20% each for land use, soil class, and slope class. This has resulted in 1870 HRUs. Hence, the 294 sub-basins are further divided into 1870 HRUs.

Precipitation

Precipitation data for the Nepalese part were obtained from the Department of Hydrology and Meteorology (DHM), Nepal. Asian Precipitation - Highly-Resolved Observational Data Integration Towards Evaluation (APHRODITE) data were used for precipitation for the Tibet part. These data were downloaded from <http://aphrodite.st.hirosaki-u.ac.jp/index.html>. The spatial resolution of APHRODITE data was $0.5^\circ \times 0.5^\circ$ (~ 50 km x 50 km). A total of 81 precipitation station data sets (59 DHM stations and 22 APHRODITE grids) were used in the model SWAT. The spatial location of precipitation stations are shown in Figure 6.7.

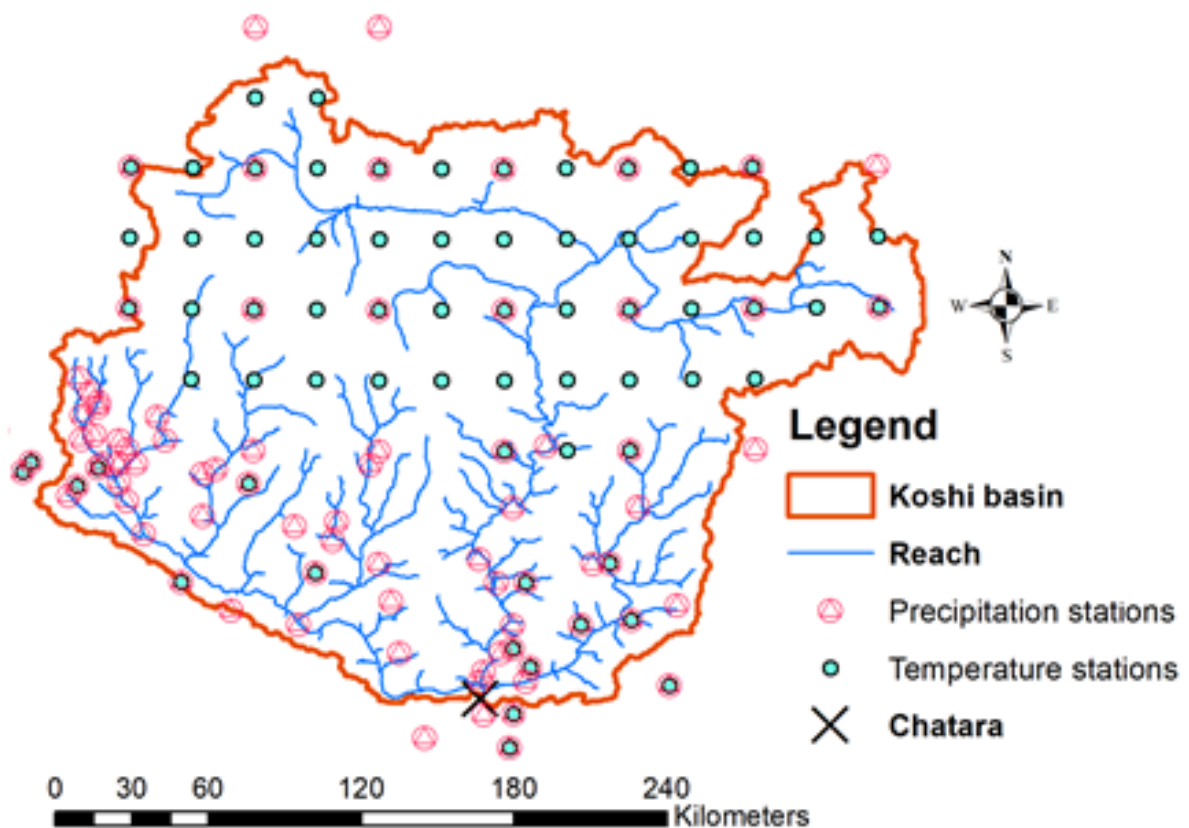


Figure 6.7: Precipitation and temperature stations used in the SWAT modelling.

Temperature

Temperature data for the Nepalese part were obtained from the Department of Hydrology and Meteorology, Nepal. European Center for Medium Range Weather Forecast ReAnalysis (ERA) data were used for the temperature for the Tibet part. These data were downloaded from <https://www.ecmwf.int/en/forecasts/datasets/reanalysis-datasets/era5>. The spatial resolution of ERA5 data was $0.25^{\circ} \times 0.25^{\circ}$ (~ 25 km x 25 km). A total of 68 temperature station data sets (16 DHM stations and 52 ERA5 grids) were used in the SWAT modelling. The spatial locations of temperature stations are shown in Figure 6.7.

Relative humidity, solar radiation, and wind speed

Relative humidity, solar radiation, and wind speed data for the Nepalese part were obtained from the Department of Hydrology and Meteorology, Nepal. As the main purpose of this research is to assess the climate change impacts on the hydrological regime of the Koshi River due to changes on precipitation and temperature, only the DHM station data available for relative humidity, solar radiation, and wind speed were used. A total of 12 relative humidity stations, 5 solar radiation stations, and 7 wind speed stations were used for SWAT modelling.

6.3.2 Sensitivity analysis, calibration and validation of SWAT model

Initially, 22 sensitive SWAT parameters were selected based on existing literature (Bharati et al., 2019, Bharati et al., 2014, Devkota and Gyawali, 2015). The sensitivity analysis of these parameters was carried out for 1000 simulations, and the results are shown in Figure 6.8.

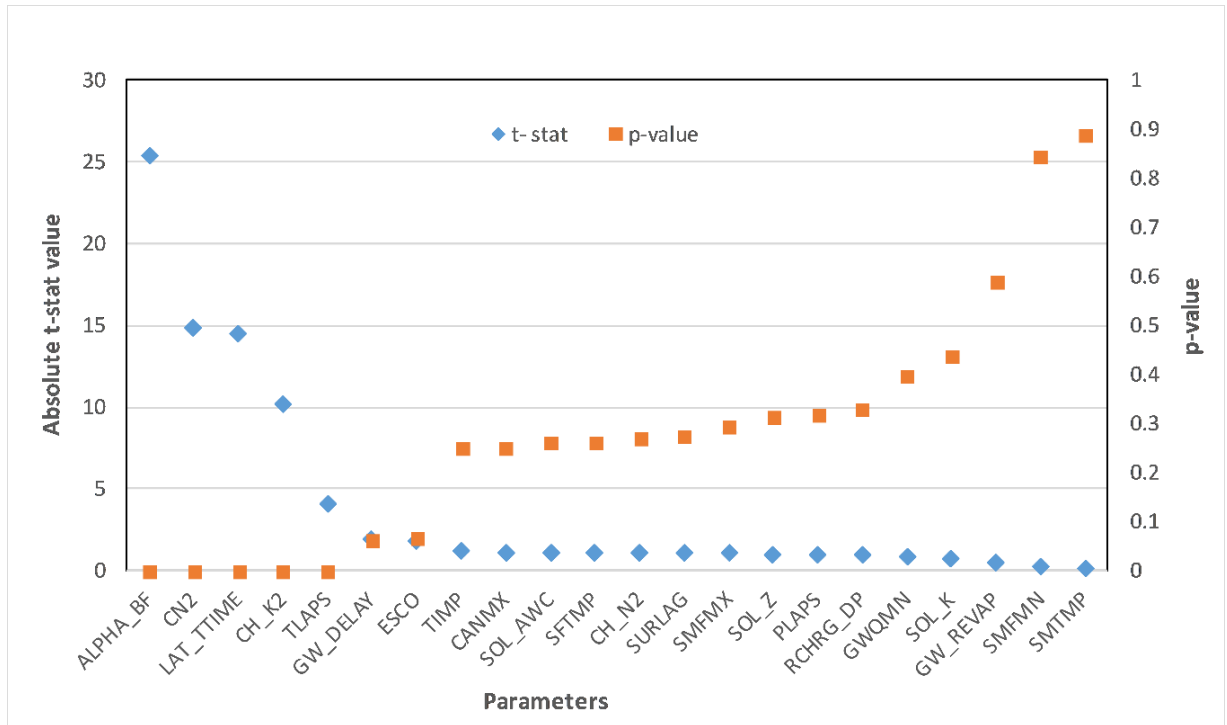


Figure 6.8: Sensitivity analysis of 22 SWAT parameters.

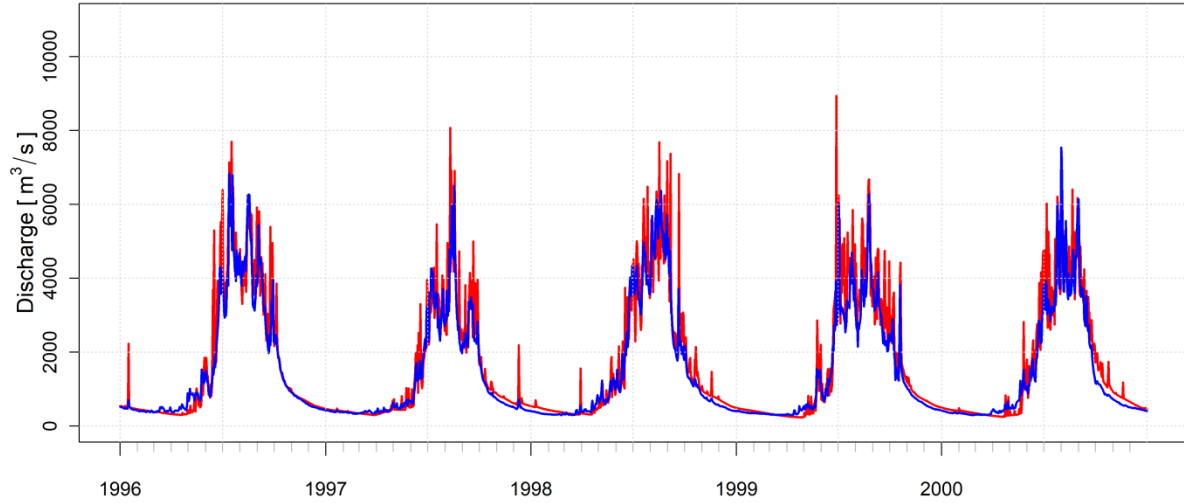
Out of 22 SWAT parameters, seven parameters: baseflow Alpha factor (ALPHA_BF.gw), initial SCS curve number (CN2.mgt), lateral flow travel time (LAT_TTIME.hru), effective hydraulic conductivity in the main channel alluvium (CH_K2.rte), temperature lapse rate (TLAPS.sub), groundwater delay time (GW_DELAY.gw), soil evaporation compensation factor (ESCO.hru) were found to be most sensitive. The second iteration was carried out for 1000 simulations for the 7 most sensitive parameters. After auto-calibration, rigorous manual calibration was carried out for the calibration period of 1996 to 2000. The calibrated values after manual calibration is shown in Table 6.1.

Table 6.1: SWAT calibrated parameter values.

Sensitivity analysis rank	Parameter	Calibrated value
1	ALPHA_BF.gw	0.097
2	CN2.mgt	97.976
3	LAT_TTIME.hru	12.225
4	CH_K2.rte	119.8975
5	TLAPS.sub	-6.059
6	GW_DELAY.gw	168.985
7	ESCO.hru	0.2885

The observed and simulated flows on a daily time step for the 1996 to 2000 calibration period are shown in Figure 6.9.

(a) Calibration at Chatara



(b) Validation at Chatara

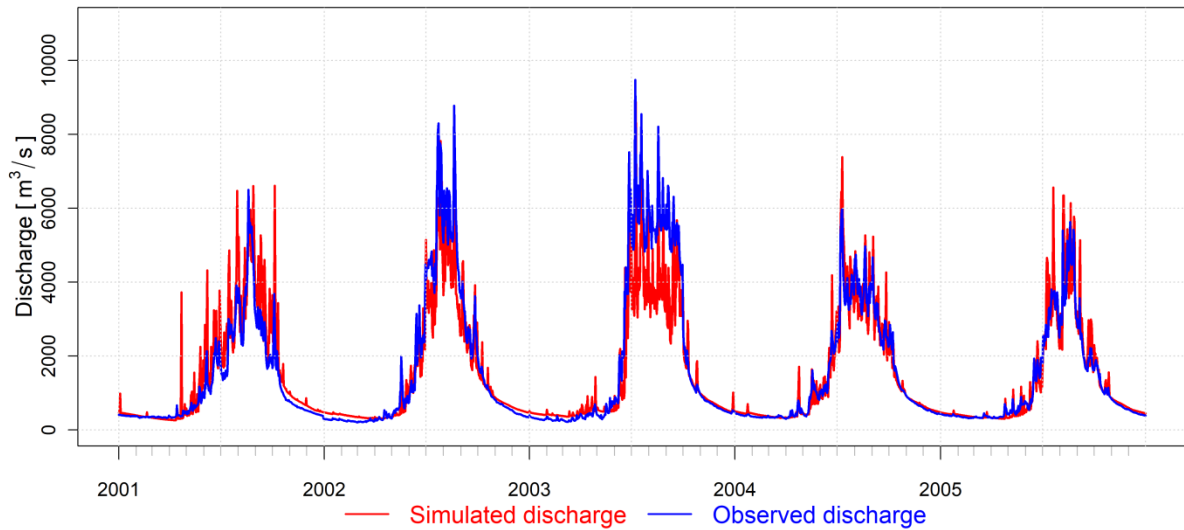


Figure 6.9: Observed and simulated daily flows (m^3/s) for the Koshi River at Chatara (the blue colour represents observed daily flows and the red colour represents simulated daily flows).

SWAT Model performance evaluation

The stream discharge data measured at the outlet of the Koshi River basin, Chatara, was used to assess the performance of the SWAT model. In this study, Nash-Sutcliffe efficiency (NSE), Percent bias (PBIAS), Coefficient of determination (R^2) and Kling–Gupta efficiency (KGE) were used to evaluate the SWAT model's performance for the Koshi River basin.

The SWAT model performance for the calibration and validation period is shown in Table 6.2. The NSE, PBIAS, R^2 and KGE values for the calibration period are 0.87, -9.46, 0.95 and 0.75 respectively. The SWAT model performance is considered very good when $NSE > 0.65$ and $PBIAS < 10\%$ (Moriassi et al., 2007). Hence, the SWAT model performance for the calibration period is very good as the $NSE > 0.65$ and $PBIAS < 10\%$. As shown in Figure 6.9, most of the observed and simulated flows coincide within the calibration period.

Table 6.2: SWAT model performance for calibration and validation.

Model performance Index	Calibration	Validation
NSE	0.87	0.86
PBIAS	-9.46	-2.73
R^2	0.95	0.93
KGE	0.75	0.65
Performance	Very good	Very good

6.3.3 Model validation

Based on the calibrated values for the period 1996 to 2000 using discharge data at Chatara in the Koshi River basin, the SWAT model was validated for the periods of 2001 to 2005 based on available flow data. The observed and simulated flows on a daily time step for the calibration and validation periods are shown in Figure 6.9. The NSE, PBIAS, R^2 and KGE values for the validation period are 0.86, -2.73, 0.93 and 0.65 respectively. The SWAT model performance for the validation period is also very good as the $NSE > 0.65$ and $PBIAS < 10\%$. As shown in Figure 6.9, most of the observed and simulated flows coincide within the validation period.

6.3.4 Scenario analysis (future hydrological analysis)

The validated SWAT model was applied to project climate change impacts on the hydrological regime of the Koshi River basin using downscaled precipitation and temperature

data for different study periods and climate scenarios. The datasets for the reference period (1981 to 2010) can be downloaded from <http://rds.icimod.org/clim>. The reference climate datasets for the Indus, Ganges and Brahmaputra river basins were prepared using Watch Forcing based on the ERA interim dataset, which was bias corrected using Global Precipitation Climatology Centre (GPCC) and glacier mass balance data. Since the ERA interim and GPCC data were also based on observed stations, it is assumed that they represent the regional climatic patterns. However, because of their regional nature, sub-variability is expected within the sub-set. These datasets have been used in various studies (Kaini et al., 2020d, Wijngaard et al., 2017, MOFE, 2019). For this assessment, additional bias correction using stations' data was not carried out.

Downscaled precipitation and temperature data for climate change scenarios RCP4.5 and RCP8.5 were considered for the short-term (2016-2045), mid-century (2036-2065) and end-of-century (2071-2100) future scenarios. The precipitation and temperature data were downscaled at a spatial resolution of 10 km x 10 km. Details on GCM selection and climate data downscaling are mentioned in Kaini et al. (2020d). Based on the downscaled data, the total number of grid stations for precipitation and temperature was 581 for the whole Koshi River basin. The spatial location of the precipitation and temperature grid stations for reference and downscaled data are shown in Figure 6.10.

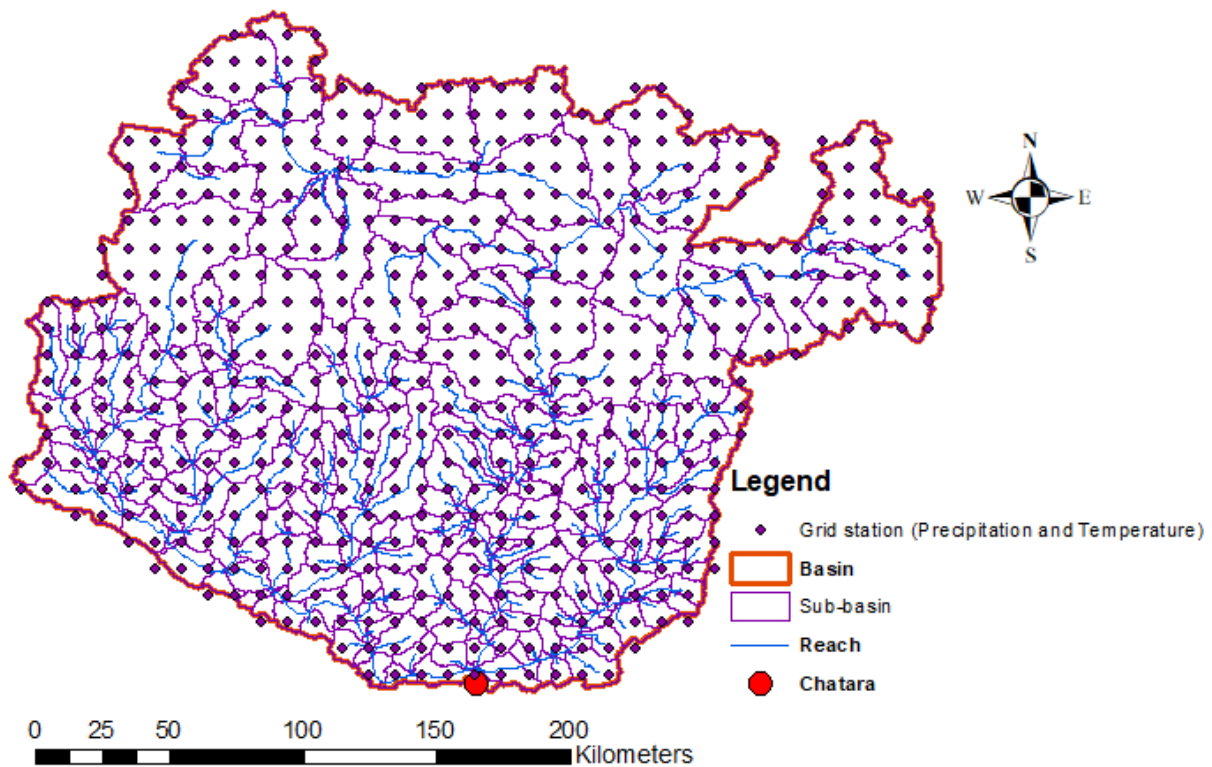


Figure 6.10: Precipitation and temperature grid stations for the reference and downscaled data.

The validated SWAT model was run for the reference period (1981-2010) using the reference datasets, and for future periods (2016-2100) for each corner of climatic extremes (Kaini et al., 2020d) for both the climate change scenarios RCP4.5 and RCP8.5. As 4 GCMs were selected for each RCPs for each study period, the SWAT model was run for 8 different datasets (4 datasets for climate change scenario RCP4.5 and 4 datasets for climate change scenario RCP8.5) for the entire study period.

6.4 Results and discussion

Figure 6.11 shows the projected mean monthly flow during the short-term, mid-century and end-of-century periods, and the reference period. The projected mean monthly flow is expected to decrease in June, but to increase in August, September, October and November in all scenarios and study periods. The projected peak mean monthly flow for climate change scenario RCP4.5 is lower than the flow for climate change scenario RCP8.5 for all study periods, and the difference in magnitude increases through the future periods. In the short-term period, the projected peak mean monthly flows for climate change scenarios RCP4.5 and RCP8.5 are 17% and 24% higher respectively, compared to the reference (base) period

(1981-2010). Likewise, the projected peak average mean monthly flows for climate change scenarios RCP4.5 and RCP8.5 in the mid-century period are 24% and 42% higher respectively, compared to the reference period. For the end-of-century period, the projected average peak mean monthly flows for climate change scenarios RCP4.5 and RCP8.5 are 35% and 67% higher respectively, compared to the reference period. Hence, an increase in the peak flow is expected in future, with the shift concentrated towards the August-September period.

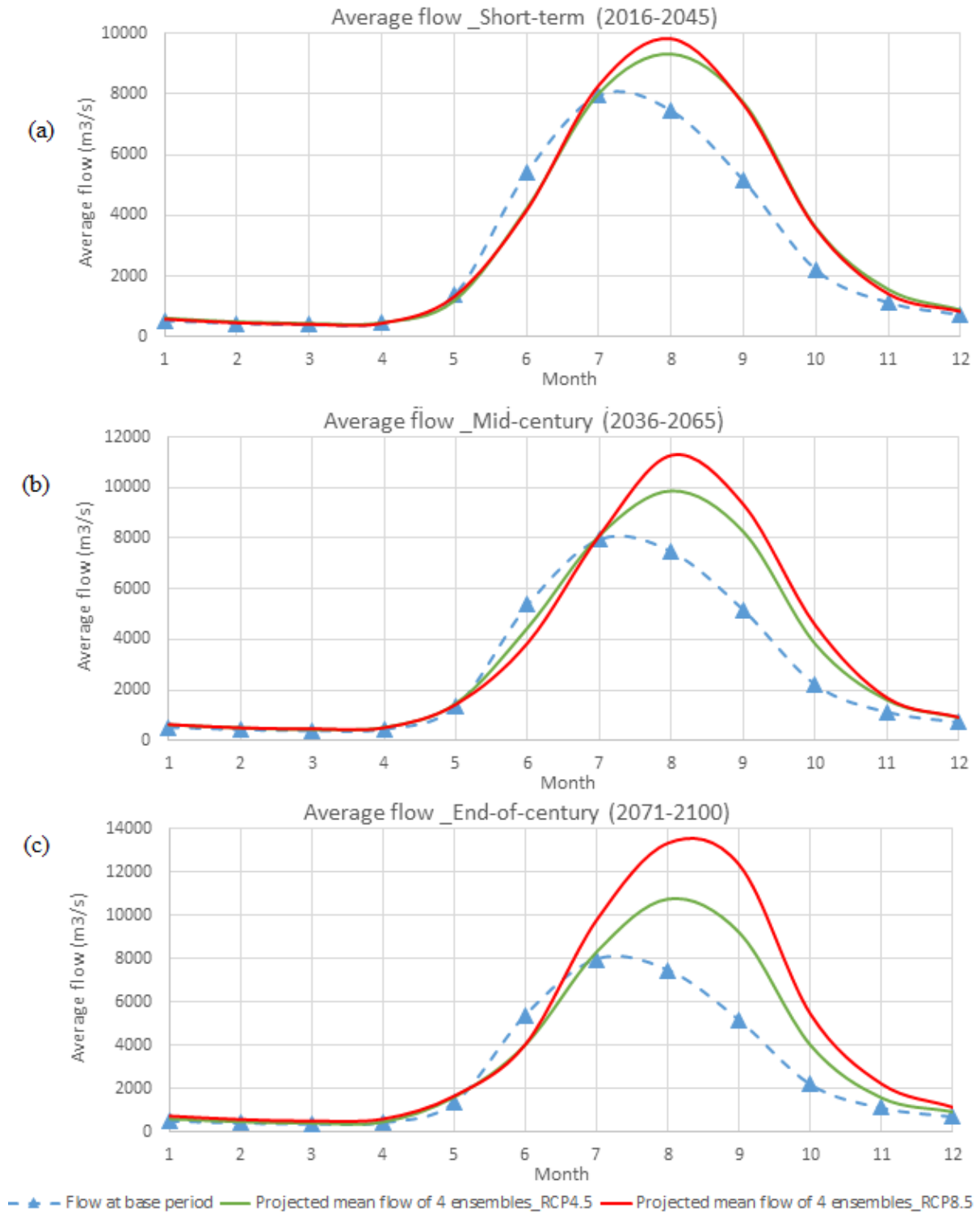


Figure 6.11: Average monthly projected discharge in the Koshi River for the short-term, mid-century and end-of-century periods. Also shown is the modelled flow during the base (reference) period (1981-2010).

Uncertainty

The projected flows based on selected ensembles in different climatic extremes show that there is high uncertainty about the future flows in the Koshi River. The uncertainty in projected annual and seasonal river flows is shown in Figure 6.12. The winter, pre-monsoon, monsoon and post-monsoon seasons refer to December–February, March–May, June–September and October–November, respectively. Most of the GCMs/ensembles result in increased uncertainty within the future time periods. The uncertainty is high for the end-of-century period compared to mid-century period. The relative uncertainty in projected mean annual flows for climate change scenario RCP4.5 are 6 to 23%, 11 to 39% and 15 to 40% for the short-term, mid-century and end-of-century periods respectively. Likewise, the relative uncertainty in projected mean annual flows for climate change scenario RCP8.5 are 12 to 29%, 16 to 54% and 25 to 70% for the short-term, mid-century and end-of-century periods respectively. Uncertainty in projected river flows is higher for climate change scenario RCP8.5 compared to the RCP4.5 scenario in the mid-century and end-of-century periods. All the GCMs/ensembles result in increased projected river flows in winter and post-monsoon seasons for all scenarios and study periods. Likewise, all the GCMs/ensembles result in increased projected river flows in the monsoon period for all scenarios and study periods, except for climate change scenario RCP4.5 during short-term period.

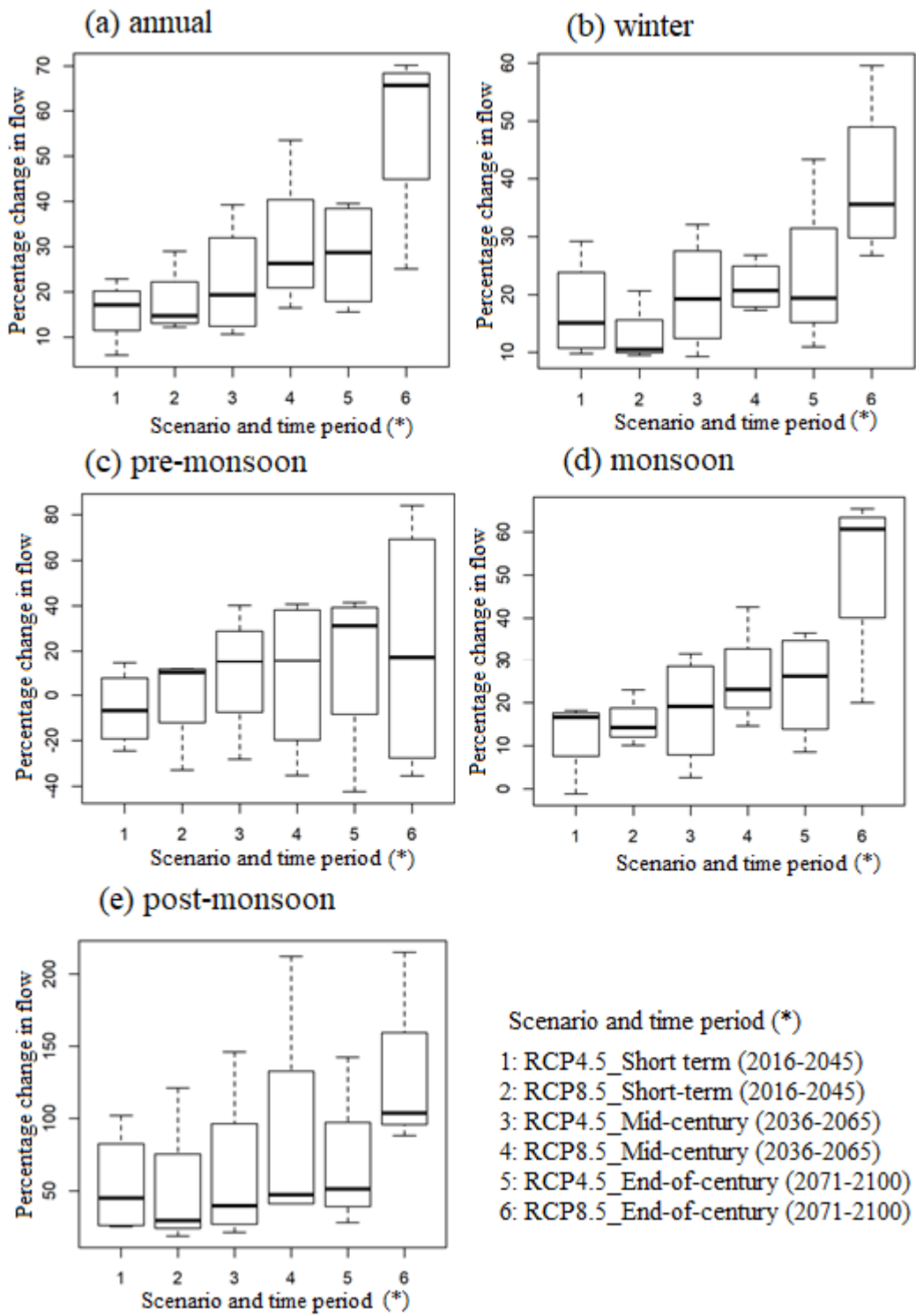


Figure 6.12: Uncertainty in projected annual and seasonal river flows (percentage change in flow based on outputs from four GCMs for the short term, mid-century, and end-of-century periods for climate change scenarios RCP4.5 and RCP8.5. Percentage changes in flows are relative to reference period flow data).

Changes in future flows

The absolute and relative changes in the annual and seasonal flows of the Koshi River based on ensembles of an average of 4 GCMs are shown in Table 6.3. The average annual river flow is projected to increase for all scenarios and study periods. For climate change scenario RCP4.5, average annual flows in the Koshi River are expected to increase by 16%, 22% and 28% in the short-term, mid-century and end-of-century periods respectively. Similarly, for the RCP8.5 climate change scenario, average annual flows are expected to increase by 18%, 31% and 57% in the short-term, mid-century and end-of-century periods respectively. The increases under the RCP8.5 scenario almost double in magnitude between the mid-century and the end-of-century periods. The projected average annual flow for RCP8.5 climate change scenario is higher than the RCP4.5 scenario. Winter flows are expected to increase by 17 to 23% and 13 to 39% for the climate change scenarios RCP4.5 and RCP8.5 respectively. However, the projected absolute increases in winter flows are smaller than the predicted increases in monsoon and post-monsoon flows. The increases in winter flows could be due to the groundwater contribution to the river flow. As the rainfall is expected to increase in future, this will cause higher infiltration which is reflected in the groundwater contribution. The Koshi River basin is particularly suitable for groundwater recharge, as around 47% of the total catchment is covered with grass-land. Baseflow Alpha Factor (ALPHA_BF.gw) and Groundwater Delay Time (GW_DELAY.gw) are sensitive SWAT parameters for the Koshi River basin. The ALPHA_BF.gw is related to the baseflow recession and GW_DELAY.gw is related to the lag between the times that water exits the soil profile and enters the shallow aquifer.

The pre-monsoon flow is expected to decrease in the short-term period, which might be due to decreases in precipitation. However, pre-monsoon flows might increase by 9 to 11% and 15 to 21% in the mid-century and end-of-century periods respectively. Monsoon flows are expected to increase by 13 to 15%, 18 to 26% and 24 to 52% in the short-term, mid-century and end-of-century periods respectively. Higher monsoon floods are expected in the future. This is likely as precipitation is also projected to increase by 10 to 13%, 15 to 21%, and 20 to 44% in the short-term, mid-century and end-of-century periods respectively. In post-monsoon season, mean river flows are expected to increase by 50 to 54%, 62 to 87% and 68 to 128% in the short-term, mid-century and end-of-century periods respectively. Although the relative increase in projected flows in the post-monsoon season is higher than other seasons, the

absolute increase is less compared to monsoonal flows. The higher increase in the post-monsoon season is due to shift (translation) in the peak flow from July to early September.

Table 6.3: Absolute and relative changes in projected annual and seasonal flows of the Koshi River.

Average annual/ seasonal flow	Short-term				Mid-century				End-of-century			
	RCP4.5		RCP8.5		RCP4.5		RCP8.5		RCP4.5		RCP8.5	
	Absolute *	Relative #	Absolute *	Relative #	Absolute *	Relative #	Absolute *	Relative #	Absolute *	Relative #	Absolute *	Relative #
Annual	404	16	452	18	567	22	785	31	720	28	1449	57
Winter	98	17	72	13	113	20	121	21	132	23	223	39
Pre-monsoon	-44	-6	-2	0	79	11	68	9	115	15	154	21
Monsoon	818	13	1001	15	1183	18	1682	26	1585	24	3362	52
Post-monsoon	906	54	828	50	1030	62	1451	87	1139	68	2131	128

*Absolute values in m³/s and #relative values in %.

Changes in projected annual and seasonal river flows in the short-term, mid-century and end-of-century periods are shown in Figure 6.13. Mean annual river flows will most likely follow an increasing trajectory under both the RCP4.5 and RCP8.5 climate change scenarios. Similarly, river discharges are projected to increase in the future in all seasons, except for the pre-monsoon season during the short-term period.

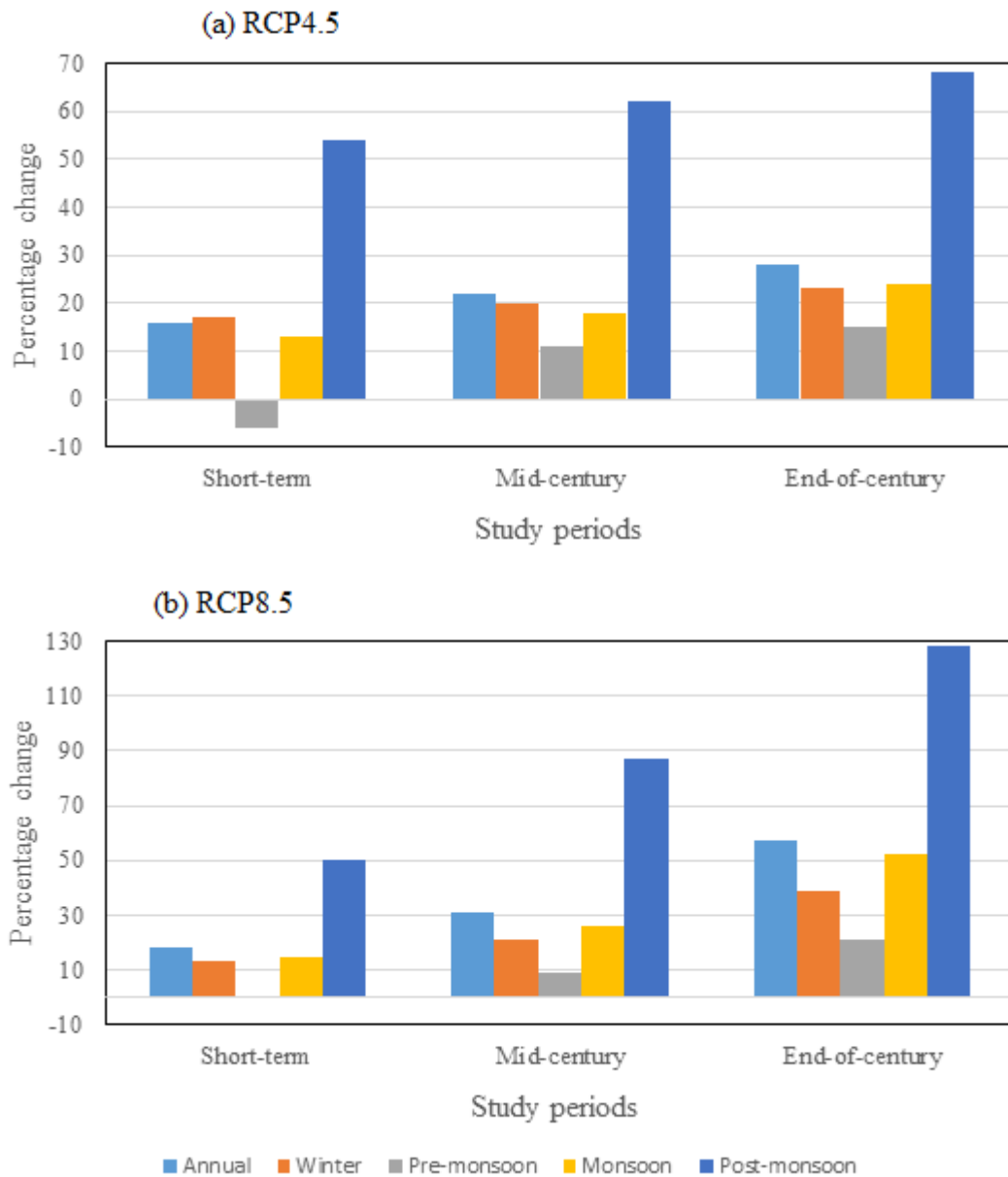


Figure 6.13: Changes in projected annual and seasonal river flows in percentage.

The percentage changes in minimum and maximum average monthly flows for three study periods in the Koshi River at Chatara are shown in Figure 6.14. The minimum average monthly flow is selected based on projected minimum average annual river

flows among the results drawn from four GCMs/ensembles for each climate scenario and study period. Likewise, the maximum average monthly flow is selected based on projected maximum average annual river flows among the results drawn from four GCMs/ensembles for each climate scenario and study period. Both the minimum and maximum average monthly flows indicate that river flows in August-March are likely to increase in future. The minimum increases in projected river flows are around 17 to 26% for climate change scenario RCP4.5 and 11 to 36% for climate change scenario RCP8.5 in January, 19 to 26% for RCP4.5 scenario and 9 to 26% for RCP8.5 scenario in February, and 6 to 15% for RCP4.5 scenario and 6 to 16% for RCP8.5 scenario in March in future periods. The minimum increases in projected river flows in August, September, October, November and December are high compared to January, February and March (see Figure 6.14). However, the minimum average monthly flows indicates that river flow is likely to decrease in April, May, June and July in future periods.

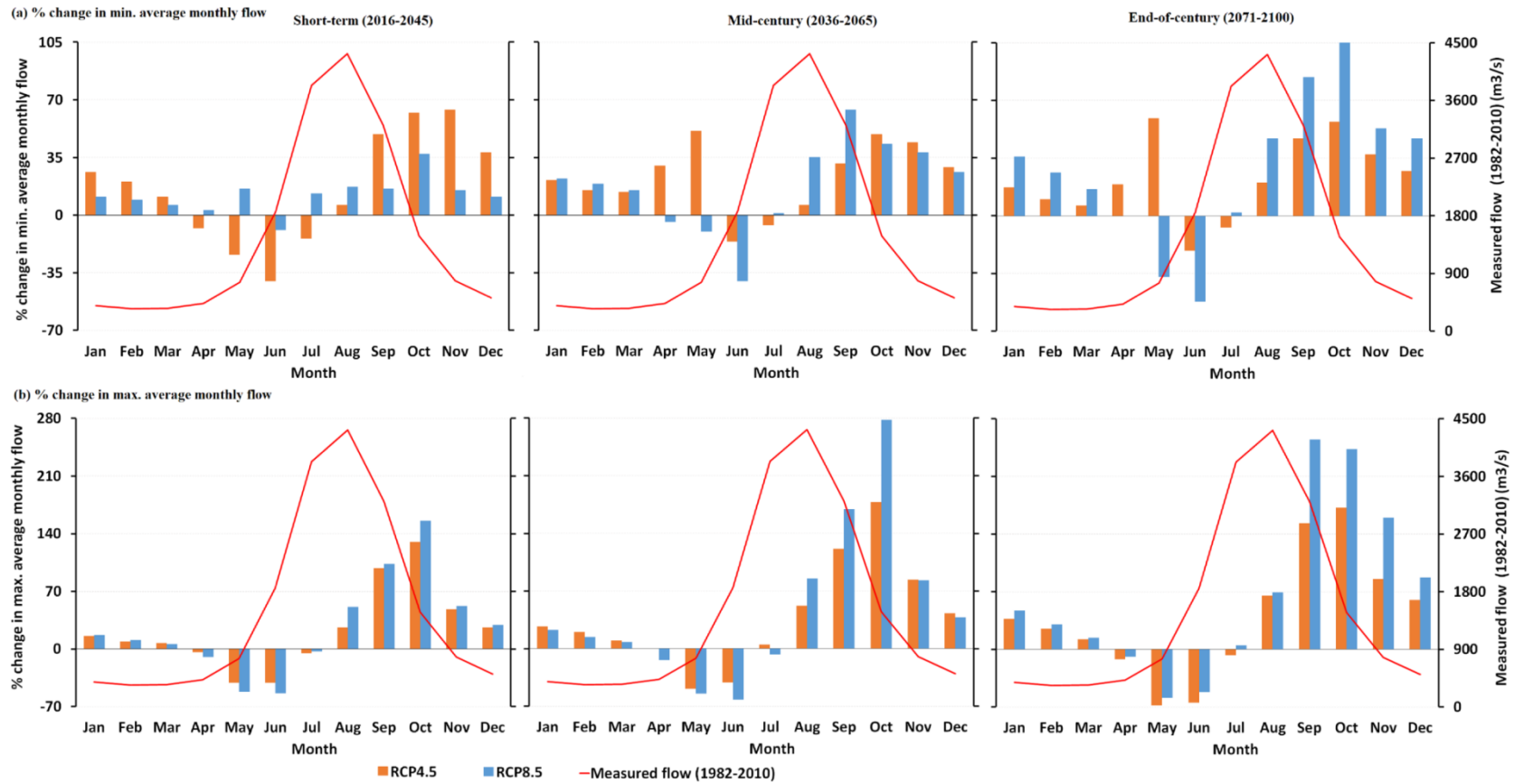


Figure 6.14: Percentage change in average minimum and maximum monthly river flows of the Koshi River at Chatara. Future projections are relative to the reference data for 1981–2010.

Figure 6.15 shows an average monthly river flows with standard deviation at Chatara on the Koshi River based on four GCMs/ensembles selected for climate change scenarios RCP4.5 and RCP8.5 considering the short-term, medium-term and end-of-century periods. The black line represents the average monthly river flow based on the reference period. The blue and red lines represent the corresponding average monthly river flow based on the ensemble outcomes of the GCMs selected for climate change scenarios RCP4.5 and RCP8.5 respectively. The sky blue and pink shaded areas represent the standard deviation based on the ensemble outcomes of the GCMs selected for climate change scenarios RCP4.5 and RCP8.5 respectively. The future flow is increasing specially during the monsoon and post-monsoon seasons. The magnitude of increase is higher in climate change scenario RCP8.5 than in RCP4.5 scenario. The monsoon flow is consistently increasing towards the end-of-century compared to recent time periods. It may be because the projection of precipitation also indicates higher increases in the monsoon and post-monsoon seasons. The peak flow shifted from July (in the reference period) to August (in the future period) in all time periods and both RCPs. The uncertainty of future flows is higher in the distant future compared to recent periods. The pre-monsoon flow is projected to decrease in the short-term. In the medium-term and end-of-century periods, the pre-monsoon flows are projected to increase less than in the winter, monsoon and post-monsoon periods. This may be because pre-monsoon precipitation is projected to decrease in the future, and precipitation would be in the form of rainfall rather than snowfall in the winter, due to increases in temperature. Therefore, the pre-monsoon flow which was due to snowmelt in the reference period would lessen in the future periods.

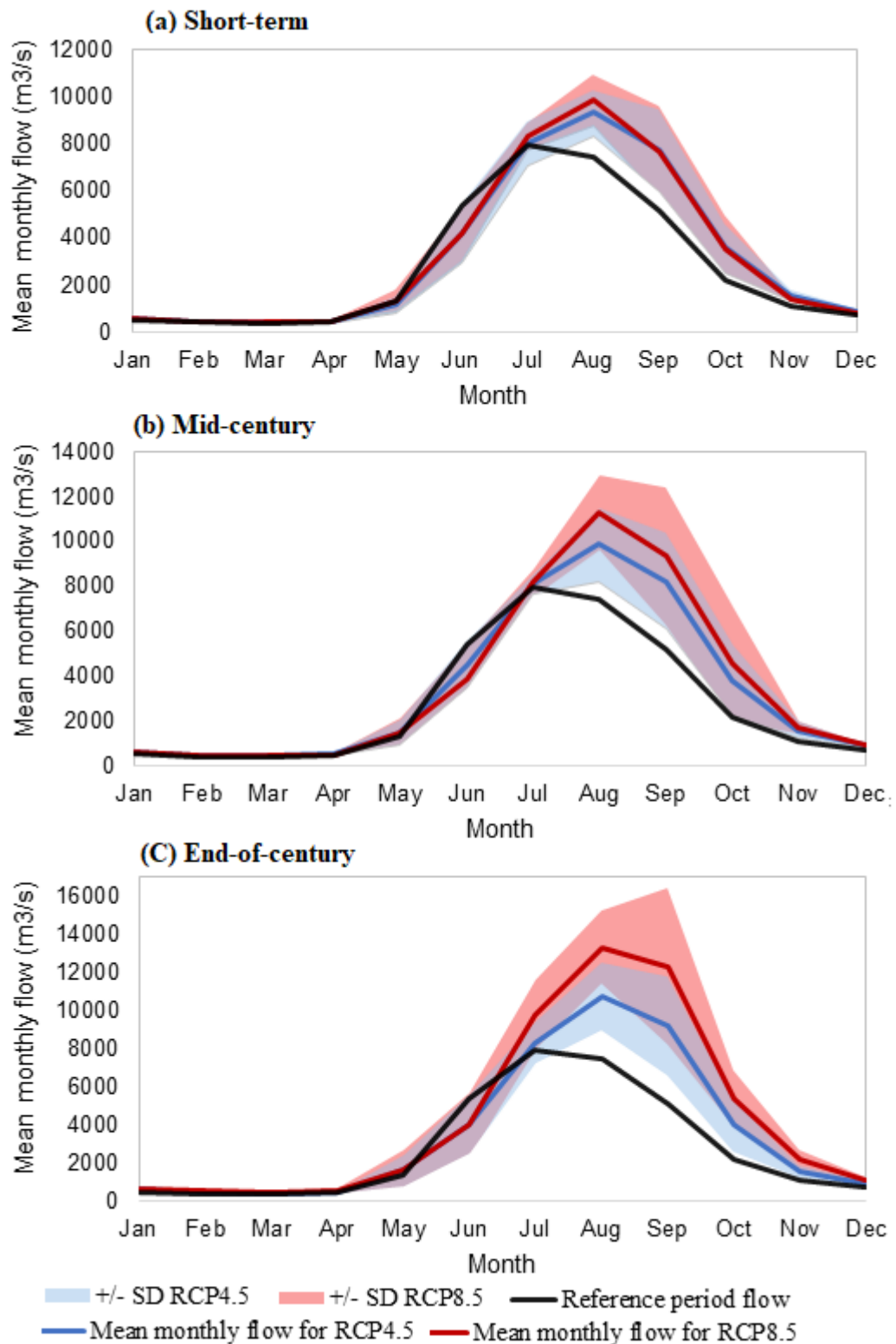


Figure 6.15: Monthly average river flow with standard deviation at Chatara of the Koshi River.

Overall, the average annual river flow (ensemble mean) is projected to increase in future in the Himalayan Koshi River basin. Immerzeel et al. (2012) and Lutz et al. (2014) have also reported that river flows in Himalayan river basins are projected to increase due to increased precipitation and temperature. Temperature increases have resulted in a rapid decline of the glacier area in Nepal (Shrestha and Aryal, 2011), and are likely to continue into the future, which in turn will contribute to increases in river flow. Similar studies have shown that river flows in most of the rivers in Nepal are likely to increase in future. For example Shrestha et al. (2016), Dahal et al. (2016), Bajracharya et al. (2018), Mishra et al. (2018), Pandey et al. (2019), and Dahal et al. (2020) assessed climate change impacts on hydrology of the Indrawati, Bagmati, Kaligandaki, Bheri, Chamelia, and Karnali River basins in Nepal respectively, and reported that annual river flows are projected to increase in future. The findings of this study also support findings of other studies in the Koshi River basin that water availability will most likely increase in the future (Bharati et al., 2019, Bharati et al., 2014, Devkota and Gyawali, 2015, Nepal, 2016). However, these studies on the Koshi River basin were based on low resolution climate data. This study has identified a range of possible future flows in the Koshi River and likely impact on irrigation water availability using high-resolution precipitation and temperature data. Uncertainty associated with future river flows needs to be taken into account while making decisions regarding water resources planning, development and management.

6.5 Conclusion

This study assessed the change in the hydrological regime of the Koshi River basin for the short-term, mid-century and end-of-century periods due to climate change. A methodology for the application of a suitable hydrological model to investigate the impacts of climate change on a river basin was developed and applied to the Koshi River basin.

The Soil and Water Assessment Tool (SWAT) hydrological model was selected for hydrological modelling, and then calibrated and validated based on the observed river flow data. Downscaled climate data, detailed in Kaini et al. (2020d), were used in the validated SWAT model to project the likely future water availability in the Koshi River basin. This study projected the future water availability at Chatara in the Koshi River

basin of Nepal in the short-term (2016-2045), mid-century (2036-2065) and end-of-century (2071-2100) time periods, considering the climate change scenarios RCP4.5 and RCP8.5. The findings for short-term periods could be immediately used by the National Planning Commission, Nepal for the forthcoming Five-Year Periodic plan.

Among the selected 22 SWAT parameters, 7 parameters - ALPHA_BF.gw, CN2.mgt, LAT_TIME.hru, CH_K2.rte, TLAPS.sub, GW_DELAY.gw and ESCO.hru - were found to be most sensitive for the Koshi River basin. The SWAT model performance for both calibration (NSE=0.87, PBIAS=-9.46, R²=0.95, KGE=0.75) and validation (NSE=0.86, PBIAS=-2.73, R²=0.93, KGE=0.65) periods was found to be very good.

The results from the selected GCMs/ensembles project the following likely future water availability at Chatara in the Koshi River basin.

- Annual flow: The average annual river flow is projected to increase for all scenarios and study periods. For the RCP4.5 climate change scenario, the average annual flow in the Koshi River is expected to increase by 16%, 22% and 28% in the short-term, mid-century and end-of-century periods respectively. Similarly, the average annual flow in the Koshi River, for the climate change scenario RCP8.5, is expected to increase by 18%, 31% and 57% in the short-term, mid-century and end-of-century periods respectively.
- Seasonal flows: The winter flow is expected to increase in future time periods by 17 to 23% and 13 to 39% for climate change scenarios RCP4.5 and RCP8.5 respectively. The pre-monsoon flow is expected to decrease in the short-term period; however, it is projected to increase by 9 to 11% and 15 to 21% in the mid-century and end-of-century periods respectively. The monsoon flow is expected to increase by 13 to 15%, 18 to 26% and 24 to 52% in the short-term, mid-century and end-of-century periods respectively. In post-monsoon season, mean river flow is expected to increase by 50 to 54%, 62 to 87% and 68 to 128% in the short-term, mid-century and end-of-century periods respectively.
- Based on RCP scenarios, the projected peak mean monthly flow for climate change scenario RCP4.5 is lower than the flow for RCP8.5 scenario for all study periods, and the difference in magnitude increases in future time periods. In short-term period, the projected peak mean monthly flow for climate change

scenarios RCP4.5 and RCP8.5 are 17% and 24% higher compared to the reference period. Likewise, the projected peak mean monthly flows for RCP4.5 and RCP8.5 scenarios in the mid-century period are 24% and 42% higher compared to the reference period. In the end-of-century period, the projected peak mean monthly flows for the climate change scenarios RCP4.5 and RCP8.5 are 35% and 67% higher compared to the reference period. Hence, higher floods are expected in future. A shift in the peak flow is expected in future, towards August-September.

- **Uncertainty:** The projected river flows based on selected ensembles in different climatic extremes show that there is a high uncertainty about future flows in the Koshi River. The uncertainty in projected annual river flows is high for the end-of-century period compared to mid-century period. Uncertainty in projected annual river flows is higher for climate change scenario RCP8.5 compared to RCP4.5 scenario in both the mid-century and end-of-century periods. The relative uncertainty in projected mean annual flows for RCP4.5 is 6-23%, 11-39% and 15-40% for short-term, mid-century and end-of-century respectively. Likewise, the relative uncertainty in projected mean annual flow for RCP8.5 is 12-29%, 16-54% and 25-70% for short-term, mid-century and end-of-century respectively.

Chapter 7: Crop water assessment for irrigation water requirement

The aim of this chapter is to investigate irrigation water requirements for winter wheat crops under climate change scenarios. Water availability in the Koshi River for irrigating the Sunsari Morang Irrigation Scheme command area is sufficient in the monsoon season; however, it is in limited supply in the winter and spring seasons. The cropping area in the Sunsari Morang Irrigation scheme command area is larger in the winter season compared to the spring season. Winter wheat crops were chosen here for assessment because wheat is the main crop during winter, and the supply of water throughout the Sunsari Morang Irrigation Scheme command area is critical to the success of these crops. The Sunsari Morang Irrigation Scheme has been considered for the crop water assessment for irrigation water requirements considering climate change impacts on the demand side of irrigation water.

7.1 Understanding local stakeholders' needs and crop area coverage under irrigation scheme

Stakeholders are generally associated with the development and management of irrigation schemes in developing countries like Nepal. These stakeholders include local farmers, the Water Users' Association (WUA), federal and provincial district irrigation department officials, agricultural department officials, groups of local traders supplying agricultural goods and purchasing agricultural products from the farmers, and other local agencies (governmental and non-governmental) associated with the irrigation scheme (Kaini et al., 2020a). The WUA of an irrigation scheme connects agencies directly associated with the irrigation scheme and the local farmers. The federal and provincial district irrigation offices are generally responsible for the management, operation and development of irrigation schemes.

Studies have shown that cropping areas in Nepalese irrigation schemes could be increased by providing optimal irrigation water at the farm level, changing the conventional paradigm of subsistence farming into a market-oriented model, adapting an appropriate land tenancy (landowner–tenant) model in crop production (Kaini et al., 2020a). They also reported that cropping areas could be increased by providing proper market facilities, ensuring the availability of machinery (thresher machines, mini-tractors), increasing sources of organic manure, farmer training, and farmers' visits to

example farmlands and other facilities where knowledge and information sharing are made available. This study also mentioned that coordination between the Water Users' Association, the district irrigation development office and the district agriculture development office is crucial for intensifying crop area coverage.

Socio-economic conditions of landowner and tenant farmers also impact on crop area coverage in an irrigation scheme. Year-round availability of irrigation water, selection of appropriate crops, land tenancy rules, and crop rotation are the key factors in motivating tenant farmers to increase cropping intensity (Kaini et al., 2020a). The cropping intensity is the ratio of the total cropped area to the command area of the irrigation scheme. It represents the frequency of crops planted on the same irrigated land per year, within the entire irrigation command area.

Water availability for irrigation during the growing season is one of the crucial components for increasing the cropped area. Research on climate change impacts on the flows in the Koshi River has projected that the average flow in the Koshi River, the water source of the Sunsari Morang irrigation scheme, is projected to increase during the mid-century and end-of-century periods (Kaini et al., 2020a). Furthermore, based on projections of average minimum monthly river flows, this study also suggested that river flows would increase in the winter and monsoon seasons.

7.2 Crop types and cropping intensity in the Sunsari Morang Irrigation Scheme

The main crops grown in the command area of the Sunsari Morang Irrigation Scheme are monsoon paddy rice, sugarcane, pulses, vegetables and other crops in the monsoon period (June/ July to October/November); wheat, pulses, oilseed, maize, sugarcane, potato, and vegetables in the winter period (November/December to March/April); and spring paddy rice, pulses, oilseed, maize, sugarcane, jute, vegetables and others in the spring season (April/May to June/July). The main crops and their average planted area in the Sunsari Morang Irrigation command area during 2008–2016 are shown in Table 7.1.

Table 7.1: Main crops and their planted area in the Sunsari Morang Irrigation command area in the period 2008-2016.

Season of the year	Crop type	Area covered (ha)
Monsoon season	Monsoon paddy	56900
	Sugarcane	2100
	Pulses	300
	Vegetables	400
	Others	1100
Winter season	Wheat	26000
	Pulses	8400
	Oilseed	2400
	Maize	1300
	Sugarcane	2000
	Potato	1200
	Vegetables	1300
	Others	1300
Spring season	Spring paddy	14000
	Pulses	4800
	Oilseed	600
	Maize	2600
	Sugarcane	2800
	Jute	900
	Vegetables	1500
	Others	1200

The average crop area coverage in the monsoon season by monsoon paddy rice, sugarcane, pulses, vegetables and other crops are 56,900 ha, 2,100 ha, 300 ha, 400 ha, and 1,100 ha respectively. The total irrigated area in the monsoon season is around 60,800 ha, with monsoon paddy rice being the dominant crop. The average crop area coverage in the winter season by wheat, pulses, oilseed, maize, sugarcane, potato, vegetables and other crops are 26,000 ha, 8,400 ha, 2,400 ha, 1,300 ha, 2,000 ha, 1,200 ha, 1,300 ha, and 1,300 ha respectively. The total irrigated area in the winter season is

around 43,900 ha, with the dominant crop being winter wheat (around 60% of irrigated area), followed by pulses and oilseed crops. The average crop area coverage in the spring season by spring paddy rice, pulses, oilseed, maize, sugarcane, jute, vegetables and others crops are 14,000 ha, 4,800 ha, 600 ha, 2,600 ha, 2,800 ha, 900 ha, 1,500 ha, and 1,200 ha respectively. The total irrigated area in the spring season is around 28,400 ha, with spring rice and pulses being the dominant crops. Overall, the total cropped area in the Sunsari Morang Irrigation Scheme in a year is 133,100 ha (the sum of cropped area in monsoon, winter and spring seasons). Since the command area of the Sunsari Morang Irrigation Scheme is 68,000 ha, the cropping intensity (the ratio of total cropped area to command area) is 195%. More details on cropping intensity are described in Kaini et al. (2020a).

7.3 Selection of Agricultural Production Systems Simulator (APSIM) crop model for crop growth and irrigation water assessment

An increasing pressure on food production system has been realised to meet the growing food demand for increasing population (Ramankutty et al., 2018). Increase in food production per unit agricultural land (ton/hectare) as well as grain yield per unit irrigation water (ton/mm of water), are required in coming decades to fulfil the demand of growing population in the climate change context. Crop models can predict grain yield per unit of agricultural land (ton/hectare) and grain yield per unit of irrigation water (ton/mm of water) under present and future climate. Crop models integrate crop development processes and their response to surrounding environment. Boote et al. (1996) reported that crops models are required to improve crop system decision making process, enhance research knowledge, and analyse policy alternatives for improving cropping systems. Crop models improve our knowledge on crop development, growing stages and grain yield (Chenu et al., 2017). Challinor et al. (2018) reported that crop models could be applied for risk assessment in food production system and preparing adaptation strategies to cope with climate change impacts on crop grain yield. Crop models are efficient tools to optimize current crop grain yields and irrigation scheduling, predict the future grain yields and irrigation water requirements, and suggest possible solutions to enhance cropping system. Crop models have been developed to incorporate cropping systems with profitability and sustainability, grain

quality, biotic effects, responses to changed climatic factors, project climate change impacts crop development and grain yield (Chenu et al., 2017).

7.3.1 Selection of crop model

Crop models have been extensively used to assess crop growth, development, water uptake, stresses due to various factors (water, nitrogen, and temperature) and crop grain yield. Among the many crop models available, a few models like the Agricultural Production Systems Simulator (APSIM), the Decision Support System for Agrotechnology Transfer (DSSAT), CROPWAT, AquaCrop, ORYZA, CERES, Dynamic Computable General Equilibrium (DCGE), CropSyst, and Simple Simulation Models (SSM) have been successfully verified in crop modelling in many farmlands around the world (Kabir et al., 2018, Soltani and Sinclair, 2015).

However, cropping system models, including DSSAT, CROPWAT, AquaCrop, ORYZA, CERES, DCGE, can represent actual farm practices depending on the complexity of the adaptation being modelled (Harrison et al., 2017, Harrison et al., 2011, Kabir et al., 2018). Soltani and Sinclair (2015) compared simpler crop models: CropSyst and SSM, and complex models: APSIM and DSSAT. They reported that (a) APSIM, CropSyst and DSSAT can simulate crop management effects like tillage and straw mulch while SSM cannot, and (b) access to the model codes is free for APSIM and SSM, however, CropSyst and DSSAT provide (limited) access to the codes after permission is granted. APSIM has the complexity needed in describing the soil, plant and atmospheric processes to be able to reliably simulate climate change impacts on cropping systems, and is simple enough that does not take too long time to setup and run.

APSIM is a modelling framework that allows individual sub-models (biophysical, management, data input and output, and simulation engine) to be linked to simulate farming system performance (Keating et al., 2003). APSIM has been developed by the Agricultural Production Systems Research Unit (APSRU), a collaborative group drawing upon expertise from Australia's Commonwealth Scientific and Industrial Research Organisation (CSIRO) and Queensland State Government agencies. APSIM combines biophysical and management modules to simulate cropping systems at a daily time-step. Different sub-models in APSIM includes meteorological data, surface

organic matter, management options (like crop type, crop sowing window, crop density, irrigation and fertilizer application etc.), soil water, soil organic matter, initial nitrogen, initial water, physical and chemical properties of soil. Management options like wheat crop, soil water, soil and residue are most relevant to the simulation of wheat-based cropping systems (Asseng et al., 1998). APSIM is able to effectively simulate different crop types including paddy rice, wheat, chickpea, canola, cotton, maize, millet, mung bean, sorghum and sunflower (APSIM-Crop Module Documentation, 2020, Harrison et al., 2019, Liu et al., 2011, Pembleton et al., 2016).

The APSIM-Wheat model has been developed for wheat crop modelling within the APSIM model framework (Zheng et al., 2015). The APSIM-Wheat module simulates crop growth, development, water and nitrogen uptake, crop nitrogen concentration, stresses (water, nitrogen, temperature), grain yield and the response of the crop to these stresses (Keating et al., 2003). The APSIM-Wheat model has been successfully calibrated and validated many parts of the world, including Australia (Asseng et al., 1998, Dreccer et al., 2018, Flohr et al., 2017, Houshmandfar et al., 2018, Luo and Kathuria, 2013, Peake et al., 2014, Zhao et al., 2014a, Harrison et al., 2012, Phelan et al., 2015), China (Bai et al., 2020, Chen et al., 2010a, Chen et al., 2010b, Zhang et al., 2013, Zhao et al., 2014b, Liu et al., 2020b), Ethiopia (Sida et al., 2018) and Iran (Deihimfard et al., 2015). Moreover, it has also been successfully applied in the South Asia region, including India (Mohanty et al., 2012, Singh et al., 2011, Singh et al., 2015), Bangladesh (Hasan et al., 2019, Kabir et al., 2018) and Pakistan (Anser et al., 2020, Haider et al., 2015, Khaliq et al., 2019).

7.3.2 APSIM crop modelling

The APSIM model has been selected for this research as it is capable of simulating the effects of climate change impacts on crop development, growth, grain yield and biomass yield. The main processes addressed in APSIM modelling include phenological development, soil water, biomass accumulation, soil nitrogen and carbon (Zheng et al., 2015).

Phenological development: There are 11 phases in the APSIM-Wheat module. They are sowing, germination, emergence, end of juvenile, floral initiation, flowering, start of grain filling, end of grain filling, maturity, harvest, end crop. Phenology is very

important in determining grain yield for any given wheat variety by climate combination. This is separate to other grain yield determining factors such as nutrients (nitrogen), water stress, planting density etc. The timing of each phase (except between sowing and germination, which is driven by sowing depth and soil moisture) is determined by the accumulation of thermal time adjusted for other factors which vary with the phase considered e.g. vernalisation, photoperiod, and nitrogen (Zheng et al., 2015). The daily thermal time is calculated from the daily average of maximum and minimum crown temperatures, and is adjusted by genetic and environmental factors. The details on phenological development can be found in *APSIM-Wheat Module Documentation* (Zheng et al., 2015).

Soil water: Crop water supply is governed by the drained upper limit of soil, the lower limit of plant-extractable soil water, and root water uptake from each soil layer. Potential extractable soil water is the difference between the drained upper limit (field capacity) and the lower limit of plant-extractable soil water for each soil layer. The actual extractable soil water is the difference between the soil moisture content and the lower limit of plant-extractable soil water for each soil layer. The details on soil water and soil water stress can be found in *APSIM-Wheat Module Documentation* (Zheng et al., 2015).

Biomass accumulation: In the APSIM-Wheat module, biomass is partitioned into root biomass and above-ground biomass. The above-ground biomass includes head, leaf and stem. Head includes grain and pod (spike without grain). Leaf includes leaf blades only. Stem includes plant stems and leaf sheaths. The details on biomass accumulation can be found in *APSIM-Wheat Module Documentation* (Zheng et al., 2015).

Nitrogen: In the APSIM-Wheat module, total nitrogen demand is the sum of the nitrogen demand in all parts of the wheat including head, leaf, stem, and head. Grain nitrogen demand starts at anthesis (i.e. flowering) and is the highest nitrogen sink of all the plant components. Nitrogen demand on any day include demands from the pre-existing biomass of each part and the nitrogen required for biomass produced on that day. Nitrogen demand in each part (except grain) is driven by the plants' behaviour to maintain nitrogen at the critical (non-stressed) concentration level. The details on

nitrogen demand and nitrogen stress can be found in *APSIM-Wheat Module Documentation* (Zheng et al., 2015).

7.4 Approach for crop modelling using APSIM

The overall methodology for the APSIM modelling is schematised in Figure 7.1. The main steps in the APSIM modelling include input data processing and model development/set up, calibration, validation, scenario analysis and output. These steps are described in the following sections:

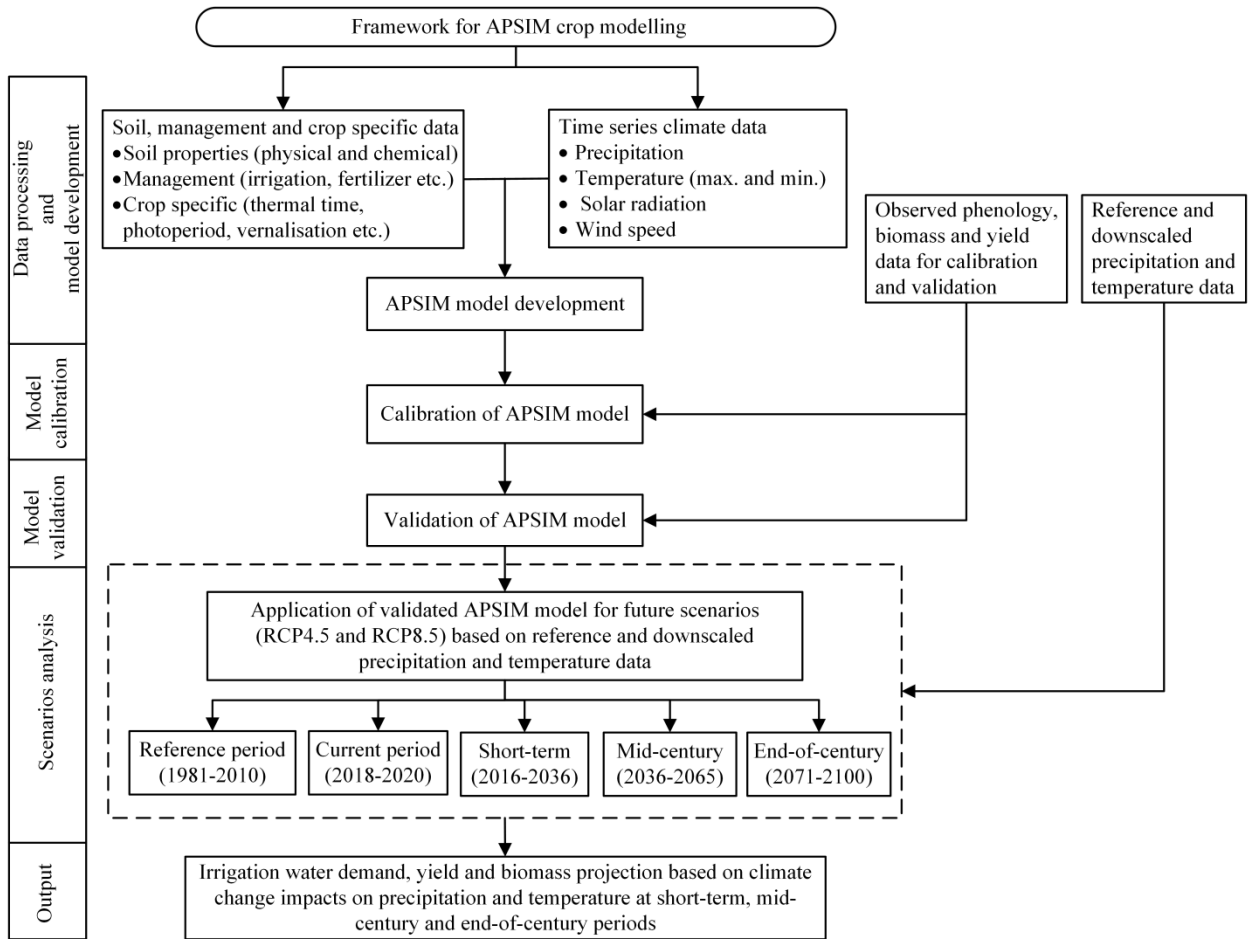


Figure 7.1: Flowchart of overall methodology for this study, including crop modelling, climate change impacts and summarization of outputs.

7.4.1 APSIM input data processing and model development (Model initialisation)

APSIM input data include soil data, crop specific data, management data and time series climate data. The observed phenology, biomass yield and grain yield data for winter wheat crops are used for the calibration and validation of the APSIM crop model. The

APSIM model was initialised following Harrison et al. (2019) for the winter wheat crop (Nepal 297 variety) using the data set for the study area. The climate data for the Sunsari Morang Irrigation command area from APSIM Next Generation (Holzworth et al., 2018) for the years 2016-2020 was adopted here. The management data used are that as measured in the field. The soil data are used as per laboratory test results. The latest version of APSIM at the time of performing this research, version 7.10-r4158, was used for this research.

7.4.2 Model calibration

After model initialisation (APSIM model development as mentioned in 7.4.1), the model was calibrated with observed phenology, biomass yield and grain yield data for the winter wheat crop. Crop specific parameters such as photoperiod, vernalisation and thermal time period were generally adjusted in the wheat base cultivar available in APSIM for model calibration. Observed phenology, biomass yield and grain yield data drawn from the Sunsari Morang Irrigation Scheme command area for the period 2018-2019 were used for the calibration of the APSIM model. Calibration was conducted by minimising the sum of squared differences between observed and simulated data, similar to that described by Harrison et al. (2019).

7.4.3 Model validation

The calibrated APSIM model (as mentioned in section 7.4.2) was validated for the winter wheat crop using observed phenology, biomass yield and grain yield data drawn from the Sunsari Morang Irrigation Scheme command area for the period 2019-2020. Validation was conducted by minimising the sum of squared differences between observed and simulated data, similar to the methodology described by Harrison et al. (2019).

7.4.4 Scenario analysis

The validated APSIM model (as mentioned in section 7.4.3) was applied to predict irrigation water demand, grain yield and biomass yield based on changes in precipitation and temperature data for different time periods and climate scenarios. The short-term (2016-2045), mid-century (2036-2065) and end-of-century (2071-2100) periods with the downscaled precipitation and temperature data for climate change scenarios RCP4.5 and RCP8.5 were considered for the future scenarios. Changes in

future periods are compared with the reference (base) period (1981-2010) data. In addition, irrigation levels required to achieve potential grain yields under current farm condition were also compared with existing observed irrigation practice.

7.5 Application of methodology for APSIM crop modelling

The application of the methodological framework described in Figure 7.1 is described in the following sections.

7.5.1 APSIM input data processing and model development (model initialisation)

The APSIM model was developed using soil data, crop specific data, management data and time series climate data as mentioned in section 7.4.1. The developed APSIM model was used for model calibration.

Location of selected farm plots: Three farm plots were selected from a command area within the Bariyati branch canal, an undeveloped command area, to monitor winter wheat crop in cropping season 2018-2019 and 2019-2020. Using the soil map produced by Government of Nepal, these farm plots were chosen because they were comprised of the dominant soil type in the irrigation command area. In addition, the farmers' willingness to provide the land for experimental activities and vicinity to a house to closely monitor field activities were also considered. Such fragmented land holding patterns and irregular shaped farm plots are common in the Sunsari Morang Irrigation Scheme command area. Within the small fragmented plots of land, farmers grow wheat, pulses, oilseed, maize, sugarcane, potato and vegetables in the winter season. Winter wheat is the main crop in the winter season. The selected field plot sizes vary from 1,231 m² to 3,772 m² in cropping season 2018-2019, and 670 m² to 2,370 m² in cropping season 2019-2020. The geographical location of field plot 1 is 26°34'17.72"N 87°25'19.19"E (Datum: WGS 1984). Likewise, the geographical location of field plot 2 is 26°34'16.18"N 87°25'21.50"E (Datum: WGS 1984). Similarly, the geographical location of field plot 3 is 26°34'16.39"N 87°25'29.39"E (Datum: WGS 1984). The location of selected field plots is shown in Figure 7.2.

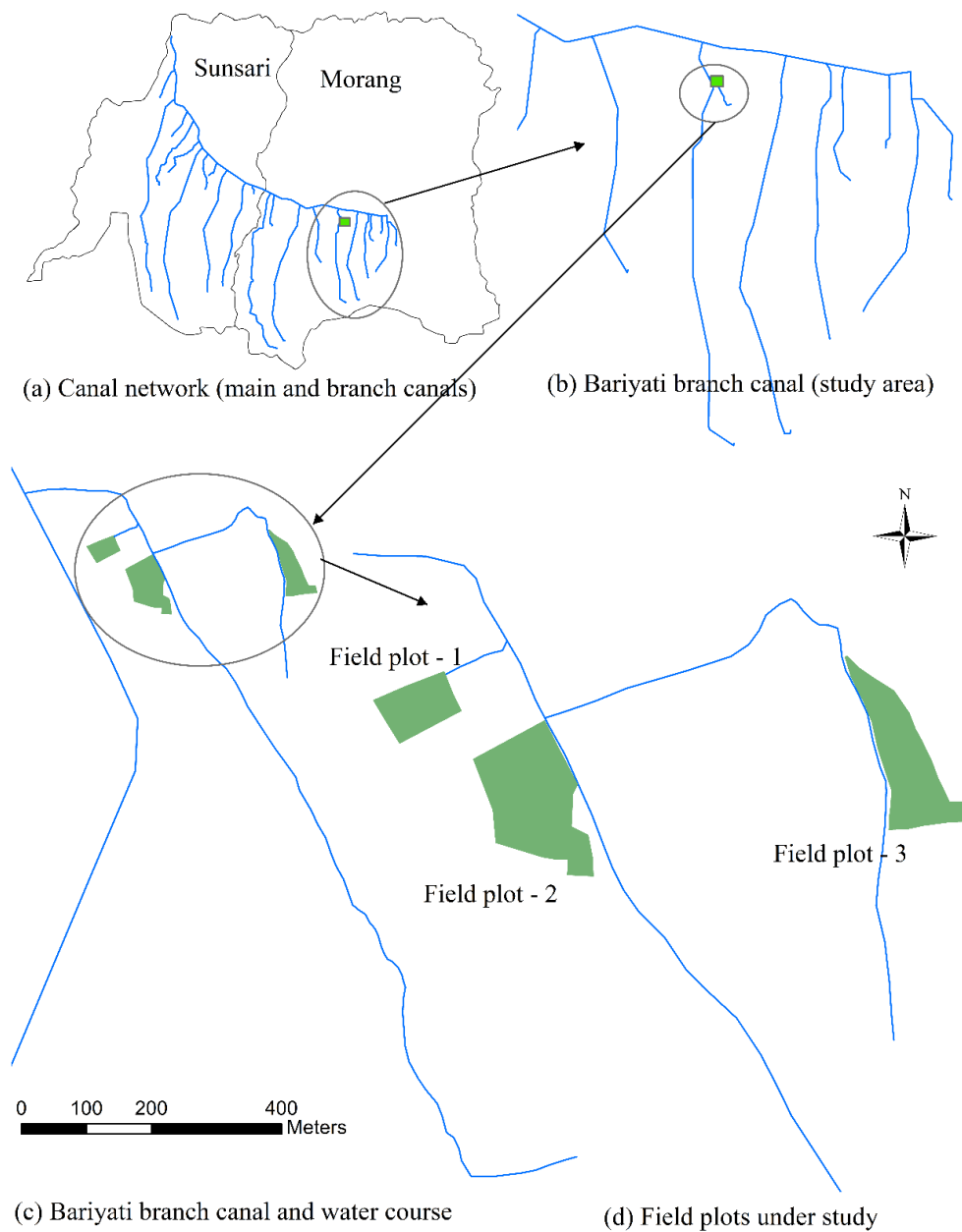


Figure 7.2: Location of selected field plots used for APSIM Wheat module calibration and validation.

Soil data: Soil samples were collected from the Sunsari Morang irrigation command area at a depth of 0-10, 10-20, 20-30, 30-50, 50-70 and 70-90 cm from three field plots. The soil samples were measured in soil laboratories in Australia and Nepal. Soil properties included both physical and chemical properties. Main soil physical properties assessed included bulk density (BD), air-dry (AD), lower limit-LL15 (wilting point), drained upper limit-DUL (field capacity), saturated volumetric water contents (Sat),

saturated hydraulic conductivity (Ks) and soil texture, as shown in Table 7.2. The bulk density was measured using a cylindrical galvanised iron pipe having 7 cm diameter and 7.5 cm height. Standard value of saturated hydraulic conductivity (Ks) was taken from Dingman (2015).

Table 7.2: Soil physical properties - bulk density (BD), air-dry (AD), lower limit-LL15 (wilting point), drained upper limit-DUL (field capacity), saturated volumetric water contents (Sat), saturated hydraulic conductivity (Ks), plant available water capacity (PAWC) and soil texture.

Depth (cm)	BD (g/cc)	AD (mm/mm)	LL15 (mm/mm)	DUL (mm/mm)	Sat (mm/mm)	Ks (mm/day)	Wheat PAWC (138.6 mm)	Texture
0-10	1.35	0.01	0.157	0.374	0.414	600	21.7	Loam
10-20	1.4	0.01	0.169	0.38	0.443	600	21.1	Loam
20-30	1.35	0.01	0.137	0.319	0.356	600	18.2	Sandy loam
30-50	1.38	0.01	0.171	0.312	0.349	600	28.2	Sandy clay loam
50-70	1.5	0.01 1	0.186	0.315	0.331	600	25.8	Sandy clay loam
70-90	1.49	0.01 1	0.184	0.302	0.359	600	23.6	Sandy clay loam

The main soil chemical properties measured included electrical conductivity (EC), pH, chloride (CL), boron (B), cation exchange capacity (CEC), calcium (Ca), Magnesium (Mg), Sodium (Na), Potassium (K), exchangeable sodium percentage (ESP) and Manganese (Mn), as shown in Table 7.3.

Table 7.3: Soil chemical properties - electrical conductivity (EC), pH, chloride (CL), boron (B), cation exchange capacity (CEC), calcium (Ca), Magnesium (Mg), Sodium (Na), Potassium (K), exchangeable sodium percentage (ESP) and Manganese (Mn).

Depth (cm)	EC (1:5 dS/m)	pH	CL (mg/kg)	B (mg/kg)	CEC (cmol+/kg)	Ca (cmol+/kg)	Mg (cmol+/kg)	Na (cmol+/kg)	K (cmol+/kg)	ESP (%)	Mn (mg/kg)
0-10	1.5	5.1	14.2	0.04	10.68	3.82	1.45	0.2	0.118	1	1.63
10-20	1.5	5.4	10.65	2.2	10.67	3.37	1.38	0.21	0.112	1	3.02
20-30	1.5	6	7.1	0.05	10.45	3.52	1.25	0.23	0.164	1	5.72
30-50	1.5	6.1	7.1	1.57	10.68	4.61	1.25	0.12	0.146	1	4.66
50-70	1.1	6.2	10.65	0.04	10.67	5.05	2.4	0.13	0.139	1	4.66
70-90	1.3	6.2	10.65	1.07	10.23	4.3	1.26	0.12	0.139	1	5.14

Management data: The main management data gathered included sowing date, sowing density (plants/m²), sowing depth, fertilizer applied at sowing, and subsequent fertilizer application. These data were taken as per actual field conditions. For model calibration (2018-2019), sowing date, sowing density, sowing depth, fertilizer applied at sowing and subsequent fertilizer application were 7 December 2018, 125 plants/m², 15 mm, DAP: 87 kg/ha, and UREA-Nitrogen 70 kg/ha, respectively. Likewise, for model validation (2019-2020), sowing date, sowing density, sowing depth, fertilizer applied at sowing and subsequent fertilizer application were 12 December 2019, 130 plants/m², 15 mm, DAP:110 kg/ha, and UREA-Nitrogen 150 kg/ha, respectively.

Irrigation data: The volume of canal water applied to the irrigated wheat field was measured using a triangular V-notch (90°) weir. Applied irrigation water was measured in the water course supplying water to the experimental field. The size of the triangular V-notch varied with the width of the canal section. The distance between the end of V-shaped triangle at top and the edge of the canal should be at least 2 x the maximum head at the V-notch weir. Likewise, distance between the end of V-shaped triangle at the bottom and the bed of the canal should be at least 2 x the maximum head at the V-notch weir as shown in Figure 7.3.

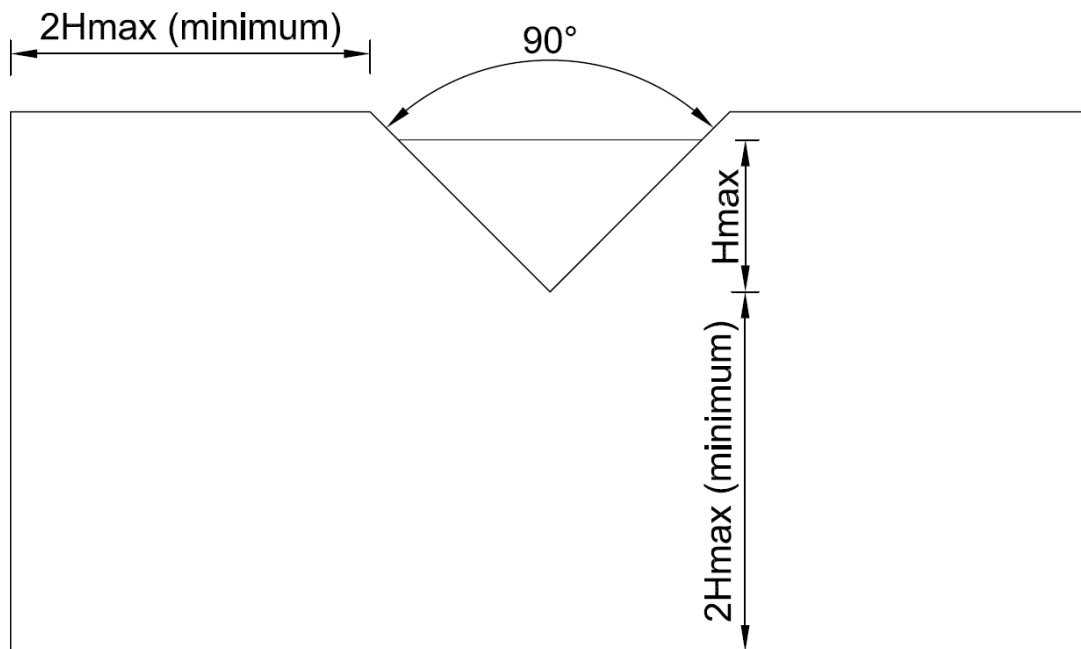


Figure 7.3: A triangular V-notch (90°) weir used to measure irrigation water supplied in the experimental field.

The hydraulic head over the V-notch crest was measured at various time interval and the water discharge passing through the V-notch was calculated using equation. 7.1 (Grant, 1989):

$$Q = K H^{2.5} \quad \text{Equation 7.1}$$

where Q is flow rate in cubic feet per second, H is the head on the weir in feet and K is a constant dependent on the angle of notch and unit of measurement. For a V-notch with a 90° angle and unit of measurement as cubic feet per second, K=2.5. The triangular V-notch used in the field is shown in Figure 7.4.

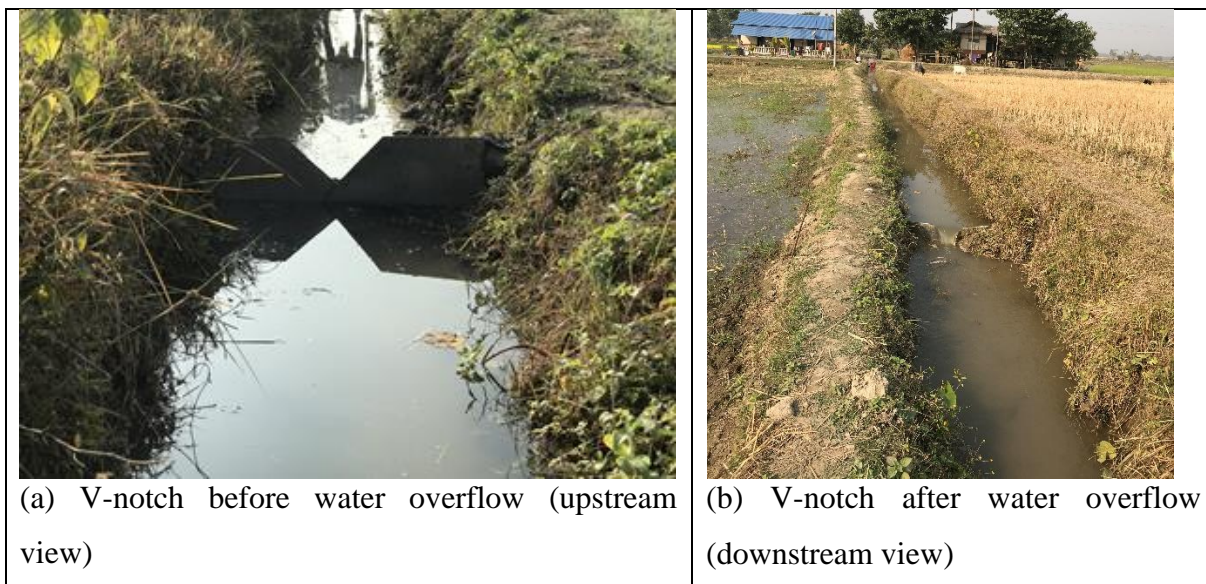


Figure 7.4: Triangular V-notch (90°) used in the field.

During the model calibration period for 2018-2019, the irrigation application was 92 mm (a single irrigation on 28 December 2018). Similarly, during the model validation period for 2019-2020, the irrigation application was 65 mm (from a single irrigation on 8 January 2020).

Crop specific data: The main crop specific data used included photoperiod, vernalisation, thermal time period and maximum grain size. Changes in crop specific parameter values like photoperiod, vernalisation and thermal time period are available in the APSIM wheat cultivar data base and were parameterised for the Nepal wheat variety because it was not part of the default APSIM release. Photoperiod, vernalisation and thermal time period parameters were adjusted for the Nepalese wheat variety. This adjustment was part of model calibration process.

Climate data: The main climate data used included daily precipitation, minimum temperature, maximum temperature, solar radiation and wind speed. The climate data for the Sunsari Morang Irrigation command area were obtained from the APSIM Next Generation (Holzworth et al., 2018) for the year 2016-2020.

7.5.2 Model calibration

Observed wheat phenology, biomass yield and grain yield data for the winter wheat crop in the Sunsari Morang Irrigation scheme command area for the period 2018-2019

were used for the calibration of the APSIM model. Rigorous systematic manual calibration was carried out for the calibration period (2018-2019) by changing photoperiod, vernalisation and thermal time period parameters for the wheat cultivar data base available in APSIM (following Harrison et al., 2011, Ibrahim et al., 2019, Liu et al., 2020b). The photoperiod and vernalisation parameters were adjusted to 4.0 and 2.4 respectively. To minimize the sum of squared residuals between measured and simulated data, the thermal time periods for end of juvenile, floral initiation and start grain fill were adjusted to 380°C days, 395°C days and 660°C days respectively. All other crop parameters were derived from the base cultivar.

The observed and simulated phenological days after sowing for the calibration (2018-2019) and validation (2019-2020) periods are shown in Table 7.4. The average observed sowing, emergence, floral initiation, start grain filling and harvest days after sowing for the calibration period (2018-2019) are 1, 7, 65, 91 and 127 days respectively. The simulated values are close to observed values. The simulated sowing, emergence, floral initiation, start grain filling and harvest days after sowing for calibration period are 1, 5, 65, 93 and 124 days respectively. The minimum (mean minus standard deviation) and maximum (mean plus standard deviation) standard deviations range for harvest days, based on three field plots, are 124 and 130 days after sowing for the calibration period. The simulated harvest days after sowing for the calibration period is within the standard deviation of the mean.

Table 7.4: Observed and simulated phenological days after sowing for the calibration (2018-2019) and validation (2019-2020) periods.

Phenological stage (Days after sowing)	Calibration		Validation	
	Observed	Simulated	Observed	Simulated
Sowing	1	1	1	1
Emergence	7	5	7	5
Floral initiation	65	65	65	67
Start grain filling	91	93	91	94
Harvest	127	124	126	125

The observed and simulated biomass yield and grain yield for the calibration (parameterisation) period are shown in Figure 7.5 (a). The average observed and simulated biomass yield are 7210 kg/ha and 7286 kg/ha respectively. The minimum and maximum standard deviations range for biomass yield, based on three field plots, are 6820 kg/ha and 7600 kg/ha. The simulated biomass yield for the calibration period is within the standard deviation of the mean. Likewise, the average observed and simulated grain yield are 1862 kg/ha and 1939 kg/ha respectively. The minimum and maximum standard deviations range for grain yield, based on three field plots, are 1623 kg/ha and 2101 kg/ha respectively. The simulated grain yield for the calibration period is within the standard deviation of the mean.

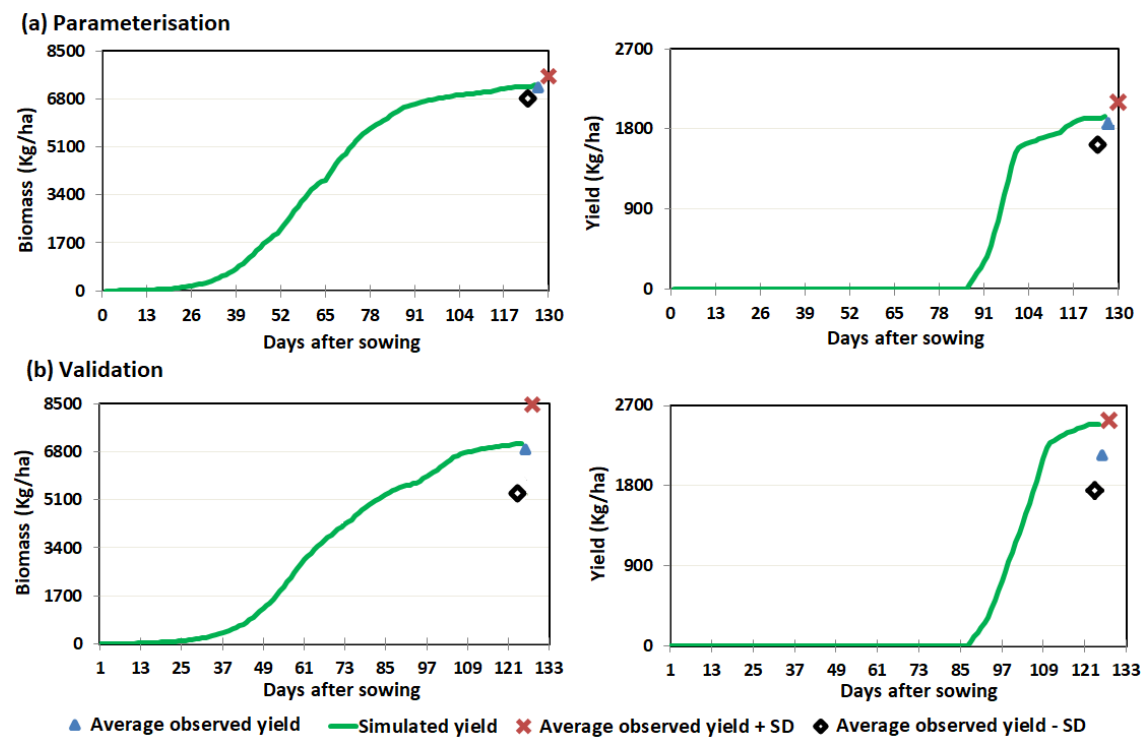


Figure 7.5: Observed and simulated biomass yield and grain yield for the calibration (parameterisation) (2018-2019) and validation (2019-2020) periods (SD = standard deviation).

The APSIM model performance for the calibration period is good, as the simulated values for phenology, biomass yield and grain yield are within the standard deviation of the mean.

7.5.3 Model validation

Using the calibrated model data for the period 2018-2019 using phenology, biomass yield and grain yield data derived from the Sunsari Morang Irrigation scheme command area, the APSIM model was validated for the 2019-2020 period based on observed phenology, biomass yield and grain yield data. Table 7.4 shows observed and simulated phenological stages for the validation period. The average observed sowing, emergence, floral initiation, start grain filling and harvest days after sowing for the validation period are 1, 7, 65, 91 and 126 days respectively. The simulated values are close to observed values. The simulated sowing, emergence, floral initiation, start grain filling and harvest days after sowing for calibration period are 1, 5, 67, 94 and 125 days respectively. The minimum (mean minus standard deviation) and maximum (mean plus standard deviation) standard deviations range for harvest days, based on three field plots, are 124 and 128 days after sowing for the validation period. The simulated harvest days after sowing for the validation period is within the standard deviation of the mean.

The observed and simulated phenology, biomass yield and grain yield data for the validation period is shown in Figure 7.5 (b). The average observed and simulated biomass yield are 6885 kg/ha and 7072 kg/ha respectively. The minimum and maximum standard deviations range for biomass yield, based on three field plots, are 5292 kg/ha and 8478 kg/ha respectively. The simulated biomass yield for the validation period is within the standard deviation of the mean. Likewise, the average observed and simulated grain yield are 2145 kg/ha and 2492 kg/ha respectively. The minimum and maximum standard deviations range for grain yield, based on three field plots, are 1753 kg/ha and 2537 kg/ha respectively. The simulated grain yield for the validation period is within the standard deviation of the mean.

From the above, it is concluded that the validation period is good, since the simulated values for phenology, biomass yield and grain yield are within the standard deviation of the mean.

7.5.4 Scenario analysis (future irrigation water demand analysis)

The main aim of scenario analysis is to predict irrigation water demand, based on changes in precipitation and temperature data for the short-term (2016-2045), mid-century (2036-2065) and end-of-century (2071-2100) time periods, and climate change

scenarios RCP4.5 and RCP8.5. The validated APSIM model was applied to predict climate change impacts on the irrigation water demand using downscaled daily precipitation, as well as minimum and maximum temperature data for different future study periods and climate scenarios. The climate datasets for the reference period (1981-2010) were downloaded from <http://rds.icimod.org/clim>. Lutz and Immerzeel (2015) developed climate datasets for the Indus, Ganges and Brahmaputra River basins using Watch Forcing based on the ERA-interim dataset, which were bias corrected using Global Precipitation Climatology Centre (GPCC) and glacier mass balance data. It was assumed that the climate datasets represent the regional climatic patterns, as ERA-interim and GPCC were also derived based on observed stations. Sub-variability can be expected within the sub-set because of the datasets' regional nature. These datasets have been widely used in various studies (Kaini et al., 2020d, Kaini et al., 2020c, MOFE, 2019, Wijngaard et al., 2017).

Future scenarios were developed for the short-term (2016-2045), mid-century (2036-2065) and end-of-century (2071-2100) periods for the climate change scenarios RCP4.5 and RCP8.5 using the downscaled daily precipitation, minimum temperature and maximum temperature data. The precipitation and temperature data were downscaled for the southern part of Nepal in the Koshi River basin including the command area of the Sunsari Morang Irrigation Scheme under this study. Details on GCM selection and climate data downscaling are described in Chapter 5 and reported by Kaini et al. (2020d).

The validated APSIM model was run for the reference period (1981-2010) using the reference datasets. The validated APSIM model was then run for the short-term (2016-2045), mid-century (2036-2065) and end-of-century (2071-2100) periods for the four corners of climatic extreme, as described in Chapter 5 and published in Kaini et al. (2020d), for both climate change scenarios RCP4.5 and RCP8.5. Details on the four corners of climatic extreme (i.e. cold/dry, cold/wet, warm/dry, and warm/wet) are explained in Chapter 5 and published in Kaini et al. (2020d). In addition, the irrigation levels required to reach potential grain yields at current conditions (2018-2019 and 2019-2020) are also compared with existing observed irrigation practice.

7.6 Results and discussion

7.6.1 Changes in projected irrigation water demand, grain yield and biomass yield

Figure 7.6 shows the changes in projected irrigation water demand required to reach potential grain yields, and biomass yield for winter wheat crops at the Sunsari Morang Irrigation Scheme command area, considering climate change scenarios RCP 4.5 and 8.5 at the short-term, mid-century and end-of-century periods compared to the reference period (1981-2010). In the reference period, 429 mm of irrigation water was required to reach a potential grain yield of 5800 kg/ha, and a biomass of 18,025 kg/ha. The projected mean irrigation water demand for winter wheat crops is likely to increase by around 2%, 1% and 3% in the short-term, mid-century and end-of-century periods, considering climate change scenario RCP4.5. For the climate change scenario RCP8.5, mean irrigation water demand is projected to increase by 2% in the short-term period. However, it is likely to decrease by about 1% and 8% in the mid-century and end-of-century periods respectively. Winter wheat crop grain yield at the Sunsari Morang Irrigation Scheme command area is expected to decrease by around 1%, 4% and 7% in the short-term, mid-century and end-of-century periods respectively, considering climate change scenario RCP4.5. For RCP8.5 scenario, equivalent projected decreases are 4%, 6% and 19% respectively. Winter wheat crop biomass yield at the Sunsari Morang Irrigation Scheme command area is projected to decrease, expect for the RCP4.5 scenario in the short-term period. Biomass yield is anticipated to increase by 1% in the short-term period, considering climate change scenario RCP4.5; however, it is likely to decrease by 4%, considering the RCP8.5 scenario in the same period. For climate change scenarios RCP4.5 and RCP8.5, biomass yield is projected to decrease by 3% and 5% in the mid-century period, and by 6% and 20% in the end-of-century period respectively. The changes (both absolute and relative) in irrigation water demand, grain yield and biomass yield for the winter wheat crop at the Sunsari Morang Irrigation Scheme command area, based on results from average of four GCMs ensembles, are shown in Table 7.5.

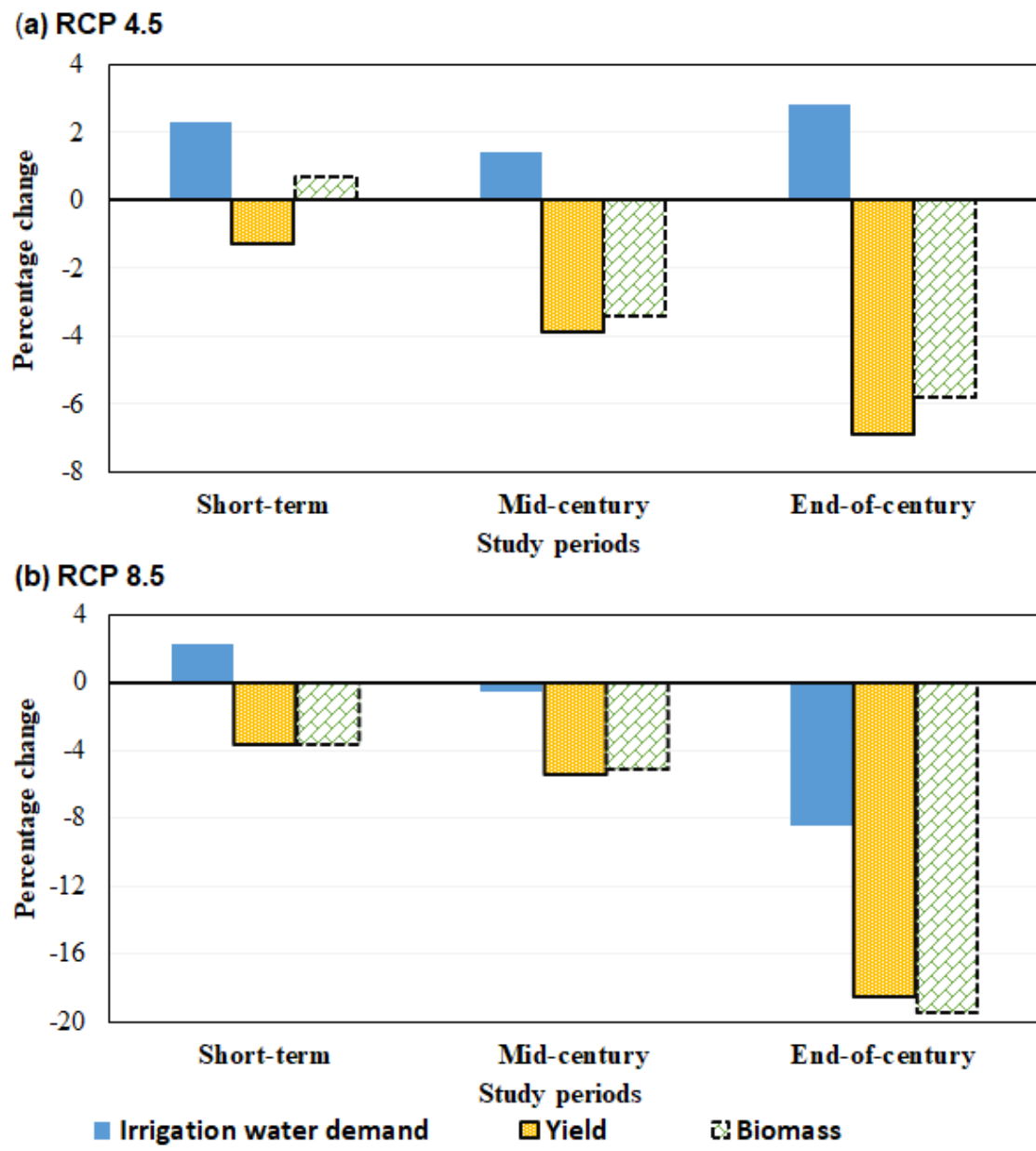


Figure 7.6: Changes in projected irrigation water demand, grain yield and biomass yield for the winter wheat crop at the Sunsari Morang Irrigation Scheme command area, considering RCP 4.5 and 8.5 climate change scenarios.

Table 7.5: Change in irrigation water demand, grain yield and biomass yield for winter wheat, based on average values from 4 GCMs and calculated against the reference period (1981-2010).

Change (based on average from 4 GCMs and base period)	Short-term (2016-2045)				Mid-century (2036-2065)				End-of-century (2071-2100)			
	RCP4.5		RCP8.5		RCP4.5		RCP8.5		RCP4.5		RCP8.5	
	Absolute change	Percentage change	Absolute change	Percentage change	Absolute change	Percentage change	Absolute change	Percentage change	Absolute change	Percentage change	Absolute change	Percentage change
Irrigation water demand	10	2.3	10	2.3	6	1.4	-2	-0.5	12	2.8	-36	-8.4
Grain yield	-76	-1.3	-215	-3.7	-228	-3.9	-320	-5.5	-399	-6.9	-1072	-18.5
Biomass yield	120	0.7	-671	-3.7	-613	-3.4	-919	-5.1	-1049	-5.8	-3509	-19.5
Absolute values for irrigation water demand, grain yield and biomass yield are in mm, kg/ha and kg/ha respectively. Relative values are in %.												

7.6.2 Uncertainty (variability) in projected irrigation water demand, grain yield and biomass yield

Based on results from selected GCM ensembles representing the four climatic extremes (cold/dry, cold/wet, warm/dry, warm/wet), a high uncertainty is projected in irrigation water demand, grain yield and biomass yield for the winter wheat crop at the Sunsari Morang Irrigation scheme command area, especially in the end-of-century period. The uncertainty (variability) in projected irrigation water demand, grain yield and biomass yield is shown in Figure 7.5.

The uncertainty in irrigation water demand, biomass yield and grain yield is projected to increase in future time periods. The uncertainty in irrigation water demand, biomass yield and grain yield is high for the end-of-century period, compared to the mid-century and short-term periods. The relative uncertainties in irrigation water demand under climate change scenario RCP4.5 are -1 to 5 %, -5 to 9 %, and -2 to 11 % for the short-term, mid-century and end-of-century periods respectively. Likewise, equivalent uncertainty projections for irrigation water demand for climate change scenario RCP8.5 are 0 to 5 %, -6 to 6 % and -20 to -1 % respectively. All the GCMs/ensembles predicted an increased irrigation water demand in the short-term, and decreased irrigation water demand in the end-of-century period for climate change scenario RCP8.5; however, for other study periods and climate change scenarios, the GCMs/ensembles' results contradicted with each other in the changes in predicted irrigation water demand. A few GCMs/ensembles resulted in decreases in predicted irrigation water demand, and a few resulted in increases in predicted irrigation water demand.

For the short-term, mid-century and end-of-century periods, the respective uncertainties in biomass yield under climate change scenario RCP4.5 are -3 to 4 %, -10 to 4 % and -15 to 7 %; while for RCP8.5 scenario the corresponding figures are -11 to 5 %, -8 to 2 % and -35 to -7 % respectively. All the GCMs/ensembles predicted a decreased biomass yield in the end-of-century period for RCP8.5 scenario. However, for other study periods and climate change scenarios, the GCMs/ensembles' results contradicted with each other in changes in predicted biomass yield.

For the short-term, mid-century and end-of-century periods, the respective uncertainties in grain yield under the climate change scenario RCP4.5 are -5 to 1 %, -10 to 2 % and -

14 to 5 %; while for RCP8.5 scenario the corresponding figures are -8 to 3 %, -8 to -2 % and -35 to -10 % respectively. All the GCMs/ensembles predicted a decreased grain yield in the mid-century and end-of-century periods for the climate change scenario RCP8.5. However, for other study periods and climate change scenarios, GCMs/ensembles' results contradicted with each other in changes in predicted grain yield.

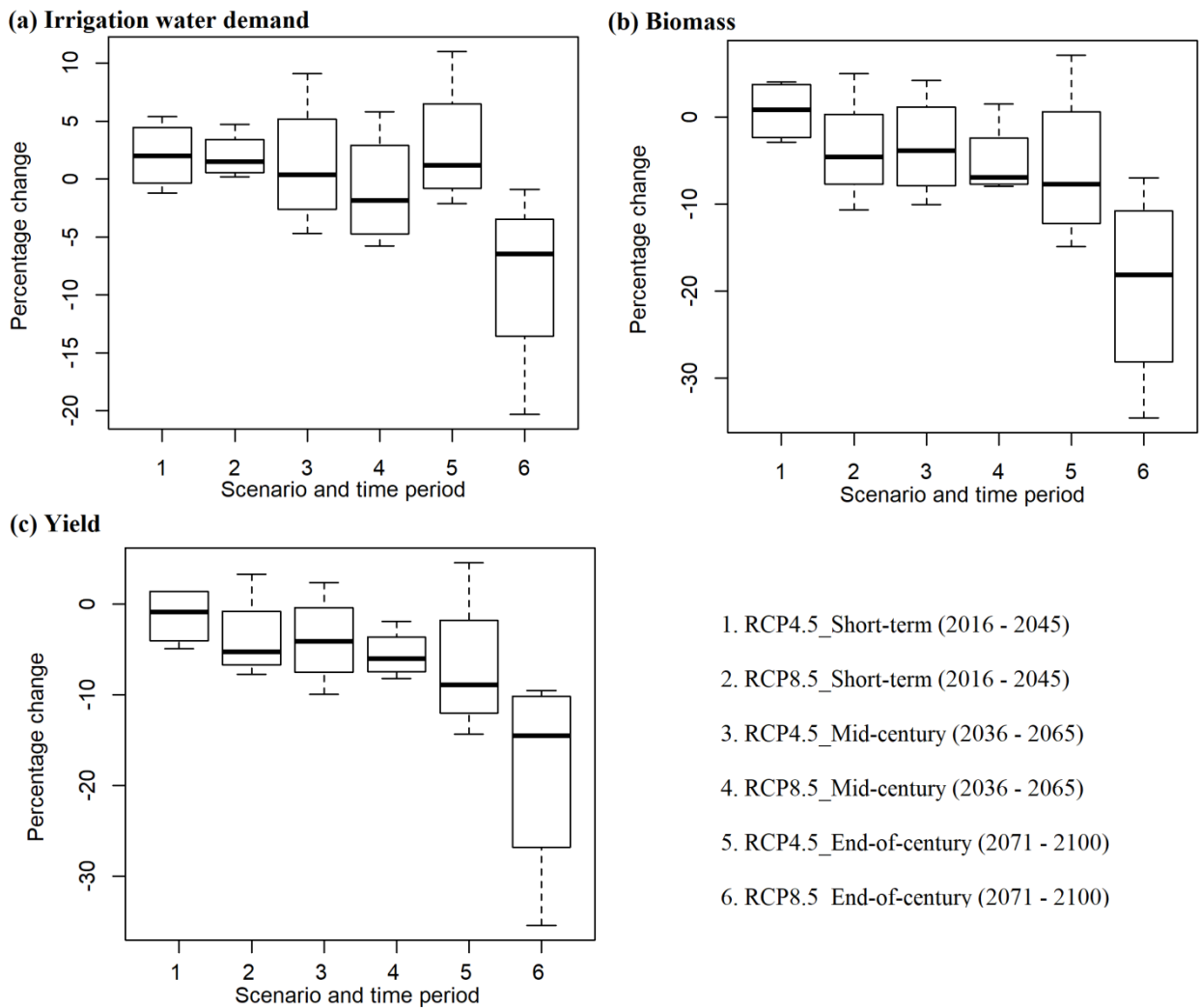


Figure 7.7: Uncertainty (variability) in projected irrigation water demand, biomass yield and grain yield compared to reference period (1981-2010).

7.6.3 Irrigation levels required to achieve potential grain yields under current climate

Irrigation levels required to achieve potential grain yields for the winter wheat crop in the Sunsari Morang Irrigation Scheme command area under current climate conditions (2018-2019 and 2019-2020) are also compared with existing observed irrigation

applications (Figure 7.8). The actual irrigation applied and the observed grain yield for the 2018-2019 crop period were 92 mm and 1862 kg/ha respectively. However, APSIM modeling showed that irrigation supply of 332 mm is required to achieve the optimal grain yield of 4312 kg/ha. Similarly, the actual irrigation applied and the observed grain yield for the 2019-2020 crop period were 65 mm and 2145 kg/ha respectively. However, APSIM modeling showed that irrigation supply of 292 mm is required to achieve the optimal grain yield of 4604 kg/ha.

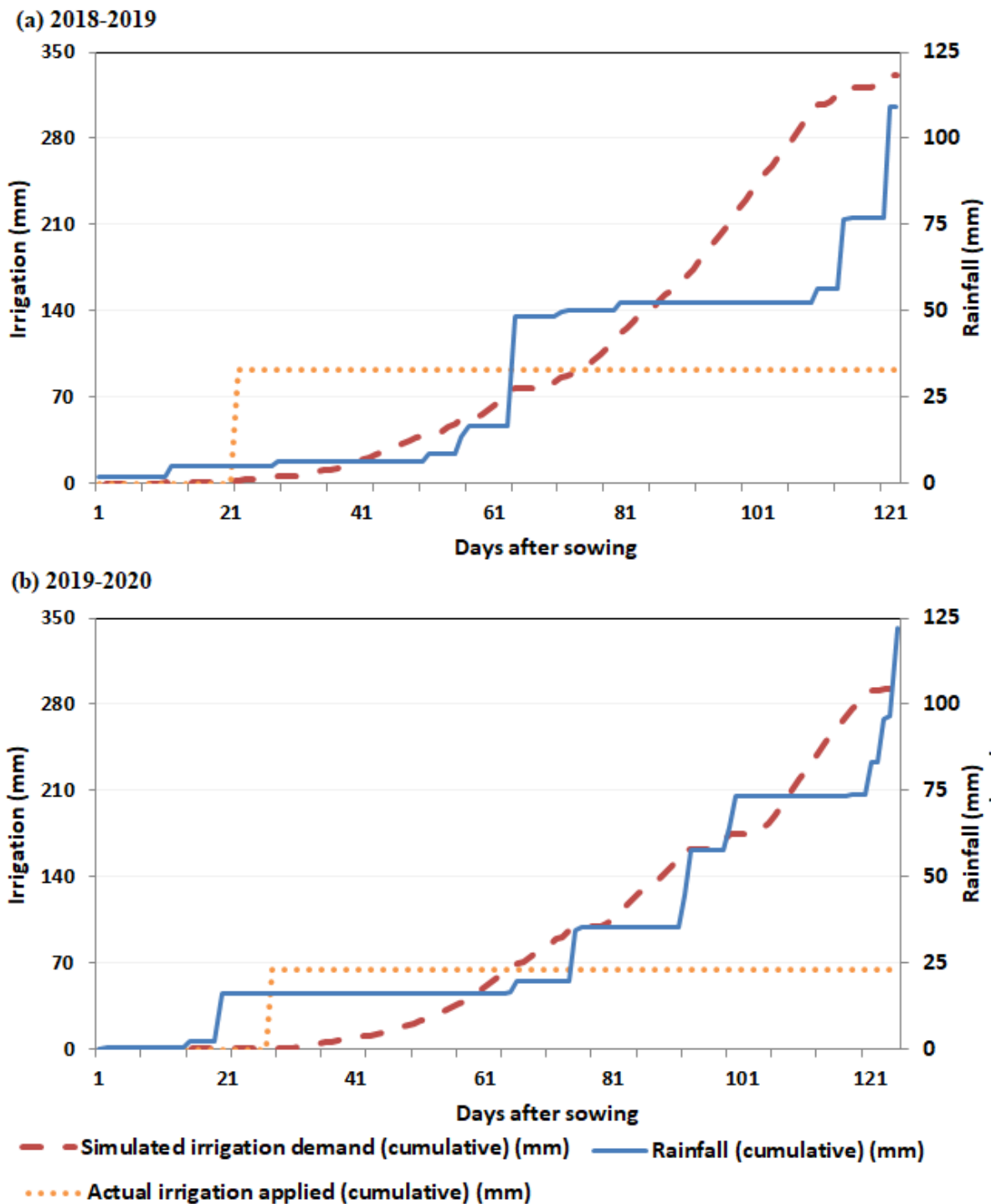


Figure 7.8: Irrigation required to reach potential grain yields, and actual irrigation supplied for the winter wheat crop in the Sunsari Morang Irrigation scheme command area in 2018-2019 and 2019-2020.

This shows that farmers were applying only 28% and 22% of the total irrigation water required to achieve optimal grain yield for the winter wheat crop in the Sunsari Morang

Irrigation scheme command area in 2018-2019 and 2019-2020 respectively. This under-irrigation had a direct impact on grain yield. In 2018-2019 and 2019-2020 respectively, the actual grain yield was only 43% and 47% of the optimal grain yield, which could have been achieved with no irrigation deficit irrigation.

Overall, irrigation water demand is projected to increase under climate change scenario RCP4.5 at all three time periods in the future, and in the short-short period under RCP8.5 scenario. However, irrigation water demand is projected to decrease in the mid-century and end-of-century under the RCP8.5 scenario. Irrigation water demand at the field level is the difference between crop water requirements and effective rainfall. Hence, the effective rainfall plays a crucial role in moderating irrigation water demand, in addition to other factors affecting crop water requirements such as temperature, solar radiation, wind speed and humidity.

Changes in total rainfall during the winter wheat period (December to mid-April) in the short-term, mid-century and end-of-century periods under climate change scenarios RCP4.5 and RCP8.5 are -5 mm, -4 mm and -10 mm respectively. Under climate change scenario RCP8.5 for the same periods, these changes are -12 mm, -2 mm and -9 mm respectively. Changes in average temperature during winter wheat season are 0.6°, 1.4° and 2.0° for RCP4.5 scenario, and 1.1°, 1.8° and 3.7° for RCP8.5 scenario in the short-term, mid-century and end-of-century periods respectively.

These data show that changes in rainfall are not significant compared to changes in temperature. Increases in temperature have resulted in increases in irrigation water demand under climate change scenario RCP4.5 in all the three time periods, and in the short-short period under RCP8.5 scenario. Decreases in irrigation water demand in the mid-century and end-of-century periods under RCP8.5 scenario could be due to more distributed rainfall throughout the crop period, rather than intense rainfall for a short period. More distributed rainfall during the crop period reduces the irrigation water demand and decreases the length of the cropping period. Total crop period (duration from sowing to harvest) is projected to decrease under both the RCP4.5 and RCP8.5 scenarios, compared to the reference period. Under RCP8.5 scenario, the total crop period is projected to decrease by 1, 2 and 5 days in the short-term, mid-century and end-of-century periods. Under RCP4.5, the equivalent predictions are 0, 1 and 2 days

respectively. Irrigation water demand is high for winter wheat crops from floral initiation to the maturity period. Decreases in irrigation water demand in the mid-century and end-of-century periods under RCP8.5 scenario could be due to the reduced total crop period.

Farmers in the tail portion of the Sunsari Morang Irrigation scheme command area (the eastern portion of the command area) generally irrigate their winter wheat crop two times between the sowing and harvest periods. The first irrigation occurs 3-4 weeks after sowing, with the second occurring during the flower initiation period. It has been observed that while all farmers irrigate 3-4 weeks after sowing, some farmers do not apply the second irrigation if there is rainfall during the flower initiation period. When deciding not to irrigate for a second time, the farmers do not consider whether the quantity of rainfall is sufficient to fulfill the crop water requirement. For instance, total rainfall during the flower initiation period in 2018-2019 crop season was only 35 mm (Figure 7.6-a). Farmers did not irrigate for second time, assuming that irrigation was not required because of rain had fallen. But 35 mm of rainfall is negligible compared to the 260 mm of total irrigation required between flower initiation and maturity.

Similarly, farmers near the observed field plots did not irrigate for a second time in 2019-2020 crop period, considering a total of 38 mm of rainfall (16 mm during flower initiation, 22 mm during flowering) to be enough to maintain crop growth (Figure 7.6-b). Again, 38 mm of rainfall is much less than the 222 mm of total irrigation required between flower initiation and maturity. Since the actual grain yields in 2018-2019 and 2019-2020 were only 43% and 47% of the optimal grain yield respectively, such under-irrigation had contributed to a significant reduction in grain yield.

Other studies have also projected that the irrigation water requirement would increase and grain yield would decrease in the future for winter wheat crops in various parts of the world. Mirgol et al. (2020) modelled climate change impacts on grain yields of winter wheat crop in the 2030s, 2050s and 2080s using a single GCM, The Canadian Earth System Model (CanESM2), applying IPCC climate change scenarios RCPs 2.6, 4.5, and 8.5 to the Qazvin Plateau, Iran. Their study projected that grain yields of winter wheat crops would decrease in future for all RCPs by 60-100%. They also reported an increase in irrigation water requirements in future by 40-80% compared to 1986-2015

period. Likewise, Goodarzi et al. (2019) evaluated climate change impacts on irrigation water requirements for different crops in Iran during 2017-2046, considering the RCP4.5 and RCP8.5 scenarios. They projected an increase in irrigation water requirements for wheat crops by 12-16% compared to 1976-2005 period. Zhang et al. (2013) assessed climate change impacts on wheat grain yield in the 2080s compared to 1961-1990 in the North China, and projected that wheat (local varieties) grain yields would decrease by 4-6 % and 1-5 % considering A2 and B2 scenarios respectively.

Bouras et al. (2019) assessed climate change impacts on irrigation water requirements and grain yield of wheat crops in the Tensift region in Morocco for the 2050s and 2090s using climate change scenarios RCP4.5 and RCP8.5. Their study reported that both irrigation water demands and wheat grain yields would decrease by 13-42% and 7-30% in the 2050s and 2090s respectively. The decrease in irrigation water demands were due to decreases in the length of cropping period. Similarly, Yuan et al. (2016) assessed climate change impacts on irrigation water requirements for winter wheat in China, and concluded that decreases in the length of crop growth period reduced irrigation water requirements. Chattaraj et al. (2014) also reported reductions in irrigation water requirements of wheat in India in 2020-2021 and 2050-2051, compared to 2009-2011. They indicated that increased temperature reduced the growth phase. The early maturity of wheat resulted in reduced irrigation water requirements. These findings are in line with the results of this study for the mid-century and end-of-century for climate change scenario RCP8.5, where the length of cropping period has decreased and consequently irrigation water demand has also decreased.

Similar to the Sunsari Morang Irrigation Scheme command area, farmers are not able to harvest potential wheat grain yields in other agricultural farms. Khaliq et al. (2019) analysed the crop grain yield gaps in Pakistan and reported that farmers are harvesting 48–56% of potential wheat grain yields at present. Li et al. (2014) assessed grain yields of winter wheat in the North China Plain, and stated that regional average grain yields were around 55% of the potential grain yields in 1981-2010. Deihimfard et al. (2015) studied the wheat grain yield gaps in Khorasan province, Iran, and reported that average wheat grain yields were around 80-98% of the potential grain yields.

The findings on projected irrigation water demand, biomass and yield could be used by Department of Water Resources and Irrigation, Nepal for management of irrigation projects in the Sunsari Morang Irrigation Scheme region. It would help project management team and local farmers for irrigation scheduling. As farmers are applying only around one-fourth of total irrigation water required to achieve optimal yield, farmers could apply more irrigation to increase the crop yield. Local farmers could directly be benefitted with increased yield resulted from proper irrigation scheduling. For improving irrigation scheduling, seasonal climate forecasts may help farmers decide whether or not to apply irrigation. Indeed, various irrigation scheduling tools are already available, that irrigators can use with the support of Water Users' Associations and the district irrigation development office to improve irrigation management. It could be explored in more detail for the Sunsari Morang irrigation area in future studies. Department of Irrigation and Water Users' Associations can help to promote the research outcome among local farmers through local workshops.

7.7 Conclusions

This study projected the future irrigation water demand, biomass yield and grain yield for the winter wheat crop in the Sunsari Morang Irrigation scheme command in Nepal in the short-term (2016-2045), mid-century (2036-2065) and end-of-century (2071-2100) time periods, considering the climate change scenarios RCP4.5 and RCP8.5. A generalised methodology for the application of a suitable crop model was developed to investigate the climate change impacts on irrigation water demand, biomass yield and grain yield and its application has been demonstrated in the Sunsari Morang Irrigation scheme command area in Nepal.

The Agricultural Production Systems Simulator (APSIM) crop model was calibrated and validated using observed phenology, biomass yield and grain yield data. The downscaled climate data documented in Chapter 5 and reported in Kaini et al. (2020d) were used in the validated APSIM model to project irrigation water demand, biomass yield and grain yield for the winter wheat crop.

Projections on irrigation water demand, biomass yield and grain yield based on the GCMs/ensembles, representing four corners of climatic extreme (i.e. cold/dry, cold/wet, warm/dry, and warm/wet), are as follows:

Current irrigation application and impacts on crop grain yield

- During the study period, farmers were applying only 28% and 22% of the total irrigation water required to achieve potential grain yield for the winter wheat crop in the Sunsari Morang Irrigation scheme command area in 2018-2019 and 2019-2020 respectively.
- Actual winter wheat crop grain yields were only 43% and 47% of optimal grain yields in 2018-2019 and 2019-2020 respectively, due to the irrigation deficit.

Changes in projected irrigation water demand, grain yield and biomass yield

- The projected mean irrigation water demand for winter wheat crops in the Sunsari Morang Irrigation Scheme command area is likely to increase by around 2%, 1% and 3% in the short-term, mid-century and end-of-century periods respectively, considering the RCP4.5 scenario. Under the RCP8.5 scenario, mean irrigation water demand is projected to increase by 2% in the short-term period, however, it is likely to decrease by about 1% and 8% in the mid-century and end-of-century periods respectively. The reduction in irrigation water demand could be due to reduced growing time in critical phenological periods.
- Winter wheat crop grain yields in the Sunsari Morang Irrigation scheme command area are expected to decrease by around 1%, 4% and 7% in the short-term, mid-century and end-of-century periods under the RCP4.5 scenario. Under the RCP8.5 scenario, the equivalent projections are 4%, 6% and 19% respectively. The larger reduction in grain yield could be due to reduced growing time in critical phenological periods.
- Winter wheat crop biomass yield is anticipated to increase by 1% in the short-term considering climate change scenario RCP4.5; however, it is likely to decrease by 4% considering the RCP8.5 scenario. For RCP4.5 and RCP8.5 scenarios, biomass yield is projected to decrease by 3% and 5% respectively in the mid-century, and by 6% and 20% respectively in the end-of-century period.

Uncertainty (variability) in projected irrigation water demand, grain yield and biomass yield

- The uncertainty in irrigation water demand, biomass yield and grain yield is projected to increase in future time periods.

- The relative uncertainties in irrigation water demand for climate change scenario RCP4.5 are -1 to 5 %, -5 to 9 %, and -2 to 11 % for the short-term, mid-century and end-of-century periods respectively. Likewise, equivalent projections for irrigation water demand for RCP8.5 scenario are 0 to 5 %, -6 to 6 % and -20 to -1 % respectively.
- The relative uncertainties in biomass yield for the RCP4.5 scenario are -3 to 4 %, -10 to 4 % and -15 to 7 % for short-term, mid-century and end-of-century periods respectively. Under the RCP8.5 scenario, the respective figures are -11 to 5 %, -8 to 2 % and -35 to -7 %.
- The relative uncertainties in grain yield for the RCP4.5 scenario are -5 to 1 %, -10 to 2 % and -14 to 5 % for short-term, mid-century and end-of-century periods respectively. Under the RCP8.5 scenario, the respective figures are -8 to 3 %, -8 to -2 % and -35 to -10 %.

Since farmers are applying less irrigation water than required, government programs should be conducted to educate farmers about irrigation quantities and timing requirements. Different adaptation programs to cope with projected grain yield reductions could be planned and implemented by relevant agencies.

Chapter 8: Canal hydraulic capacity assessment

The aim of this chapter is to assess the canal hydraulic capacity of the main canal of the Sunsari Morang Irrigation Scheme under climate change scenarios. Water availability for future irrigation requirements is dependent on water levels in Koshi River and irrigation canal intake characteristics, which are used to project the future winter wheat area coverage in the Sunsari Morang Irrigation Scheme command area. Current hydraulic capacity of the main canal is investigated, and the canal discharge capacity of the main canal for future available flows is also assessed.

8.1 Canal discharge measurement and losses in the irrigation canal network

8.1.1 Canal discharge measurement

Canal discharge was measured at various locations on the main canal. A vertical axis-current meter, where a series of conical cups mounted in a vertical axis rotates on a horizontal axis, was used to measure the number of revolutions of the cup assembly every 60 seconds. The current meter used in the field is shown in Figure 8.1. The cup assembly was fixed at 0.2, 0.6 and 0.8 times the depth of water below the water surface in the main canal to measure the average flow velocity. The cup assembly was fixed at three vertical profiles in the main canal because of greater water depth (>1 m).

The current meter readings were taken at various cross sections along the canal width, considering the segment width should not be greater than 1/15 to 1/20 of the total canal width (Subramanya, 2007). The current meter rating equation, as provided by the manufacturer, Government of Punjab, P.W.D. (I.B.), Hydraulic Research Station, Malikpur (Pathankot), is mentioned in Equation 8.1.

$$V = 0.8021 \times N - 0.0065 \qquad \text{Equation 8.1}$$

where V is flow velocity (m/s) and N is number of revolutions of cup assembly per sec.



Figure 8.1: Current meter used for discharge measurement in the main irrigation canal.

Water discharge was estimated using the velocity and measured cross sectional area. The measured discharge at various locations was used to estimate the losses in the canal network. Measured water discharge was calculated using Equation 8.2. Details of the field measurement and calculation process for discharge measurement in open channels are mentioned in Subramanya (2007).

$$Q = V \times A \quad 8.2$$

where Q is discharge (m^3/s), V is average flow velocity (m/s), and A is the wetted cross sectional area (m^2).

With known measured velocity, canal geometry and canal slope, the Manning's roughness coefficient was estimated using Equation 8.3.

$$V = \frac{1}{n} \times R^{2/3} \times S^{1/2} \quad 8.3$$

where n is Manning's roughness coefficient, R is the hydraulic radius (wetted area/wetted perimeter) (meter) and S is slope of the canal (meter/meter).

A longitudinal and cross section survey of the canal network was also conducted. The canal geometry data and slope are used to estimate the Manning's roughness coefficient with a known flow velocity in the canal network section. The canal geometry, slope, Manning's roughness coefficient and seepage rate data were used in the hydraulic model.

8.1.2 Losses in the irrigation canal network

The analytical methods used to estimate losses are generally applied in the planning phase of the irrigation schemes. These methods are grounded on the coefficient of hydraulic conductivity of soil layers and the associated boundary conditions. In the existing canals, direct measurement methods to measure loss, rather than analytical methods, are generally applied (Indian Standards Institution, 1980). The direct measurement methods include the inflow-outflow method, ponding method, seepage meter, tracer technique, electrical logging (resistivity measurement), piezometric surveys and remote sensing. Among these methods, the inflow-outflow and pond methods are suitable for various canal and soil conditions (Indian Standards Institution, 1980). Seepage meters measure seepage loss through a small area and cannot be applied in canal with velocities higher than 0.6 m/sec (Worstell, 1976). The inflow-outflow method was applied in this research as it can be applied without affecting the canal operation.

Inflow-outflow method: Losses in the canal are measured based on the water volume entering into and outgoing from a particular reach (section) of the canal. The difference in water volume calculated by accounting for discharge to offtakes, and losses from structures due to leakage, seepage and evaporation. The water balance of the reach considered for the experiment is depicted in Equation 8.4.

$$T_{losses} = Q_{in} - Q_{out} - Q_{offtakes} \quad 8.4$$

where,

$$T_{losses} = \text{Total Losses (m}^3/\text{s)}$$

$$Q_{in} = \text{inflow discharge at upstream end of the reach (m}^3/\text{s)}$$

$$Q_{out} = \text{outflow discharge at the downstream end of the reach (m}^3/\text{s)}$$

Q_{offtakes} = discharge at offtakes located within the reach (m^3/s)

The inflow-outflow method is described in Figure 8.2.

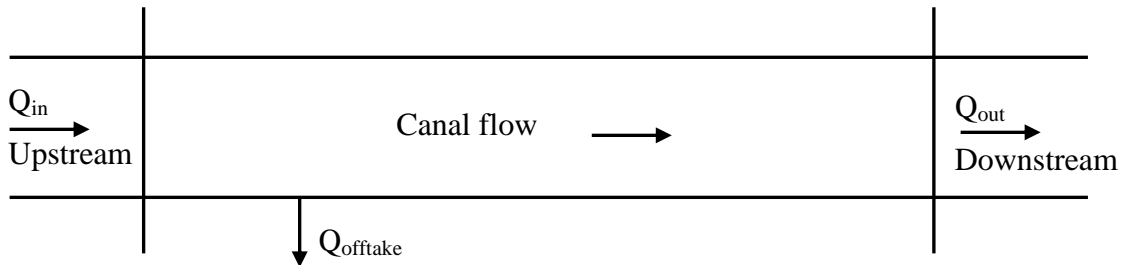


Figure 8.2: Losses measurement in an irrigation canal (Inflow-outflow method).

The selection of canal reach for loss measurement depends on the availability of flow measurement devices or structures. The current meters or other flow measuring devices can be used in well-defined sections. Alternatively, existing measuring structures with no submergence, for example, a drop (fall) structure with a calibrated rating curve, can also be used. A longer canal reach length is preferable, so that the measured losses shall be sufficiently higher than the accuracy of the measuring structures. After selecting a suitable canal reach, the offtakes within the reach are closed if possible, or are opened with a constant opening for the measurement period. The discharge entering into the canal reach is kept constant for the test period. The water levels at different portions of the canal reach are measured. When a steady water level obtained, the incoming discharge, discharge from outlets and outgoing discharge are measured by flow measuring devices or based on the rating curves.

The inflow-outflow method can be applied when canal is in operation, hence, without affecting the canal operation. The measured losses represent real canal operating conditions. However, this method has a few limitations. The computed loss is generally a small quantity compared to the larger water quantities measured as inflow and outflow. Hence, small errors in flow measurement lead to large errors in loss calculation. The inflow-outflow method is affected by a particular ground water table, and by the temperature and humidity conditions in the canal reach during the measurement, which may vary with time and space along the total canal length. The spatial distribution of losses along the measured canal reach is considered uniform.

Moreover, it may take a long time to maintain a steady state condition if the longer canal reach is considered, and it may be difficult to monitor the offtakes within the reach during the experiment.

8.2 Personal Computer Storm Water Management Model (PCSWMM) for canal hydraulic modelling

The Storm Water Management Model (SWMM) was developed by United States Environmental Protection Agency (US-EPA). It is open source software which can perform hydraulic and hydrological modelling (Rossman, 2017, Rossman, 2016). The Personal Computer Storm Water Management Model (PCSWMM) is an improved version of SWMM developed by Computational Hydraulics International (CHI), Canada. The computational principles in PCSWMM are same as SWMM. However, graphical representation is better in PCSWMM than in SWMM.

Open channels or pipes are represented by conduits in PCSWMM, and two channels are connected by a junction. Input data in PCSWMM include the size and length of the conduits, the elevation and height of the junctions, inflows or outflows at the junctions, Manning's roughness coefficient of conduits, losses from the conduits, and climate data (temperature, precipitation, wind speed). Different flow routing options are available in PCSWMM. SWMM hydraulic modelling offers a range of different flowing options, including steady flow (which translates the inflow hydrograph at the upstream end of the conduit to the downstream end, with no delay and no change in shape, i.e. no routing), kinematic wave (which models continuity and simplified momentum, i.e. while flow and area can vary spatially and temporally, this option does not consider the backwater effect, entrance/exit losses or pressurised flow) and dynamic routing (which considers the continuity equation and the Saint Venant equation, i.e. a complete routing including channel storage, backwater effects, losses and pressurised flow) (Rossman, 2017). Details of the capacities and principles of SWMM hydraulic modelling are mentioned in Rossman (2017). The capacities and principles of SWMM hydraulic modelling are valid for PCSWMM modelling, too.

SWMM and PCSWMM hydraulic models have been successfully used around the world for the hydraulic assessment of irrigation canal networks (Kim et al., 2016, Schoenfelder et al., 2006). SWMM and PCSWMM hydraulic models are being

increasingly used for assessing hydraulic performance of irrigation canal networks (Bang et al., 2019, Do et al., 2019, Ha et al., 2019). Similarly, Shin et al. (2020a) and Shin et al. (2020b) have also successfully used SWMM for hydraulic analysis of irrigation canals. In this study, the PCSWMM hydraulic model (version 5.0.012) was used for the assessment of canal hydraulic capacity of the main canal in the Sunsari Morang Irrigation Scheme.

8.3 Methodological approach for PCSWMM hydraulic modelling

A complete methodology for PCSWMM hydraulic modelling is schematised in Figure 8.3. The main steps in the hydraulic modelling include input data processing and model development/set up, calibration, validation, and scenario analysis. These steps are described in the following sections:

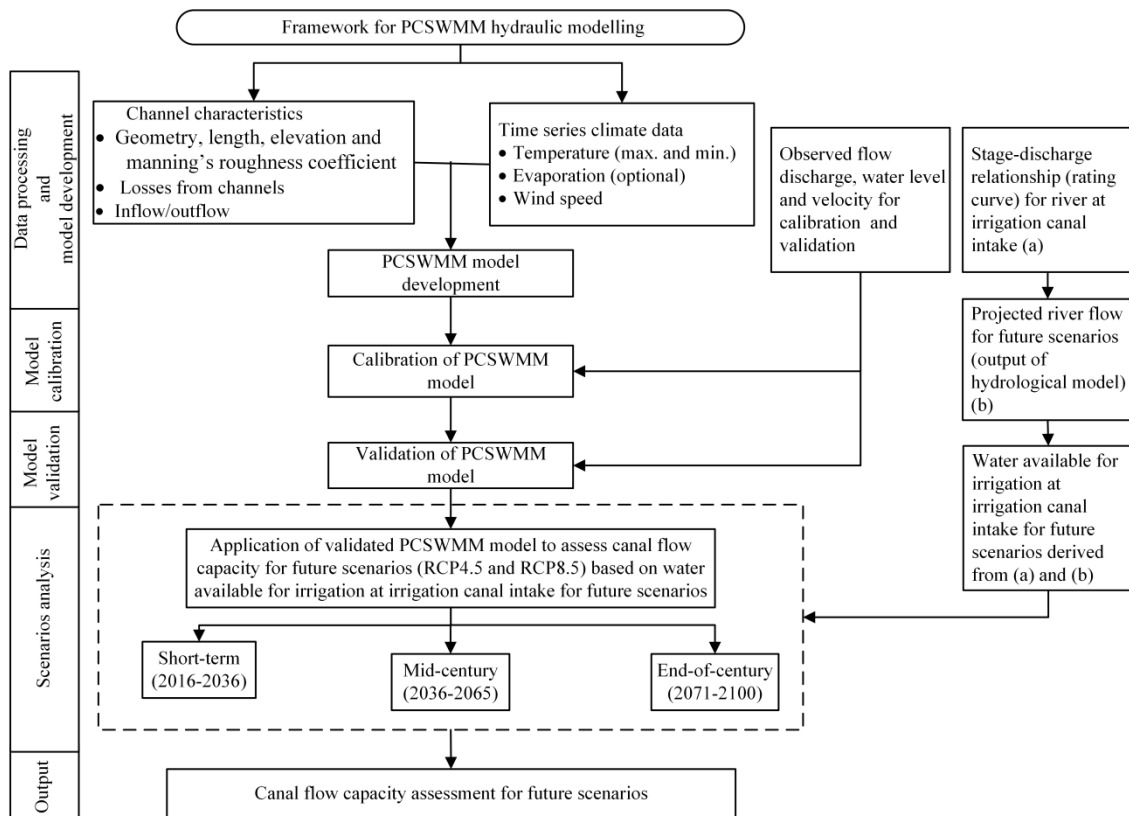


Figure 8.3: Flowchart of methodology for hydraulic modelling using the PCSWMM model.

8.3.1 PCSWMM input data processing and model development (Model initialisation)

PCSWMM input data include the size, length, elevation and slope of the canal, inflow or outflow from the canal, Manning's roughness coefficient of the canal, losses from the canal, and climate data (temperature, precipitation, wind speed). The observed discharge, velocity and water depth at main canal of the Sunsari Morang Irrigation canal were used for the calibration and validation of the PCSWMM model.

8.3.2 Model calibration

After model initialisation (PCSWMM model development as mentioned in 8.3.1), the model was calibrated using observed discharge, flow velocity and water depth at the main canal of the Sunsari Morang Irrigation canal. Observed discharge, flow velocity and water depth at the main canal of the Sunsari Morang Irrigation canal network for the period 2018-2020 were used for the calibration of the PCSWMM model.

8.3.3 Model validation

The calibrated PCSWMM model (section 8.3.2) was validated using observed discharge, flow velocity and water depth at the main canal of the Sunsari Morang Irrigation canal network. Observed discharge, flow velocity and water depth at the main canal of the Sunsari Morang Irrigation canal for the period 2018-2020 were used for the validation of the PCSWMM model.

8.3.4 Scenario analysis (canal capacity assessment)

The validated PCSWMM model (section 8.3.3) was applied to assess the hydraulic capacity of the canal, based on water availability for irrigation at the irrigation canal intake considering future climate change scenarios. The short-term (2016-2045), mid-century (2036-2065) and end-of-century (2071-2100) periods with the projected Koshi River flows under climate change scenarios RCP4.5 and RCP8.5 were considered for the future scenarios. Changes in future water availability for irrigation at the irrigation canal intake were compared with the reference (base) period (1981-2010) data. The flow capacity of the main canal was assessed with respect to future water availability for irrigation at the irrigation canal intake.

8.4 Application of methodology for PCSWMM hydraulic modelling

The application of the methodological framework described in Figure 8.3 is demonstrated in the following sections.

8.4.1 PCSWMM input data processing and model development

The PCSWMM model was developed using the size, length, elevation and slope of the canal, inflow or outflow from the canal, Manning's roughness coefficient of the canal, losses from the canal, and climate data (temperature, precipitation, wind speed) as mentioned in section 8.3.1. The developed PCSWMM model was used for model calibration.

Input data: Irrigation canal geometry including size (canal sections), length, elevation and slope were measured during field visits as well as being collected from the Sunsari Morang Irrigation Project Office. Climate data for 2016-2020 were taken from APSIM Next Generation (Holzworth et al., 2018). These climate data were also used in APSIM crop modelling (Chapter 7).

Canal discharge measurements were carried out at different locations of the main canal. The canal network of the Sunsari Morang Irrigation Scheme, including the main canal and branch canals, is shown in Figure 3.5. Canal discharge measurements were carried out on the main canal, at the following distances from the irrigation intake: 5.2 km (Table 8.1), 11.8 km (Table 8.2), 13 km (Table 8.3), 15 km (Table 8.4), 22.5 km (Table 8.5) and 25.3 km (Table 8.6). Canal discharge measurements were taken using the current meter as mentioned in Section 8.1.1. A conceptual diagram showing the channel section, distances and depths for measuring discharge is shown in Figure 8.4. As shown in Figure 8.4, the current cup assembly was fixed at 0.2, 0.6 and 0.8 times the depth of water below the water surface at each segment to measure the average flow velocity of the respective segment.

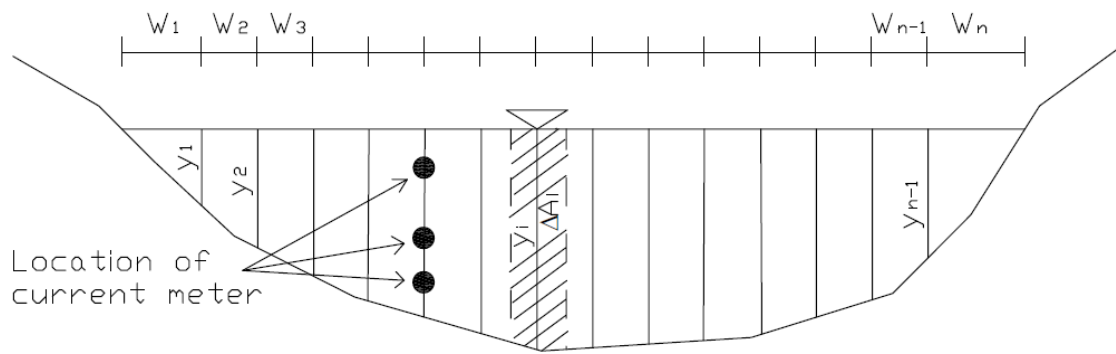


Figure 8.4: A conceptual diagram showing the channel section, distances and depths for measuring discharge.

Discharge measurements at 5.2 km and 11.8 km were conducted considering the calculation of losses between these two measuring stations. Discharge measurements at 13 km and 15 km were performed considering the calculation of losses between these two measuring stations. Likewise, discharge measurements at 22.5 km and 25.3 km were carried out considering the calculation of losses between these the two measuring stations. In all three cases, there was no outflow in between the two respective measuring stations. The discharge was kept constant in the canal during the discharge measurements at 5.2 km and 11.8 km, 13 km and 15 km, and 22.5 km and 25.3 km. Details on canal discharge measurements at 5.2 km, 11.8 km, 13 km, 15 km, 22.5 km, and 25.3 km from the irrigation intake along the main canal of Sunsari Morang Irrigation are presented in Tables 8.1, 8.2, 8.3, 8.4, 8.5 and 8.6 respectively.

Table 8.1: Canal discharge measurement at 5.2 km from the irrigation intake along the main canal.

Distance from intake	Total width (W) (m)	Distance from left (m)	Water depth (m)	Revolution per 60 sec (current meter placed at ...from bottom)			Velocity (m/s)	Area (m ²)	Discharge (m ³ /s)
				0.2 x water depth	0.4 x water depth	0.8 x water depth			
5.2 km	W = 19.5 m, W/15 = 1.3 m, W/20 = 0.97 m	1	1.4	28	32	35	0.417	1.575	0.657
		2	1.3	30	34	38	0.448	1.3	0.582
		3	1.3	31	41	45	0.515	1.3	0.67
		4	1.3	30	38	40	0.475	1.3	0.618
		5	1.3	28	32	35	0.417	1.3	0.542
		6	1.4	27	31	31	0.39	1.4	0.546
		7	1.5	24	27	28	0.346	1.5	0.519
		8	1.5	22	24	24	0.305	1.5	0.458
		9	1.5	26	28	30	0.368	1.5	0.552
		10	1.5	31	35	37	0.452	1.5	0.678
		11	1.5	33	38	42	0.497	1.5	0.746
		12	1.5	36	40	43	0.524	1.5	0.786
		13	1.5	38	41	44	0.542	1.5	0.813
		14	1.5	42	46	50	0.608	1.5	0.912
		15	1.48	45	50	52	0.649	1.48	0.961
		16	1.48	47	52	55	0.68	1.48	1.006
		17	1.48	43	48	50	0.622	1.48	0.921
		18	1.5	43	49	52	0.635	1.5	0.953
		19	1.4	42	46	50	0.608	1.4	0.851
Total =								27.515	13.771

Table 8.2: Canal discharge measurement at 11.8 km from the irrigation intake along the main canal.

Distance from intake	Total width (W) (m)	Distance from left (m)	Water depth (m)	Revolution per 60 sec (current meter placed at ...from bottom)			Velocity (m/s)	Area (m ²)	Discharge (m ³ /s)
				0.2 x water depth	0.4 x water depth	0.8 x water depth			
11.8 km	W = 19.5 m, W/15 = 1.3 m, W/20 = 0.97 m	1	1.1	17	18	19	0.234	1.238	0.29
		2	1.3	20	22	24	0.288	1.3	0.374
		3	1.5	25	27	27	0.346	1.5	0.519
		4	1.8	26	27	27	0.35	1.8	0.63
		5	1.8	28	35	35	0.43	1.8	0.774
		6	1.9	27	28	28	0.363	1.9	0.69
		7	1.9	26	28	28	0.359	1.9	0.682
		8	2	24	25	29	0.341	2	0.682
		9	2	28	33	34	0.417	2	0.834
		10	2.2	31	33	35	0.435	2.2	0.957
		11	2.2	34	36	39	0.479	2.2	1.054
		12	2.1	31	33	36	0.439	2.1	0.922
		13	2	27	31	33	0.399	2	0.798
		14	1.9	24	25	25	0.323	1.9	0.614
		15	1.9	22	25	26	0.319	1.9	0.606
		16	1.8	20	23	24	0.292	1.8	0.526
		17	1.55	17	18	19	0.234	1.55	0.363
		18	1.3	15	16	17	0.207	1.3	0.269
		19	1.1	15	16	17	0.207	1.1	0.228
Total =								33.488	11.81

Table 8.3: Canal discharge measurement at 13 km from the irrigation intake along the main canal.

Distance from intake	Total width (W) (m)	Distance from left (m)	Water depth (m)	Revolution per 60 sec (current meter placed at ...from bottom)			Velocity (m/s)	Area (m ²)	Discharge (m ³ /s)
				0.2 x water depth	0.4 x water depth	0.8 x water depth			
13 km	W = 29 m, W/15 = 1.9 m, W/20 = 1.45 m	1.5	0.5	6	7	8	0.087	0.844	0.073
		3	0.8	7	8	9	0.1	1.2	0.12
		4.5	0.9	10	11	12	0.141	1.35	0.19
		6	1.2	12	13	14	0.167	1.8	0.301
		7.5	1.5	13	15	17	0.194	2.25	0.437
		9	1.5	14	15	17	0.198	2.25	0.446
		10.5	1.7	15	17	19	0.221	2.55	0.564
		12	1.9	18	20	23	0.265	2.85	0.755
		13.5	2	18	21	23	0.27	3	0.81
		15	1.9	18	19	22	0.256	2.85	0.73
		16.5	1.75	19	21	24	0.279	2.625	0.732
		18	1.7	22	24	27	0.319	2.55	0.813
		19.5	1.55	20	22	25	0.292	2.325	0.679
		21	1.4	18	19	22	0.256	2.1	0.538
		22.5	1.4	15	17	20	0.225	2.1	0.473
		24	1.3	13	16	18	0.203	1.95	0.396
		25.5	0.9	12	13	15	0.172	1.35	0.232
27	0.7	10	11	13	0.145	1.05	0.152		
28.5	0.5	8	9	10	0.114	0.781	0.089		
Total =								37.775	8.53

Table 8.4: Canal discharge measurement at 15 km from the irrigation intake along the main canal.

Distance from intake	Total width (W) (m)	Distance from left (m)	Water depth (m)	Revolution per 60 sec (current meter placed at ...from bottom)			Velocity (m/s)	Area (m ²)	Discharge (m ³ /s)
				0.2 x water depth	0.4 x water depth	0.8 x water depth			
15 km	W = 29 m, W/15 = 1.9 m, W/20 = 1.45 m	1.5	1.3	5	7	9	0.087	2.194	0.191
		3	1.5	7	10	11	0.118	2.25	0.266
		4.5	1.5	7	11	13	0.132	2.25	0.297
		6	1.5	9	12	14	0.149	2.25	0.335
		7.5	1.9	8	10	11	0.123	2.85	0.351
		9	1.9	9	12	13	0.145	2.85	0.413
		10.5	1.9	10	12	14	0.154	2.85	0.439
		12	1.5	11	13	16	0.172	2.25	0.387
		13.5	1.5	13	17	19	0.212	2.25	0.477
		15	1.7	16	20	23	0.256	2.55	0.653
		16.5	1.8	19	22	25	0.288	2.7	0.778
		18	1.9	18	22	25	0.283	2.85	0.807
		19.5	1.9	15	18	21	0.234	2.85	0.667
		21	1.6	13	17	19	0.212	2.4	0.509
		22.5	1.5	12	16	17	0.194	2.25	0.437
		24	1.5	9	12	14	0.149	2.25	0.335
		25.5	1.5	7	10	11	0.118	2.25	0.266
27	1.5	6	9	10	0.105	2.25	0.236		
28.5	1.3	4	7	9	0.083	2.031	0.169		
Total =								46.375	8.013

Table 8.5: Canal discharge measurement at 22.5 km from the irrigation intake along the main canal.

Distance from intake	Total width (W) (m)	Distance from left (m)	Water depth (m)	Revolution per 60 sec (current meter placed at ...from bottom)			Velocity (m/s)	Area (m ²)	Discharge (m ³ /s)
				0.2 x water depth	0.4 x water depth	0.8 x water depth			
22.5 km	W = 20 m, W/15 = 1.3 m, W/20 = 1.0 m	1	0.7	3	4	5	0.047	0.788	0.037
		2	0.9	4	5	6	0.06	0.9	0.054
		3	1.1	8	13	15	0.154	1.1	0.169
		4	1.3	12	14	16	0.181	1.3	0.235
		5	1.5	14	16	17	0.203	1.5	0.305
		6	1.5	15	16	18	0.212	1.5	0.318
		7	1.5	16	18	21	0.239	1.5	0.359
		8	1.45	19	23	26	0.297	1.45	0.431
		9	1.45	20	24	26	0.305	1.45	0.442
		10	1.45	20	23	27	0.305	1.45	0.442
		11	1.5	19	21	24	0.279	1.5	0.419
		12	1.5	18	21	23	0.27	1.5	0.405
		13	1.5	17	20	21	0.252	1.5	0.378
		14	1.5	15	16	18	0.212	1.5	0.318
		15	1.45	14	16	18	0.207	1.45	0.3
		16	1.35	12	13	16	0.176	1.35	0.238
		17	1.1	7	8	9	0.1	1.1	0.11
		18	0.8	4	5	6	0.06	0.8	0.048
		19	0.6	3	4	5	0.047	0.6	0.028
Total =								24.24	5.036

Table 8.6: Canal discharge measurement at 25.3 km from the irrigation intake along the main canal.

Distance from intake	Total width (W) (m)	Distance from left (m)	Water depth (m)	Revolution per 60 sec (current meter placed at ...from bottom)			Velocity (m/s)	Area (m ²)	Discharge (m ³ /s)
				0.2 x water depth	0.4 x water depth	0.8 x water depth			
25.3 km	W = 19 m, W/15 = 1.26 m, W/20 = 0.95 m	1	0.8	2	6	9	0.069	0.9	0.062
		2	1.1	3	8	11	0.092	1.1	0.101
		3	1.35	5	8	12	0.105	1.35	0.142
		4	1.55	8	11	15	0.145	1.55	0.225
		5	1.65	10	14	17	0.176	1.65	0.29
		6	1.8	13	15	16	0.19	1.8	0.342
		7	1.9	15	17	19	0.221	1.9	0.42
		8	1.8	15	18	19	0.225	1.8	0.405
		9	1.7	16	18	19	0.23	1.7	0.391
		10	1.6	16	18	19	0.23	1.6	0.368
		11	1.6	15	17	18	0.216	1.6	0.346
		12	1.65	15	18	19	0.225	1.65	0.371
		13	1.55	15	17	18	0.216	1.55	0.335
		14	1.5	12	13	15	0.172	1.5	0.258
		15	1.4	10	11	13	0.145	1.4	0.203
		16	1.3	8	10	11	0.123	1.3	0.16
		17	1.15	8	10	12	0.127	1.15	0.146
		18	0.9	6	8	9	0.096	0.9	0.086
Total =								26.4	4.651

The losses and Manning's roughness coefficient at different portions of the main canal are shown in Table 8.7. The water losses between 5.2 km and 11.8 km, 13 km and 15

km, and 22.5 km and 25.3 km distance from irrigation canal intake are 0.014 liter/sec/m² (l/s/m²), 0.009 l/s/m² and 0.007 l/s/m² respectively. The average water loss in the Sunsari Morang Irrigation main canal was 0.01 l/s/m². The Manning's roughness coefficient varies from 0.037 to 0.093 at different locations of the main canal (Table 8.7). The average value of Manning's roughness coefficient was 0.066 in the main canal of the Sunsari Morang Irrigation.

Table 8.7: Losses and Manning's roughness coefficient at different portions of the main canal.

Distance from intake	Discharge (m ³ /s)	Wetted perimeter (m)	Losses (l/s/m ²)*	Manning's roughness coefficient (n)
5.2 km	13.771	21.231	0.014	0.047
11.8 km	11.81	20.92		0.037
13 km	8.53	29.72	0.009	0.060
15 km	8.013	30.58		0.093
22.6 km	5.036	20.56	0.007	0.074
25.4 km	4.651	19.734		0.083

*Liter/sec/sq. meter (l/s/m²)

Kilic and Tuylu (2011) investigated water losses in the conveyance system of the Ahmetli irrigation scheme in Turkey using the inflow-out flow method. They reported that the average water loss in the main canal was 0.067 l/s/m² with the loss varying from 0.012 – 0.142 l/s/m² at different sections of the main canal. Likewise, Eshetu and Alamirew (2018) evaluated water losses in irrigation canals in Ethiopia using the inflow-outflow method. They reported that average water loss in sections of the main canal which were lined with geo-membrane was 0.0126 l/s/m² with the loss varying from 0.0123 – 0.0129 l/s/m² at different sections of the main canal. In the earthen portion of the main irrigation canal, the average water loss was 0.0180 l/s/m². Mohammadi et al. (2019) analysed water losses in the main irrigation channels in Iran and reported an average water losses of 0.014 l/s/m² in the main canal. Water losses varied from 0.013 l/s/m² to 0.016 l/s/m². Akkuzu (2012) assessed water losses in an irrigation canal in Turkey using the inflow-outflow method, and reported an average

water loss of 0.014 l/s/m^2 varying from 0.002 l/s/m^2 to 0.036 l/s/m^2 at different locations of the canal. Manning's roughness coefficient values for earthen canals are 0.02 for newly constructed, very smooth canal sections without meandering, 0.1 for very high vegetation conditions, and 1.3 for severe meandering conditions (Department of Irrigation, 2014). When designing earthen irrigation canals in Nepal, Manning's roughness coefficient values is generally taken as 0.025 to 0.03. Bakry et al. (1992) investigated the Manning's roughness coefficient in an irrigation canal in Egypt, and reported a maximum Manning's coefficient of 0.083 in an earthen canal. Salah Abd Elmoaty and El-Samman (2020) conducted an investigation on Manning's roughness coefficient for different weed density scenarios in channels. They reported the maximum value of Manning's roughness coefficient for high weed, medium weed and low weed densities as 0.12, 0.08 and 0.07 respectively. These findings support the results from this research as some reaches of the earthen irrigation canals in the Sunsari Morang Irrigation Scheme have silt deposits and medium to high vegetation.

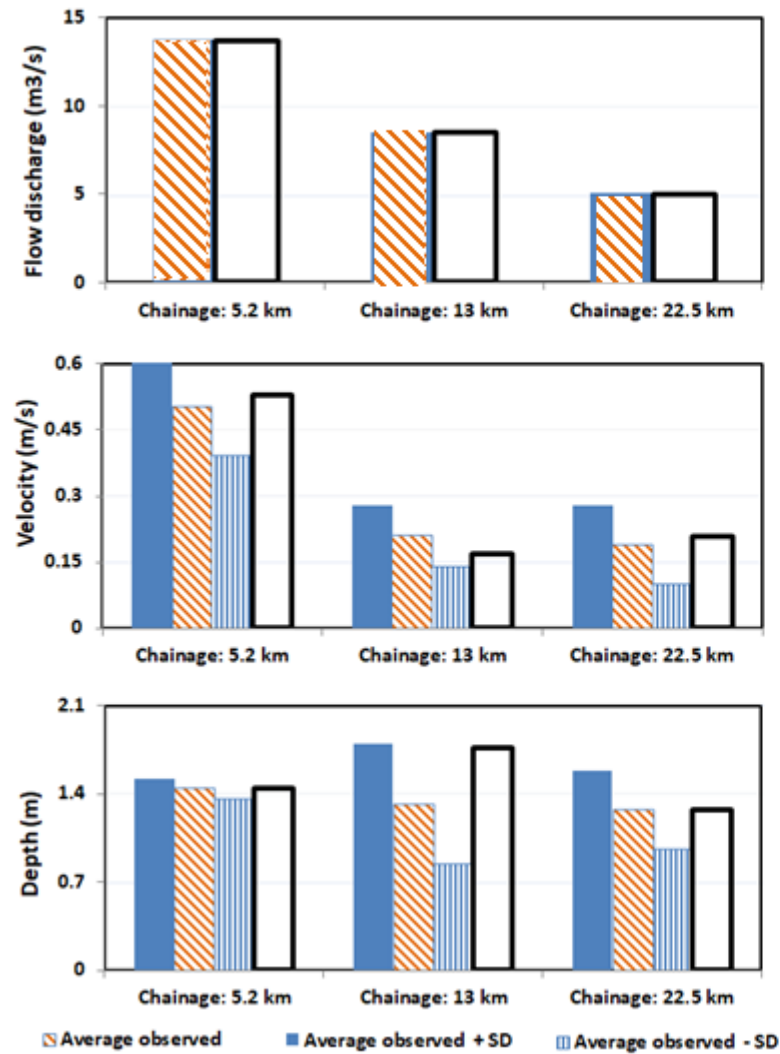
8.4.2 Model calibration

Observed discharge, velocity and water depth data in the main canal of the Sunsari Morang Irrigation canal system were used for the calibration of the PCSWMM model. Initially, canal discharge at the intake of the main irrigation canal was adjusted to match the simulated discharge with the observed discharge at the 5.2 km distance from the irrigation intake. Rigorous systematic manual adjustment of the canal discharge at the intake point was carried out so that the simulated discharge value was close to observed discharge at the 5.2 km distance from the irrigation intake. After this, simulated velocity and simulated water depth are compared with observed values. Similar processes were carried out to calibrate measurements at the 13 km and 22.5 km distances from the irrigation intake along the main canal. The observed and simulated discharge, velocity and water depth for the calibration period are shown in Figure 8.5 (a).

The average observed discharge, velocity and water depth data for the calibration period at 5.2 km distance along the main canal from the irrigation intake are $13.77 \text{ m}^3/\text{s}$, 0.5 m/s , and 1.44 m respectively. The simulated values are close to observed values. The simulated discharge, velocity and water depth data for the calibration period are $13.71 \text{ m}^3/\text{s}$, 0.53 m/s , and 1.45 m respectively. The minimum (mean minus standard deviation)

and maximum (mean plus standard deviation) standard deviations range for velocity are 0.39 m/s and 0.61 m/s for the calibration period based on the variation in velocity within the measured canal section. The simulated velocity for the calibration period is within the standard deviation of the mean. Likewise, the minimum and maximum standard deviations range for water depth are 1.36 m and 1.52 m for the calibration period, based on the variation in water depth within the measured canal section. The simulated water depth for the calibration period is within the standard deviation of the mean.

(a) Calibration



(b) Validation

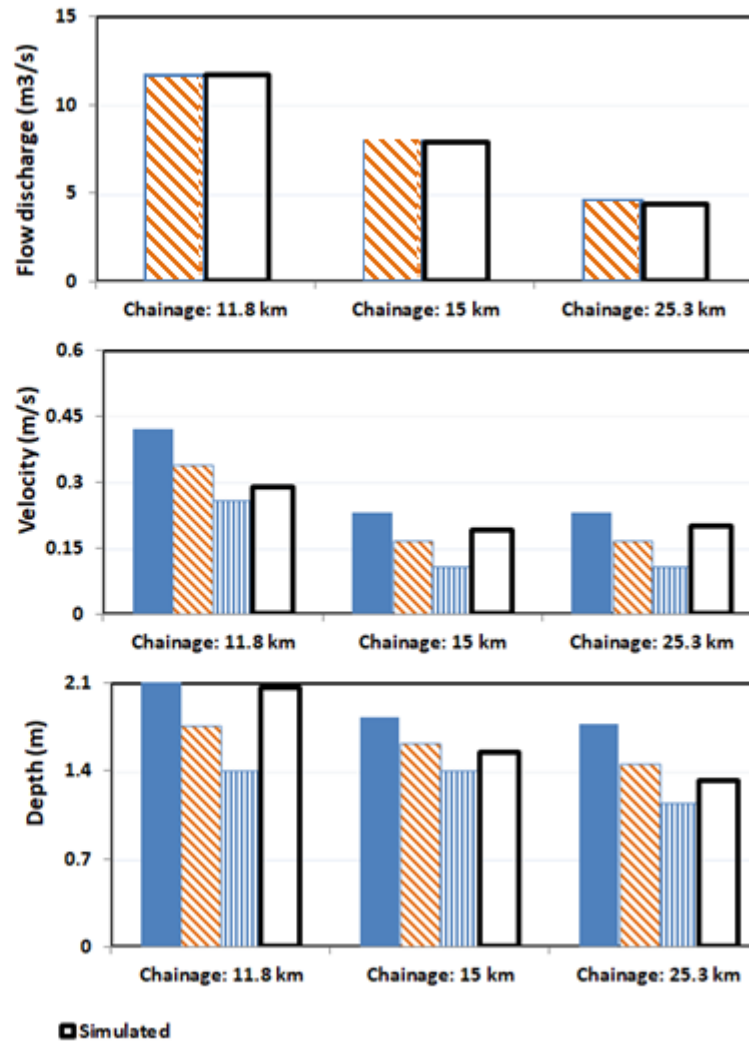


Figure 8.5: Observed and simulated discharge, velocity and water depth for the (a) calibration and (b) validation periods.

On the main canal, the average observed discharge, velocity and water depth data for the calibration period at 13 km distance from the irrigation intake are 8.53 m³/s, 0.21 m/s, and 1.32 m respectively. The simulated values are close to observed values. The simulated discharge, velocity and water depth data for the calibration period are 8.53 m³/s, 0.17 m/s, and 1.77 m respectively. The minimum (mean minus standard deviation) and maximum (mean plus standard deviation) standard deviations range for velocity are 0.14 m/s and 0.28 m/s for the calibration period based on the variation in velocity within the measured canal section. The simulated velocity for the calibration period is within the standard deviation of the mean. Likewise, the minimum and maximum standard deviations range for water depth are 0.84 m and 1.80 m for the calibration period based on the variation in water depth within the measured canal section. The simulated water depth for the calibration period is within the standard deviation of the mean.

On the main canal, the average observed discharge, velocity and water depth data for the calibration period at 22.5 km distance from the irrigation intake are 5.04 m³/s, 0.19 m/s, and 1.27 m respectively. The simulated values are close to observed values. The simulated discharge, velocity and water depth data for the calibration period are 5.01 m³/s, 0.21 m/s, and 1.27 m respectively. The minimum (mean minus standard deviation) and maximum (mean plus standard deviation) standard deviations range for velocity are 0.10 m/s and 0.28 m/s for the calibration period, based on the variation in velocity within the measured canal section. The simulated velocity for the calibration period is within the standard deviation of the mean. Likewise, the minimum and maximum standard deviations range for water depth are 0.96 m and 1.58 m for the calibration period based on the variation in water depth within the measured canal section. The simulated water depth for the calibration period is within the standard deviation of the mean.

The PCSWMM model performance for the calibration period is good as the simulated values for discharge, velocity and water depth are close to observed values and within the standard deviation of the mean.

8.4.3 Model validation

Using the calibrated model based on discharge, velocity and water depth data in the main canal of the Sunsari Morang Irrigation scheme, the PCSWMM model was

validated using discharge, velocity and water depth data at different canal sections than those used for model calibration. Different data sets were used for calibration and validation. For model validation, discharge, velocity and water depth data at 11.8 km, 15 km and 25.3 km distance along the main canal from the irrigation intake were used. The observed and simulated discharge, velocity and water depth data for the validation period are shown above in Figure 8.5 (b).

On the main canal, the average observed discharge, velocity and water depth data for the validation period at 11.8 km distance from the irrigation intake are 11.81 m³/s, 0.34 m/s, and 1.76 m respectively. The simulated values are close to observed values. The simulated discharge, velocity and water depth for the validation period are 11.73 m³/s, 0.29 m/s, and 2.06 m respectively. The minimum (mean minus standard deviation) and maximum (mean plus standard deviation) standard deviation range for velocity are 0.26 m/s and 0.42 m/s for the validation period. Likewise, the minimum and maximum standard deviation range for water depth are 1.41 m and 2.11 m for the validation period. The simulated velocity and water depth for validation period are within the standard deviation of the mean.

On the main canal, the average observed discharge, velocity and water depth data for the validation period at 15 km distance from the irrigation intake are 8.01 m³/s, 0.17 m/s, and 1.62 m respectively. The simulated values are close to observed values. The simulated discharge, velocity and water depth for the validation period are 7.9 m³/s, 0.19 m/s, and 1.62 m respectively. The minimum (mean minus standard deviation) and maximum (mean plus standard deviation) standard deviation range for velocity are 0.11 m/s and 0.23 m/s for the validation period. Likewise, the minimum and maximum standard deviation range for water depth are 1.41 m and 1.83 m for the validation period. The simulated velocity and water depth for the validation period are within the standard deviation of the mean.

On the main canal, the average observed discharge, velocity and water depth data for the validation period at 25.3 km distance from the irrigation intake are 4.65 m³/s, 0.17 m/s, and 1.46 m respectively. The simulated values are close to observed values. The simulated discharge, velocity and water depth for the validation period are 4.39 m³/s, 0.20 m/s, and 1.32 m respectively. The minimum (mean minus standard deviation) and

maximum (mean plus standard deviation) standard deviation range for velocity are 0.11 m/s and 0.23 m/s for the validation period. Likewise, the minimum and maximum standard deviation range for water depth are 1.15 m and 1.77 m for the validation period. The simulated velocity and water depth for the validation period are within the standard deviation of the mean.

The PCSWMM model performance for the validation period is good, as the simulated values for discharge, velocity and water depth are close to observed values and within the standard deviation of the mean.

8.4.4 Scenario analysis (canal capacity assessment)

The main aim of scenario analysis was to assess the hydraulic capacity of the main canal of the Sunsari Morang Irrigation Scheme considering future water availability for irrigation at the irrigation canal intake for the short-term (2016-2045), mid-century (2036-2065) and end-of-century (2071-2100) time periods, under different climate change scenarios. The validated PCSWMM model was applied to assess the hydraulic capacity of the main canal for different future study periods and climate scenarios. The analysis will provide information on the carrying capacity of canal system based on water availability in Koshi River at the canal intake.

The short-term (2016-2045), mid-century (2036-2065) and end-of-century (2071-2100) periods, with the future water availability for irrigation at the irrigation canal intake under climate change scenarios RCP4.5 and RCP8.5 were considered for the future scenarios.

Future water availability for irrigation at the irrigation canal intake was projected based on future river discharge available in the Koshi River at irrigation canal intake (Chapter 6). This was carried out in the following steps:

- (a) Development of a stage-discharge relationship (rating curve) for the Koshi River at irrigation canal intake.
- (b) Projected river flow for future scenarios (output of hydrological model).
- (c) Water availability for irrigation at the irrigation canal intake for future scenarios derived from (a) and (b) above.

Records of Koshi River water levels at the irrigation intake were taken from the Sunsari Morang Irrigation Project office, and the river discharge data were obtained from the Department of Hydrology and Meteorology, Nepal. Although the record-keeping system exists at the irrigation intake, the record-keeping books are missing and only around six years' data are available. Data available on the river water level at the irrigation intake for around six years from 1996 – 2012 were used for developing a stage-discharge relationship (rating curve) for the Koshi River at the irrigation canal intake (Figure: 8.6). The elevation of the intake crest level at the entry point to the main irrigation canal is 107 m above mean sea level (AMSL). More concentrated dotted points near 107 m AMSL represent river water at dry season. When the river water level is ≤ 107 m, there is no water flow into the canal system. The relationship between water level elevation and river discharge is mentioned in Equation 8.5.

$$\text{Water level elevation} = 100.65 \times \text{river flow discharge}^{0.0113} \quad 8.5$$

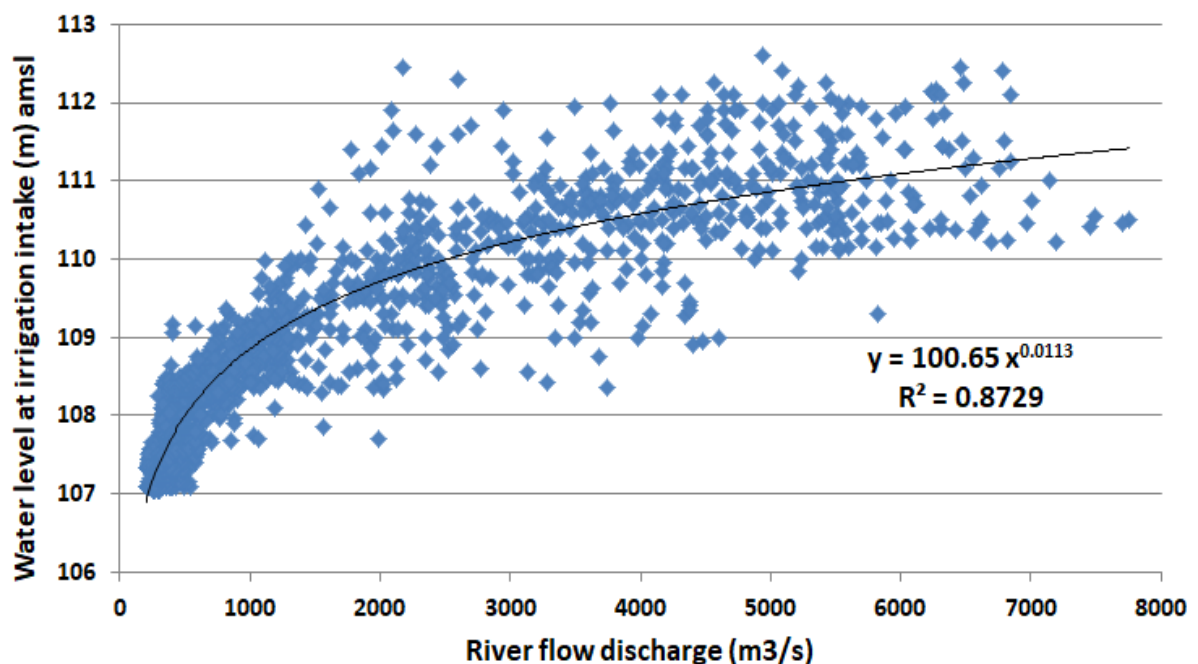


Figure 8.6: Stage-discharge relationship for the Koshi River at the irrigation canal intake, based on data available from 1996 to 2012.

Using the rating curve at Figure 8.6, water level elevations for observed river discharge for reference (base) period (1981-2010) were calculated. The minimum average monthly flows in the Koshi River at the irrigation canal intake for the three study

periods were taken from the hydrological analysis described in Chapter Six and published in (Kaini et al., 2020b). Water level elevations for projected future minimum average monthly flows in the Koshi River at the irrigation canal intake during the dry season (December – May) were calculated using rating curve Equation 8.5.

Based on water level elevations at the canal intake for projected future minimum average monthly flows, water availability for irrigation at the irrigation canal intake in future during the dry season was calculated. In the dry season, water flows into the canal from the river as a broad-crested free flow. The weir acts as a broad-crested weir when the head over the crest is less than the 1.5 times the width of crest (Garg, 2006). The weir crest elevation at the irrigation intake is 107 m AMSL. The width of weir in the flow direction at the intake of the Sunsari Morang Irrigation Scheme is 2 m. The average and median values of the head over the weir crest at intake in the dry season (December – May) during 1982-2010 were 107.78 m and 107.72 m respectively. The water level at the intake and river discharge derived from the stage-discharge relationship in the dry season (December – May) during 1982-2010 is shown in Figure 8.3. The head over the weir crest at intake in the dry season (December – May) is never 4.5 m (1.5 x 2 m). Hence, weir always acts as broad-crested weir in the dry season.

The discharge from a broad-crested weir can be calculated by Equation 8.6 (Garg, 2006).

$$Q = 1.7 (L - K n H) H^{3/2} \quad 8.6$$

Where Q = discharge in m³/s, L = clear waterway length (m), K = coefficient of end contraction general taken as 0.1, n = number of end contractions (twice the number of gated bays) and H = head over the crest (m).

Water availability for irrigation at the irrigation canal intake in future dry seasons was calculated based on water level elevations at the canal intake for the projected future minimum average monthly flow using Equation 8.6.

8.5 Results and discussion

8.5.1 Average monthly water availability for irrigation at the irrigation canal intake for dry season during 1982-2010

Average monthly water availability for irrigation at the irrigation canal intake for dry seasons during 1982-2010 is shown in Figure 8.7. The average monthly water availability for irrigation at the irrigation canal intake during 1982-2010 in December, January, February, March, April and May were 76.69 m³/s, 41.68 m³/s, 27.87 m³/s, 29.39 m³/s, 50.50 m³/s and 124.84 m³/s respectively. The lowest flow into the canal was in February, followed by March. The standard deviation of the mean varies from 13.30 m³/s to 42.44 m³/s in February, and 13.49 m³/s to 45.29 m³/s in March. This shows that there was a low discharge into the canal during January, February, March and April, compared to the designed discharge of 60 m³/s.

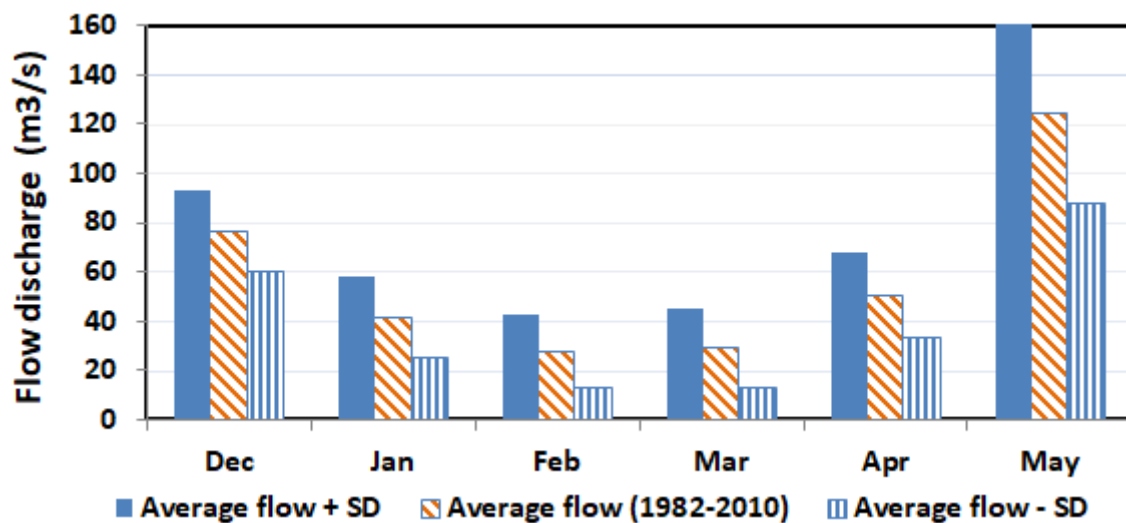


Figure 8.7: Average monthly water availability for irrigation at the irrigation canal intake for dry seasons during 1982-2010.

8.5.2 Projected average monthly minimum flow availability for irrigation at canal intake

Data about monthly or half-monthly water availability in the river, rather than annual or seasonal water availability, is crucial for design and management of irrigation schemes in developing countries. In many irrigation schemes in developing countries,

mechanisms which divert water from the source into the irrigation canal are still operating on gravity flow, and lack pumping mechanisms and impoundment structures.

Projected average monthly minimum flow availability for irrigation at the Sunsari Morang Irrigation Scheme canal intake for the short-term (2016-2045), mid-century (2036-2065) and end-of-century (2071-2100) periods, considering climate change scenarios RCP4.5 and RCP8.5, is shown in Table 8.8. Water availability for irrigation at the canal intake is expected to increase for all time periods and climate change scenarios in December, January, February and March. However, there is no consensus in increases or decreases in projected flows for April and May. This is due to the projected flow variation in river water availability (Kaini et al., 2020c), as the discharge in the river directly affects the water availability for irrigation at the irrigation canal intake. Table 8.8 shows that although there is an increase in water availability for irrigation in December, January, February and March, the designed discharge of 60 m³/s would not be available in February and March for all future scenarios.

Table 8.8: Projected average monthly minimum flow (m³/s) availability for irrigation at the canal intake, with reference (base) period flow for comparison.

Scenarios	Dec	Jan	Feb	Mar	Apr	May
Reference period (1982-2010)	76.69	41.68	27.87	29.39	50.50	124.84
Short-term (2016-2045)_RCP4.5	124.80	70.42	47.65	40.50	42.02	90.64
Short-term (2016-2045)_RCP8.5	92.18	54.35	36.96	35.57	55.26	155.43
Mid-century (2036-2065)_RCP4.5	114.41	65.15	42.80	43.46	85.89	200.22
Mid-century (2036-2065)_RCP8.5	110.84	66.21	46.69	44.44	46.87	115.34
End-of-century (2071-2100)_RCP4.5	112.03	60.87	37.93	35.57	73.78	209.31
End-of-century (2071-2100)_RCP8.5	134.76	80.70	53.43	45.42	51.68	65.51

Projected average monthly minimum flow availability for irrigation at the canal intake along with their standard deviation of the mean is shown in Figure 8.8. In December and January, the lower value of the standard deviation of the mean for future average monthly minimum flow availability for irrigation at the canal intake is above the mean

flow for the period 1982-2010. In February, the lower value of the standard deviation of the mean for future average monthly minimum flow availability for irrigation at the canal intake is almost the same as the mean flow for the period 1982-2010. In March, April and May, the lower value of the standard deviation of the mean for future average monthly minimum flow availability for irrigation at the canal intake is below the mean flow for the period 1982-2010.

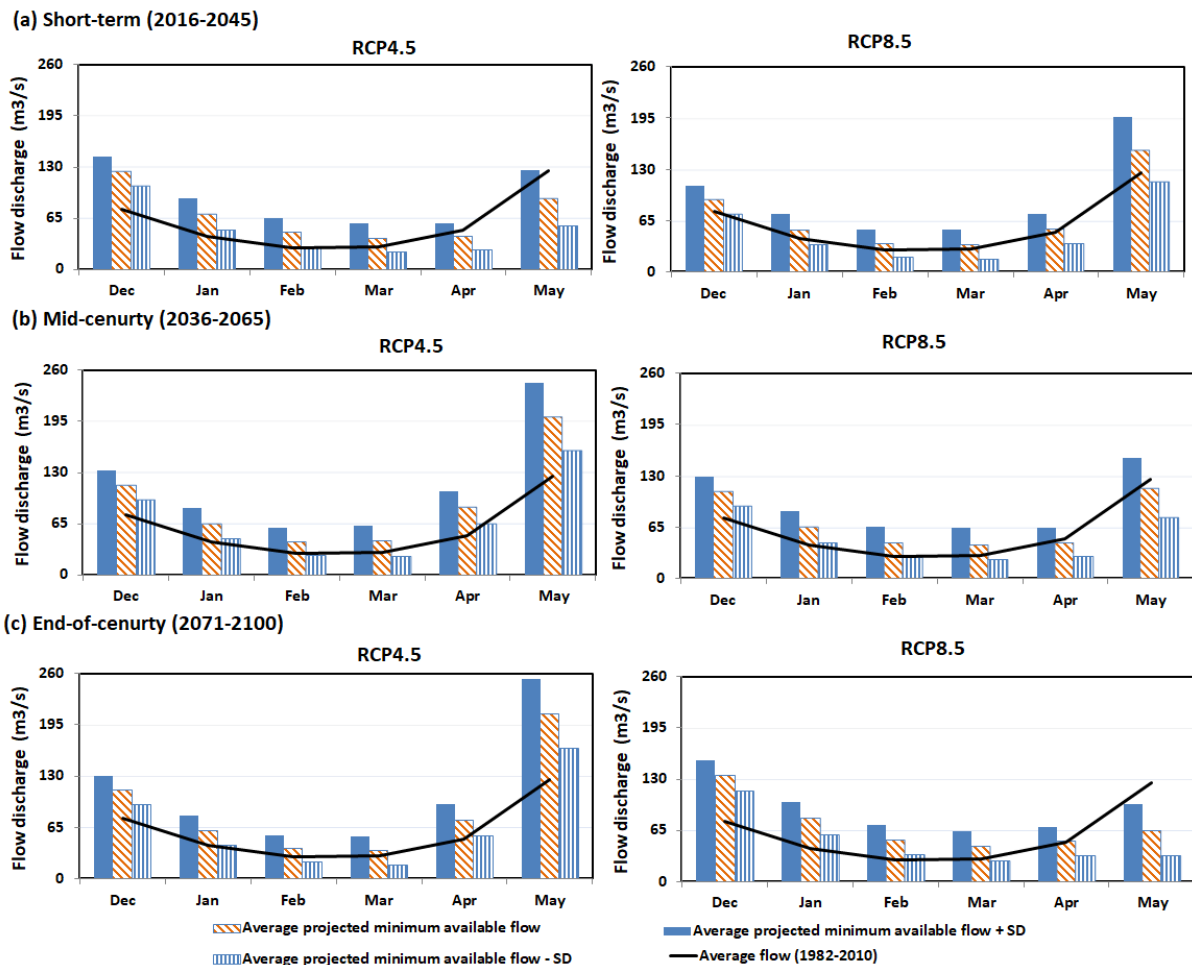


Figure 8.8: Projected average monthly minimum flow availability for irrigation at the canal intake, along with their standard deviation of the mean.

8.5.3 Projected area coverage for winter wheat crop

Irrigation water requirements for winter wheat crops at farm level, derived from crop modelling, are shown in Table 8.9. Table 8.9 shows that the highest irrigation water demand occurs in March, followed by February, for winter wheat crops in future.

However, water availability for irrigation at the canal intake will be less in March and February than in December, January and April.

Table 8.9: Irrigation water requirement (mm) for winter wheat crops at field level, derived from crop modelling.

Irrigation water requirement (mm) for winter wheat crop at field level					
Scenarios	Dec	Jan	Feb	Mar	Apr
Short-term (2016-2045)_RCP4.5	4	48	125	195	67
Short-term (2016-2045)_RCP8.5	4	50	130	197	58
Mid-century (2036-2065)_RCP4.5	4	49	126	198	58
Mid-century (2036-2065)_RCP8.5	5	53	127	192	50
End-of-century (2071-2100)_RCP4.5	4	55	135	196	51
End-of-century (2071-2100)_RCP8.5	4	52	125	183	29
Reference period (1982-2010)	3	44	118	198	66

Irrigation water requirements for winter wheat at the canal intake is shown in Table 8.10. In Nepal, average irrigation field efficiency, distribution canal efficiency, and main canal efficiency values for winter wheat crops are considered as 0.60, 0.75 and 0.75 respectively (Department of Irrigation, 1990). Considering these values of efficiencies, irrigation water requirements for winter wheat at the irrigation canal intake were estimated.

Table 8.10: Irrigation water requirements (liter/sec/ha) for winter wheat crop at the irrigation canal intake.

Irrigation water requirement (liter/sec/ha) for winter wheat at the irrigation canal intake					
Scenarios	Dec	Jan	Feb	Mar	Apr
Short-term (2016-2045)_RCP4.5	0.05	0.55	1.43	2.23	0.77
Short-term (2016-2045)_RCP8.5	0.05	0.57	1.49	2.25	0.66
Mid-century (2036-2065)_RCP4.5	0.05	0.56	1.44	2.26	0.66
Mid-century (2036-2065)_RCP8.5	0.06	0.61	1.45	2.19	0.57
End-of-century (2071-2100)_RCP4.5	0.05	0.63	1.54	2.24	0.58
End-of-century (2071-2100)_RCP8.5	0.05	0.59	1.43	2.09	0.33
Reference period (1982-2010)	0.03	0.5	1.35	2.26	0.75

Based on projected average monthly minimum flow availability for irrigation at the canal intake, and irrigation water requirements for winter wheat crops at the canal intake, the potential area coverage by winter wheat crop was projected (Table 8.11). For example, projected average monthly minimum flow availability for irrigation at the canal intake in the short-term (2016-2045) for climate change scenario RCP4.5 is 40.50 m³/s (Table 8.8), and the irrigation water requirements for this period is 2.23 liter/sec/ha (Table 8.10). Hence, the potential winter wheat area coverage for short-term (2016-2045), considering RCP4.5 scenario is 18200 hectares. The minimum area that can be covered throughout the cropping period of the winter wheat crop (December – April) should be taken as the potential area coverage for the winter wheat crop. Hence, area that could be covered in March is considered as potential area coverage, as it describes the minimum area coverage during the month when the irrigation demand is at its maximum.

Table 8.11: Potential area coverage by the winter wheat crop (in hectares).

Scenarios	Dec	Jan	Feb	Mar	Apr
Short-term (2016-2045)_RCP4.5	2496000	128000	33300	18200	54600
Short-term (2016-2045)_RCP8.5	1843600	95400	24800	15800	83700
Mid-century (2036-2065)_RCP4.5	2288200	116300	29700	19200	130100
Mid-century (2036-2065)_RCP8.5	1847300	108500	32200	20300	82200
End-of-century (2071-2100)_RCP4.5	2240600	96600	24600	15900	127200
End-of-century (2071-2100)_RCP8.5	2695200	136800	37400	21700	156600
Reference period (1982-2010)	2556300	83400	20600	13000	67300

Although water available for irrigation was sufficient for irrigating 13,000 ha of wheat during 1982-2010 reference period with no water deficit conditions, the average winter wheat area coverage during 2008-2016 was 26,000 ha (Table 7.1). This shows that there is water deficit in the winter wheat crop in the Sunsari Morang Irrigation Scheme command area and farmers are still practicing protective irrigation, which was also observed during field visits. The Sunsari Morang Irrigation Scheme was designed without considering crop water requirement criteria, and the main foci were to increase the crop area coverage and to protect crops from failure (Paudel, 2010, Adhikari, 2016, Renault and Wahaj, 2006). Jurriens et al. (1996) argued that protective design criteria, spreading available water thinly over a large command area rather than considering crop water requirements, have been followed in most of the irrigation schemes in India and nearby countries since 1880, and that such design criteria still prevail.

From Table 8.9, the minimum winter wheat area coverage that could be irrigated without any irrigation deficit is governed by the potential area coverage in March. Potential area coverage in March could be irrigated throughout the cropping period (December – April). With the existing irrigation intake, the winter wheat crop area could be increased by 3,000-5,000 ha in the short-term period, 6,000-7,000 ha in the mid-century period, and 3,000-9,000 ha in the end-of-century period with no water deficit conditions in the Sunsari Morang Irrigation Scheme command area. However,

winter wheat area coverage at present is 26,000 ha, and there is potential to increase the area coverage, water diversion or pumping mechanism at the irrigation canal intake, which could be realised to utilise the increased river discharge and to increase the winter wheat area coverage in the Sunsari Morang Irrigation Scheme command area.

8.5.4 Canal flow capacity assessment

Canal flow capacity in the Sunsari Morang Irrigation Scheme has been governed by the silt deposition and weed growth in the canal sections, thus resulting in reduced hydraulic capacity. Silt deposition has been an issue since the beginning of the project. Silt deposition in the canal varies along the length of the canal. In 2018-2020, a maximum silt depth of 0.80 m was observed in the main canal. Maximum flow capacity of the main canal was assessed in the validated PCSWMM model. The Sunsari Morang Irrigation Scheme was designed for 60 m³/s of discharge. However, the current canal capacity at the head reach portion of the main canal is only 53 m³/s at up to 10.7 km distance from the new canal intake. It shows that discharge capacity of canal has reduced by 12% in this portion of canal. Similarly, canal flow capacity was simulated as 35 m³/s at 13.8 km distance from new canal intake against the designed discharge capacity of 48 m³/s. In this portion of canal, the flow capacity of the canal has reduced by 27%. Likewise, canal flow capacity was simulated as 27 m³/s at 22.1 km distance from new canal intake against the designed flow capacity of 39 m³/s. In this portion of canal, the discharge capacity of the canal has reduced by 31%. Both the silt deposit (0.80 m) and Manning's roughness coefficient (0.093) were the highest at this portion. The average discharge reduction was 23%, which was due to inadequate maintenance of the canal system.

As potential area coverage in March could be irrigated throughout the cropping period, canal discharge available for irrigation at the canal intake was considered to assess the canal capacity needs for future scenarios. The maximum flow available in the irrigation canal during March in future is 45 m³/s for the end-of-century (2071-2100) period for the RCP8.5 scenario (Table 8.8). As the existing canal capacity at the head reach portion of the main canal is 53 m³/s, the canal system is adequate to pass the future flows for irrigating winter wheat crops with the existing irrigation intake.

There is the possibility to increase canal discharge capacity by reducing the Manning's roughness coefficient (n) as 0.03, considering less flow obstruction by silt and weeds. Canal discharge capacity is inversely proportional to the Manning's roughness coefficient. With regular maintenance of the canal system, the value of Manning's roughness coefficient can be reduced, and consequently canal discharge capacity can be increased compared to its current discharge capacity. Reduction in the current Manning's roughness coefficient values from 0.093 to 0.03 and 0.06 to 0.03 by regular maintenance of the canal network could significantly increase canal discharge capacity in the Sunsari Morang Irrigation Scheme main canal. However, any further increase in flow capacity would require a pumping system at the canal intake.

8.6 Conclusions

This study assessed the canal hydraulic capacity of the main canal of the Sunsari Morang Irrigation under climate change scenarios. Water availability in the Koshi River for irrigation has been investigated based on the irrigation canal intake characteristics. These water availability data have been used to project the future winter wheat area coverage in the Sunsari Morang Irrigation Scheme command area based on future irrigation water requirement. The current hydraulic capacity of the main canal has been assessed. A methodology for the application of a hydraulic model to investigate the irrigation canal discharge capacity was developed and applied to the Sunsari Morang Irrigation Scheme main canal.

The Personal Computer Storm Water Management Model (PCSWMM) hydraulic model was used for hydraulic modelling, being calibrated and validated based on the observed canal discharge, velocity and water depth. This study projected the future water availability for irrigation at the irrigation canal intake of the Sunsari Morang Irrigation Scheme, and potential winter wheat area coverage in the irrigation command area in the short-term (2016-2045), mid-century (2036-2065) and end-of-century (2071-2100) time periods considering the climate change scenario RCP4.5 and RCP8.5. These projections were done based on results from hydrological modelling (Chapter 6) and crop modelling (Chapter 7). The canal discharge capacity at present, and discharge capacity of the main canal considering future water availability were also investigated. The findings could be applied by the Department of Water Resources and Irrigation, Nepal

for increasing the discharge capacity of the irrigation canal, and increasing crop area coverage of the winter wheat crop in the irrigation command area.

The results from the discharge measurements in the main canal, assessment of water availability for irrigation at the irrigation canal intake and potential winter wheat area coverage, and a hydraulic capacity assessment of the Sunsari Morang Irrigation Scheme are as follows.

Water losses and manning's roughness coefficient

- The water losses between various canal sections as measured were 0.014 liter/sec/m² (l/s/m²), 0.009 l/s/m² and 0.007 l/s/m² respectively. Average water loss in the main canal was 0.01 l/s/m² in the Sunsari Morang Irrigation canal.
- The Manning's roughness coefficient varies from 0.037 to 0.093 at different locations of the main canal. The average value of Manning's roughness coefficient was 0.066 at the main canal of the Sunsari Morang Irrigation which is more than twice compared to the current design value for an earthen canal (0.025 - 0.03).

Water availability for irrigation at irrigation canal intake and potential winter wheat area coverage

- The average monthly water availability data for irrigation at the canal intake during 1982-2010 in December, January, February, March, April and May were 76.69 m³/s, 41.68 m³/s, 27.87 m³/s, 29.39 m³/s, 50.50 m³/s and 124.84 m³/s respectively. The lowest flow into the canal was in February followed by March. The standard deviation of the mean varies from 13.30 m³/s to 42.44 m³/s in February, and 13.49 m³/s to 45.29 m³/s in March. This shows that there was a low discharge into the canal during January, February, March and April, compared to the designed discharge of 60 m³/s.
- Water availability for irrigation at the canal intake is expected to increase for all time periods and climate change scenarios in December, January, February and March. Although there is an increase in water availability for irrigation in December, January, February and March, the designed discharge of 60 m³/s will not be available in February and March for all future scenarios.

- Although the amount of water available for irrigation was sufficient for irrigating 13,000 ha of wheat during 1982-2010 with no water deficit conditions, the average winter wheat area coverage during 2008-2016 was 26,000 ha. This shows a water deficit in the winter wheat crop in the Sunsari Morang Irrigation Scheme command area, and that farmers are still practicing protective irrigation, which was also observed during field visits.
- Based on the projected average monthly minimum flow availability for irrigation at the canal intake, and irrigation water requirements for winter wheat crop at the irrigation canal intake, and considering the existing irrigation intake and canal discharge capacity, the winter wheat crop area could be increased by 3,000-5,000 ha in the short-term period, 6,000-7,000 ha in the mid-century period, and 3,000-9,000 ha in the end-of-century period with no water deficit conditions in the Sunsari Morang Irrigation Scheme command area.
- Water diversion or a pumping mechanism at the irrigation canal intake could be realised to utilise the increased river discharge and to increase the winter wheat area coverage in the Sunsari Morang Irrigation Scheme command area.

Assessment of canal flow capacity

- The existing canal system is adequate to pass the future canal flows from the existing irrigation intake for irrigating the winter wheat crop, considering the flow available in the irrigation canal during March.
- The discharge capacity of canal has reduced by 12-31% at different sections of the main canal. The average discharge reduction is 23% due to inadequate maintenance of the canal system.
- Reduction in the current Manning's roughness coefficient values from 0.093 to 0.03 and from 0.06 to 0.03 by regular maintenance of the canal network could increase the canal flow capacity significantly in the Sunsari Morang Irrigation Scheme main canal.
- The quality and regularity of maintenance of the canal play a crucial role in terms of carrying the flow required under future climate change driven irrigation water demand conditions. Lining, relining, or piping the sections of the channel are growing trends across the globe for most major irrigation schemes. Thus,

lining, relining, or piping the sections of channel followed by regular maintenance could improve flow carrying capacity in the Sunsari Morang Irrigation Scheme canal network.

Chapter 9: Summary, conclusions and future research directions

This chapter summarizes all the research tasks conducted to accomplish the research aims, and presents the conclusions based on the results discussed in the earlier chapters. Furthermore, future research directions in this area are also provided.

9.1 Summary

The impacts of climate change on water resources and agriculture, accompanied by growing population, have contributed to increasing food and water scarcity. Due to continuing growth in population and changes in food requirement habits, the demand for agricultural products is increasing continuously. The irrigation sector plays a crucial role in agricultural food security, utilizing about 70% of the world's total annual water consumption. Climate variability and change have influenced on water availability for agriculture, crop water demands, and crop grain yields, rendering global food security vulnerable to climate change.

From the literature review, it is highlighted that a comprehensive methodology for irrigation schemes to investigate the impacts of climate change on both the supply and demand sides of irrigation water, and to simultaneously cope with changes in future water availability is missing. This research aims to holistically investigate the climate change impacts on both the supply and demand sides of irrigation water, and addresses the research gap. The methodology developed in this research was applied in the Sunsari Morang Irrigation Scheme in the Koshi River basin of Nepal, which has an irrigation command area of 68,000 hectares.

This research is divided into four major components. These components are: (a) understand the climate change impacts on daily rainfall and temperature (minimum and maximum) in the river basin and the irrigation command area, (b) assess future impacts of climate change on river water flow rates at the irrigation canal intake, (c) assess crop water requirements due to climate change, and (d) assess the existing irrigation canal system's hydraulic capacity and requirements for irrigation water supply in the climate change context.

Climate change is the main driver in assessing the river water availability for irrigation, crop irrigation requirements and canal system capacity needs. In this study,

Representative Concentration Pathways (RCPs) 4.5 and 8.5 climate change scenarios for the short-term (2016–2045), mid-century (2036–2065) and end-of-century (2071–2100) periods were considered. Representative General Circulation Models (GCMs) were selected for the study area for each climate change scenario and study periods. Daily precipitation and temperature data based on selected GCMs were downscaled to a higher resolution (10 km x 10 km). The downscaled daily precipitation and temperature data were applied to assess the climate change impacts on water availability in the river, and irrigation water demand in the irrigation scheme command area. An irrigation canal system capacity assessment was conducted based on the water availability in the river and irrigation water demand.

The Soil and Water Assessment Tool (SWAT) hydrological model was used for hydrological modelling, which was calibrated and validated based on the observed river flow data near the headwork of the Sunsari Morang Irrigation Scheme in the Koshi River. Impacts of climate change on the flow of the Koshi River at the headwork of the Sunsari Morang Irrigation Scheme was projected for the short-term, mid-century and end-of-century periods using downscaled daily precipitation and temperature data.

The Agricultural Production Systems Simulator (APSIM) crop model was selected for crop modelling, which was calibrated and validated based on the observed field-level data on phenological development, biomass yield and grain yield for the winter wheat crop in the Sunsari Morang Irrigation Scheme command area over two years. Impacts of climate change on the irrigation water demand, biomass yield and grain yield were projected for the short-term, mid-century and end-of-century periods, using downscaled daily precipitation and temperature data. In addition, the amount of irrigation water required to reach potential grain yields under current climate conditions was also compared with existing observed irrigation practices.

The hydraulic capacity of the main canal network, in terms of canal losses and flow carrying capacity of the irrigation canal system of the Sunsari Morang Irrigation Scheme, was assessed using the Personal Computer Stormwater Management Model (PCSWMM) hydraulic model, which was calibrated and validated based on the measured canal characteristics, discharge, flow velocity and water depth data. Based on hydrological assessments, information on daily water availability at the headwork

(intake) of the Sunsari Morang Irrigation Scheme in the Koshi River was used to estimate water intake into the canal network system. Considering irrigation water availability at the headwork and irrigation water amounts required for winter wheat crops at present, and in the future due to changes in climatic conditions, potential winter wheat area coverage and the water carrying capacity of the main canal were assessed.

9.2 Conclusions

The main conclusions of this research are summarised below.

9.2.1 General circulation models selection and climate data downscaling for the Koshi River basin

- The GCM selection for a catchment varies with the future climate change pathways selected (RCP4.5 and RCP8.5), as well as the future analysis periods (short-term, mid-century and end-of-century periods).
- Uncertainty in an average increase in annual precipitation is large in future. Higher uncertainty in precipitation is expected under climate change scenario RCP8.5, as compared to the RCP4.5 scenario.
- Monsoon precipitation is expected to increase in all scenarios and study periods. Similarly, post-monsoon precipitation is also expected to increase in future. However, winter precipitation is projected to decrease in future. The pre-monsoon precipitation is also expected to decrease in the coming decades.
- Uncertainty in an average increase in annual temperature is large in future. Higher uncertainty in mean annual temperature is expected in climate change scenario RCP8.5 as compared to RCP4.5 scenario.
- Mean annual temperature is expected to increase in all scenarios and study periods. An increase in temperature during winter is expected to be higher than that in the monsoon period. An increase in winter temperature will have an effect on the phenological development of winter wheat crop.

9.2.2 Hydrology of the Koshi River basin

- A river basin scale hydrological tool is needed to assess effects of climate change on river runoff. Soil and Water Assessment Tool (SWAT) can successfully be calibrated and validated using measured river discharge

parameter. SWAT is capable of projecting the effects of climate change on river runoff.

- The average annual river flow is projected to increase for all scenarios and study periods.
- The winter flow is expected to increase in future time periods. The pre-monsoon flow is expected to decrease in the short-term period; however, it is projected to increase in the mid-century and end-of-century periods. The monsoon and post-monsoon season flows are expected to increase in all study periods.
- The projected peak mean flow for climate change scenario RCP4.5 is lower than the flow for RCP8.5 scenario for all study periods, and the difference in magnitude increases in future time periods. A shift in the peak flow is expected in future, shifting towards the month of August and September, rather than occurring in July.
- The projected river flows based on selected ensembles in different climatic extremes show that there is high uncertainty about future flows in the Koshi River. The uncertainty in projected annual river flows is high for the end-of-century period compared to the mid-century period. Uncertainty in projected annual river flows is higher for the climate change scenario RCP8.5, compared to RCP4.5 scenario in the mid-century and end-of-century periods.

9.2.3 Crop water assessment for irrigation water requirement

- A crop growth/water balance model is needed to assess effects of climate change on crop growth, irrigation water demand, grain yield and biomass yield.
- The Agricultural Production Systems Simulator (APSIM) crop growth model can successfully be calibrated and validated using measured crop growth, grain yield and biomass yield indicators. APSIM has a good projection capacity.
- Farmers were applying only around one-fourth of the total irrigation water required to achieve optimal grain yields for the winter wheat crop in the Sunsari Morang Irrigation Scheme command area in the 2018-2019 and 2019-2020 seasons.
- The actual winter wheat crop grain yield was less than half of optimal grain yield in 2018-2019 and 2019-2020 respectively, due to irrigation deficit.

- The projected mean irrigation water demand for winter wheat crops in the Sunsari Morang Irrigation Scheme command area is likely to increase in the short-term, mid-century and end-of-century periods considering the climate change scenario RCP4.5. For the climate change scenario RCP8.5, mean irrigation water demand is projected to increase at the short-term period; however, it is likely to decrease in the mid-century and end-of-century periods.
- An increase in winter temperature would reduce the cropping periods (sowing – harvest) of winter wheat crops, resulting in a decrease in mean irrigation water demand at mid-century and end-of-century periods considering the climate change scenarios RCP4.5 and RCP8.5.
- The winter wheat crop grain yield at the Sunsari Morang Irrigation Scheme command area is expected to decrease in the short-term, mid-century and end-of-century periods for both climate change scenarios RCP4.5 and RCP8.5.
- The largest decrease in winter wheat crop grain yield is expected for end-of-century period under the climate change scenario RCP8.5, which is probably the result of reduced growing time due to increased winter temperature.
- The uncertainties in irrigation water demand, biomass yield and grain yield are projected to increase with the future time periods. The uncertainties are high at the end-of-century period compared to short-term and mid-century periods.

9.2.4 Canal hydraulic capacity assessment

- The Personal Computer Stormwater Management Model (PCSWMM) can successfully be calibrated and validated using measured discharge, velocity and water depth indicators.
- Inadequate maintenance of the canal system has resulted in the reduced flow capacity of the main canal. The discharge capacity of the canal has reduced by 12 to 31%. The average discharge capacity of the main canal has decreased by 23% due to inadequate maintenance of the canal system.
- Average monthly irrigation water availability at the irrigation canal intake during 1982-2010 was low during January, February, March and April, as compared to the designed discharge. There is a water deficit in the winter wheat crop in the Sunsari Morang Irrigation Scheme command area due to less water

being available in the main canal, and the farmers are still practicing protective irrigation.

- Water availability for irrigation at the canal intake is expected to increase for all time periods and climate change scenarios in December, January, February and March compared to the reference period (1982-2010). However, the increased future flow is less than the designed discharge, and the existing canal system is adequate to pass the future canal flows from the existing irrigation intake. Water diversion or a pumping mechanism at the irrigation canal intake could be realised to utilise the increased river discharge and to increase the winter wheat area coverage in the Sunsari Morang Irrigation Scheme command area, using the existing canal system.
- Projections on average monthly minimum discharge in Koshi River indicates that water availability into the canal will increase for all combinations of time periods (short-term, mid-century, and end-of-century) and climate change scenarios RCP4.5 and RCP8.5. Based on projected average monthly minimum flow availability for irrigation at the canal intake, and irrigation water requirements at irrigation canal intake for maximum winter wheat crop grain yield, winter wheat cropping area could be increased in future compared to the area cropped during 1982-2010, using the existing irrigation intake.
- Canal discharge capacity of $60 \text{ m}^3/\text{s}$ could be recaptured by regular maintenance of canal system which includes desilting and weed removal to reduce hydraulic roughness coefficient in the canal network.

9.3 Benefits, limitations and future research directions

The key innovation of this research is the development of a comprehensive methodology to assess the climate change impacts on the supply and demand sides of irrigation water. Moreover, this research has demonstrated its effectiveness through its successful application in the Sunsari Morang Irrigation Scheme in the Koshi River of Nepal. The methodology could be adopted to any physical-climatic conditions around the world to holistically assess the climate change impacts on both the supply and demand sides of irrigation water. The findings of this research are beneficial to water practitioners, the agricultural community, policy makers, and planners and researchers both in Nepal and internationally. The findings on projected climate change impacts on

water resources, irrigation water demand and hydraulic assessment of the irrigation canal network could be used by the Department of Water Resources and Irrigation, Nepal, to manage irrigation projects in the region and by local farmers to increase crop yield in study area.

However, this methodology and its application have a few limitations which can be improved by conducting further research as discussed below:

- The demand side of irrigation water is affected by many factors, including the socio-economic behaviour of users, the use of technology, irrigation application methods and stakeholders' involvement. These aspects have not been included in this research, and it is recommended to integrate these aspects into future research.
- Results from the Soil and Water Assessment Tool (SWAT) hydrological model have been analysed at Chatara near the intake of the Sunsari Morang Irrigation Scheme. Analysis of results from SWAT hydrological model could be extended to the Koshi sub-basin scale to assess water availability for irrigation at sub-basins. It could provide potential expansion of the cropping area at each sub-basin.
- In this study, water availability for irrigation has been analysed for winter wheat crop only and it could be extended to all crops grown throughout the year.
- The Agricultural Production Systems Simulator (APSIM) crop model for winter wheat crop has been calibrated and validated based on two years' data. This model could be used to investigate impacts of different irrigation scheduling on crop grain yield and biomass yield. The application part of APSIM model could further be used to explore the effects of different sowing times on irrigation water requirement, grain yield and biomass yield. Further field data would be required for such investigation in detail focused on crop modelling.
- The research could be extended to investigate the water-energy-food nexus in the irrigation command area.
- The Personal Computer Stormwater Management Model (PCSWMM) hydraulic model was calibrated and validated for the main canal of the Sunsari Morang Irrigation Scheme and it could be extended to the entire canal network in a

separate study for detailed investigation and improvements at intake structure and canal network to meet future water demand in the irrigation command area. The whole of scheme model could be used to assess the timing and volume of water availability to farmers in different parts of the Sunsari Morang Irrigation Scheme command area. Usually remote farmers (further from the main canal) have reduced access to the water. The water distribution (timing and volume) could be improved with a complete hydraulic modelling of the irrigation network from the intake to farm level.

- The uncertainties for GCMs selection and downscaling, SWAT hydrological modelling, APSIM crop modelling and PCSWMM hydraulic modelling are assessed in this research individually. However, cumulative uncertainty that is propagated through the selection of appropriate GCMs and the downscaling, and then the application of this information towards the SWAT, APSIM and PCSWMM modelling aspects has not been assessed. It could be extended to explore the cumulative uncertainty. However, a comprehensive modelling tool would be required to develop, which was outside the scope of this work. This aspect has included in the limitations of this research.

Appendix

Appendix -1: Distance of the first ten GCMs/ensembles from four corners, based on the short-term future period (2016-2045) and the reference period (1981-2010), for RCP8.5

Model	Distance from Corner			
	Cold and Dry	Warm and Dry	Cold and Wet	Warm and Wet
ACCESS1-0_r1ilp1	0.3793	0.6787	0.5199	0.7662
ACCESS1-3_r1ilp1	0.2867	0.7944	0.5221	0.9063
bcc-csm1-1_r1ilp1	0.6123	0.7519	0.3801	0.5787
BNU-ESM_r1ilp1	0.7109	0.4361	0.7265	0.4611
CanESM2_r1ilp1	1.1321	0.807	0.794	0.0092
CanESM2_r2ilp1	1.0113	0.7057	0.7346	0.1216
CanESM2_r3ilp1	1.2538	0.903	0.8787	0.1238
CanESM2_r4ilp1	1.1641	0.7599	0.8871	0.0971
CanESM2_r5ilp1	0.9732	0.544	0.8466	0.2561
CCSM4_r1ilp1	0.7	0.7159	0.4423	0.467

Appendix -2: Distance of the first ten GCMs/ensembles from four corners, based on the mid-century future period (2036-2065) and the reference period (1981-2010), for RCP4.5

Model	Distance from Corner			
	Cold and Dry	Warm and Dry	Cold and Wet	Warm and Wet
ACCESS1-0_r1ilp1	0.4376	0.4727	0.6959	0.7185
ACCESS1-3_r1ilp1	0.539	0.8223	0.3264	0.7015
bcc-csm1-1_r1ilp1	0.6513	0.9331	0.2006	0.6976
bcc-csm1-1-m_r1ilp1	0.4238	0.4238	0.7718	0.7718
BNU-ESM_r1ilp1	0.6551	0.62	0.525	0.4804
CanESM2_r1ilp1	0.9643	0.6134	0.7696	0.1966
CanESM2_r2ilp1	1.0487	0.8366	0.6504	0.1518
CanESM2_r3ilp1	1.1518	0.7674	0.8617	0.0703
CanESM2_r4ilp1	0.6291	0.2413	0.8921	0.6769
CanESM2_r5ilp1	0.963	0.7575	0.6243	0.1901

Appendix -3: Distance of the first ten GCMs/ensembles from four corners, based on the mid-century future period (2036-2065) and the reference period (1981-2010), for RCP8.5

Model	Distance from Corner			
	Cold and Dry	Warm and Dry	Cold and Wet	Warm and Wet
ACCESS1-0_r1ilp1	0.4488	0.5152	0.6424	0.6904
ACCESS1-3_r1ilp1	0.3041	0.6233	0.6233	0.8273
bcc-csm1-1_r1ilp1	0.8476	1.144	0.0563	0.7704
BNU-ESM_r1ilp1	0.5944	0.6129	0.5197	0.5408
CanESM2_r1ilp1	1.1557	0.8879	0.747	0.1037
CanESM2_r2ilp1	1.0985	0.8383	0.7158	0.0915
CanESM2_r3ilp1	1.1889	0.873	0.8103	0.0733
CanESM2_r4ilp1	1.0029	0.558	0.8687	0.2454
CanESM2_r5ilp1	1.1444	0.8612	0.7574	0.075
CCSM4_r1ilp1	0.5231	0.5028	0.6325	0.6158

Appendix -4: Distance of the first ten GCMs/ensembles from four corners, based on the end-of-century future period (2071-2100) and the reference period (1981-2010), for RCP4.5

Model	Distance from Corner			
	Cold and Dry	Warm and Dry	Cold and Wet	Warm and Wet
ACCESS1-0_r1ilp1	0.6696	0.5142	0.6353	0.4686
ACCESS1-3_r1ilp1	0.769	0.6959	0.5038	0.3829
bcc-csm1-1_r1ilp1	0.486	0.6256	0.5179	0.6507
bcc-csm1-1-m_r1ilp1	0.2851	0.5166	0.8254	0.9311
BNU-ESM_r1ilp1	0.6902	0.723	0.4303	0.4812
CanESM2_r1ilp1	1.0068	0.9196	0.51	0.3034
CanESM2_r2ilp1	0.8642	0.6521	0.6271	0.2677
CanESM2_r3ilp1	1.1549	0.8923	0.7415	0.1104
CanESM2_r4ilp1	0.8235	0.646	0.5971	0.3095
CanESM2_r5ilp1	1.0084	0.9039	0.5285	0.2817

Appendix -5: Distance of the first ten GCMs/ensembles from four corners, based on the end-of-century future period (2071-2100) and the reference period (1981-2010), for RCP8.5

Model	Distance from Corner			
	Cold and Dry	Warm and Dry	Cold and Wet	Warm and Wet
ACCESS1-0_r1ilp1	0.4075	0.5611	0.6142	0.7253
ACCESS1-3_r1ilp1	0.6391	0.8268	0.3053	0.607
bcc-csm1-1_r1ilp1	0.769	0.953	0.2102	0.6008
BNU-ESM_r1ilp1	0.3288	0.4842	0.7965	0.8723
CanESM2_r1ilp1	1.0939	0.8689	0.6787	0.1378
CanESM2_r2ilp1	1.1284	0.8771	0.7187	0.112
CanESM2_r3ilp1	1.1916	0.9002	0.7874	0.1018
CanESM2_r4ilp1	1.107	0.8371	0.7288	0.0796
CanESM2_r5ilp1	1.1725	0.8866	0.7728	0.0918
CCSM4_r1ilp1	0.4815	0.6656	0.4815	0.6656

References

- Abbaspour, K. C. 2015. SWAT-CUP. *SWAT Calibration and Uncertainty Program - A User Manual*.
- Adhikari, B. 2016. Design of Water Distribution System: Appropriateness of Structured System in Large Irrigation Projects in Nepal. *Hydro Nepal: Journal of Water, Energy and Environment*, 19, 25-30.
- Agarwal, A., Babel, M. S. & Maskey, S. 2014. Analysis of future precipitation in the Koshi river basin, Nepal. *Journal of Hydrology*, 513, 422-434.
- Agarwal, A., Babel, M. S. & Maskey, S. 2015. Estimating the impacts and uncertainty of climate change on the Hydrology and Water Resources of the Koshi River Basin. *Managing Water Resources under Climate Uncertainty*. Springer.
- Agarwal, A., Babel, M. S., Maskey, S., Shrestha, S., Kawasaki, A. & Tripathi, N. K. 2016. Analysis of temperature projections in the Koshi River Basin, Nepal. *International Journal of Climatology*, 36, 266-279.
- Ahmed, K. F., Wang, G., Silander, J., Wilson, A. M., Allen, J. M., Horton, R. & Anyah, R. 2013. Statistical downscaling and bias correction of climate model outputs for climate change impact assessment in the US northeast. *Global and Planetary Change*, 100, 320-332.
- Akkuzu, E. 2012. Usefulness of empirical equations in assessing canal losses through seepage in concrete-lined canal. *Journal of irrigation and drainage engineering*, 138, 455-460.
- Alcamo, J., Dronin, N., Endejan, M., Golubev, G. & Kirilenko, A. 2007. A new assessment of climate change impacts on food production shortfalls and water availability in Russia. *Global Environmental Change*, 17, 429-444.
- Alexandratos, N. & Bruinsma, J. 2012. World agriculture towards 2030/2050: the 2012 revision. ESA Working paper No. 12-03. Rome, FAO.
- Anser, M. K., Hina, T., Hameed, S., Nasir, M. H. & Ahmad, I. 2020. Modeling Adaptation Strategies against Climate Change Impacts in Integrated Rice-Wheat Agricultural Production System of Pakistan. *International Journal of Environmental Research and Public Health*, 17, 2522.
- Apsim-Crop Module Documentation. 2020. *Crop Module Documentation* [Online]. Available: <https://www.apsim.info/documentation/model-documentation/crop-module-documentation/> [Accessed on 18 October 2020].

- Arnold, J. G., Srinivasan, R., Muttiah, R. S. & Williams, J. R. 1998. Large area hydrologic modeling and assessment part I: model development 1. *JAWRA Journal of the American Water Resources Association*, 34, 73-89.
- Asres, S. B. 2016. Evaluating and enhancing irrigation water management in the upper Blue Nile basin, Ethiopia: The case of Koga large scale irrigation scheme. *Agricultural Water Management*, 170, 26-35.
- Asseng, S., Keating, B., Fillery, I., Gregory, P., Bowden, J., Turner, N., Palta, J. & Abrecht, D. 1998. Performance of the APSIM-wheat model in Western Australia. *Field Crops Research*, 57, 163-179.
- Awulachew, S. B. & Ayana, M. 2011. Performance of irrigation: An assessment at different scales in Ethiopia. *Experimental Agriculture*, 47, 57-69.
- Bai, H., Wang, J., Fang, Q. & Huang, B. 2020. Does a trade-off between yield and efficiency reduce water and nitrogen inputs of winter wheat in the North China Plain? *Agricultural Water Management*, 233, 106095.
- Bajracharya, A. R., Bajracharya, S. R., Shrestha, A. B. & Maharjan, S. B. 2018. Climate change impact assessment on the hydrological regime of the Kaligandaki Basin, Nepal. *Science of the Total Environment*, 625, 837-848.
- Bakry, M. F., Gates, T. K. & Khattab, A. F. 1992. Field-measured hydraulic resistance characteristics in vegetation-infested canals. *Journal of Irrigation and Drainage Engineering*, 118, 256-274.
- Banda, D. & Kasitu, R. 2018. Modeling of storm water runoff for Kitwe CBD drainage system using SWMM software. *Rwanda Journal of Engineering, Science, Technology and Environment*, 1.
- Bang, N.-K., Nam, W.-H., An, H.-U., Ha, T.-H. & Lee, K.-Y. 2019. OPTIMAL OPERATION OF IRRIGATION CANAL NETWORK SYSTEM USING SWMM. *3rd World Irrigation Forum (WIF3), 1-7 September 2019, Bali, Indonesia*.
- Barker, R. & Molle, F. 2004. *Evolution of irrigation in South and Southeast Asia*, International Water Management Institute, Colombo, Sri Lanka.
- Baulcombe, D., Crute, I., Davies, B., Dunwell, J., Gale, M., Jones, J., Pretty, J., Sutherland, W. & Toulmin, C. 2009. Reaping the benefits: science and the sustainable intensification of global agriculture. *The Royal Society, Science Policy*, October 2009.
- Beven, K. 2002. Towards an alternative blueprint for a physically based digitally simulated hydrologic response modelling system. *Hydrological processes*, 16, 189-206.

- Bharati, L., Bhattarai, U., Khadka, A., Gurung, P., Neumann, L., Penton, D., Dhaubanjari, S. & Nepal, S. 2019. *From the mountains to the plains: impact of climate change on water resources in the Koshi River Basin*, International Water Management Institute (IWMI).
- Bharati, L., Gurung, P., Jayakody, P., Smakhtin, V. & Bhattarai, U. 2014. The projected impact of climate change on water availability and development in the Koshi Basin, Nepal. *Mountain Research and Development*, 34, 118-130.
- Bharati, L., Gurung, P., Maharjan, L. & Bhattarai, U. 2016. Past and future variability in the hydrological regime of the Koshi Basin, Nepal. *Hydrological Sciences Journal*, 61, 79-93.
- Bhattarai, P. 2013. *Improving hydrological process modelling of the Koshi River basin in Nepal*. MSc, Unesco-IHE, The Netherlands.
- Biemans, H., Speelman, L., Ludwig, F., Moors, E., Wiltshire, A., Kumar, P., Gerten, D. & Kabat, P. 2013. Future water resources for food production in five South Asian river basins and potential for adaptation—A modeling study. *Science of the Total Environment*, 468, S117-S131.
- Boé, J., Terray, L., Habets, F. & Martin, E. 2007. Statistical and dynamical downscaling of the Seine basin climate for hydro-meteorological studies. *International Journal of Climatology*, 27, 1643-1655.
- Bolding, A., Mollinga, P. P. & Van Straaten, K. 1995. Modules for modernisation: colonial irrigation in India and the technological dimension of agrarian change. *The Journal of Development Studies*, 31, 805-844.
- Boote, K. J., Jones, J. W. & Pickering, N. B. 1996. Potential uses and limitations of crop models. *Agronomy journal*, 88, 704-716.
- Borah, D. & Bera, M. 2003. Watershed-scale hydrologic and nonpoint-source pollution models: Review of mathematical bases. *Transactions of the ASAE*, 46, 1553-1566.
- Bouraoui, F., Benabdallah, S., Jrad, A. & Bidoglio, G. 2005. Application of the SWAT model on the Medjerda river basin (Tunisia). *Physics and Chemistry of the Earth, Parts A/B/C*, 30, 497-507.
- Bouras, E., Jarlan, L., Khabba, S., Er-Raki, S., Dezetter, A., Sghir, F. & Trambly, Y. 2019. Assessing the impact of global climate changes on irrigated wheat yields and water requirements in a semi-arid environment of Morocco. *Scientific reports*, 9, 1-14.
- Brooks, K. N., Ffolliott, P. F. & Magner, J. A. 2013. *Hydrology and the Management of Watersheds*, John Wiley & Sons, Fourth edition.

- Bumbudsanpharoke, W. & Prajamwong, S. 2015. Performance Assessment for Irrigation Water Management: Case Study of the Great Chao Phraya Irrigation Scheme. *Irrigation and Drainage*, 64, 205-214.
- Cao, W., Bowden, W. B., Davie, T. & Fenemor, A. 2006. Multi-variable and multi-site calibration and validation of SWAT in a large mountainous catchment with high spatial variability. *Hydrological Processes: An International Journal*, 20, 1057-1073.
- Challinor, A. J., Müller, C., Asseng, S., Deva, C., Nicklin, K. J., Wallach, D., Vanuytrecht, E., Whitfield, S., Ramirez-Villegas, J. & Koehler, A.-K. 2018. Improving the use of crop models for risk assessment and climate change adaptation. *Agricultural systems*, 159, 296-306.
- Chandran, K. M. & Joseph, E. 2015. Innovativeness of Farmers in Irrigation Scheduling for Major Plantation Crops: Analysis from Kerala State, India. *Journal of Agricultural Sciences*, 10.
- Chattaraj, S., Chakraborty, D., Sehgal, V., Paul, R., Singh, S., Daripa, A. & Pathak, H. 2014. Predicting the impact of climate change on water requirement of wheat in the semi-arid Indo-Gangetic Plains of India. *Agriculture, ecosystems & environment*, 197, 174-183.
- Checkol, G. & Alamirew, T. 2008. Technical and Institutional Evaluation of Geray Irrigation Scheme in West Gojjam Zone, Amhara Region, Ethiopia. *Journal of Spatial Hydrology*, 8, 36-48.
- Chen, C., Wang, E. & Yu, Q. 2010a. Modeling wheat and maize productivity as affected by climate variation and irrigation supply in North China Plain. *Agronomy Journal*, 102, 1037-1049.
- Chen, C., Wang, E. & Yu, Q. 2010b. Modelling the effects of climate variability and water management on crop water productivity and water balance in the North China Plain. *Agricultural Water Management*, 97, 1175-1184.
- Chen, J., Brissette, F. P., Chaumont, D. & Braun, M. 2013. Finding appropriate bias correction methods in downscaling precipitation for hydrologic impact studies over North America. *Water Resources Research*, 49, 4187-4205.
- Chen, J. & Chang, H. 2020. Relative impacts of climate change and land cover change on streamflow using SWAT in the Clackamas River Watershed, USA. *Journal of Water and Climate Change*.
- Chen, S.-T., Yu, P.-S. & Tang, Y.-H. 2010c. Statistical downscaling of daily precipitation using support vector machines and multivariate analysis. *Journal of hydrology*, 385, 13-22.

- Chen, S. C., Roads, J. O., Juang, H. M. H. & Kanamitsu, M. 1999. Global to regional simulations of California wintertime precipitation. *Journal of Geophysical Research: Atmospheres*, 104, 31517-31532.
- Chenu, K., Porter, J. R., Martre, P., Basso, B., Chapman, S. C., Ewert, F., Bindi, M. & Asseng, S. 2017. Contribution of crop models to adaptation in wheat. *Trends in plant science*, 22, 472-490.
- Dahal, P., Shrestha, M. L., Panthi, J. & Pradhananga, D. 2020. Modeling the future impacts of climate change on water availability in the Karnali River Basin of Nepal Himalaya. *Environmental Research*, 109430.
- Dahal, V., Shakya, N. M. & Bhattarai, R. 2016. Estimating the impact of climate change on water availability in Bagmati Basin, Nepal. *Environmental Processes*, 3, 1-17.
- De Silva, C., Weatherhead, E., Knox, J. W. & Rodriguez-Diaz, J. 2007. Predicting the impacts of climate change—A case study of paddy irrigation water requirements in Sri Lanka. *Agricultural water management*, 93, 19-29.
- Deihimfard, R., Mahallati, M. N. & Koocheki, A. 2015. Yield gap analysis in major wheat growing areas of Khorasan province, Iran, through crop modelling. *Field Crops Research*, 184, 28-38.
- Department of Irrigation 1990. Design Manuals for Irrigation Projects in Nepal, M3: Hydrology and Agro-Meteorology Manual. Department of Irrigation, Nepal.
- Department of Irrigation 1995. Sunsari Morang Irrigation III Detail Feasibility and Design, Volume-1, Main Report. NIPPON KOEI Co. Ltd. In association with MULTI Disciplinary Consultants (P) Ltd and Nepal Consult (P) Ltd, Department of Irrigation, Nepal.
- Department of Irrigation 2014. Irrigation Hand Book. Department of Irrigation, Nepal.
- Devi, G. K., Ganasri, B. & Dwarakish, G. 2015. A review on hydrological models. *Aquatic Procedia*, 4, 1001-1007.
- Devkota, L. P. & Gyawali, D. R. 2015. Impacts of climate change on hydrological regime and water resources management of the Koshi River Basin, Nepal. *Journal of Hydrology: Regional Studies*, 4, 502-515.
- Dingman, S. L. 2015. *Physical hydrology. Third edition*, Waveland Press, Inc. United States of America.
- Dixit, A., Upadhyaya, M., Dixit, K., Pokhrel, A. & Rai, D. R. 2009. Living with water stress in the hills of the Koshi Basin, Nepal. *International Centre for Integrated Mountain Development, Nepal*.

- Do, J.-W., Nam, W.-H., Lee, K.-Y., Ha, T.-H., Lee, S.-Y. & Jung, E.-Y. Optimal irrigation management system based on hydraulic analysis of irrigation canal. 2019 ASABE Annual International Meeting, 2019. American Society of Agricultural and Biological Engineers, 1.
- Döll, P. 2002. Impact of climate change and variability on irrigation requirements: a global perspective. *Climatic change*, 54, 269-293.
- Dreccer, M. F., Fainges, J., Whish, J., Ogbonnaya, F. C. & Sadras, V. O. 2018. Comparison of sensitive stages of wheat, barley, canola, chickpea and field pea to temperature and water stress across Australia. *Agricultural and Forest Meteorology*, 248, 275-294.
- Elliott, J., Deryng, D., Müller, C., Frieler, K., Konzmann, M., Gerten, D., Glotter, M., Flörke, M., Wada, Y. & Best, N. 2014. Constraints and potentials of future irrigation water availability on agricultural production under climate change. *Proceedings of the National Academy of Sciences*, 111, 3239-3244.
- Eriksson, M., Xu, J., Shrestha, A. B., Vaidya, R. A., Santosh, N. & Sandström, K. 2009. *The changing Himalayas: impact of climate change on water resources and livelihoods in the greater Himalayas.*, International centre for integrated mountain development (ICIMOD), Nepal.
- Eshetu, B. & Alamirew, T. 2018. Estimation of seepage loss in irrigation canals of Tendaho sugar estate, Ethiopia. *Irrig. Drain. Syst. Eng*, 7, 3-7.
- Fao. 2016a. *AQUASTAT:Nepal, Food and Agriculture Organization of the United Nations, Rome, Italy* [Online]. Food and Agriculture Organization of the United Nations (FAO). Available: http://www.fao.org/nr/water/aquastat/countries_regions/NPL/NPL-CP_eng.pdf [Accessed 30th May 2017].
- Fao. 2016b. *Water withdrawal by sector, around 2010* [Online]. Food and Agriculture Organization of the United Nations. Available: http://www.fao.org/nr/Water/aquastat/tables/WorldData-Withdrawal_eng.pdf [Accessed 23rd August 2017].
- Fao/Unesco 1973. *Irrigation, Drainage and Salinity An International Source Book*, The Camelot Press Ltd, London.
- Fischer, G., Tubiello, F. N., Van Velthuisen, H. & Wiberg, D. A. 2007. Climate change impacts on irrigation water requirements: effects of mitigation, 1990–2080. *Technological Forecasting and Social Change*, 74, 1083-1107.
- Flohr, B. M., Hunt, J. R., Kirkegaard, J. A. & Evans, J. R. 2017. Water and temperature stress define the optimal flowering period for wheat in south-eastern Australia. *Field Crops Research*, 209, 108-119.

- Garg, S. K. 2006. *Irrigation engineering and hydraulic structures*, Nineteenth edition, Khanna Publishers, Delhi, India.
- Gassman, P. W., Reyes, M. R., Green, C. H. & Arnold, J. G. 2007. The soil and water assessment tool: historical development, applications, and future research directions. *Transactions of the ASABE*, 50, 1211-1250.
- Gleckler, P. J., Taylor, K. E. & Doutriaux, C. 2008. Performance metrics for climate models. *Journal of Geophysical Research: Atmospheres*, 113.
- Godfray, H. C. J., Beddington, J. R., Crute, I. R., Haddad, L., Lawrence, D., Muir, J. F., Pretty, J., Robinson, S., Thomas, S. M. & Toulmin, C. 2010. Food security: the challenge of feeding 9 billion people. *science*, 327, 812-818.
- Golmohammadi, G., Prasher, S., Madani, A. & Rudra, R. 2014. Evaluating three hydrological distributed watershed models: MIKE-SHE, APEX, SWAT. *Hydrology*, 1, 20-39.
- Gon-Climate Change Management Division 2015. National Adaptation Plan Formulation Process Launching Workshop Proceeding. Government of Nepal, Ministry of Science, Technology and Environment, Climate Change Management Division, Kathmandu, Nepal.
- Gon-National Adaptation Plan Formulation Process 2017. Vulnerability and Risk Assessment Framework and Indicators for National Adaptation Plan (NAP) Formulation Process in Nepal. Government of Nepal, Ministry of Population and Environment, Climate Change Management Division, National Adaptation Plan Formulation Process, Kathmandu, Nepal.
- Goodarzi, M., Abedi-Koupai, J. & Heidarpour, M. 2019. Investigating impacts of climate change on irrigation water demands and its resulting consequences on groundwater using CMIP5 models. *Groundwater*, 57, 259-268.
- Grant, D. M. 1989. *ISCO open channel flow measurement handbook, Third edition.*, ICVO Inc., Nebraska, USA.
- Gupta, H. V., Kling, H., Yilmaz, K. K. & Martinez, G. F. 2009. Decomposition of the mean squared error and NSE performance criteria: Implications for improving hydrological modelling. *Journal of hydrology*, 377, 80-91.
- Gupta, H. V., Sorooshian, S. & Yapo, P. O. 1999. Status of automatic calibration for hydrologic models: Comparison with multilevel expert calibration. *Journal of Hydrologic Engineering*, 4, 135-143.
- Gupta, R., Somanathan, E. & Dey, S. 2017. Global warming and local air pollution have reduced wheat yields in India. *Climatic Change*, 140, 593-604.

- Gurung, P. & Bharati, L. 2012. Downstream impacts of the Melamchi Inter-Basin Water Transfer Plan (MIWTP) under current and future climate change projections. *Hydro Nepal: Journal of Water, Energy and Environment*, 11, 23-29.
- Ha, T.-H., Nam, W.-H., Do, J., Lee, S.-Y., Jung, E.-Y. & Lee, K.-Y. Improving operational performance of irrigation canal network system for drought risk management using hydraulic model. 2019 ASABE Annual International Meeting, 2019. American Society of Agricultural and Biological Engineers, 1.
- Haider, M. M., Ahmad, A., Khaliq, T. & Shahbaz, M. 2015. Simulating the effects of sowing time on growth and yield of wheat in arid environment using APSIM-model. *Appl Sci Bus Econ*, 2, 1-7.
- Harrison, M. T., Cullen, B. R. & Armstrong, D. 2017. Management options for dairy farms under climate change: Effects of intensification, adaptation and simplification on pastures, milk production and profitability. *Agricultural Systems*, 155, 19-32.
- Harrison, M. T., Evans, J. R., Dove, H. & Moore, A. D. 2011. Recovery dynamics of rainfed winter wheat after livestock grazing 2. Light interception, radiation-use efficiency and dry-matter partitioning. *Crop and Pasture Science*, 62, 960-971.
- Harrison, M. T., Evans, J. R. & Moore, A. D. 2012. Using a mathematical framework to examine physiological changes in winter wheat after livestock grazing: 1. Model derivation and coefficient calibration. *Field Crops Research*, 136, 116-126.
- Harrison, M. T., Roggero, P. P. & Zavattaro, L. 2019. Simple, efficient and robust techniques for automatic multi-objective function parameterisation: Case studies of local and global optimisation using APSIM. *Environmental Modelling & Software*, 117, 109-133.
- Hasan, M., Akhter, S., Chowdhury, M., Chaki, A., Chawdhery, M. & Zahan, T. 2019. Prediction of changing climatic effect and risk management by using simulation approaches for rice-wheat system in Bangladesh. *Bangladesh Journal of Agricultural Research*, 44, 311-326.
- Hock, R., Rasul, G., Adler, C., Cáceres, B., Gruber, S., Hirabayashi, Y., Jackson, M., Kääh, A., Kang, S., Kutuzov, S., Milner, A., Molau, U., Morin, S., Orlove, B. & Steltzer, H. 2019. High mountain areas. In: *IPCC Special Report on the Ocean and Cryosphere in a Changing Climate* [H.-O. Pörtner, D.C. Roberts, V. Masson-Delmotte, P. Zhai, M. Tignor, E. Poloczanska, K. Mintenbeck, A. Alegría, M. Nicolai, A. Okem, J. Petzold, B. Rama, N.M. Weyer (eds.)]. In press.
- Holzworth, D., Huth, N. I., Fainges, J., Brown, H., Zurcher, E., Cichota, R., Verrall, S., Herrmann, N. I., Zheng, B. & Snow, V. 2018. APSIM Next Generation: Overcoming

- challenges in modernising a farming systems model. *Environmental Modelling & Software*, 103, 43-51.
- Hossain, F., Biswas, N., Ashraf, M. & Bhatti, A. Z. 2017. Growing more with less using cell phones and satellite data. *EoS*, 98 [Online]. Available: <https://doi.org/10.1029/2017EO075143> [Accessed 6th July 2017].
- Houshmandfar, A., Fitzgerald, G. J., O'leary, G., Tausz-Posch, S., Fletcher, A. & Tausz, M. 2018. The relationship between transpiration and nutrient uptake in wheat changes under elevated atmospheric CO₂. *Physiologia plantarum*, 163, 516-529.
- Humphreys, E., Meisner, C., Gupta, R., Timsina, J., Hg, B., Lu, T. Y., Ma, G., Masih, I., Guo, Z. J. & Ja, T. 2005. Water saving in rice-wheat systems. *Plant Production Science*, 8, 242-258.
- Ibrahim, A., Harrison, M. T., Meinke, H. & Zhou, M. 2019. Examining the yield potential of barley near-isogenic lines using a genotype by environment by management analysis. *European Journal of Agronomy*, 105, 41-51.
- Idnani, L. & Kumar, A. 2013. Performance of wheat (*Triticum aestivum*) under different irrigation schedules and sowing methods. *The Indian Journal of Agricultural Sciences*, 83.
- Immerzeel, W. W., Van Beek, L., Konz, M., Shrestha, A. & Bierkens, M. 2012. Hydrological response to climate change in a glacierized catchment in the Himalayas. *Climatic change*, 110, 721-736.
- Indian Standards Institution 1980. Indian Standard Code of Practice for Measurement of Seepage Losses from Canals Part II: Inflow-outflow Method (IS:9452 (Part II)-1980. Indian Standards Institution, New Delhi.
- Ippc 2007. *Climate Change 2007: The Physical Science Basis. Contribution of Working Group I to the Fourth Assessment Report of the Intergovernmental Panel on Climate Change.*, Cambridge University Press, Cambridge, United Kingdom and New York, NY, USA, 996 pp.
- Ippc 2013. *Climate Change 2013: The Physical Science Basis. Contribution of Working Group I to the Fifth Assessment Report of the Intergovernmental Panel on Climate Change.*, Cambridge University Press, Cambridge, United Kingdom and New York, NY, USA, 1535 pp.
- Ippc 2014. *Climate Change 2014: Synthesis Report. Contribution of Working Groups I, II and III to the Fifth Assessment Report of the Intergovernmental Panel on Climate Change.*, IPCC, Geneva, Switzerland, 151 pp.

Jurriens, M., Mollinga, P. P. & Wester, P. 1996. *Scarcity by design: protective irrigation in India and Pakistan*, International Institute for Land Reclamation and Improvement (ILRI).

Kabir, M. J., Gaydon, D. S., Cramb, R. & Roth, C. H. 2018. Bio-economic evaluation of cropping systems for saline coastal Bangladesh: I. Biophysical simulation in historical and future environments. *Agricultural Systems*, 162, 107-122.

Kaini, S., Gardner, T. & Sharma, A. K. 2020a. Assessment of socio-economic factors impacting on the cropping intensity of an irrigation scheme in developing countries. *Irrigation and Drainage*, 69, 363-375. <https://doi.org/10.1002/ird.2427>.

Kaini, S., Nepal, S., Pradhananga, S., Gardner, T. & Sharma, A. K. 2020b. Impacts of climate change on the flow of the transboundary Koshi River, with implications for local irrigation. *International Journal of Water Resources Development*, 1-26.

Kaini, S., Nepal, S., Pradhananga, S., Gardner, T. & Sharma, A. K. 2020c. Impacts of climate change on the flow of the transboundary Koshi River, with implications for local irrigation. *International Journal of Water Resources Development*, 1-26, <https://doi.org/10.1080/07900627.2020.1826292>.

Kaini, S., Nepal, S., Pradhananga, S., Gardner, T. & Sharma, A. K. 2020d. Representative General Circulation Models selection and downscaling of climate data for the transboundary Koshi river basin in China and Nepal. *International Journal of Climatology*, 40, 4131–4149. <https://doi.org/10.1002/joc.6447>.

Keating, B. A., Carberry, P. S., Hammer, G. L., Probert, M. E., Robertson, M. J., Holzworth, D., Huth, N. I., Hargreaves, J. N., Meinke, H. & Hochman, Z. 2003. An overview of APSIM, a model designed for farming systems simulation. *European journal of agronomy*, 18, 267-288.

Khaliq, T., Gaydon, D. S., Cheema, M. & Gull, U. 2019. Analyzing crop yield gaps and their causes using cropping systems modelling—A case study of the Punjab rice-wheat system, Pakistan. *Field Crops Research*, 232, 119-130.

Khoi, D. N. 2016. Comparison of the HEC-HMS and SWAT hydrological models in simulating the stream flow. *Journal of Science and Technology*, 53, 189-195.

Kiesel, J., Gericke, A., Rathjens, H., Wetzig, A., Kakouei, K., Jähnig, S. C. & Fohrer, N. 2019. Climate change impacts on ecologically relevant hydrological indicators in three catchments in three European ecoregions. *Ecological engineering*, 127, 404-416.

Kilic, M. & Tuylu, G. I. 2011. Determination of water conveyance loss in the ahmetli regulator irrigation system in the lower Gediz Basin Turkey. *Irrigation and drainage*, 60, 579-589.

- Kim, H. D., Kim, J. T., Nam, W. H., Kim, S. J., Choi, J. Y. & Koh, B. S. 2016. Irrigation Canal Network Flow Analysis by a Hydraulic Model. *Irrigation and Drainage*, 65, 57-65.
- Kling, H., Fuchs, M. & Paulin, M. 2012. Runoff conditions in the upper Danube basin under an ensemble of climate change scenarios. *Journal of Hydrology*, 424, 264-277.
- Knoben, W. J., Freer, J. E. & Woods, R. A. 2019. Inherent benchmark or not? Comparing Nash–Sutcliffe and Kling–Gupta efficiency scores. *Hydrology and Earth System Sciences*, 23, 4323-4331.
- Krupnik, T. J., Ahmed, Z. U., Timsina, J., Shahjahan, M., Kurishi, A. A., Miah, A. A., Rahman, B. S., Gathala, M. K. & McDonald, A. J. 2015. Forgoing the fallow in Bangladesh's stress-prone coastal deltaic environments: Effect of sowing date, nitrogen, and genotype on wheat yield in farmers' fields. *Field Crops Research*, 170, 7-20.
- Lee, J., Sperber, K. R., Gleckler, P. J., Bonfils, C. J. & Taylor, K. E. 2019. Quantifying the agreement between observed and simulated extratropical modes of interannual variability. *Climate Dynamics*, 52, 4057-4089.
- Li, K., Yang, X., Liu, Z., Zhang, T., Lu, S. & Liu, Y. 2014. Low yield gap of winter wheat in the North China Plain. *European Journal of Agronomy*, 59, 1-12.
- Liu, H., Yang, J., Drury, C. A., Reynolds, W., Tan, C., Bai, Y., He, P., Jin, J. & Hoogenboom, G. 2011. Using the DSSAT-CERES-Maize model to simulate crop yield and nitrogen cycling in fields under long-term continuous maize production. *Nutrient cycling in agroecosystems*, 89, 313-328.
- Liu, J. & Savenije, H. H. 2008. Food consumption patterns and their effect on water requirement in China. *Hydrology and Earth System Sciences Discussions*, 12, 887-898.
- Liu, J., Xue, B. & Yan, Y. 2020a. The Assessment of Climate Change and Land-Use Influences on the Runoff of a Typical Coastal Basin in Northern China. *Sustainability*, 12, 10050.
- Liu, K., Harrison, M. T., Hunt, J., Angessa, T. T., Meinke, H., Li, C., Tian, X. & Zhou, M. 2020b. Identifying optimal sowing and flowering periods for barley in Australia: A modelling approach. *Agricultural and Forest Meteorology*, 282, 107871.
- Lobell, D. B., Burke, M. B., Tebaldi, C., Mastrandrea, M. D., Falcon, W. P. & Naylor, R. L. 2008. Prioritizing climate change adaptation needs for food security in 2030. *Science*, 319, 607-610.
- Luo, Q. & Kathuria, A. 2013. Modelling the response of wheat grain yield to climate change: a sensitivity analysis. *Theoretical and applied climatology*, 111, 173-182.

Lutz, A. & Immerzeel, W. 2015. Reference Climate Dataset for the Indus, Ganges and Brahmaputra River Basins. *Report FutureWater , HI-AWARE Research Component 1*. HI-AWARE/FutureWater, The Netherlands.

Lutz, A., Immerzeel, W., Shrestha, A. & Bierkens, M. 2014. Consistent increase in High Asia's runoff due to increasing glacier melt and precipitation. *Nature Climate Change*, 4, 587.

Lutz, A. F., Ter Maat, H. W., Biemans, H., Shrestha, A. B., Wester, P. & Immerzeel, W. W. 2016. Selecting representative climate models for climate change impact studies: an advanced envelope-based selection approach. *International Journal of Climatology*, 36, 3988-4005.

Malano, H., Burton, M. & Makin, I. 2004. Benchmarking performance in the irrigation and drainage sector: a tool for change. *Irrigation and drainage*, 53, 119-133.

Malek, K., Adam, J. C., Stöckle, C. O. & Peters, R. T. 2018. Climate change reduces water availability for agriculture by decreasing non-evaporative irrigation losses. *Journal of Hydrology*, 561, 444-460.

Manjan, S. & Aggarwal, S. 2014. Hydrological modeling of Bagmati River Basin, Nepal. *International Journal of Current Engineering and Technology*, 4, 3978-3984.

Max-Planck Institute for Meteorology. 2018. *Overview Climate Data Operators*. [Online]. Available: <https://code.mpimet.mpg.de/projects/cdo/> [Accessed 15th August 2018].

Meehl, G. A., Covey, C., Delworth, T., Latif, M., Mcavaney, B., Mitchell, J. F., Stouffer, R. J. & Taylor, K. E. 2007. The WCRP CMIP3 multimodel dataset: A new era in climate change research. *Bulletin of the American Meteorological Society*, 88, 1383-1394.

Memon, A. A., Leghari, K. Q., Pathan, A. F., Khatri, K. L., Shah, S. A., Pinjani, K. K., Soomro, R. & Ansari, K. 2013. Design and evaluation of Dadu canal lining for sustainable water saving. *Journal of Water Resource and Protection*, 5, 689.

Milly, P. C. & Dunne, K. A. 2016. Potential evapotranspiration and continental drying. *Nature Climate Change*, 6, 946.

Ministry of Irrigation 2013. Irrigation Policy 2013. Kathmandu, Nepal: Government of Nepal.

Ministry of Water Resources 1997. Irrigation Policy 1992 (First Amendment 1997). Kathmandu, Nepal: His Majesty's Government of Nepal.

Ministry of Water Resources 2003. Irrigation Policy 2003. Kathmandu, Nepal: His Majesty's Government of Nepal.

Mirgol, B., Nazari, M. & Eteghadipour, M. 2020. Modelling climate change impact on irrigation water requirement and yield of winter wheat (*Triticum aestivum* L.), barley

(*Hordeum vulgare* L.), and fodder maize (*Zea mays* L.) in the semi-arid Qazvin Plateau, Iran. *Agriculture*, 10, 60.

Mishra, Y., Nakamura, T., Babel, M. S., Ninsawat, S. & Ochi, S. 2018. Impact of climate change on water resources of the Bheri River Basin, Nepal. *Water*, 10, 220.

Mofe 2019. Climate change scenarios for Nepal for National Adaptation Plan (NAP). Ministry of Forests and Environment, Kathmandu.

Moghazi, H. & Ismail, E.-S. 1997. A study of losses from field channels under arid region conditions. *Irrigation Science*, 17, 105-110.

Mohammadi, A., Rizi, A. P. & Abbasi, N. 2019. Field measurement and analysis of water losses at the main and tertiary levels of irrigation canals: Varamin Irrigation Scheme, Iran. *Global Ecology and Conservation*, 18, e00646.

Mohanty, M., Probert, M., Reddy, K. S., Dalal, R., Mishra, A., Rao, A. S., Singh, M. & Menzies, N. 2012. Simulating soybean–wheat cropping system: APSIM model parameterization and validation. *Agriculture, ecosystems & environment*, 152, 68-78.

Molden, D., Frenken, K., Barker, R., Fraiture, C. D., Mati, B., Svendsen, M., Sadoff, C., Finlayson, C. M., Attapatu, S. & Giordano, M. 2007. Trends in water and agricultural development. *Water for food, Water for Life: A compressive Assessment of Water Management in Agriculture*. Colombo: International Water Management Institute.

Moreno-Pérez, M. F. & Roldán-Cañas, J. 2013. Assessment of irrigation water management in the Genil-Cabra (Córdoba, Spain) irrigation district using irrigation indicators. *Agricultural water management*, 120, 98-106.

Moriasi, D. N., Arnold, J. G., Van Liew, M. W., Bingner, R. L., Harmel, R. D. & Veith, T. L. 2007. Model evaluation guidelines for systematic quantification of accuracy in watershed simulations. *Transactions of the ASABE*, 50, 885-900.

Motovilov, Y. G., Gottschalk, L., Engeland, K. & Rodhe, A. 1999. Validation of a distributed hydrological model against spatial observations. *Agricultural and Forest Meteorology*, 98, 257-277.

Nam, W.-H., Hong, E.-M. & Choi, J.-Y. 2016. Assessment of water delivery efficiency in irrigation canals using performance indicators. *Irrigation Science*, 34, 129-143.

National Oceanic and Atmospheric Administration. 2018. *The First Climate Model* [Online]. National Ocean Service, National Oceanic and Atmospheric Administration, U.S. Department of Commerce. Available: https://celebrating200years.noaa.gov/breakthroughs/climate_model/welcome.html [Accessed 24 September 2018].

- National Planning Commission 2012. Impact Evaluation of Sunsari Morang Irrigation Project. Project Research and Engineering Associates / National Planning Commission, Kathmandu.
- Ncvst 2009. Vulnerability through the eyes of the vulnerable: climate change induced uncertainties and Nepal's development predicaments. *Institute for Social and Environmental Transition, Nepal (ISET-N), Kathmandu and Institute for Social and Environmental Transition (ISET, Boulder, Colorado) for Nepal Climate Vulnerability Study Team (NCVST) Kathmandu.*
- Neitsch, S. L., Arnold, J. G., Kiniry, J. R. & Williams, J. R. 2011. Soil and water assessment tool theoretical documentation version 2009. Texas Water Resources Institute.
- Nepal, S. 2016. Impacts of climate change on the hydrological regime of the Koshi river basin in the Himalayan region. *Journal of Hydro-environment Research*, 10, 76-89.
- Neupane, R. P., Yao, J. & White, J. D. 2014. Estimating the effects of climate change on the intensification of monsoonal-driven stream discharge in a Himalayan watershed. *Hydrological processes*, 28, 6236-6250.
- Nie, Y., Pritchard, H. D., Liu, Q., Hennig, T., Wang, W., Wang, X., Liu, S., Nepal, S., Samyn, D. & Hewitt, K. 2021. Glacial change and hydrological implications in the Himalaya and Karakoram. *Nature Reviews Earth & Environment*, 1-16.
- Ojeda-Bustamante, W., Ontiveros-Capurata, R. E., Flores-Velázquez, J. & Iñiguez-Covarrubias, M. 2017. Changes in water demands under adaptation actions to climate change in an irrigation district. *Journal of Water and Climate Change*, 8, 191-202.
- Pandey, V. P., Dhaubanjari, S., Bharati, L. & Thapa, B. R. 2019. Hydrological response of Chamelia watershed in Mahakali Basin to climate change. *Science of the Total Environment*, 650, 365-383.
- Panofsky, H. A. & Brier, G. W. 1968. *Some applications of statistics to meteorology*, Pennsylvania State University Press, University Park, Mineral Industries Extension Services, College of Mineral Industries.
- Paudel, K. P. 2010. *Role of sediment in the design and management of irrigation canals*. PhD, UNESCO-IHE, Institute for Water Education, Delft, The Netherlands.
- Peake, A., Huth, N., Carberry, P., Raine, S. & Smith, R. 2014. Quantifying potential yield and lodging-related yield gaps for irrigated spring wheat in sub-tropical Australia. *Field Crops Research*, 158, 1-14.

- Pembleton, K., Cullen, B., Rawnsley, R., Harrison, M. & Ramilan, T. 2016. Modelling the resilience of forage crop production to future climate change in the dairy regions of Southeastern Australia using APSIM. *Journal of Agricultural Science*, 154, 1131-1152.
- Pereira, L. S. 2017. Water, agriculture and food: challenges and issues. *Water Resources Management: An International Journal, Published for the European Water Resources Association (EWRA)*, 31, 2985-2999.
- Peterson, T. 2005. Climate change indices. *World Meteorological Organization (WMO) bulletin*, 54, 83-86.
- Phelan, D. C., Harrison, M. T., Kemmerer, E. P. & Parsons, D. 2015. Management opportunities for boosting productivity of cool-temperate dairy farms under climate change. *Agricultural Systems*, 138, 46-54.
- Pickler, C. & Mölg, T. GCM Selection for Detection and Attribution of climate change at the summit of a tropical high mountain. EGU General Assembly Conference Abstracts, 2018. 3514.
- Pierce, D. W., Barnett, T. P., Santer, B. D. & Gleckler, P. J. 2009. Selecting global climate models for regional climate change studies. *Proceedings of the National Academy of Sciences*, pnas. 0900094106.
- Piniewski, M., Szcześniak, M., Huang, S. & Kundzewicz, Z. W. 2018. Projections of runoff in the Vistula and the Odra river basins with the help of the SWAT model. *Hydrology Research*, 49, 303-317.
- Pundarikanthan, N. & Santhi, C. 1996. Irrigation scheduling in a developing country: experiences from Tamil Nadu, India. *Food and Agriculture Organization of the United Nations (FAO)*.
- Rajbhandari, R., Shrestha, A. B., Nepal, S. & Wahid, S. 2016. Projection of future climate over the Koshi River basin based on CMIP5 GCMs. *Atmospheric and Climate Sciences*, 6, 190.
- Rajbhandari, R., Shrestha, A. B., Nepal, S., Wahid, S. & Ren, G.-Y. 2017. Extreme climate projections over the transboundary Koshi River Basin using a high resolution regional climate model. *Advances in Climate Change Research*, 8, 199-211.
- Ramankutty, N., Mehrabi, Z., Waha, K., Jarvis, L., Kremen, C., Herrero, M. & Rieseberg, L. H. 2018. Trends in global agricultural land use: implications for environmental health and food security. *Annual review of plant biology*, 69, 789-815.

- Renault, D. & Wahaj, R. 2006. MASSCOT: a methodology to modernize irrigation services and operations in canal systems. *Applications to two systems in Nepal Terai: Sunsari Morang Irrigation System and Narayani Irrigation System*. FAO. Rome, 1-42.
- Rossman, L. A. 2016. Storm Water Management Model Reference Manual Volume I – Hydrology (Revised). U.S. Environmental Protection Agency, USA.
- Rossman, L. A. 2017. Storm Water Management Model Reference Manual Volume II – Hydraulics. U.S. Environmental Protection Agency, USA.
- Rotich, S. C. & Mulungu, D. M. 2017. Adaptation to climate change impacts on crop water requirements in Kikafu Catchment Tanzania. *Journal of Water and Climate Change*, jwc2017058.
- Rstudio Team 2016. RStudio: Integrated Development for R. RStudio, Inc., Boston, MA.
- Saha, P. P., Zeleke, K. & Hafeez, M. 2019. Impacts of land use and climate change on streamflow and water balance of two sub-catchments of the Murrumbidgee River in South Eastern Australia. *Extreme Hydrology and Climate Variability*. Elsevier.
- Salah Abd Elmoaty, M. & El-Samman, T. 2020. Manning roughness coefficient in vegetated open channels. *Water Science*, 34, 124-131.
- Salman, S. A., Shahid, S., Ismail, T., Ahmed, K. & Wang, X.-J. 2018. Selection of climate models for projection of spatiotemporal changes in temperature of Iraq with uncertainties. *Atmospheric research*, 213, 509-522.
- Santhi, C., Arnold, J. G., Williams, J. R., Dugas, W. A., Srinivasan, R. & Hauck, L. M. 2001. Validation of the swat model on a large river basin with point and nonpoint sources 1. *JAWRA Journal of the American Water Resources Association*, 37, 1169-1188.
- Schoenfelder, C., Kenner, S. & Hoyer, D. Hydraulic Model of the Belle Fourche Irrigation District Using EPA SWMM 5.0. World Environmental and Water Resource Congress 2006: Examining the Confluence of Environmental and Water Concerns, 2006. 1-10.
- Schultz, B., Tardieu, H. & Vidal, A. 2009. Role of water management for global food production and poverty alleviation. *Irrigation and drainage*, 58.
- Seager, R., Ting, M., Held, I., Kushnir, Y., Lu, J., Vecchi, G., Huang, H.-P., Harnik, N., Leetmaa, A. & Lau, N.-C. 2007. Model projections of an imminent transition to a more arid climate in southwestern North America. *Science*, 316, 1181-1184.
- Setegn, S. G., Srinivasan, R. & Dargahi, B. 2008. Hydrological modelling in the Lake Tana Basin, Ethiopia using SWAT model. *The Open Hydrology Journal*, 2.

- Shin, J.-H., Nam, W.-H., Bang, N.-K., Kim, H.-J., An, H.-U., Do, J.-W. & Lee, K.-Y. 2020a. Assessment of water distribution and irrigation efficiency in agricultural reservoirs using SWMM model. *Journal of the Korean Society of Agricultural Engineers*, 62, 1-13.
- Shin, J.-H., Nam, W.-H., Bang, N.-K., Kim, H.-J., An, H.-U. & Lee, K.-Y. 2020b. Assessment of Irrigation Efficiency and Water Supply Vulnerability Using SWMM. *Journal of The Korean Society of Agricultural Engineers*, 62, 73-83.
- Shiru, M. S., Chung, E.-S., Shahid, S. & Alias, N. 2020. GCM selection and temperature projection of Nigeria under different RCPs of the CMIP5 GCMS. *Theoretical and Applied Climatology*, 141, 1611-1627.
- Shrestha, A. B. & Aryal, R. 2011. Climate change in Nepal and its impact on Himalayan glaciers. *Regional Environmental Change*, 11, 65-77.
- Shrestha, M. K., Recknagel, F., Frizenschaf, J. & Meyer, W. 2017. Future climate and land uses effects on flow and nutrient loads of a Mediterranean catchment in South Australia. *Science of the Total Environment*, 590, 186-193.
- Shrestha, S., Gyawali, B. & Bhattarai, U. 2013. Impacts of climate change on irrigation water requirements for rice–wheat cultivation in Bagmati River Basin, Nepal. *Journal of Water and Climate Change*, 4, 422-439.
- Shrestha, S., Shrestha, M. & Babel, M. S. 2016. Modelling the potential impacts of climate change on hydrology and water resources in the Indrawati River Basin, Nepal. *Environmental Earth Sciences*, 75, 280.
- Sida, T. S., Baudron, F., Kim, H. & Giller, K. E. 2018. Climate-smart agroforestry: *Faidherbia albida* trees buffer wheat against climatic extremes in the Central Rift Valley of Ethiopia. *Agricultural and forest meteorology*, 248, 339-347.
- Sillmann, J., Kharin, V., Zhang, X., Zwiers, F. & Bronaugh, D. 2013a. Climate extremes indices in the CMIP5 multimodel ensemble: Part 1. Model evaluation in the present climate. *Journal of Geophysical Research: Atmospheres*, 118, 1716-1733.
- Sillmann, J., Kharin, V., Zwiers, F., Zhang, X. & Bronaugh, D. 2013b. Climate extremes indices in the CMIP5 multimodel ensemble: Part 2. Future climate projections. *Journal of Geophysical Research: Atmospheres*, 118, 2473-2493.
- Singh, B., Gaydon, D., Humphreys, E. & Eberbach, P. 2011. The effects of mulch and irrigation management on wheat in Punjab, India—Evaluation of the APSIM model. *Field Crops Research*, 124, 1-13.
- Singh, B., Humphreys, E., Yadav, S. & Gaydon, D. 2015. Options for increasing the productivity of the rice–wheat system of north-west India while reducing groundwater

depletion. Part 1. Rice variety duration, sowing date and inclusion of mungbean. *Field Crops Research*, 173, 68-80.

Soltani, A. & Sinclair, T. R. 2015. A comparison of four wheat models with respect to robustness and transparency: Simulation in a temperate, sub-humid environment. *Field Crops Research*, 175, 37-46.

Subramanya, K. 2007. *Engineering Hydrology, Second edition.*, Tata McGraw-Hill Publishing Company Limited, India.

Sunsari Morang Irrigation Project 2015. Sunsari Morang Irrigation Project Maser Plan, Sunsari Morang Irrigation Project, Department of Irrigation, Nepal.

Swamee, P. K., Mishra, G. C. & Chahar, B. R. 2002. Design of minimum water-loss canal sections. *Journal of Hydraulic Research*, 40, 215-220.

Taylor, K. E., Stouffer, R. J. & Meehl, G. A. 2012. An overview of CMIP5 and the experiment design. *Bulletin of the American Meteorological Society*, 93, 485-498.

Tesfaye, K., Zaidi, P., Gbegbelegbe, S., Boeber, C., Getaneh, F., Seetharam, K., Erenstein, O. & Stirling, C. 2017. Climate change impacts and potential benefits of heat-tolerant maize in South Asia. *Theoretical and Applied Climatology*, 130, 959-970.

Thakuri, S. & Salerno, F. 2016. Glacio-Hydrological Simulation in Dudh Koshi River Basin, Nepal. *International Journal of Scientific Development and Research (IJS DR)*, 1, 72-78.

Thiemeßl, M. J., Gobiet, A. & Heinrich, G. 2012. Empirical-statistical downscaling and error correction of regional climate models and its impact on the climate change signal. *Climatic Change*, 112, 449-468.

Thiemeßl, M. J., Gobiet, A. & Leuprecht, A. 2011. Empirical-statistical downscaling and error correction of daily precipitation from regional climate models. *International Journal of Climatology*, 31, 1530-1544.

Tilman, D., Balzer, C., Hill, J. & Befort, B. L. 2011. Global food demand and the sustainable intensification of agriculture. *Proceedings of the National Academy of Sciences*, 108, 20260-20264.

Tisseuil, C., Vrac, M., Lek, S. & Wade, A. J. 2010. Statistical downscaling of river flows. *Journal of Hydrology*, 385, 279-291.

Trzaska, S. & Schnarr, E. 2014. A review of downscaling methods for climate change projections. *United States Agency for International Development by Tetra Tech ARD*, 1-42.

Unfccc 2011. Report of the Conference of the Parties on its sixteenth session, held in Cancun from 29 November to 10 December 2010. United Nations Framework Convention on Climate Change.

- Unfccc. 2018. *Status of Ratification of the Convention*. [Online]. the United Nations Framework Convention on Climate Change. Available: <https://unfccc.int/process/the-convention/what-is-the-convention/status-of-ratification-of-the-convention> [Accessed 14th August 2018].
- United States Geological Survey 1989. Guide for Selecting Manning's Roughness Coefficients for Natural Channels and Flood Plains. United States Geological Survey Water-Supply Paper 2339, USA.
- Van Liew, M. W., Veith, T. L., Bosch, D. D. & Arnold, J. G. 2007. Suitability of SWAT for the conservation effects assessment project: Comparison on USDA agricultural research service watersheds. *Journal of Hydrologic Engineering*, 12, 173-189.
- Van Vuuren, D. P., Edmonds, J., Kainuma, M., Riahi, K., Thomson, A., Hibbard, K., Hurtt, G. C., Kram, T., Krey, V. & Lamarque, J.-F. 2011a. The representative concentration pathways: an overview. *Climatic change*, 109, 5.
- Van Vuuren, D. P., Stehfest, E., Den Elzen, M. G., Kram, T., Van Vliet, J., Deetman, S., Isaac, M., Goldewijk, K. K., Hof, A. & Beltran, A. M. 2011b. RCP2. 6: exploring the possibility to keep global mean temperature increase below 2°C. *Climatic Change*, 109, 95.
- Van Vuuren, D. P., Stehfest, E., Den Elzen, M. G., Van Vliet, J. & Isaac, M. 2010. Exploring IMAGE model scenarios that keep greenhouse gas radiative forcing below 3 W/m² in 2100. *Energy Economics*, 32, 1105-1120.
- Water and Energy Commission Secretariate 2005. National Water Plan. Water and Energy Commission Secretariate, Government of Nepal, Kathmandu, Nepal.
- Wester, P., Mishra, A., Mukherji, A. & Shrestha, A. B. 2019. *The Hindu Kush Himalaya Assessment—Mountains, Climate Change, Sustainability and People.*, Springer Nature Switzerland AG, Cham.
- Wijngaard, R. R., Lutz, A. F., Nepal, S., Khanal, S., Pradhananga, S., Shrestha, A. B. & Immerzeel, W. W. 2017. Future changes in hydro-climatic extremes in the Upper Indus, Ganges, and Brahmaputra River basins. *PloS one*, 12, e0190224.
- Wilby, R. L. & Wigley, T. 1997. Downscaling general circulation model output: a review of methods and limitations. *Progress in physical geography*, 21, 530-548.
- Wilkinson, R. W. 1985. Plastic lining on riverton unit, Wyoming. *Journal of irrigation and drainage engineering*, 111, 287-298.
- Willems, P. & Vrac, M. 2011. Statistical precipitation downscaling for small-scale hydrological impact investigations of climate change. *Journal of hydrology*, 402, 193-205.

- Wood, A. W., Leung, L. R., Sridhar, V. & Lettenmaier, D. 2004. Hydrologic implications of dynamical and statistical approaches to downscaling climate model outputs. *Climatic change*, 62, 189-216.
- Worstell, R. V. 1976. Estimating seepage losses from canal systems. *Proceedings of the American Society of Civil Engineers, Journal of the Irrigation and Drainage Division*, 102, 137-147.
- Yan, B., Fang, N., Zhang, P. & Shi, Z. 2013. Impacts of land use change on watershed streamflow and sediment yield: An assessment using hydrologic modelling and partial least squares regression. *Journal of Hydrology*, 484, 26-37.
- Yan, R., Cai, Y., Li, C., Wang, X. & Liu, Q. 2019. Hydrological responses to climate and land use changes in a watershed of the Loess Plateau, China. *Sustainability*, 11, 1443.
- Yuan, Z., Yan, D., Yang, Z., Yin, J., Breach, P. & Wang, D. 2016. Impacts of climate change on winter wheat water requirement in Haihe River Basin. *Mitigation and Adaptation Strategies for Global Change*, 21, 677-697.
- Zhang, Y., Feng, L., Wang, J., Wang, E. & Xu, Y. 2013. Using APSIM to explore wheat yield response to climate change in the North China Plain: the predicted adaptation of wheat cultivar types to vernalization. *The Journal of Agricultural Science*, 151, 836.
- Zhao, G., Bryan, B. A. & Song, X. 2014a. Sensitivity and uncertainty analysis of the APSIM-wheat model: Interactions between cultivar, environmental, and management parameters. *Ecological Modelling*, 279, 1-11.
- Zhao, Z., Wang, E., Wang, Z., Zang, H., Liu, Y. & Angus, J. F. 2014b. A reappraisal of the critical nitrogen concentration of wheat and its implications on crop modeling. *Field Crops Research*, 164, 65-73.
- Zheng, B., Chenu, K., Doherty, A. & Chapman, S. 2015. The APSIM-Wheat Module (7.5 R3008). The Commonwealth Scientific and Industrial Research Organisation (CSIRO) and Queensland State Government agencies, Australia.